

Applications of Graph Cutting for Probabilistic  
Characterization of Microstructures in Ferrous Alloys

Dissertation

Presented in Partial Fulfillment of the Requirements for the Degree  
Doctor of Philosophy in the Graduate School of The Ohio State  
University

By

Alexander Frederick Brust, B.S., M.S.

Graduate Program in Materials Science and Engineering

The Ohio State University

2019

Dissertation Committee:

Stephen R. Niezgoda, Advisor

Antonio J. Ramirez

Yunzhi Wang

Nick Brunelli

Eric J. Payton

© Copyright by

Alexander Frederick Brust

2019

## Abstract

Processing of martensitic steels requires a thermally driven phase transformation into the austenite phase field, where rapid cooling initiates the diffusionless transformation into martensite. The resultant microstructural constituent is a hard, brittle phase that requires subsequent heat treatment to soften the material for optimized mechanical properties. Although the transformation microstructure has the largest influence on these mechanical properties, the prior austenite microstructure has been shown to significantly affect the final product material in the form of ductile to brittle fracture occurrence, classification of creep and cavitation sites, increasing martensite packet and block sizes resulting in Hall-Petch effects, and temper embrittlement. Therefore, reconstruction of the prior austenite phase field can help optimize both the processing of a sample steel or binary ferrous alloy and predicitve examinations on the material.

However, analysis of the austenite to martensite transformation is hindered by the large volume of noise associated with the transformation. This can be attributed to the scale of the transformation, which results in a single prior austenite grain producing up to 24 martensitic variants; the plasticity associated with the massive formation of martensite; variations in the orientation relationship across variable compositions and morphologies; errors associated with the EBSD-indexing of the transformation microstructure; and annealing twins forming across the prior austenite microstructure.

Due to the inherent noise associated with the transformation, modern reconstruction algorithms using point-to-point or flood-fill algorithms struggle to produce accurate and consistent reconstructions of the austenite microstructure. We therefore propose a probabilistic approach to austenite reconstruction in steels and ferrous alloys based on the graph cutting algorithm. This technique can be applied to a number of inverse problems in materials science, such as image segmentation, microstructure phase and constituent segmentation, atomic cluster identification from atom probe tomography data sets, and the reconstruction of the parent microstructure from the EBSD-indexed post-transformation data set.

The chosen algorithm used an energy-minimization technique known as graph cutting to perform the reconstructions. In order to most properly describe the algorithm, information related to the misorientation relationships between martensite variants associated with the same prior austenite grain or twin were utilized. Additionally, an accurate and automated measurement of the orientation relationship for the desired steel data sets was performed through a Bayesian implementation and used conditionally within the reconstruction algorithm. This information was used to perform automated reconstructions on the prior austenite microstructure from transformation martensite. Analysis of a number of steel and binary ferrous alloy data sets with variable orientation relationships was then performed to assess the range of the technique, as well as an analysis on the amount of noise that could be handled within a single data set and the identification of twins across the microstructure. Additionally, segmentations were performed to extract the packet boundaries residing within both a large and small PAG, as well as an analysis on a parent-twin system to identify packets containing shared variants.

It was found that the technique can sufficiently produce reasonable, probabilistically defined reconstructions of the prior austenite microstructure, even with the addition of copious amounts of noise. Additionally, it further separated itself from existing techniques through its ability to capture a number of prior austenite twins spanning across the parent grains. Validation was performed through both comparisons to an optical micrograph of the same chemically etched steel and comparison of retained austenite orientations associated with surrounding, reconstructed grains. A comparison to a manual segmentation was also performed, along with crystallographic analysis on the packet segmentations in order to compare the experimentally segmented martensite orientations with their theoretical counterparts.

This thesis is dedicated to the memories of my deda, Protopresbyter-stavrophor Dr. Mateja Matejic—a profoundly intelligent man whose influence over me is ineffable, and whose legacy is fit for history books, as well as his beloved Protopresbytera Ljubica, my baba. Additionally, to my grandparents Frederick and Theresa Brust, and my aunt Kathy Ladebue. And finally, to my friend Nikolas Heidel, whose warm smile, wicked sense of humor, and general affability endeared him to the hearts and souls of anyone privileged enough to know him—Vjecnaja Pamjat.

## Acknowledgments

First and foremost, I would like to thank my beautiful wife, Lauren, whose love and support has shown no bounds. From cooking our meals after 10 hour shifts at the hospital to cleaning the house of the mess I mostly created, I don't know why the hell you married me but I am forever grateful for you, even if I sometimes fail at expressing that. This is a shared accomplishment, as without you, this thesis doesn't exist. At my wife's behest, I'll also acknowledge my dog, Nora, for the long walks that helped ease my active mind as I laboriously wrote this, and my cat, Lucy, who may have contributed a few errors to this thesis from constantly walking on my keyboard.

I would also like to thank my father, Dr. Frederick Brust, an inspiration who explained to me early on that he was too stupid to realize he was too stupid to get his PhD—I guess the apple really doesn't fall too far from the tree. I would also like to thank my mother, Milica Brust, whose blunt criticisms coupled with her constant support and unconditional love have morphed me into the man I am today. Additionally, to my brothers, Zachary Brust and Nenad Resonavic, who have always been constant pillars to me as I pursued in my pursuit of my goals, my parents-in-law, Craig and Kerri Stump, as well as the rest of my large, supportive, and oftentimes wild family. Finally, I would like to thank all of my friends for all of the gatherings and many, many beers.

I would like to thank my graduate research group, especially my colleagues Dr. Mengfei Yuan, (rock star and likely future Dr.) Nicholas Galbincea, (future Dr.) Denielle Ricciardo and, most notably, Dr. Thaddeus Song-En Low. Your support, company, and friendship have been critical in assisting me to this point. Additionally, to (future Dr.) Alejandro Hinojos, our adopted graduate student, and Dr. Collin Whitt for their friendship, as well as the rest of the Mill's group for welcoming this computational guy into their prestigious clique. I would also like to acknowledge Toren Hobbs, Dr. Victoria Yardley, and Dr. Vikas Sinha for their various contributions to my work.

I would also like to thank the committee, Professor Yunzhi Wang, Professor Antonio Ramirez, and Professor Nicholas Brunelli, for taking the time to read this and serve on my committee, and Dr. Eric Payton, who served as a collaborator and undocumented co-advisor—your mentorship and friendship is most greatly appreciated. Last but not least, I would like to thank my advisor, Dr. Stephen Niezgoda—who took in a kid with no mechanical, materials, nor computational background and assisted him to this point. I'm forever grateful for your patience, tutelage, friendship, and the many beers you've bought for me. I think I owe you the first round for life.

## Vita

2014 .....	B.S. Chemistry, The Ohio State University
2017 .....	M.S. Materials Science and Engineering, The Ohio State University
2014-present .....	Graduate Research Assistant, The Ohio State University.

## Publications

### Research Publications

- A. Brust, S.R. Niezgoda, V.A. Yardley and E.J. Payton “Analysis of Misorientation Relationships between Austenite Parents and Twins”. *Metallurgical and Materials Transactions A*, 50(4):837–855, Feb. 2019.
- A. Brust, E.J. Payton, T.J. Hobbs and S.R. Niezgoda “Application of the Maximum Flow–Minimum Cut Algorithm to Segmentation and Clustering of Materials Datasets”. *Mictroscopy and Microanalysis*, Under Review.
- A. Brust, E.J. Payton, V. Sinha, V.A. Yardley and S.R. Niezgoda “Characterization of Martensite Orientation Relationships in Steels and Ferrous Alloys from EBSD Data using Bayesian Inference”. *Metallurgical and Materials Transactions A*, Under Review.
- A. Brust, E.J. Payton, T.J. Hobbs, V. Sinha and S.R. Niezgoda “Probabilistic Reconstruction of Austenite Microstructure from Electron Backscatter Diffraction Observations of Post-Transformation Martensite Using Graph Cutting”. *Mictroscopy and Microanalysis*, Under Review.

## **Fields of Study**

Major Field: Materials Science and Engineering

## Table of Contents

	Page
Abstract . . . . .	ii
Dedication . . . . .	v
Acknowledgments . . . . .	vi
Vita . . . . .	viii
List of Tables . . . . .	xiv
List of Figures . . . . .	xvi
1. Introduction . . . . .	1
2. Background . . . . .	5
2.1 Inverse Problems in Materials Science . . . . .	5
2.2 Regularization and Bayesian Estimation . . . . .	7
2.3 Graph Cutting . . . . .	9
2.3.1 Graph Cut Notation . . . . .	12
2.3.2 Min-Cut/Max-Flow . . . . .	13
2.3.3 Graph Cutting Algorithm . . . . .	14
2.4 Austenite → Martensite Transformation . . . . .	15
2.4.1 Martensite Morphology . . . . .	17
2.4.2 Crystallography of Austenite to Martensite Transformation	21
2.5 Outline and Motivation . . . . .	24

3.	Application of the Maximum Flow–Minimum Cut Algorithm to Segmentation and Clustering of Materials Datasets . . . . .	28
3.1	Introduction . . . . .	28
3.2	Image Segmentation . . . . .	29
3.2.1	Graph Definition for Segmentation and Clustering . . . . .	30
3.2.2	Segmentation Examples . . . . .	33
3.3	Microstructure Phase Segmentation and Identification . . . . .	40
3.3.1	Identification and Segmentation of Bainite and Martensite .	40
3.3.2	Prior Austenite Grain Identification . . . . .	46
3.4	Atomic Clustering . . . . .	52
3.5	Discussion . . . . .	60
3.6	Conclusion . . . . .	63
4.	Analysis of Misorientation Relationships between Austenite Parents and Twins . . . . .	65
4.1	Introduction . . . . .	65
4.2	Materials and Methodology . . . . .	66
4.3	Results . . . . .	69
4.3.1	Kurdjumov-Sachs Orientation Relationship With Cubic Symmetry . . . . .	69
4.3.2	Nishiyama-Wassermann Orientation Relationship . . . . .	76
4.3.3	Experimentally Observed Orientation Relationship . . . . .	78
4.4	KS Orientation Relationship Considering Tetragonal Based Crystal Symmetry . . . . .	85
4.5	Discussion . . . . .	88
4.6	Conclusions . . . . .	92
5.	Characterization of Martensite Orientation Relationships in Steels and Ferrous Alloys from EBSD Data using Bayesian Inference . . . . .	94
5.1	Introduction . . . . .	94
5.2	Methodology . . . . .	96
5.2.1	Formulation of the Bayesian Inference Problem . . . . .	97
5.2.2	MAP estimate and Posterior distribution . . . . .	102
5.3	Results . . . . .	104
5.3.1	Variation of OR with Composition . . . . .	104
5.3.2	Effect of Varying Window Size During OR Estimation . . .	109
5.4	Correlation of $\xi$ Angles . . . . .	114
5.4.1	Reproducibility of OR Measurement . . . . .	116

5.5	Discussion . . . . .	117
5.6	Conclusion . . . . .	119
6.	Probabilistic Reconstruction of Austenite Microstructure from Electron Backscatter Diffraction Observations of Post-Transformation Martensite Using Graph Cutting . . . . .	120
6.1	Introduction . . . . .	120
6.2	Methodology and Implementation . . . . .	124
6.2.1	Graph Cutting . . . . .	125
6.3	Austenite Reconstruction Algorithm . . . . .	128
6.3.1	Martensite Space . . . . .	130
6.3.2	Austenite Space . . . . .	131
6.4	Results . . . . .	135
6.4.1	Pure-Space Reconstructions . . . . .	138
6.4.2	Algorithm Validation and Comparison to Optical Etch . . . . .	146
6.4.3	Algorithm Validation of Proposed Austenite Orientations . . . . .	149
6.4.4	Misindexed Points . . . . .	152
6.4.5	Twin Identification . . . . .	156
6.4.6	Variable Steel Compositions . . . . .	160
6.5	Discussion . . . . .	167
6.6	Conclusion . . . . .	177
7.	Application of Graph Cutting to Probabilistic Segmentation of Martensitic Packet Boundaries and Analysis of Shared Variants Across Parent-Twin Interfaces . . . . .	179
7.1	Introduction . . . . .	179
7.2	Methodology . . . . .	180
7.3	Results . . . . .	185
7.3.1	Packet Segmentation . . . . .	185
7.3.2	Packet Segmentation for Twin Analysis of Shared Variants . . . . .	192
7.4	Discussion . . . . .	196
7.5	Conclusion . . . . .	198
8.	Conclusions and Future Work . . . . .	199
8.1	Summary of Results . . . . .	199
8.1.1	Summary of Graph Cutting Implementation to Inverse Problems in Materials Science . . . . .	200
8.1.2	Summary of the Martensite Analysis of Misorientations Between Martensite Parent and Twin Variants . . . . .	201

8.1.3	Summary of the Measurement of the Orientation Relationship Via Bayesian Inference . . . . .	202
8.1.4	Summary of the Probabilistic Reconstruction of the Prior Austenite Microstructure from EBSD-Indexed Martensite Data Using the Graph Cutting Algorithm . . . . .	202
8.1.5	Summary of Application of Graph Cutting to Probabilistic Segmentation of Martensitic Packet Boundaries and Analysis of Shared Variants Across Parent-Twin Interfaces . . . . .	204
8.2	Outlook and Future Work . . . . .	205
8.2.1	Application of Graph Cutting to Additional Problems in Materials Science . . . . .	206
8.3	Extension of Graph Cutting to Identification of Shared Parent-Twin Austenite Variants . . . . .	209
8.3.1	Application of Reconstruction Algorithm to Ausforming Examples and Potential Limitations . . . . .	210
	Appendices . . . . .	214
A.	Martensite Misorientation Information . . . . .	214
A.1	Appendix . . . . .	214
A.2	KS-Cubic Orientation Relationship Misorientation Data . . . . .	214
A.3	NW-Cubic Orientation Relationship Misorientation Data . . . . .	217
A.4	Experimental-Cubic Orientation Relationship Misorientation Data . . . . .	218
A.5	KS-Tetragonal Orientation Relationship Misorientation Data . . . . .	222
A.6	Similar Misorientation Comparisons . . . . .	226
B.	Supplemental Material Related to Chapter 4 . . . . .	227
B.1	Kurdjumov-Sachs Orientation Relationship With Cubic Symmetry . . . . .	228
B.2	Experimentally Observed Orientation Relationship . . . . .	231
B.3	Kurdjumov-Sachs Orientation Relationship Applying Tetragonal Symmetry . . . . .	235
	Bibliography . . . . .	240

## List of Tables

<b>Table</b>	<b>Page</b>
3.1 The SNR values for the EM/MPM, Otsu threshold, and Graph Cutting segmentations . . . . .	39
3.2 Respective volume fractions for ferrite, bainite, and martensite using the graph cutting technique and KAM distribution deconvolution [153] method. . . . .	45
3.3 Scaling parameters corresponding to the cases displayed in Figure 3.9, where subscript BG represents favoring background atom designation and C is related to clusters . . . . .	57
3.4 The percentage of atoms removed from each synthetic cluster and dispersed within the background compared with the amount of flagged atoms in each cut cluster for the 10:1 BG:C ratio . . . . .	58
3.5 Scaling parameters corresponding to Figure 3.10, where atoms were randomly displaced from clusters and added to the background . . . . .	59
5.1 Bayesian measurement of ORs and corresponding halfwidth and OR distribution variance for the three samples compared with prior experimental measurements [177] (indicated by “P-Y”) and the KS, GT, and NW theoretical ORs. . . . .	107
5.2 Computationally determined $\xi$ angles for variable window sizes of the P122 steel sample, including number of data points for each window and the Payton-Yardley (P-Y) determined OR . . . . .	111
5.3 Computed ORs from five different grains within the same AF9628 steel specimen, with numbering corresponding to Figure 5.6 . . . . .	117

6.1 Comparative information for the martensite space, KS, three different austenite techniques and the mixed space reconstructions as well as the optically etched micrograph. . . . .	149
6.2 Regularization parameters for respective cases of misindexed points using the mixed reconstruction method. . . . .	156
A.1 Intra-parent misorientation list for KS orientation relationship considering cubic symmetry. . . . .	215
A.2 Parent-twin misorientation list for KS orientation relationship considering cubic symmetry. . . . .	215
A.3 Twin-twin misorientation list for KS orientation relationship considering cubic symmetry. . . . .	216
A.4 Misorientation list for NW orientation relationship with cubic symmetry.	218
A.5 intra-parent misorientation list for experimental orientation relationship considering cubic symmetry. . . . .	218
A.6 Parent-twin misorientation list for experimental orientation relationship applying cubic symmetry. . . . .	219
A.7 Twin-twin misorientation list for experimental orientation relationship using cubic symmetry. . . . .	220
A.8 intra-parent misorientation list for KS orientation relationship with respect to tetragonal symmetry. . . . .	222
A.9 Parent-twin misorientation list for KS orientation relationship with tetragonal symmetry. . . . .	223
A.10 Twin-twin misorientation list applying KS orientation relationship with tetragonal symmetry. . . . .	224
A.11 The possible misorientation pairs that may be indistinguishable upon experimental observation. KS-Cubic refers to KS orientation relationship assuming cubic symmetry, Low-C Expt. is the referenced experimental orientation relationship and KS-Tetrag as the KS orientation relationship assuming tetragonal symmetry. . . . .	226

## List of Figures

Figure	Page
2.1 Graph construction where $g$ is separated by the terminal nodes, $s$ and $t$ . The $t$ -link edges are colored in red and blue and the $n$ -link edges are colored in gray, with corresponding cut colored in green . . . . .	14
2.2 Occupation of the octahedral sites by carbon atoms results in the c-axis extension of the bcc unit cell, resulting in a bct crystal structure. Sourced from M. Cohen [37] . . . . .	17
2.3 Hierarchical structure of sub-blocks, blocks, and packets transformed from the same PAG. Sourced from Morito et al. [110] . . . . .	18
2.4 Plot of the morphology of martensite varying as a function of carbon content. Sourced from [87] . . . . .	19
2.5 FE-SEM/EBSD measurement of 0.2 wt.% C steel displaying lath martensite, sourced from Kitahara et al. [84] and a light optical micrograph (LOM) of 1.67 wt.% C steel exhibiting plate martensite embedded in an austenitic matrix, sourced by Stormvinter et al. [149] . . . . .	20
2.6 Schematic of the shearing produced by the martensite formation and subsequent rotational tilt at the surface. Sourced from [87] . . . . .	21
2.7 $\{100\}_\gamma$ pole figures and related variant ordering for the NW (top) and KS (bottom) orientation relationships. Sourced by Kitahara et al. [85] and Kitahara et al. [84] . . . . .	23
3.1 The graph setup utilized to solve the problems mentioned in this paper along with a specified, arbitrary case involving image segmentation . .	32
3.2 Input image, ground truth segmentation, and pixel-intensity histogram for the René 88DT dataset . . . . .	34

3.3	Series of segmented images using various segmentation techniques for the René 88DT dataset . . . . .	36
3.4	Segmentations and input texture for René 104 nickel-based superalloy . . . . .	38
3.5	Graph cut applied to segmentation of EBSD data from a multi-component steel microstructure (a) using IQ (b) and KAM map data (c). In (d), red corresponds to ferrite, blue corresponds to bainite, and green corresponds to martensite regions. . . . .	45
3.6	Segmentation of austenite grain from martensitic steel EBSD dataset. The color key in (a) is identical to that for the EBSD data in Figure 3.5a. . . . .	50
3.7	Grain boundary misorientation austenite reconstructions performed using MTEX [7] for five separate angular tolerances: 0.25° (top left), 0.75° (top middle), 1.25° (top right), 1.75° (bottom left) and 2.25° (bottom right) . . . . .	51
3.8	The graph schematic utilized to solve the problems mentioned in this paper along with a specified, arbitrary case involving image segmentation . . . . .	54
3.9	Variable background:clustered atom ratios with the corresponding graph cut solutions for a synthetic, 2D dataset . . . . .	56
3.10	Performance of graph cuts when removing clustered atoms and randomly dispersing them throughout the background. The number of clusters is consistent with those denoted in Table 3.4 . . . . .	58
3.11	The $k$ -means segmentations for the graph cut cases represented in Figure 3.9 with relative distance tolerances of 0.025 and 0.025 for the 1:1 and 10:1 background to cluster ratio, respectively. . . . .	60
4.1	Composition table exhibiting the possible variant-variant misorientations for prior intra-parent austenite grains. . . . .	70
4.2	The possible variant-variant misorientations for prior parent- $60^\circ[111]$ twin austenite grains. . . . .	71

4.3	Composition table exhibiting the possible variant-variant misorientations for differing twins that nucleated from the same parent austenite grain. . . . .	73
4.4	Misorientations directional axes overlayed on stereographic triangles for the KS orientation relationship for: (a) the intra-parent case, (b) the parent-twin case, and (c) and (d) the twin-twin case (split into two subfigures to reduce the density of points). . . . .	75
4.5	Full composition table derived from NW orientation relationship. The subfigure at the upper right can be identified within the full table and comprises the truncated portions at the upper left and lower right portions of the table, representing misorientations derived from intra-parent variant intersections. The key relates the variant numbers to the parent or twin type of the grain the martensite transformed from.	77
4.6	Stereographic triangle plotting all misorientation axes with colored points corresponding to degree of misorientation angle for the NW orientation relationship. . . . .	78
4.7	Composition table exhibiting intra-parent variant intersections given an experimentally determined orientation relationship. . . . .	79
4.8	Composition table displaying parent-twin variant intersections given an experimentally determined orientation relationship. . . . .	80
4.9	Composition table showing differing twin-twin variant intersections given an experimentally determined orientation relationship. . . . .	82
4.10	Misorientations directional axes overlayed on stereographic triangles for the experimentally-measured orientation relationship for: (a) the intra-parent case, (b) the parent-twin case, and (c) and (d) the twin-twin case (split into two subfigures to reduce density of points). . . .	83
4.11	Pole Figures containing variant orientations for the three orientation relationships: KS (left), NW, and Experimental (right), all considering cubic symmetry . . . . .	84
4.12	intra-parent composition table for tetragonal symmetry using KS orientation relationship. . . . .	86

4.13	Composition table exhibiting the possible variant-variant intersections for prior parent-twin austenite grains using tetragonal symmetry. . . . .	86
4.14	Composition table exhibiting the possible variant-variant intersections for differing twin-twin PAGs using tetragonal symmetry. . . . .	87
5.1	IPF maps for the low-C (top left), FV535 (top right), and Fe-30Ni (bottom) samples, with overlaying IPF key. . . . .	106
5.2	The set of variants for the theoretical ORs of KS, GT, and NW (far left column), martensite orientations rotated by the inverse of their respective austenite orientations and displayed on {001} pole figures for KS, GT, and NW (middle left column), the experimental martensite data for the low-C, FV535, and Fe-30Ni samples (middle right column) and the martensite points generated from the $\Xi, \kappa$ parameters from the input experimental data (far right column) . . . . .	110
5.3	IPF map of P122 martensitic steel containing variable window sizes of martensitic variants . . . . .	112
5.4	{001} martensitic pole figures on ASTM P122 12 wt%Cr steel sample for a selection of four variable windows . . . . .	114
5.5	Correlation plots and histogram distributions of computed $\xi$ angles for the low-C steel specimen . . . . .	115
5.6	Five labeled regions within five independent grains for the same AF9628 steel sample . . . . .	116
6.1	Graph construction where $g$ is separated by the terminal nodes, $s$ and $t$ . The $t$ -link edges are colored in red and blue and the $n$ -link edges are colored in gray, with corresponding cut colored in green. . . . .	127
6.2	Transformation microstructure for AF9628 sample (top) with reconstructions performed using the martensite space feature with the experimental OR (middle left) and the austenite space using the KS OR (bottom left) with adjacent likelihood maps. . . . .	140

6.3	$\{001\}_\gamma$ pole figures displaying the KS variants (left), the experimental OR variants (middle left), KS-generated noisy martensite orientations (middle right), and the experimental-OR generated noisy martensite orientations (right). . . . .	142
6.4	Austenite reconstructions and likelihood maps generated by only using the austenite space reconstruction algorithm for 756 iterations (top), 1042 iterations (middle), and 1472 iterations (bottom). . . . .	144
6.5	The post-transformation martensite microstructure (top left), mixed space austenite reconstruction (top right), corresponding likelihood plot with colorbar (bottom left) and optically etched micrograph image (bottom right). . . . .	147
6.6	The transformation microstructure (left), resultant reconstruction (middle), and corresponding likelihood plot with color bar (right) for the Fe 30 at. % Ni binary ferrous alloy. . . . .	151
6.7	Truncated portion of the original martensite data set (top left), same region with 25% (top middle right) and 50% (bottom left) of orientations misindexed with respective reconstructions to the immediate right of each figure. . . . .	153
6.8	Truncated portion of same data set in Figure 6.7 with 75% misindexed orientations (left), the reconstruction (middle) and the corresponding likelihood plot . . . . .	155
6.9	Parent (black) and $60^\circ \langle 111 \rangle$ twin (red) variants plotted on a $\{001\}_\gamma$ pole figure for the KS OR (left) and experimental OR (right). . . . .	157
6.10	An isolated parent-twin system presented as both the transformation variants (top left) and reconstructed austenite (top middle) with respective likelihood maps related to the parent orientation (top right) and the three rotational twins $\langle 111 \rangle$ (bottom left), $\langle \bar{1}\bar{1}1 \rangle$ (bottom middle), and $\langle \bar{1}11 \rangle$ (bottom right). . . . .	159
6.11	The post-transformation microstructure (left), austenite reconstruction (middle) and likelihood map for the KS-like low-C steel sample . . . . .	161



B2	Composition tables displaying misorientation information for parent variants intersecting with twin-generated variants omitted from the main manuscript. . . . .	230
B3	Remaining composition tables for twin-twin misorientations. . . . .	232
B4	Composition tables displaying misorientation information for twin-generated variants intersecting with themselves. . . . .	233
B5	Composition tables displaying misorientation information for parent variants intersecting with the remaining twin-generated variants for the experimental orientation relationship. . . . .	234
B6	Remaining composition tables for the twin-twin misorientations. . . .	236
B7	Composition tables showing misorientation information for twin-generated variants intersecting with themselves. . . . .	237
B8	Composition tables displaying misorientation information for parent variants intersecting with the remaining twin-generated variants for the KS orientation relationship applying tetragonal symmetry. . . . .	238
B9	Composition tables for remaining twin-twin misorientations. . . . .	239

## Chapter 1: Introduction

The manufacturing of low-carbon steel dates back to the Assyrian Colony Period at Kama-Kalehöyük, Turkey, from approximately 20<sup>th</sup> – 18<sup>th</sup> century B.C. [5]. As humans evolved, so did our employment of steel. From the main source of weaponry at the dawn of the Iron Age to its ubiquitous presence in buildings and bridges today, steel has ingrained itself one of the most important engineered materials in human existence. In fact, over 1 billion tons of steel are consumed annually, making it the most abundant metal used by man [15]. Defined as the solid solution of iron (Fe) and up to  $\sim 2\%$  carbon (C), steel is readily available due to the abundance of the former in the earth's crust and the latter in the universe. It is also cheap to manufacture whilst maintaining highly desirable mechanical properties, from corrosion resistance to high-strength structural applications.

Our need for steel stems from its inherent versatility. With over 3500 different grades of steel identified by the World Steel Association, it can be easily manipulated with the addition of numerous alloying elements and specific processing conditions in order to optimize it for a specific performance. It can be composed of several different phases and microstructural constituents, with the most important being the austenite phase ( $\gamma$ ), which exists as a face centered cubic (*fcc*) crystal structure mainly at high temperatures in low alloy steels. Austenite can sustain a high dissolution of

carbon and subsequently be cooled to produce the body centered cubic (*bcc*) ferrite ( $\alpha$ ) phase or a combination of phases and carbides. Of these combinations, one of the most universally attained is martensite ( $\alpha'$ ), a solid solution of body centered cubic/tetragonal iron and carbon. Martensite has a high hardness and, although brittle if left untreated, subsequent tempering increases ductility and overall strength of the steel [147].

The martensite transformation occurs from the rapid cooling of the material from the austenite phase field, resulting in a diffusionless, shear-induced transformation that produces 24 crystallographic variants. The morphology can therefore be either lath-like or plate-like depending on the composition of the steel, which can have substantial effects on the mechanical behavior [61, 88, 101, 113]. Additionally, the prior austenite microstructure also contributes to the mechanical properties of the transformation product, resulting in a need to characterize both the post-and pre-transformation microstructures [83, 175].

The reconstruction of pre-transformation microstructures from post-transformation data sets, such as  $\gamma$  from  $\alpha'$  in steels or  $\beta-Ti$  from  $\alpha-Ti$  in titanium, can be classified as an inverse problem in materials science. These are problems where desired information can only be inferred from observations on measurements containing significant noise which subsequently require an idealized model of the overarching measurement process. Additional examples of these types of problems in materials science include image segmentation, atomic cluster identification/indexing, and microstructure constituent segmentation, to name a few.

As such, encompassing models must therefore be able to sufficiently account for noise. Since inverse problems typically represent the data in the form of distributions, Bayesian Inference becomes an ideal technique to tackle them because it can inherently account for noise through the use of Bayes Theorem [11]. Consequently, an optimal computational method with close ties to Bayesian Statistics is a technique known as graph cutting [23, 24], a clustering algorithm that constructs a graph from a series of nodes (data points) and makes energy minimized cuts to effectively extract desired information. What makes the technique useful with regards to inverse problems is the clustering aspect, where probabilistically favorable data can be grouped together with noisy data based on common characteristics.

In terms of the  $\gamma \rightarrow \alpha'$  transformation, the specific details are muddled with noise for a variety of reasons. These include the magnitude of the variant transformation, which can result in  $n \times 24$  martensite variants for n austenite grains; the typically complete transformation of the austenite to martensite, requiring analysis on the austenite phase field to be inferred from observations on the transformation martensite; variation in the orientation relationship (OR) as a product of composition, and so on.

Because of this, chemical etchant techniques have been concocted to identify prior austenite grain boundaries (PAG) for several compositions [45, 78, 104, 161, 184], but the process is time-consuming, inconsistent, and requires steels with a substantial amount of Phosphorous impurity content and large grain sizes, all factors that typically deter the corresponding mechanical properties. Conversely, existing computational algorithms have similarly struggled to amend the aforementioned hindrances [14, 31, 36, 65, 105, 150]. This results in incomplete and noisy reconstructions

that can only handle small portions of the representative transformation microstructure.

These limitations are oftentimes due to common approximations of the OR and point-to-point methodologies that fail to effectively group like-martensite variants together. Therefore, the purpose of this work is to introduce an existing clustering technique known as graph cutting as a new application to a variety of inverse problems in materials science, such as image segmentation, atomic cluster identification, and microstructure phase and feature segmentation. The notable emphasis lies on the reconstruction of the prior austenite microstructure from transformed martensite, as well as the characterization of martensite packets from user-selected PAGs.

## Chapter 2: Background

Since the reconstruction of austenite from EBSD-indexed martensite can be classified as an inverse problem in materials science, we will begin with a brief description of generalized inverse problems that have troubled the computational materials science community. Next, Bayesian inference will be described since it is the mathematical foundation upon which we solve these problems. The algorithmic technique used to solve the problems, graph cutting, will then be explicated. These sections will then be followed by descriptions of the austenite to martensite transformation, which can all be related to the ensuing chapters in this thesis. It must be noted that some of these sections were taken either directly from portions of manuscripts (such as the Graph Cutting and Bayesian description) either as is, slightly adjusted, or expounded upon. It was the author's opinion that this would create a more cohesive and appealing thesis that would eliminate excessive redundancy associated with several introductory sections of chapters.

### 2.1 Inverse Problems in Materials Science

Let us begin with a definition of inverse problems in materials science. These are defined as problems where data extracted from measurements introduce noise into the sample, and the desired information that is attempting to be gathered must

consequently be compared to an idealized model of the measurement process [119]. They are difficult problems to solve computationally because they are typically ill-posed, meaning small errors in the measurement technique can produce significant errors that obfuscate the solution. Take for instance the process of characterizing microstructural information from Electron Backscatter Diffraction (EBSD). Parameterization of cameras and other relevant image processing conditions, as well as the use of filters and arbitrary error correction software, result in deviations of orientational information associated with a particular scan. This can be further skewed by various types of etchants used to polish the surface of a sample, plastic deformation resulting from the sample preparation, microstructural and phase-based deviations in different regions of the same material, etc. The process of data collection through EBSD is inherently ill-conditioned, yet it remains an incredibly powerful and vital characterization technique within the materials community.

This means that analysis on the observable data must account for the all of the uncertainty and noise associated with a single measurement. The most successful way to approach these problems is by using *a priori* information to guide the model through assumptions about what is actually known. This can be done by establishing *a priori* information as probabilistic distributions that inherently account for deviations in the measurement. Oftentimes, solutions to inverse problems are deduced through assumptions about the state of the observable information. In this case, the state of the information is a collection of data points with similar features whose scatter is integrated into its foundation. Therefore, if the noise is built-in to the characterized data set, it must also be accounted for with the underlying model. One of the more powerful mathematical processes related to statistics and inverse problems is the

concept of regularization, which involves adding relevant, biased information to a particular data set in order to solve an ill-posed problem.

## 2.2 Regularization and Bayesian Estimation

Most readers will be familiar with the concept of regularization, a formal process for introducing additional information in order to solve ill-posed inverse problems. If we consider the standard linear problem for a known model matrix,  $\mathbf{A}$ , and vector of observations,  $\mathbf{b}$ , we wish to find  $\mathbf{x}$  such that  $\mathbf{Ax} = \mathbf{b}$ . Ordinary least squares regression solves the problem by minimization of the sum of squared residuals as  $\min_x \|\mathbf{Ax} - \mathbf{b}\|_2$ . However, most imaging problems are underdetermined, meaning there are numerous possible solutions to the least squares problem. Regularization adds additional soft constraints in order to ensure selection of the “most desirable” solution (in some sense). Examples of regularization include Tikhonov regularization [115], which finds the solution with the smallest Euclidean norm; the least absolute shrinkage and selection operator (LASSO) [154], which favors a sparse solution; and total variation (TV) [136], which favors a smooth solution. The regularized problem is typically formulated as:

$$\min_x (\|\mathbf{Ax} - \mathbf{b}\|_2 + \lambda \|f(\mathbf{x})\|_p) \quad (2.1)$$

Here,  $\|\mathbf{Ax} - \mathbf{b}\|_2$  is the data fidelity term and ensures that the solution is consistent with the measured data and  $f(\mathbf{x})$  is the regularization term ensuring the constraints.

Regularization can also be interpreted probabilistically or through a Bayesian lens. In terms of Bayesian inference, we are concerned with the probability of  $\mathbf{x}$  given our observation  $\mathbf{b}$ , or  $P(\mathbf{x}|\mathbf{b})$ . In other words, we want to estimate the posterior

probability distribution of  $\mathbf{x}$  given the data we have observed. Using Bayes theorem, we can write:

$$P(\mathbf{x}|\mathbf{b}) = \frac{P(\mathbf{b}|\mathbf{x})P(\mathbf{x})}{P(\mathbf{b})} \quad (2.2)$$

where  $P(\mathbf{x}|\mathbf{b})$  is the posterior probability,  $P(\mathbf{x})$  is the prior probability which encodes our belief about what  $\mathbf{x}$  should be *before* observation and  $P(\mathbf{b})$  is referred to as the evidence and gives the probability of obtaining the observation  $\mathbf{b}$ . Note that the prior probability is philosophically similar to the regularization, in the sense that it encodes what we believe the solution should “look” like. However, there is a subtle difference with Equation 2.1: We are searching for the values of  $\mathbf{x}$  that minimize our total cost whereas in the Bayesian sense we are looking for the maximizer of the posterior given our observations. Therefore,  $P(b|x)$  can be considered the *Bayesian* fidelity term which assures consistency between the added regularization, the observable data, and the obtained solution. In terms of an optimization, this refers to the maximum *a posteriori* probability, or MAP estimate, shown below:

$$\begin{aligned} \hat{\mathbf{x}}_{\text{MAP}} &= \max_x P(\mathbf{x}|\mathbf{b}) \\ &= \max_x \left( \frac{P(\mathbf{b}|\mathbf{x})P(\mathbf{x})}{P(\mathbf{b})} \right) \\ &= \max_x (P(\mathbf{b}|\mathbf{x})P(\mathbf{x})) \end{aligned} \quad (2.3)$$

Note that the evidence can be ignored since it is a constant with respect to the maximization. Many common regularization formulations have an exact equivalent MAP formulation, meaning the optimizations defined by Equations 2.1 and 2.3 have the same solution. For example, Tikhonov regularization is equivalent to assuming a

zero-mean Gaussian prior on  $\mathbf{x}$ , with  $\lambda$  (Eq. 2.1) being expressed as function of the variance [76]. Similar equivalences can be derived for LASSO and TV. For this work, we will favor a Bayesian interpretation as it aids in formulating the regularization problem as a graph, thus allowing for interpretation of the final graph cut solution.

## 2.3 Graph Cutting

The analysis and post-processing of materials characterization datasets is often more challenging and time consuming than the acquisition of the raw data [44]. For example, image segmentation, or the problem of automatically separating and classifying features of interest from the background, is a common analysis task where it is trivial to complete by the human eye but often difficult for a computer to reliably and repeatably accomplish. Consider the problem of segmenting a micrograph of a material containing multiple thermodynamic phases: A naïve approach for segmentation consists of identifying a threshold on the intensity which will classify the image pixels by phase. More often than not, this approach will fail due to insufficient contrast between the phases, uneven illumination of the sample, surface topology of the sample, noise in the image, etc [42, 102, 183]. Denoising, or some other form of cleanup, will oftentimes be applied to the data in order to remove some of these artifacts before or after segmentation; however, this approach can be resource intensive, is not easily automated, and may only be partially successful [132, 144].

Common analysis procedures such as segmentation and clustering are particular examples of a larger class of inverse imaging problems [94, 123]. As in the segmentation example above, these inverse problems are often ill-posed without a unique solution (i.e. for the segmentation problem, the pixels cannot be assigned to a class based

solely on their intensity). Instead, we need to regularize the problem by including some additional information. Oftentimes, this involves basic physical considerations such as a high interfacial energy between two phases making it more likely to result in smoother, shorter interfaces and compact regions of secondary phases. Similar physical intuition can be applied to other imaging modalities as well. For example, in electron backscatter diffraction (EBSD) datasets, it might be reasonable to assume that the lattice orientation changes slowly across a grain and the dataset can be approximated by a piecewise smooth orientation field, where sharp transitions in orientation occur only at grain boundaries.

As imaging techniques and data-collection become faster and more automated, it is important to simultaneously automate the data analysis. In microscopy, the application of advanced techniques such as generalized Markov Random Field (MRF) techniques [91, 109] to regularize segmentation based with an interfacial energy penalty is steadily becoming more popular. The goal of the present work is extend these ideas and to introduce a general computational framework which common imaging and data analysis inverse problems can be easily and intuitively formulated, resulting in quick, efficient solutions.

Graph cutting algorithms are a common technique in the area of low-level computer vision for solving problems such as image correspondence (feature registration) from multiple cameras, feature extraction, and model-based smoothing and filtering [8, 74, 75, 159, 171], all of which can be formulated as an energy minimization problem [24, 59]. Graph cutting is gaining traction for feature segmentation in a few biological imaging applications. In general, its utility has been demonstrated in applications involving segmentation of predefined shapes like ellipses for features with

good contrast against the backgrounds, such as cells, chromosomes, and protein segmentation and identification [12, 92, 146], as well as analysis of bone tissue images to quantify the blood permeability of bone marrow [140].

Despite its maturity in computer vision applications, graph cutting has not found wide application within the materials science community. One notable exception is the work of Waggoner et al., where a graph-cut formulation was successfully applied to segment grains from 3D serial sectioned polycrystalline datasets by propagating features from a template or one segmented image to the others in the stack [162, 164]. In the present work, we present a new framework which is particularly suited to clustering and phase segmentation of microscopy images and multi-modal materials datasets.

Graph cutting relies on recasting the dataset to be operated on as a graph, or network, with individual data points redefined as nodes and relationships between the data points acting as edges or connections between the nodes. The goal of the graph cut approach is to separate the graph into two disjoint sets while minimizing the energy of the cut (i.e. the number of cut edges and the penalty associated with cutting each edge). As will be described below, the penalty associated with cutting each edge does not need to be uniform, but can be assigned based on the particular regularization problem being solved. In this way, a natural association with graph cutting and Bayesian estimation exists in that the edge weights may be thought of as prior probabilities that encode a priori knowledge about the physics of the system.

### 2.3.1 Graph Cut Notation

This section contains a brief description of some key definitions and notations used in this thesis. The interested reader can find a more complete description of graph theory, and graph cuts in particular, in reference [24]. A graph,  $\mathcal{G} = \langle \mathcal{V}, \mathcal{E} \rangle$ , consists of a set of  $n$  vertices or nodes,  $\mathcal{V} = [v^{(1)}, v^{(2)}, \dots, v^{(n)}]$ , connected to each other by a set of  $m$  corresponding edges,  $\mathcal{E} = [e^{(1)}, e^{(2)}, \dots, e^{(m)}]$ . The goal of the algorithm is to find an energy minimized cut, or maximum flow path, through the series of linked nodes. In terms of the latter, consider the edges connecting nodes as pipes with water flowing through them. The objective becomes redefined as a search for a series of interconnected pipes that will produce the maximum flow of water (max flow value) from the source to the sink. Pipes with a larger diameter will produce a higher flow rate, ergo severing the “thinner” pipes will result in a network of pipes that produce the maximum flow of water from the source to the sink. In the same sense, if one were to physically cut the series of pipes in half, it would require less energy to cut the larger pipes than the smaller pipes. This constitutes the terminology of max-flow/min-cut, which will be described in more detail below.

In general, edges may be either directed or undirected. A directed edge necessitates a direction of flow for a single edge, such that forward and reverse directions for two edges connecting the same set of nodes are not equal. An undirected edge refers to the opposite, where the forward and reverse edges connecting the same set of nodes are symmetrical. Associated with each edge,  $e^{(k)}$ , joining arbitrary nodes  $v^{(i)}$  and  $v^{(j)}$ , is a weight,  $w^{(k)}$ . As  $e^{(k)}$  is a directed edge, in general,  $w(v^{(i)}, v^{(j)}) \neq w(v^{(j)}, v^{(i)})$ . In other words, the flow between the nodes does not possess inversion symmetry. The

weights would equate to the diameter thickness of the pipes, such that larger weights require more energy to cut.

$$A \not\subset B$$

The series of interconnected edges and nodes can be considered a *grid*,  $g$ , with the exclusion of two terminal nodes separating  $g$ , a *source*,  $s$ , and a *sink*,  $t$ . We can then define these subsets of non-terminal nodes,  $\mathcal{P}$ , and edges,  $\mathcal{N}(v^{(i)}, v^{(j)})$ , as  $(\mathcal{P} \in \mathcal{V} \wedge \{s, t\} \not\subset \mathcal{P})$  and  $(\mathcal{N}(v^{(i)}, v^{(j)}) \in \mathcal{E} \wedge \{v^{(i)}, v^{(j)}\} \subset \mathcal{N})$ , the latter of which are referred to as *n-links* [24]. Edges connecting  $\mathcal{P}$  and  $s$  or  $t$  are denoted *t-links*, displayed below in Figure 6.1. Finally, weights can be classified into two sets by virtue of the edges they connect. In-plane weights ( $w^{IP}(v^{(i)}, v^{(j)}) \wedge \{v^{(i)}, v^{(j)}\} \subset \mathcal{N}$ ) connect *n-links* and out-of-plane weights ( $w^{OP}(v^{(i)}, v^{(j)}) \wedge \{v^{(i)}|v^{(j)}\} \equiv s|t$ ) connect *t-links*, with each specific weight having a non-negative value associated with it.

### 2.3.2 Min-Cut/Max-Flow

A cut,  $\mathcal{C}$ , between  $s$  and  $t$  creates a partition of two distinct, mutually exclusive subsets,  $\mathcal{S}$  and  $\mathcal{T}$ . The cost of the cut therefore becomes a function of these two partitions,  $\mathbf{C} = \{\mathcal{S}, \mathcal{T}\}$ , where it holds that  $s \in \mathcal{S}$  and  $t \in \mathcal{T}$ . Mathematically,  $\mathbf{C} = \{\mathcal{S}, \mathcal{T}\}$  can be interpreted as the summation of the weights of the aforementioned edges separating nodes within a continuous cut. Therefore, for any two arbitrary nodes,  $v^{(i)}$  and  $v^{(j)}$ , separated by  $\mathcal{C}$ , it must follow that  $v^{(i)} \in \mathcal{S}$  and  $v^{(j)} \in \mathcal{T}$ . The goal of the algorithm is to find an energetically favorable cut that minimizes the cost associated with dividing the graph into two subsets. While not proven here, it can be shown that, for the energy minimizing cut, the total flow through all severed

edges is exactly equal to the maximum flow possible from  $s$  to  $t$  through  $\mathcal{G}$ . The Ford-Fulkerson theorem [49] states that the saturation of a set of edges that divides a graph into subsets  $\mathcal{S}$  and  $\mathcal{T}$  can be achieved through a maximum flow from  $s$  to  $t$ , where the resultant cut is energetically minimized. Therefore, as previously mentioned, the energy minimized cut is equivalent to the maximum flow in the graph, and the two terms can be used interchangeably. A traditional graph setup can be seen below in Figure 6.1, along with a partitioning cut traversing edges with arbitrarily low weights (depicted as thinner lines).

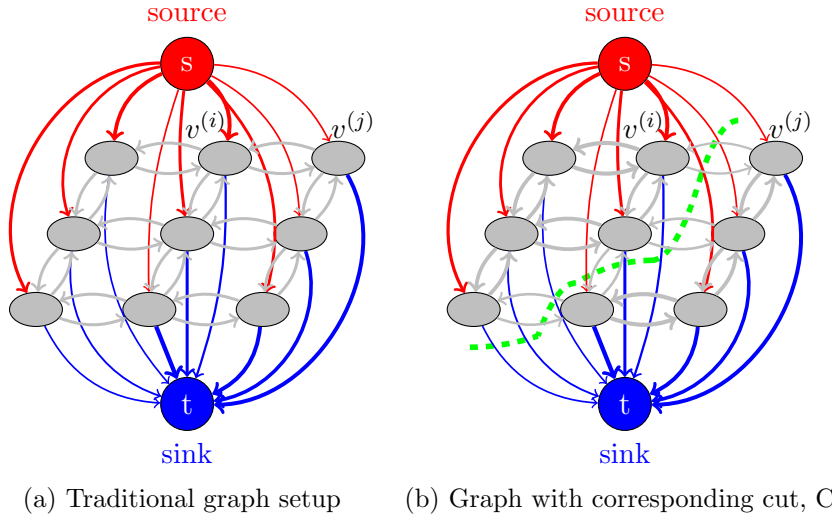


Figure 2.1: Graph construction where  $g$  is separated by the terminal nodes,  $s$  and  $t$ . The  $t$ -link edges are colored in red and blue and the  $n$ -link edges are colored in gray, with corresponding cut colored in green

### 2.3.3 Graph Cutting Algorithm

In applications of graph cutting, several algorithms can be utilized to perform either the energy-minimized or max-flow cut. Greig et al. [59] initially discovered

that combinatorial optimization algorithms employing min-cut/max-flow techniques could be used for energy minimization in vision. Starting with a labeling of an image,  $\mathcal{L} = \{\mathcal{L}_{v^{(i)}} | v^{(i)} \in \mathcal{I}\}$ , where  $\mathcal{I}$  represents an image, the energy function can be set up as follows:

$$\mathcal{E}(\mathcal{L}) = \sum_{v^{(i)} \in \mathcal{I}} \mathcal{D}_{v^{(i)}}(\mathcal{L}_{v^{(i)}}) + \sum_{\{v^{(i)}, v^{(j)}\} \in \mathcal{N}} \mathcal{U}_{\{v^{(i)}, v^{(j)}\}}(\mathcal{L}_{v^{(i)}}, \mathcal{L}_{v^{(j)}}) \quad (2.4)$$

where  $\mathcal{D}_{v^{(i)}}$  is a data penalty function and  $\mathcal{U}_{\{v^{(i)}, v^{(j)}\}}$  is an interaction potential. Data penalties are typically incurred from observed intensities and pre-specified likelihood functions on fixed, labelled pixels. The interaction potential penalizes discontinuities between neighboring pixels, thereby encouraging spatial consistency. This technique was limited due to the requisite binary nature of the problem setup, and consequently remained stagnant for years. However, it gained momentum when min-cut/max-flow algorithms were introduced that could solve non-binary problems.

As such, three main groups of graph cutting algorithms exist: Goldberg-Tarjan [57] “push-relabel” methods, Ford-Fulkerson [49] “augmenting paths” implementation, and the newer “search tree” method [23]. The “maxflow” function within MATLAB (R2016a, Mathworks, Inc., Natick, MA USA) utilizing the Boykov-Kolmogorov “search tree” method [23, 24] is implemented in order to solve each of the subsequent problems described within this paper. For more detailed information on the aforementioned algorithms, refer to the following references [24, 40].

## 2.4 Austenite → Martensite Transformation

The main objective associated with this thesis is the reconstruction of austenite from EBSD-indexed transformation martensite microstructures in steel and binary

ferrous alloys. Upon formation of the austenite phase field in steels at elevated temperatures, the rapid quenching to room temperature produces the diffusionless formation of martensite, where a single prior austenite grain (PAG) results in the formation of 24 crystallographic martensitic variants. The transformation oftentimes goes to full completion before the material reaches room temperature, leaving little to no parent austenite. In fact, the transformation rate can reach fractions of the speed of sound in steel, close to  $1100\text{ms}^{-1}$  [15]. In the process, the fcc ( $\gamma$ ) austenite becomes deformed due to a large shear and concurrent volume expansion of the austenite lattice, resulting in the metastable bcc/t ( $\alpha'$ ) martensite and the retention of carbon within the solution [69, 118, 138]. The ambiguity of the crystal structure is actually concrete, as the composition of the steel affects the morphology of the transformed martensite, where a carbon content of  $< 0.6\%$  typically results in a lath morphology with a bcc crystal structure. Exceeding carbon concentrations produce a coincident c-axis elongation, resulting in tetragonality of the crystal structure due to carbon atoms filling the interstitial sites. However, characterizing the tetragonality of the martensite through EBSD measurements is not possible with current measurement techniques, so martensite is commonly indexed and therefore assumed to be bcc. This c-axis extension can be seen below in Figure 2.2.

The morphology of the martensite has been tied to the composition of the steel and external processing conditions, which can also result in mixtures of phases and microstructural constituents [84, 85, 88, 111]. The latter aspect can be related to either the austenitic phase field, where prior austenite grain size, heat-treatment temperature, requisite cooling rate to initiate the transformation and deformation of the austenitic material can alter the morphology and mechanical properties of the

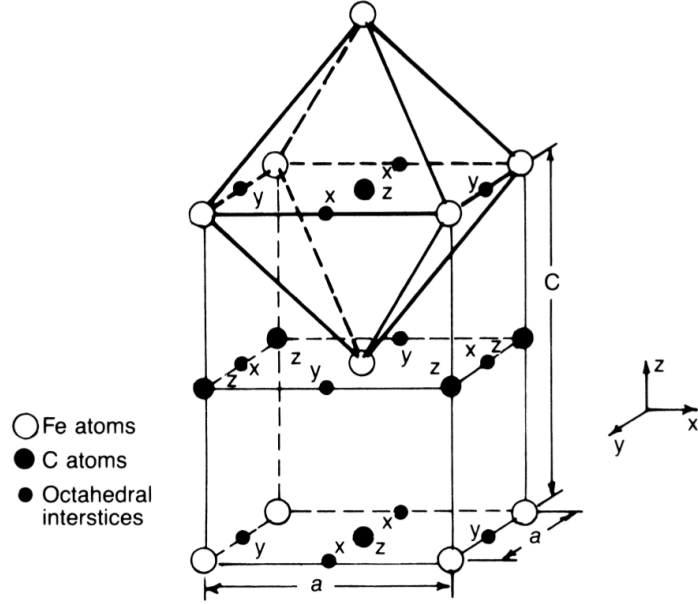


Figure 2.2: Occupation of the octahedral sites by carbon atoms results in the c-axis extension of the bcc unit cell, resulting in a bct crystal structure. Sourced from M. Cohen [37]

martensite, or the post-transformation processing conditions, such as tempering times and temperatures of the martensite, which increase the strength and ductility of the steel [86, 116, 120, 121].

### 2.4.1 Martensite Morphology

The formation of martensite can result in two variable morphologies; lath martensite and plate martensite, which describe the shape of the individual laths within these microstructures. The individual sizes of laths are extremely small, typically on the order of  $0.2 - 0.5\mu m$ , and the interstitial (carbon) content remains relatively low. For low-C steels, the lath morphology groups martensite orientations within a single PAG into a hierarchical structure consisting of laths, sub-blocks, blocks and

packets. A pair of related laths consisting of similar variant orientations comprise sub-blocks, which are clustered together to form blocks. Blocks subsequently share a habit plane, which is a preferred austenite plane that favors the formation of martensite. Blocks are then grouped together into packets, with the latter two boundaries resulting in important hindrances to plastic deformation and crack propagation in steels [61, 84, 85, 101, 112, 113]. Moreover, each PAG can exhibit up to four packets, with three associated block types that contain one or both sub-block variants. The representation of these intra-granular interfaces is presented below in Figure 2.3.

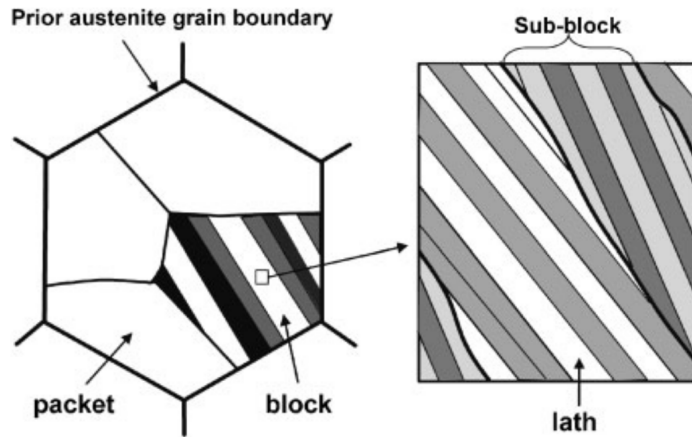


Figure 2.3: Hierarchical structure of sub-blocks, blocks, and packets transformed from the same PAG. Sourced from Morito et al. [110]

Packet formation is the result of a homogeneous shear which results in a packet of laths containing a high density of dislocations [84, 88]. For lath martensite, packet formation can occur by nonadjacent, parallel variants that become intervened with the rapid nucleation and growth of other parallel, concurrent packets situated between the initially formed laths. This could effectively lead to the growth impediment of

one packet due to constraints from the other. Alternatively, parallel laths grow in a successive order immediately adjacent to each other, which would therefore result in a continuous array of packets from one boundary to the next.

The formation of plate martensite is favored by either a higher concentration of interstitial elements such as carbon or nitrogen, or alloying elements like Ni or Mn [18, 85]. These elements lower the respective martensite start temperature ( $M_s$ ), which represents the threshold where enough of a driving force exists to initiate the shear transformation of austenite to martensite [87]. Figure 2.4 shows the range of martensite morphology that varies with increasing carbon wt.%, as well as the slope of the  $M_s$  temperature as a function of carbon content.

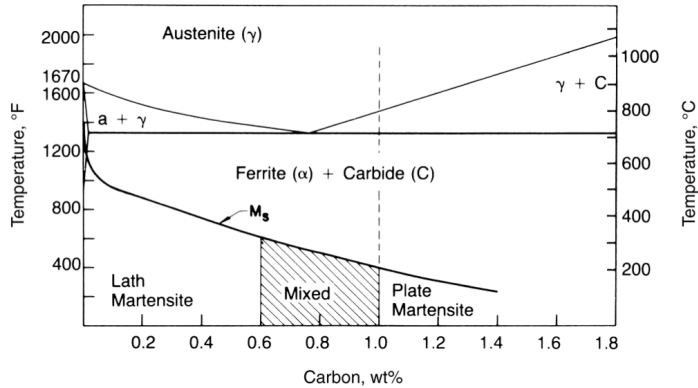


Figure 2.4: Plot of the morphology of martensite varying as a function of carbon content. Sourced from [87]

Contrary to the ordered arrangement of lath martensite, plates form across the PAG in a non-parallel fashion, extending either above or below the surface of the PAG. These are typically largest in size, and as the temperature decreases, subsequent plates oftentimes become limited in size and form between the larger, existing plates, which

ultimately act as barriers to subsequent plate growth. Additionally, as new plates grow, existing plates can continue to grow, which can lead to a complex entanglement of plates that essentially conform around a matrix of retained austenite [88]. Detailed micrographs of both lath and plate martensite can be seen below in Figure 2.5.

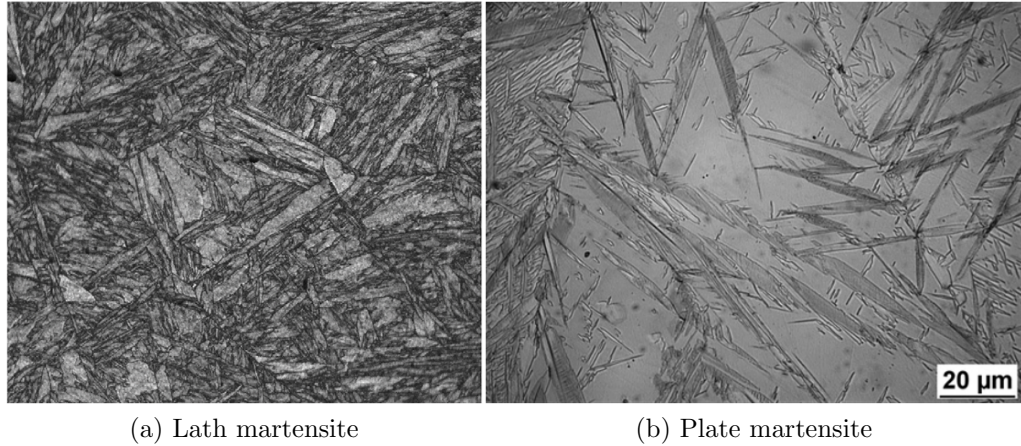


Figure 2.5: FE-SEM/EBSD measurement of 0.2 wt.% C steel displaying lath martensite, sourced from Kitahara et al. [84] and a light optical micrograph (LOM) of 1.67 wt.% C steel exhibiting plate martensite embedded in an austenitic matrix, sourced by Stormvinter et al. [149]

As mentioned previously, the formation of the martensite is the result of shearing, which requires an accommodation of the austenite grains through plastic deformation. Since the transformation is diffusionless, the atoms move in a cooperative and almost simultaneous fashion. Formation of the lath deforms the surface of the austenite at the point of emergence. This results in a rotation, or tilting, of the martensite crystal, such that the new crystal is oriented different than the austenite orientation [16]. This combination of the shear-induced rotation initiated at a common habit plane reflects the underlying crystallography of the  $\gamma \rightarrow \alpha'$  transformation. A schematic depicting

the associated deformation at the austenite surface can be seen below in Figure 2.6, where the directional half-arrows point in the direction of the shearing.

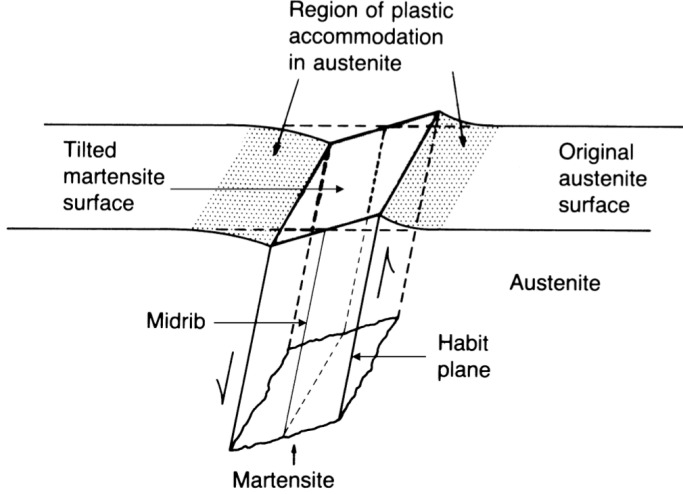


Figure 2.6: Schematic of the shearing produced by the martensite formation and subsequent rotational tilt at the surface. Sourced from [87]

## 2.4.2 Crystallography of Austenite to Martensite Transformation

Associated with the martensite transformation is a strong crystallographic connection between the parent austenite and the product martensite. As mentioned previously, a single PAG transforms to up to 24 crystallographic variants. Within this transformation is a paired relationship between the specific parallel planes and directions between the austenite and martensite. This is known as the orientation relationship (OR), of which it is often assumed that the exhibited orientation relationship is close to one of two “named” orientation relationships in iron alloys. When

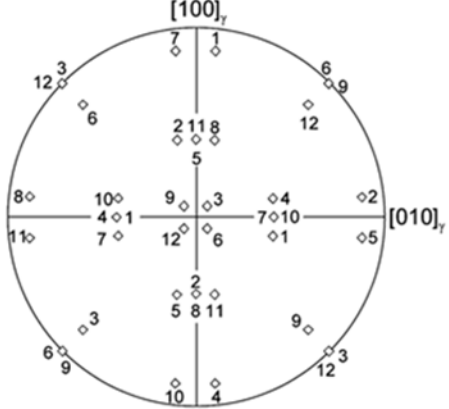
approximately 12 variants are observed, the Nishiyama-Wassermann (NW) orientation relationship is referenced [117, 166]:

$$\{111\}_\gamma // (011)_{\alpha'}; \quad <\bar{1}\bar{1}2>_\gamma // <0\bar{1}1>_{\alpha'} \quad (2.5)$$

When 24 variants are observed, the Kurdjumov-Sachs (KS) orientation relationship is often cited [89]:

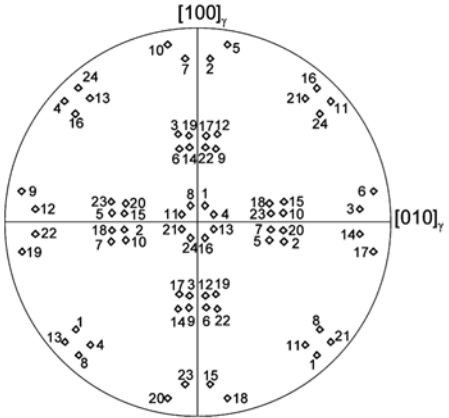
$$\{111\}_\gamma // (011)_{\alpha'}; \quad <\bar{1}01>_\gamma // <\bar{1}\bar{1}1>_{\alpha'} \quad (2.6)$$

In accordance with the variant pairing system presented by Kitahara in papers related to both the KS and NW orientation relationships [84,85], a brief description of the ordering of variants used through out the rest of the thesis will be described below. Further analysis on the misorientation relationships between variants is presented in Chapter 4, and will subsequently be omitted from this Chapter. Variants are denoted  $\mathbf{V}_i$ , where  $i$  represents the sequence of the variant. In terms of the KS OR, where 24 crystallographic variants exist, the ordering is set to cluster sets of variants into corresponding blocks or packets. For instance, consecutive pairs of variants, such  $\mathbf{V}_1$  and  $\mathbf{V}_2$  or  $\mathbf{V}_9$  and  $\mathbf{V}_{10}$  form blocks,  $\mathbf{B}_i$ . Similarly, since packets,  $\mathbf{P}_i$ , contain blocks which share the same habit plane, there exist three possible blocks within each packet, formed by a tri-sequential pair of blocks ( $\{\mathbf{B}_1 \rightarrow \mathbf{B}_3\} \in \mathbf{P}_1$ ,  $\{\mathbf{B}_4 \rightarrow \mathbf{B}_6\} \in \mathbf{P}_2$ , and so on). The specific variant orientations for the KS and NW orientation relationships can be visualized through the use of  $\{100\}_\gamma$  pole figures in Figure 2.7 along with the corresponding tables that relate each variant with their corresponding parallel plane and directions.



(a) NW  $\{100\}_\gamma$  pole figure and variant ordering table

Variant	Plane parallel	Direction parallel
V <sub>1</sub>	$(1\ 1\ 1)_\gamma // (0\ 1\ 1)_{x'}$	$[2\ \bar{1}\ \bar{1}]_\gamma // [0\ \bar{1}\ 1]_{x'}$
V <sub>2</sub>		$[\bar{1}\ 2\ \bar{1}]_\gamma // [0\ \bar{1}\ 1]_{x'}$
V <sub>3</sub>		$[\bar{1}\ \bar{1}\ 2]_\gamma // [0\ \bar{1}\ 1]_{x'}$
V <sub>4</sub>	$(\bar{1}\ 1\ 1)_\gamma // (0\ 1\ 1)_{x'}$	$[\bar{2}\ \bar{1}\ \bar{1}]_\gamma // [0\ \bar{1}\ 1]_{x'}$
V <sub>5</sub>		$[1\ 2\ \bar{1}]_\gamma // [0\ \bar{1}\ 1]_{x'}$
V <sub>6</sub>		$[1\ \bar{1}\ 2]_\gamma // [0\ \bar{1}\ 1]_{x'}$
V <sub>7</sub>	$(1\ \bar{1}\ 1)_\gamma // (0\ 1\ 1)_{x'}$	$[2\ 1\ \bar{1}]_\gamma // [0\ \bar{1}\ 1]_{x'}$
V <sub>8</sub>		$[\bar{1}\ \bar{2}\ \bar{1}]_\gamma // [0\ \bar{1}\ 1]_{x'}$
V <sub>9</sub>		$[\bar{1}\ 1\ 2]_\gamma // [0\ \bar{1}\ 1]_{x'}$
V <sub>10</sub>	$(\bar{1}\ \bar{1}\ 1)_\gamma // (0\ 1\ 1)_{x'}$	$[\bar{1}\ 2\ \bar{1}]_\gamma // [0\ \bar{1}\ 1]_{x'}$
V <sub>11</sub>		$[\bar{1}\ 2\ 1]_\gamma // [0\ \bar{1}\ 1]_{x'}$
V <sub>12</sub>		$[\bar{1}\ \bar{1}\ \bar{2}]_\gamma // [0\ \bar{1}\ 1]_{x'}$



(b) KS  $\{100\}_\gamma$  pole figure and variant ordering table

Variant	Plane parallel	Direction parallel
V <sub>1</sub>	$(111)_\gamma // (011)_x$	$[101]_y // [\bar{1}\bar{1}1]_x$
V <sub>2</sub>		$[101]_y // [111]_x$
V <sub>3</sub>		$[011]_y // [111]_x$
V <sub>4</sub>		$[011]_y // [111]_x$
V <sub>5</sub>		$[110]_y // [111]_x$
V <sub>6</sub>		$[110]_y // [111]_x$
V <sub>7</sub>	$(\bar{1}\bar{1}1)_\gamma // (011)_x$	$[101]_y // [\bar{1}\bar{1}1]_x$
V <sub>8</sub>		$[101]_y // [111]_x$
V <sub>9</sub>		$[110]_y // [111]_x$
V <sub>10</sub>		$[110]_y // [111]_x$
V <sub>11</sub>		$[011]_y // [111]_x$
V <sub>12</sub>		$[011]_y // [111]_x$
V <sub>13</sub>	$(11\bar{1})_\gamma // (011)_x$	$[011]_y // [\bar{1}\bar{1}1]_x$
V <sub>14</sub>		$[011]_y // [111]_x$
V <sub>15</sub>		$[101]_y // [111]_x$
V <sub>16</sub>		$[101]_y // [111]_x$
V <sub>17</sub>		$[110]_y // [111]_x$
V <sub>18</sub>		$[110]_y // [111]_x$
V <sub>19</sub>	$(11\bar{1})_\gamma // (011)_x$	$[110]_y // [\bar{1}\bar{1}1]_x$
V <sub>20</sub>		$[110]_y // [111]_x$
V <sub>21</sub>		$[011]_y // [111]_x$
V <sub>22</sub>		$[011]_y // [111]_x$
V <sub>23</sub>		$[101]_y // [111]_x$
V <sub>24</sub>		$[101]_y // [111]_x$

Figure 2.7:  $\{100\}_\gamma$  pole figures and related variant ordering for the NW (top) and KS (bottom) orientation relationships. Sourced by Kitahara et al. [85] and Kitahara et al. [84]

However, the KS and NW orientation relationships are idealized depictions of the orientation relationship that oftentimes do not accurately represent the true nature of the transformation. In the actual orientation relationships, the parallel directions and planes cited above are irrational. Cahn and Kalonji [29] argued that, in regards to certain rotations, a symmetry dictated energy extremum exists, although the symmetry does not specify whether the extremum is a minimum, maximum or saddle point. They then determined that no symmetry dictated energy extremum exists for KS, and that the NW orientation relationship produces either a maximum or a shallow minimum. Therefore, both of these cases (KS and NW) can be considered idealized orientation relationships. Deviations from exact parallelism have been characterized by Greninger and Troiano [60] and are predicted by the phenomenological theory of martensitic transformations [20–22, 95, 96, 118, 167, 169]. Experimentally measured orientation relationships will always contain 24 variants but depart from KS or NW orientation relationships, and the departure has been shown to vary with composition and cooling rate [85, 116]. Accurate analysis of the austenite phase field from observable martensitic data set therefore requires an accurate and composition-specific measurement of the OR to most adequately represent the crystallography of the transformation.

## 2.5 Outline and Motivation

A brief outline will now be presented that details what to expect within each subsequent chapter. It is then followed up by a brief paragraph that describes the motivation associated with the development of the reconstruction algorithm. Motivation for all subsequent chapters are related to the reconstruction of the prior

austenite microstructure, and as such, everything is geared towards an understanding of techniques and crystallographic analysis that will optimize reconstruction results. These motivations are then briefly summarized as the introductions to each respective chapter.

Chapter 3 introduces the graph cutting technique to a variety of inverse problems in materials science. These include image segmentation, identification of clusters for synthetically produced atom probe tomography (APT) data sets, segmentation of ferrite, bainite, and martensite from a single multi-phasic steel, and finally, the reconstruction of a single PAG. The graph cutting technique is described in full along with a description of the graph set up. Several results are compared against existing techniques except for the microstructure constituent segmentation section, which has not been done effectively in either experimental or computational endeavors.

Chapter 4 introduces a rigorous and exhaustive analysis of the martensitic misorientation profiles associated with specific ORs. An experimentally determined OR is compared against the KS and NW orientation relationships for parent- and twin-transformed martensite variants. This effectively highlights the differences across ORs and why a specific sample requires an accurate measurement of the OR in the first place. Finally, the cubic and tetragonal crystal symmetry of the martensite is compared to analyze how the tetragonality of the crystal structure would affect the corresponding martensitic misorientation profiles assuming the KS orientation relationship.

Chapter 5 then introduces an automated process for measuring the  $\gamma \rightarrow \alpha'$  OR in steels and ferrous alloys. The analysis is performed on five different samples, four of which are directly compared against experimental measurements of the same

datasets. Samples span from KS-like, GT-like, and NW-like to exhibit the range of the computational measurement technique. Variable window sizes containing differing numbers of data points are then compared to highlight the versatility of the technique in the face of limited variants and/or excessive noise. A final sample relates to the main steel analyzed in Chapter 6, where regions within five PAGs have OR analysis performed on them to study the variance in the OR across a single sample.

Chapter 6 finally presents the reader with the reconstruction algorithm, including an intricate description of how it works and utilizes information from the previous three chapters to optimize the results. A variety of different martensitic steel samples as well as a binary ferrous alloy are then analyzed, some presented with validation and others as standalone reconstructions. The versatility of the algorithm is highlighted by the number of successful reconstructions performed on a variety of different samples; how the OR measurement affects the quality of the reconstructions; how the algorithm handles excessive additions of EBSD-misindexed points (noise) artificially introduced into the data set; and how the algorithm handles the existence of annealing twins within the microstructure.

Chapter 7 utilizes a single reconstructed austenite microstructure and selects three PAGs to perform packet segmentations on. The first grain is a large grain with clearly defined packets; the second is a much smaller grain exhibiting variant selection; and the third is a parent-twin system that was chosen to determine whether the graph cutting technique could also identify the packets containing shared variants across the parent-twin interface. These results are then compared with the theoretical crystallography of the variant transformation in order to validate the results with expectation.

Chapter 8 serves as a conclusion of the thesis. The chapters are first summarized as a brief overview of what was contained in the thesis. Subsequent sections then serve to present the reader with future work that could be applied either with the graph cutting technique or to further analyze/test the ability of the reconstruction algorithm.

The goal of this thesis was to create a reconstruction algorithm that adequately reproduced the prior austenite microstructure based solely on the EBSD-characterized martensite data. The algorithm was intended to be as computationally efficient as possible, where large data sets could be effectively reconstructed in a reasonable amount of time. The algorithm itself is almost fully automated, such that scientists and engineers with limited computational knowledge could easily perform the reconstruction with limited instructions. Several reconstruction results have been paired with experimentally or theoretically validated data sets. To the author's knowledge, no austenite reconstruction technique has been compared side-by-side to an accurate, optical etchant of the same material. In Chapter 6, this thesis changes that by displaying fully-automated reconstruction results compared against a strong, accurate optically etched sample of the same microstructure by Sinha et al. [143]. Subsequent validation is performed on a binary ferrous alloy with a significant amount of retained austenite, and a comparison is also delivered based on a manual reconstruction performed by an expert in steel metallurgy. Finally, accurate and fully-automated packet segmentations are performed from the reconstructed PAGs as an added feature of the algorithm. This allows for a complete analysis of the austenite to martensite transformation, from the parent microstructure, misorientation analysis of transformed variants, orientation relationship, and transformation microstructure.

## **Chapter 3: Application of the Maximum Flow–Minimum Cut Algorithm to Segmentation and Clustering of Materials Datasets**

The majority of the contents in this chapter and the related section with Chapter 2 have been submitted to Microscopy and Microanalysis [25] and is currently under review with the co-authors Toren Hobbs, Dr. Eric Payton, and Dr. Stephen Niezgoda.

### **3.1 Introduction**

An overarching description, corresponding notation used throughout the thesis, and details about the specific type of graph cutting algorithm were previously described in Chapter 2. Therefore, the graph cutting technique will only briefly be revisited here in relation to the problems encountered throughout this chapter. Graph cutting relies upon data sets that can be operated on as a graph, where data points can be recast as a series of interconnected nodes. In order to establish the system implemented to solve a certain problem, relationships between these data points must be established that can ultimately define the weighting factors associated with edges within the graph.

For example, in terms of image segmentation, the pixels of an image would be represented as nodes in the graph which might be connected to all neighboring pixels

by graph edges. Weighting factors would then represent the similarities and deviations between associated nodes that can effectively cluster data points into corresponding sets. The objective is then to establish a pathway that minimizes the energy of a theoretical cut in order to separate the graph into two disjoint sets. Minimization of the cut is oftentimes associated with decreasing both the number of cut edges and the penalty associated with cutting each edge. For example, in terms of clustering atoms from atom probe tomography (APT) data sets, the weight of an edge may be a function of the spatial distance measured between two adjacent data points.

As will be demonstrated below, this allows for an intuitive picture for the formulation of regularized inverse analysis problems and a computationally efficient framework for identifying optimal solutions. The goal of this chapter is to explore and demonstrate the applicability of the graph cutting technique with respect to characterization of some inverse problems in materials science. Specific examples include image segmentation, atomic cluster identification, constituent phase segmentation and parent grain identification from transformation microstructure (i.e. parent austenitic identification from the transformed martensite structure).

## 3.2 Image Segmentation

Image segmentation is the process of partitioning an image into sets of related pixels in order to classify regions of the image or identify features in an image. In materials science, this is often applied to noisy images, where the goal is to identify and measure morphological attributes of microstructural features, propagate 3D structures from a series of 2D images, medical imaging, etc [47, 67, 124, 125, 163]. Accurate identification of features and separation from the background is critical

for subsequent analysis of volume fraction, size, and spatial distributions of second phase particles, which typically have a large impact on properties and whose morphological distributions are strongly correlated to processing. Conventional image processing operations (simple thresholding, opening, closing, dilation, erosion, etc.) are often found to be inadequate or require significant user intervention due to inhomogeneities in contrast and noise. Segmentation, specifically for materials imaging, has recently become reinvigorated with development of both machine learning approaches and new toolsets for stringing together new recipes of conventional image processing algorithms [6, 30, 38, 145]. The most prominent new image segmentation algorithm may be EM/MPM (Expectation-Maximization/Maximization of the Posterior Marginals) [35, 38, 39, 142]. This approach is a stochastic algorithm which combines parameter estimation using the EM [182] algorithm combined with an Markov random field (MRF) estimate for segmentation. The values for the marginal conditional probability mass functions are approximated in terms of the pixel label field through use of the MPM [100] algorithm.

### 3.2.1 Graph Definition for Segmentation and Clustering

The general problem of image segmentation can be abstracted into the classification of all pixels in an image into two sets: those which belong to a feature of interest and a background consisting of all other pixels. As a specific instance, consider the identification of  $\gamma'$  particles from a background of the  $\gamma$  matrix in Ni and Co superalloys [46, 133]. For the segmentation problem, we introduce a different graph structure which contains two connected grids, denoted as  $g_1$  and  $g_2$ , which correspond to the

background and features of interest. This graph structure is shown schematically in Figure 3.1a.

The in-plane or intra-grid weights for  $g_1$  and  $g_2$  are identical for both grids and correspond to the probability that connected pixels come from the same set (either background or pixel), therefore existing as a measure of similarity between the pixels. Edges between pixels that are similar in intensity have higher weights than those that have significantly different intensities. This corresponds to the Bayesian *prior*, or interaction potential, between the pixels,  $\mathcal{U}$  in Equation 2.4. This leads to high penalties for cutting through edges that connect two similarly valued nodes and low penalties for placing an interface between pixels that differ strongly in intensity. The end result is continuous cuts that cluster like-nodes into the same family (background or feature).

The out-of-plane weights, associated to a subset of inter-grid edges, correspond to the data fidelity term  $\mathcal{D}$  in Equation 2.4 and are related to the probability that given pixels belongs to either the background or the feature of interest based on the intensity. The first set of out-of-plane weights, connecting each node in  $g_1$  to the corresponding node in  $g_2$ , represents the likelihood that each pixel came from the background. A second set of out-of-plane weights, from each node in  $g_2$  to the feature of interest. In this way, the dual-grid system permits the effective separation of the system into background and features. This is schematically shown in Figure 3.1b, where red edges denote uncuttable weights from  $s \rightarrow g_1$  and  $g_2 \rightarrow g_1$ , and the cuttable weights are represented with the following colors: gray edges indicate intra-grid weights, yellow edges stand

for inter-grid weights connecting  $g_1 \rightarrow g_2$ , and the blue edges signify the second set of out-of-plane weights connecting  $g_2 \rightarrow t$ .

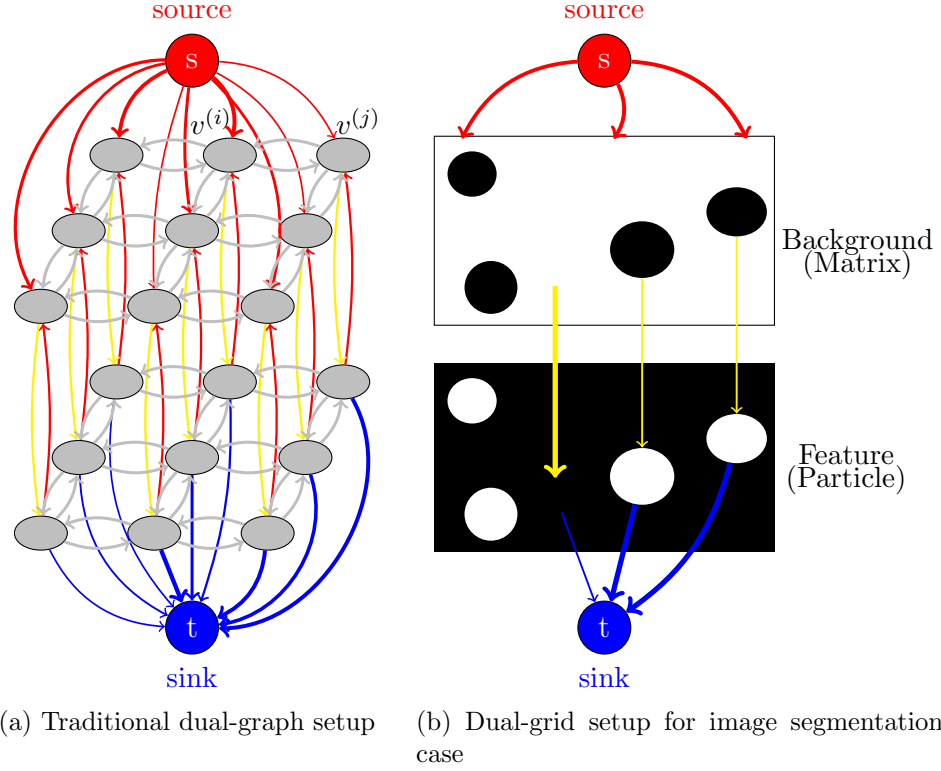


Figure 3.1: The graph setup utilized to solve the problems mentioned in this paper along with a specified, arbitrary case involving image segmentation

Additional inter-grid edges need to be introduced to complete the graph structure and prevent pixels from being assigned to either both the background and feature or neither set. I can be seen that all edges in the direction from  $t \rightarrow s$  are also not cuttable. This structure ensures that, in order to separate  $s$  from  $t$  with a continuous cut, that *i*) one and only one of the out-of-plane edges in the nodes in  $g_1$  and  $g_2$  associated with each pixel are cut and *ii*) the the corresponding in-plane edges related to the

appropriate interface penalty are added when the class assignment changes between pixels. While adding some abstraction to the graph structure, this prohibits the cut from looping around a pixel and cutting both sets of out-of-plane-edges or cutting in-plane edges without a change of classification, ensuring topological consistency of the final cut.

### 3.2.2 Segmentation Examples

In order to demonstrate the efficacy of the graph cutting algorithm for image segmentation, segmentations of the  $\gamma'$  phase in  $\gamma - \gamma'$  Ni superalloys (René 88DT [98] and René 104 [125, 126]) from back scattered electron (BSE) images were performed. Direct comparisons were prepared using three separate techniques—the well-established Otsu threshold method [123], the modern EM/MPM algorithm, [39] and the present graph cutting procedure.

Figure 3.2a shows the original gray scale BSE image, a histogram of the pixel intensities, and a ground truth segmentation for the René 88DT image [157]. As can be seen from the histogram (Figure 3.2c), the intensity distribution from both phases overlap, resulting in an ambiguity of class assignment for a range of intensities. The ground truth image, found in Figure 3.4b, was obtained from BlueQuartz Software [157] and was constructed by first applying a threshold to obtain a first estimate of the ground truth segmentation. Then Photoshop<sup>TM</sup> was utilized to further classify pixels as either part of a particle or the matrix [157]. The Otsu method chooses a single threshold value based on a minimization of the intra-class variances of the feature and background [123]. For this image, a gray scale threshold value of 0.322 was used. For the EM/MPM segmentations, the exchange energy and number of iterations (loops)

were optimized to find the best segmentation. Optimal segmentations were found with an exchange energy of 1.5 with 5 total segmentation loops.

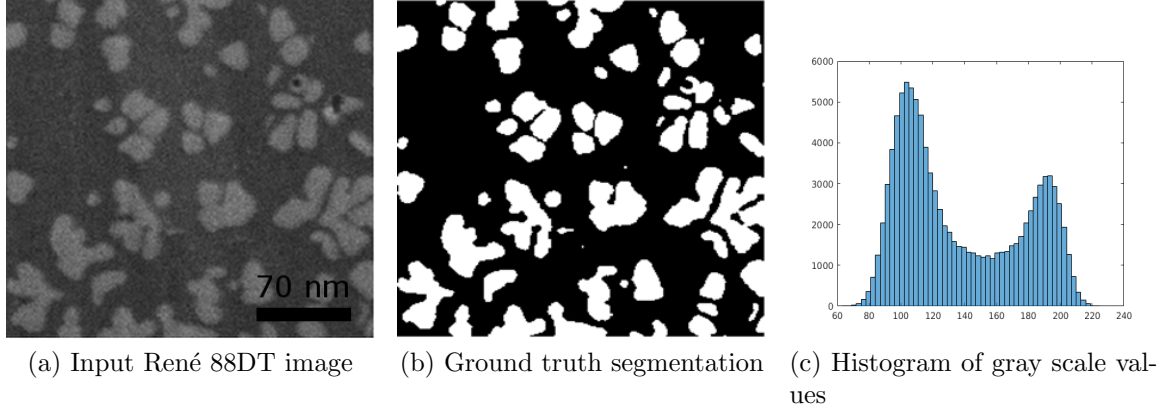


Figure 3.2: Input image, ground truth segmentation, and pixel-intensity histogram for the René 88DT dataset

The graph for the segmentation problem was defined as follows. Each individual pixel within the input micrograph was labeled as  $v^{(i)} \in g_k$ , and the respective intensity value for each node was used to construct the *prior*. An adjacency array was constructed between each node and the set of four nearest neighbors. The in-plane weights between neighboring pixels were then computed as:

$$w^{IP}(v^{(i)}, v^{(j)}) = \lambda \left( \frac{1}{|I(v^{(i)}) - I(v^{(j)})|} \right) + \beta \quad (3.1)$$

where  $I(v^{(i)})$  is the intensity of the pixel associated with node  $v^{(i)}$  and  $\lambda$  is a meta-parameter which controls the degree of regularization or the balance between fidelity and interaction energy. Since it holds that if two neighbored pixels have the similar gray scale values, it is more likely that they belong to the same class, inverting

these values effectively penalizes the graph cutting algorithm for making a cut between these nodes. This increases the probability that these nodes would be clustered together. In contrast, cutting between neighboring pixels with greatly disparate intensities would be highly favored. The  $\beta$  parameter adds a uniform penalty for making any in-plane cut, and can be thought of as being analogous to the interfacial energy between the phases. A high value of  $\beta$  is useful in highly noisy images or heavily overlapped histograms and acts to enforce that the segmented features are compact and connected. For this image,  $\lambda = 2.55$  and  $\beta = 10.5$  values were used. In principle, the penalty associated with regularization of interaction energy can be any arbitrary function. Other choices could include second-nearest or higher-order neighbors (increase the number of edges) or other modifications to the penalty, including adding an ignoring intensity mismatch for obviously bad pixels such as from salt-and-pepper noise (identical intensity values of 0 or 1 which can occur during analog to digital conversion) [19, 32, 131, 156]).

The out-of-plane weights were established by modeling the intensity distributions for the background and feature pixels as independent Gaussian distributions with means  $[\mu_\gamma, \mu_{\gamma'}]$  and standard deviations  $[\sigma_\gamma, \sigma_{\gamma'}]$  for the background  $\gamma$  and feature  $\gamma'$  phases, respectively. The first set of out-of-plane weights, which connect  $g_1 \rightarrow g_2$ , are proportional to the probability that each pixel is a member of the background given its intensity, and were calculated using the following equation:

$$\begin{aligned} w^{g_1 \rightarrow g_2}(v^{(i)}) &= f(I(v^{(i)}) | \mu_\gamma, \sigma_\gamma) \\ &= \alpha_\gamma \left( \frac{1}{\sigma_\gamma \sqrt{2\pi}} \exp \left( \frac{-(I(v^{(i)}) - \mu_\gamma)^2}{2\sigma_\gamma^2} \right) + \omega_\gamma \right) \end{aligned} \quad (3.2)$$

Here,  $v^{(i)}$  is the node in  $g_1$  associated with pixel  $i$ ,  $\alpha$  is a scaling parameter analogous to  $\lambda$  in Equation 3.1 and  $\omega$  is a user-defined penalty term similar to  $\beta$  in Equation 3.1. For the René 88DT image, values of 2.75 and 4.45 were used for  $\alpha_\gamma$  and  $\alpha_{\gamma'}$  and 2.75 and 8.55 for  $\omega_\gamma$  and  $\omega_{\gamma'}$ , respectively. The second set of out-of-plane weights from  $g_2 \rightarrow t$  are defined in a completely analogous manner with  $\mu_{\gamma'}$  and  $\sigma_{\gamma'}$  replacing the mean and standard deviation for  $\gamma$ .

After designating both sets of weights, the graph cut algorithm is exercised to find the energy minimized cut that segments all of the particles from the matrix. The results for the graph cut segmentation are given below in Figure 3.3, along with the results for the Otsu thresholding and EM/MPM segmentation on the same image..

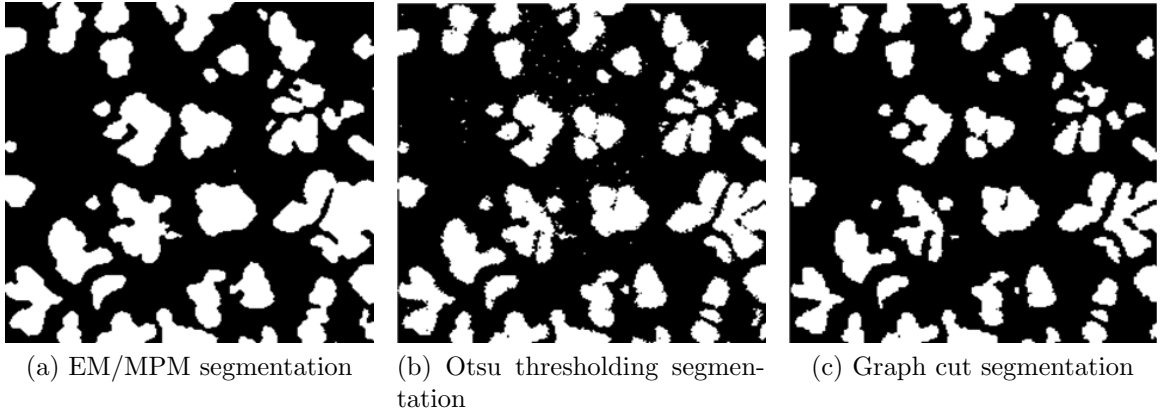


Figure 3.3: Series of segmented images using various segmentation techniques for the René 88DT dataset

Images of superalloy microstructures often contain particles that are more difficult to distinguish from the matrix using automated image processing than those shown in Figure 3.2a. The gray scale values show a smooth blend between each other, limiting the range of the bimodal RGB/gray scale distribution and effectively minimizing

distinguishing factors. Therefore, a second segmentation on a truncated section of the nickel-based superalloy René 104 characterized by Payton et al. [125, 126] with less contrast between particles and matrix was performed for further validation of the graph cutting algorithm relative to other available approaches. The overlap of grayscale values between particle and matrix is displayed in the histogram in Figure 3.4c. The parameterization for all three segmentation methods for the René 104 image are as follows: the Otsu thresholding value was determined to be 0.498, the energy exchange parameter for EM/MPM ( $\beta$  in reference [44]) was found to be 1.7, with 5 iteration/segmentation loops performed, and the graph cutting procedure had values of  $\lambda = 6.0$ ,  $\beta = 0$ ,  $\alpha_\gamma = 1.0$ ,  $\omega_\gamma = 1e^{-2}$ ,  $\alpha_{\gamma'} = 1.0$  and  $\omega_{\gamma'} = 1.7$ , respectively. The ground truth image was obtained through meticulous use of MS Paint. The input image was magnified to the point where discrete pixels were visible and pixels were manually marched across from border to border, subsequently coloring particles white and the surrounding  $\gamma$  matrix black. A threshold was then applied to rid the image of any non-binary pixels and reclassify them accordingly, as either particle or matrix, to rid the image of any residual noise. The segmentations for all three methods are shown in Figure 3.4.

As the results in Figures 3.3 and 3.4 show, the graph cutting algorithm does a good job of segmenting the image. The particle features mimic the geometry found within the ground truth sample, although all techniques have trouble identifying separate but spatially close particles that are clustered into groups. In order to determine how effective each method was in performing the segmentation, through consideration of the ground truth dataset as the signal, the signal-to-noise ratios (SNR) for all three techniques can be computed through the following equation:

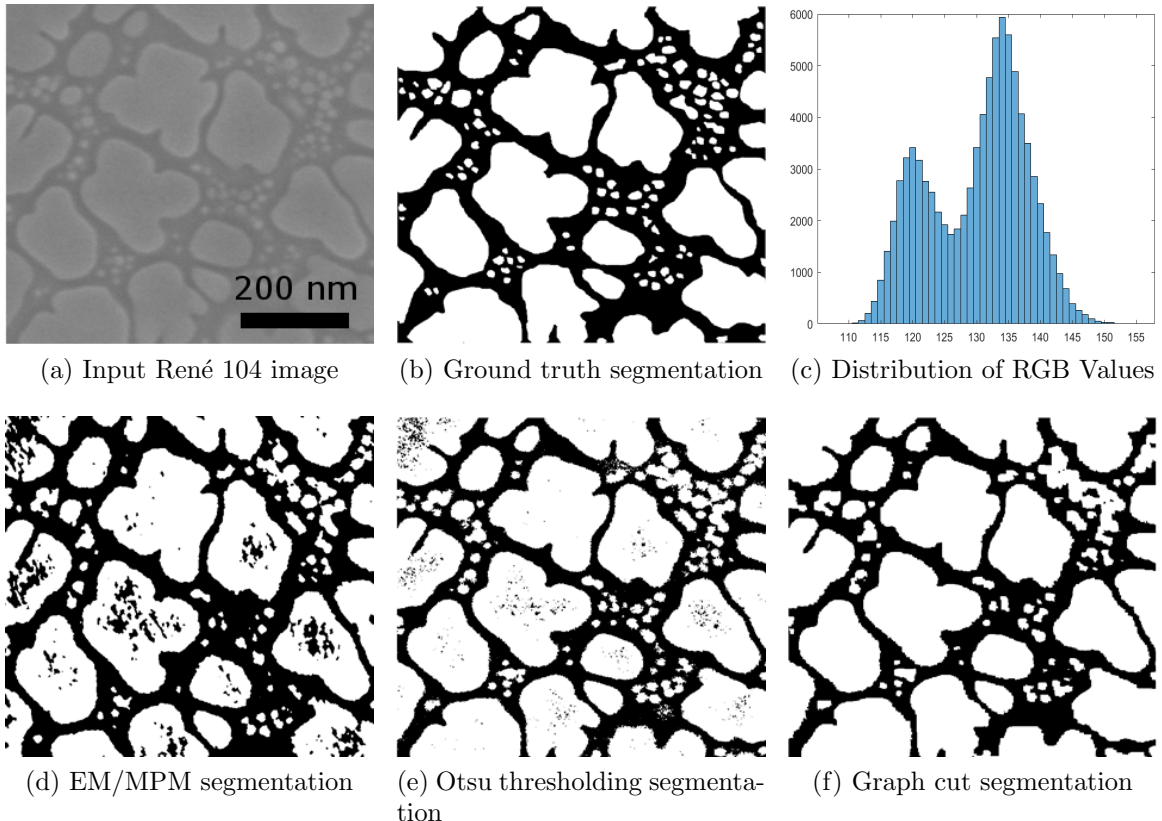


Figure 3.4: Segmentations and input texture for René 104 nickel-based superalloy

$$SNR = 20 * \log \frac{||S_0||_F}{||S_0 - S_n||_F} \quad (3.3)$$

Where  $S_0$  represents the clean image (ground truth),  $S_n$  is the noisy image (segmented image) and the notation  $||...||_F$  represents the Frobenius norm. The SNR values for each segmentation are given below in Table 3.1.

Table 3.1: The SNR values for the EM/MPM, Otsu threshold, and Graph Cutting segmentations.

	<i>EM/MPM</i>	<i>Otsu Threshold</i>	<i>Graph Cut</i>
René 88DT	17.74	24.12	23.14
René 104	5.58	17.02	17.97

The SNR for the graph cut segmentation is found to be better than the segmentation performed using EM/MPM for both images, especially considering the case of the René 104 image where greater overlap is found in the contrast histogram. In terms of the Otsu thresholding method, the SNR value is higher than the graph cutting value for the René 88DT image. This is most likely due to the fact that a large contrast between matrix and particle gray scale values exists, which allows for effective segmentation using the simplest possible algorithms.

In comparison to Otsu and EM/MPM, the graph cutting method does a better job of capturing the extent of larger particles without requiring a hole filling step, especially when a grayscale gradient exists within the particle (as in the case of the René 104 particles, *cf.* Figure 3.4). However, both Otsu and EM/MPM are better at distinguishing the smaller tertiary  $\gamma'$  particles from the matrix. For this population

of particles, the present graph cut algorithm tends to merge more clusters of closely spaced particles. Overall, the graph cut approach results in a cleaner image with respect to the more difficult to segment René 104 dataset, with EM/MPM producing a significantly lower SNR than the other methods for both datasets.

### 3.3 Microstructure Phase Segmentation and Identification

#### 3.3.1 Identification and Segmentation of Bainite and Martensite

The ability to quantitatively characterize the volume fractions and spatial arrangements of microstructural constituents remains a challenge in hyperspectral and multi-modal datasets, in which the data collected comes from multiple acquisition modes or there is a spectrum of values for each spatial coordinate. This characterization problem is particularly complex in materials where the microstructural features of interest are characteristic arrangements of phases, as is often the case with advanced steels. This includes transformation induced plasticity (TRIP) steels, dual-phase (DP) steels, and complex phase (CP) steels, where there can be significant overlap between the signals for austenite, ferrite, bainite and/or martensite [80]. In terms of the latter two, it becomes exceedingly difficult to segment these microstructure constituents due to their shared plate-like morphologies. Although the bainite transformation takes place at a temperature above the martensite transformation temperature, commercially relevant heat treatment processes can result in a mixture of the two constituents which can have important effects on the mechanical properties of the post-processed material [41]. Therefore, as a second case study, we have applied the graph cutting technique to microstructure constituent segmentation in steels through use of EBSD-measured kernel average misorientation (KAM) values,

which are the average misorientation angles between a discrete point and a kernel of its neighboring points.

Experimentally, several techniques have been used in the characterization of microstructure constituents. Typically, the surface preparation of the sample drives the identification of different microstructures of steels. For example, certain etchants (and etchant time) can magnify the contrast between phases and/or microstructural constituents by distinguishing them as colored regions [54, 90]. However, these color-etching methods are difficult to reproduce and the color ranges of microstructure constituents (most notably martensite and bainite) overlap. Color etching is also limited by the spatial resolution of optical microscopy. Significant overlap also exists between the gray levels of constituents in SEM imaging [152, 153].

Tackling the issue through computational methods seems to be even more difficult as the significant overlap between the observable bainite and martensite characteristics makes it difficult to distinguish between the constituents. Wu et al. [174] investigated the variation in EBSD pattern image quality (IQ) with microstructure constituent and showed that, while significant overlap in the signals existed, the differences in IQ can provide useful information for identifying and locating microstructure constituents in multiphase steels. IQ is a data describes the level of contrast within the collected backscatter diffraction pattern but can also correlated to the local elastic strain, thermodynamic phases, proximity to interfaces and interface properties, and the defect state of the microstructure [72, 81, 129, 141, 155, 173]. Zaefferer et al. [179] utilized KAM values in order to separate a mixture of ferrite, bainite, and austenite in an Al-TRIP steel, but for practical application of the technique it is found that reproducibility is limited by a subjective identification of the relevant features in the

KAM histogram, which for many alloys differs significantly from the KAM histogram of the material analyzed in their work.

Tan et al. [152, 153] used KAM values to estimate the volume fractions for each constituent using a KAM deconvolution distribution mixture model. Although this method produces relatively accurate volume fractions for each constituent, it lacks the ability to resolve the locality of constituents and phases. Therefore, based on the observations of Zaefferer et al., Tan et al., Wu et al. and others, utilizing the correlations between pattern quality, KAM, and microstructure constituent seems to bode well for application of a graph cut algorithm through consideration of distributions of values for the individual phases in multi-modal or hyperspectral datasets such as those obtained by EBSD.

A key benefit of the graph cut approach is the flexibility in how the data fidelity and interaction potential are formulated. For this example, we will use the KAM angles to define the data fidelity component and EBSD Image Quality (IQ) values for the interaction potential. In formulating the interaction potential based on IQ, the underlying assumption is if neighboring data points have similar IQ values, there is a high probability of them belonging to the same phase.

In order to test the graph cutting algorithm in terms of microstructural constituent segmentation on hyperspectral data, an EBSD dataset from AISI 5160 steel, provided by Tan et al. [152, 153], was used to create a segmentation case study. The steel samples were processed through austenization and subsequent heat treatment and quenching to acquire specimens comprised nearly completely of a single constituent (martensite, bainite, and ferrite) at the same nominal chemical composition. Corresponding distributions for the KAM values of these specimens were computed

using TSL OIM<sup>TM</sup> Analysis 7 applied to third nearest neighbors, with a maximum KAM value of 5° applied to training EBSD datasets. Any values above this threshold were considered either noise or grain boundary pixels and were appropriately flagged.

Analogous to the segmentation of BSE images, the out-of-plane weights were assigned by considering the probability of phase assignment. The distribution of KAM angles for each phase was again assumed to be independent of the other phases and Gaussian. Let  $P = \{\text{martensite, bainite, ferrite, ...}\}$  be the set of phases of interest, indexed by  $\rho$ . For phase  $\rho$ , the discrete probability density of the KAM angle,  $\Theta$ , is given by  $P_\rho(\Theta)$ . The mean and standard deviation of KAM angles  $\Theta$  for each phase can then be given by:

$$\begin{aligned}\mu_\rho &= E(\Theta_\rho(j)) = \sum_{\theta} \theta_\rho * P_\rho(\Theta = \theta) \\ \sigma_\rho &= \sqrt{\sum_{\theta} (\theta_\rho - \mu_\rho)^2 * P_\rho(\Theta = \theta)}\end{aligned}\tag{3.4}$$

where  $E(\cdot)$  is the expectation operator. These values, calculated from the single component datasets, were then used for segmentation of EBSD datasets containing a mixture of all three constituent microstructures.

As in the segmentation of BSE images, the distribution of the out-of-plane weights for the segmentation case study is given by:

$$w^{g_1 \rightarrow g_2}(v^{(i)}) = f(\Theta(v^i) | \mu_\rho, \sigma_\rho)\tag{3.5}$$

which is identical to Equation 3.2, with the KAM angle distribution for phase  $\rho$  replacing the pixel intensity distribution and the  $\alpha$  parameter set to unity. Again, the out-of-plane weights for the other phases is formulated in a manner analogous to Equation 3.2.

As described above, the interaction penalty or regularization is formulated as a function of EBSD Image Quality (IQ). Assuming that similar IQ values would indicate two adjacent points came from the same constituent, the in-plane weights for adjacent nodes were computed through a normalized difference of these values:

$$w^{IP}(v^{(i)}, v^{(j)}) = \left\| \lambda \sqrt{\frac{1}{IQ(v^{(i)}) - IQ(v^{(j)})}} \right\| + \beta \quad (3.6)$$

where the regularization parameters were set as  $\lambda = 2^2$  and  $\beta = 0$ . The out-of-plane edges associated with EBSD points containing KAM values outside the range  $\Theta > 5^\circ$  were assigned equal but numerically small ( $w \approx 0$ ) for each of the potential constituents. This ensures that the interaction penalty or regularization term dominated, thereby heavily favoring each pixel's local neighborhood in phase or constituent assignment.

As there are three microstructure constituents of interest in this example, the graph structure for the complete problem should contain three grids. However, since bainite and martensite are so similar with respect to their KAM distributions, the problem was solved in two stages. The first cut involved segmenting ferrite from the background of martensite and bainite, using a two grid graph structure. For the next cut, the identified ferrite was removed from the EBSD dataset, and a second cut was made segmenting the martensite from a background of bainite. The cuts can be seen in Figure 3.5, along with the corresponding IQ and KAM maps. The graph cut segmentation generally locates the correct bainitic regions within the martensite matrix, and finds plausible locations for proeutectoid ferrite adjacent to the bainite. The volume fractions predicted by the graph cut are in good agreement with those predicted by the KAM distribution deconvolution method of Tan et al [152, 153], as shown in Table 3.2.

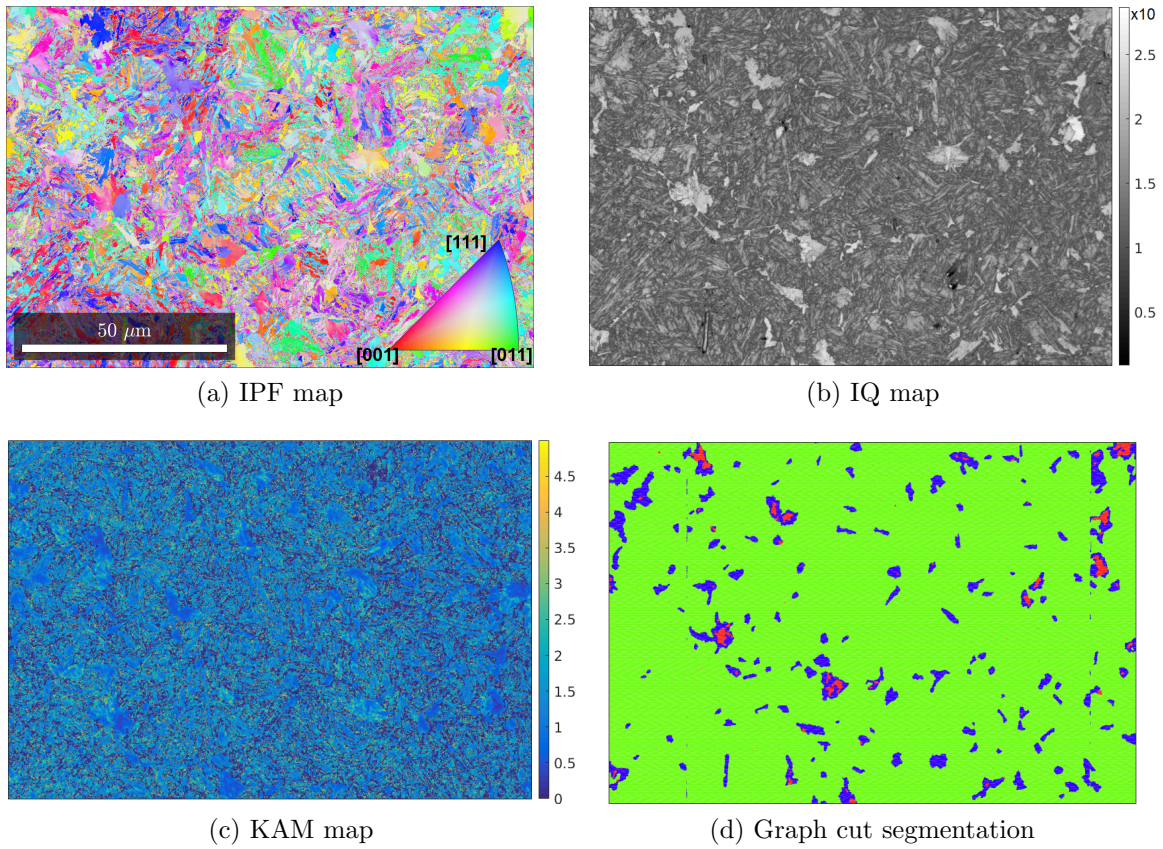


Figure 3.5: Graph cut applied to segmentation of EBSD data from a multi-component steel microstructure (a) using IQ (b) and KAM map data (c). In (d), red corresponds to ferrite, blue corresponds to bainite, and green corresponds to martensite regions.

Table 3.2: Respective volume fractions for ferrite, bainite, and martensite using the graph cutting technique and KAM distribution deconvolution [153] method.

		$v_f(fer)$	$v_f(bain)$	$v_f(mart)$
KAM	Distribution	1%	6%	93%
	Deconvolution [152, 153]			
Graph Cut		1.0%	6.5%	92.5%

### 3.3.2 Prior Austenite Grain Identification

The motivating application for the development of the graph cutting technique was the identification of parent grains given EBSD datasets of a transformation microstructure (e.g. identification of prior  $\beta$  grains from  $\alpha$  Ti microstructures or identification of austenite grains from observations of martensite). In terms of the austenite  $\rightarrow$  martensite transformation ( $\gamma \rightarrow \alpha'$ ), the athermal transformation results in a series of martensite laths exhibiting 24 crystallographic variants [84, 112]. Although the martensite microstructure controls the effective mechanical properties of the material, localization and failure can be heavily influenced by the prior austenite microstructure, including increasing prior austenite grain (PAG) diameters affecting ductile to brittle fracture occurrence [83, 178], the classification of creep and cavitation sites [70, 176], and temper embrittlement due to impurity segregation at prior austenite grain boundaries [10, 71]. For many alloy compositions, the transformation goes to completion such that inferences on the prior austenite microstructure can only be made from observations on the transformed martensitic microstructure. Determining the prior austenite orientation is complicated by uncertainty in the EBSD orientation indexing, the prevalence of annealing twins in the austenite, variation in the OR with composition, and heterogeneous plastic deformation due to accommodation of the martensitic shear [3, 56, 82, 112, 137, 139, 168].

Several prior austenite reconstruction algorithms exist, typically employing similar flood-fill-like approaches in which the misorientations between potential prior austenite orientations of neighboring pixels are analyzed and compared with a tolerance [14, 31, 36, 65]. If the misorientation falls below the tolerance, the two martensitic points are considered to come from the same PAG and are grouped together. This

continues between neighboring points until the tolerance cannot be reached, at which point a grain boundary is drawn between points and the process starts over at another node. For our procedure, we want to demonstrate, in a proof-of-concept manner, that it is feasible to use graph-cut segmentation to simultaneously identify all of the martensite points contained within a prior-austenite grain. This will serve as a basis for the development of a complete reconstruction algorithm but, for the purposes of this paper, serves as an additional case study for demonstrating the utility of the graph-cut method for a wide range of segmentation problems. A full description of the austenite reconstruction algorithm is beyond the scope of this paper and will be detailed in a subsequent manuscript. The EBSD dataset used for this example came from a 9-12%Cr tempered martensite ferritic steel, for which more information is available in reference [178]. While the orientation relationship (OR) is well-known to vary with composition [26, 60, 127], for the purposes of the present example we will simply assume a Kurdjumov-Sachs (KS) orientation relationship [89].

Consider an EBSD dataset of a completely martensitic structure, where the martensite orientation measurements can be labeled,  $G_{\alpha'} = [g_{\alpha'}^{(1)}, g_{\alpha'}^{(2)}, \dots, g_{\alpha'}^{(n)}]$  and correspond to graph vertices  $\mathcal{V} = [v^{(1)}, v^{(2)}, \dots, v^{(n)}]$ . Note that this labeling, and the resultant graph structure, is agnostic with respect to the EBSD sampling grid (either square or hexagonal). Following the pattern of the previous examples, the weights of the in-plane edges should relate the probability that the martensite orientations measured at two neighboring EBSD scan points are consistent with coming from the same PAG. In previous work, the authors described the set of possible martensite-to-martensite misorientations given a common parent [26]. Payton et al. have characterized the degree of scatter, or variability in the OR observable from EBSD [127].

From this information, a martensite-martensite misorientation distribution function (MODF) can be constructed and denoted  $f(\Delta G_{\alpha'})$ . The MODF was constructed by convolving the admissible martensite-martensite misorientations with a de La Valee Poussin kernel function [7]. The halfwidth of the kernel was taken as  $1.7^\circ$  to best match the variability observed by Payton et al. [127]. The misorientation between the two martensite orientations associated with the edge with end vertices  $v^{(i)}$  and  $v^{(j)}$  is denoted  $\Delta g_{\alpha'}(v^{(i)}, v^{(j)})$ , and the in-plane weights can then be calculated as:

$$w^{IP}(v^{(i)}, v^{(j)}) = \lambda \Delta(g_{\alpha'}(v^{(i)}, v^{(j)})) + \beta \quad (3.7)$$

The out-of-plane weights are related to the probability that the martensite orientations,  $G_{\alpha'}$ , were generated from a trial austenite orientation,  $g_\gamma$ . If the austenite  $\rightarrow$  martensite OR is denoted  $\Delta g_{\gamma \rightarrow \alpha'}$ , then  $f(g_{\alpha'}|g_\gamma, \Delta g_{\gamma \rightarrow \alpha'})$  denotes an ODF which gives this probability. The term  $f(g_{\alpha'}|g_\gamma, \Delta g_{\gamma \rightarrow \alpha'})$  can be constructed by convolving the trial austenite orientation with a kernel with suitable half-width to create a unimodal ODF. The ODF can be transformed by all variants of the OR,  $\Delta g_{\gamma \rightarrow \alpha'}$ , producing an ODF with 24 peaks, each corresponding to one martensite variant from the given parent. For this example, the weights  $w^{g_2 \rightarrow t}(v^i)$  are simply:

$$w^{g_2 \rightarrow t}(v^i) = \lambda f(g_{\alpha'}|g_\gamma, \Delta g_{\gamma \rightarrow \alpha'}) + \beta \quad (3.8)$$

The weights  $w^{g_1 \rightarrow g_2}$  relate to the probability that a data point is part of the background. In this case, the background refers to all martensite orientations that did not come from a parent grain with orientation  $g_\gamma$ . This can be approximated by the uniform ODF which is unity for all orientations, giving us:

$$w^{g_1 \rightarrow g_2} = \lambda f_{\text{uniform}}(g) + \beta = \kappa \quad (3.9)$$

A portion of the transformed microstructure was analyzed to find a region of interest that did not include any twins. A small but sufficient section of this region was then extracted and each martensite orientation was transformed through the 24 crystallographic variants into austenite. A local austenite ODF was finally computed and a relative maximum  $g_\gamma$  was chosen as the guess orientation to perform likelihood calculations on.

Figure 3.6a shows the input EBSD dataset, with orientations colored according to a standard cubic IPF key found in Figure 3.5. Figure 3.6b maps the likelihood  $f(g_{\alpha'}|g_\gamma, \Delta g_{\gamma \rightarrow \alpha'})$  for the evaluated trial austenite orientation. Lighter values indicate higher likelihoods and the darker points correspond to low likelihood positions. High likelihood values are concentrated within the boundary of the central PAG in the image, suggesting a reasonable austenite guess orientation was chosen, while a few scattered high likelihood points appear generally well separated within the plot. Figure 3.6c shows the result of the graph cut, colored again using a cubic IPF key such that the color of the segmented region corresponds to the guessed prior austenite orientation. The background of scattered colors is related to an array of randomly assorted austenite orientations at each individual point assuming a completely transformed microstructure. Since the chosen austenite orientation is highly favored within the central PAG but nowhere else, it is consistent that the likelihood values in Figure 3.6 corresponding to these random orientations are low ( $\sim 0$ ).

In order to assess the potential efficacy of our proposed method, a grain boundary misorientation tolerance method was applied through MTEX. [7] This method employs a similar misorientation-based methodology adopted by some austenite reconstruction codes. This was accomplished by computing the 16 theoretical martensitic

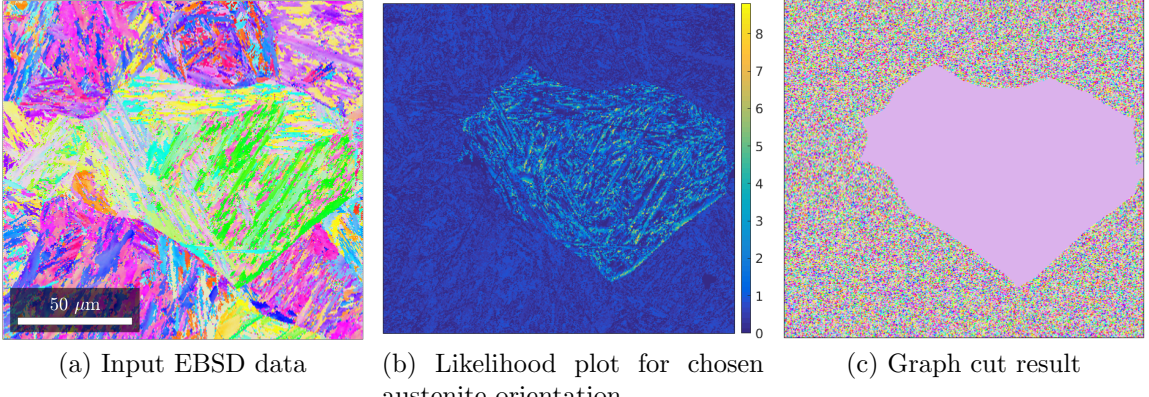


Figure 3.6: Segmentation of austenite grain from martensitic steel EBSD dataset. The color key in (a) is identical to that for the EBSD data in Figure 3.5a.

misorientations corresponding to a single PAG for variants generated from the KS OR. The grain boundary misorientations from the input data were then calculated and a spatially resolved list was generated detailing each respective misorientation. The grain boundary misorientations were finally compared with the PAG-induced martensite misorientations with respect to a user-defined tolerance. Higher tolerances mean more grain boundary misorientations are accepted as having come from the same PAG and subsequently assigned an austenite orientation, whereas lower tolerance values create more stringent acceptance guidelines. Additionally, each austenite grain is colored by unique grain ID to easily distinguish between reconstructed grains. The resultant full austenite reconstructions can be seen below in Figure 3.7 for several tolerances.

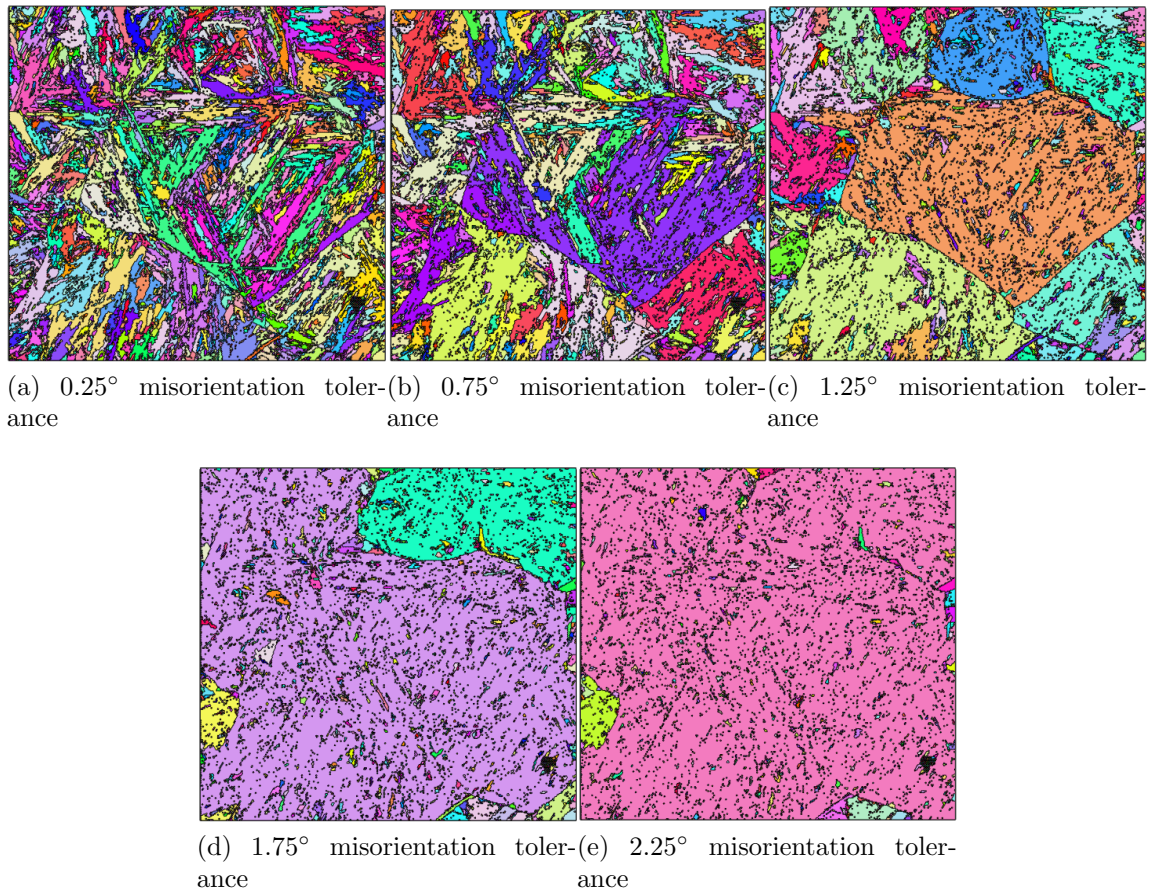


Figure 3.7: Grain boundary misorientation austenite reconstructions performed using MTEX [7] for five separate angular tolerances:  $0.25^\circ$  (top left),  $0.75^\circ$  (top middle),  $1.25^\circ$  (top right),  $1.75^\circ$  (bottom left) and  $2.25^\circ$  (bottom right)

### 3.4 Atomic Clustering

Detailed analyses and descriptions of microstructures, including classification of precipitates and clustered atoms in solid solutions, can be achieved through the use of atom probe tomography (APT). Spatially correlated atoms within a solid solution can be used to identify clusters of atoms, which in turn serve as precursors to spinodal decomposition, precipitation, and chemical ordering [48]. Although several clustering techniques have been applied to APT data, including  $k$ -means clustering [97], the maximum separation method [73], the core-linkage algorithm [148], Voronoi Partitioning [48] and Gaussian mixture model Expectation Maximization Algorithm [180], they often require extensive manual intervention and have difficulty in segmenting clusters within a dense background of uniformly distributed atoms. As a final example of applications of the graph-cut method we explore the potential for analysis of APT data by performing cluster identification and analysis for simulated 2D “APT-like” datasets. This final case study also demonstrates how the graph-cut approach can easily be extended to data that is not on a regular grid.

The setup for the identification of clustered atoms given synthetic ATP data was similar to the ones used for the aforementioned segmentation examples, including the one displayed in Figure 3.1b. The differences that arise between the clustering and segmentation examples are minimal in terms of implementation into our graph cutting algorithm and highlight the versatility of the technique in terms of grid construction. Mainly, instead of a square grid for image pixel intensities or hexagonal or square grid for phase and parent grain segmentation, the grid can be randomly assigned based on the coordinates of each individual atom with respect to an arbitrary reference frame. This allows for the spatial distance between neighboring atoms to be utilized

to generate pertinent weights for each system based on the classification of atoms as coming from either a cluster (smaller distances between neighboring atoms) or the background (larger distances between atoms). The dual-grid setup is shown schematically below in Figure 3.8 for an arbitrary system of atoms, represented as the black circles. Again, the  $s \rightarrow g_1$  edges are uncuttable and displayed in red, and the yellow edges from  $g_1 \rightarrow g_2$  indicate the probability that atoms came from the background. The blue edges then constitute the probability that atoms are situated within clusters. Finally, the gray intra-grid edges found between neighboring atoms have thicknesses proportional to spatial distances, where thicker edges are found between atoms that are spatially nearer to each other.

Each respective system was then established through the use of weights, and each atom comprising the entire system was considered a node  $v^{(i)}$  within  $g_k$ . The versatility of node placement is most notable for this set up as the distances between adjacent nodes are entirely random, fluctuating both relative to the population of atoms within the system and how dense the population is that surrounds any given atom. The in-plane weights were computed through the calculation of discrete, multivariate probability distributions for each atom's specific coordinates,  $x$ , using the following equation:

$$\begin{aligned} w^{IP}(v^{(i)}, v^{(j)}) &= f(X, x, \Sigma) \\ &= \frac{1}{\sqrt{|\Sigma|(2\pi)^2}} \exp\left(-\frac{1}{2}(X - x)\Sigma^{-1}(X - x)'\right) \end{aligned} \quad (3.10)$$

Where  $X$  represents the entire distribution of atoms in a 2D Cartesian coordinate frame and  $\Sigma$  is the covariance matrix. Through consideration of each atom as an individual distribution, spatial correlations for each atom with respect to the rest

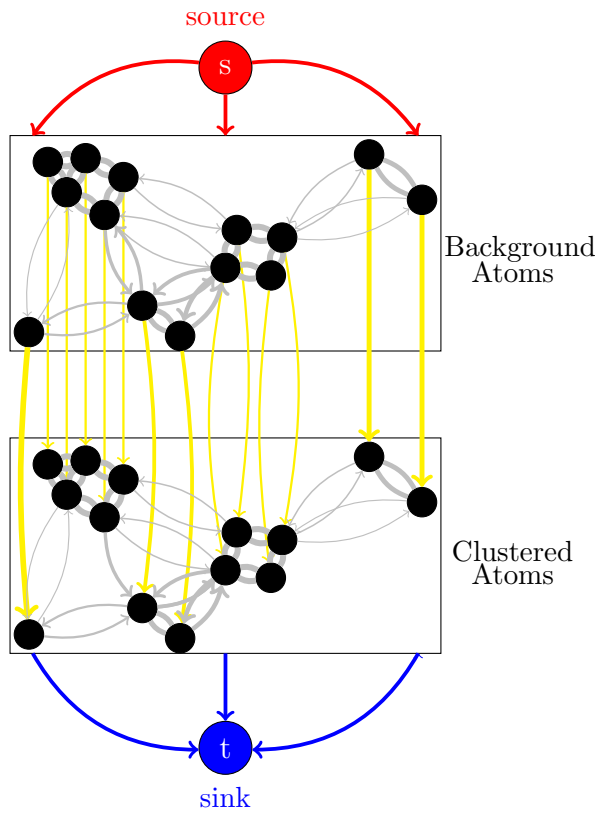


Figure 3.8: The graph schematic utilized to solve the problems mentioned in this paper along with a specified, arbitrary case involving image segmentation

could be quantified. This assisted in the identification of regions of dense populations, thereby allowing the algorithm to effectively group atoms within these regions as likely clustered atoms.

The out-of-plane weights were computed through utilization of the discrete multivariate probability distribution values. The population density composition of in-plane weights resulted in a bimodal distribution of values detailing the likelihood that an atom belongs to a cluster or the background. This allowed for the assignment of respective  $\mu$  and  $\sigma$  values, since clustered atoms are more likely to come from the more densely populated regions and background atoms should fall within the sparser regions:

$$\begin{aligned} w^{OP}(v^{(i)}, v^{(j)}) &= f(w^{IP}(v^{(i)}, v^{(j)}) | \{\mu_\eta, \sigma_\eta\}) \\ &= \alpha_\eta \left( \frac{1}{\sigma_\eta \sqrt{2\pi}} \exp \left( \frac{-(w^{IP}(v^{(i)}, v^{(j)}) - \mu_\eta)^2}{2\sigma_\eta^2} \right) + \omega_\eta \right) \end{aligned} \quad (3.11)$$

Here,  $\eta$  refers to either a background or clustered designation for each respective atom and  $\alpha$  and  $\omega$  are equivalent to the parameters found in Equation 3.2.

Cuts were then performed on a per-atom basis, where the technique only extracted nodes that were identified as residing within a cluster. In total, 10 clusters of 100 atoms each were created and distributed randomly throughout the background. This resulted in 1000 total clustered atoms, which remained static throughout the analysis. The number of background atoms was increased dramatically, from a 1:1 ratio of 2000 total atoms to a 50:1 ratio of 51000 atoms in order to test the efficacy of the algorithm in the face of increasing noise (background atoms), hindering the ocular distinction of clusters within the dataset. The generated cuts for varied ratios of background-to-clustered atoms can be seen below in Figure 3.9:

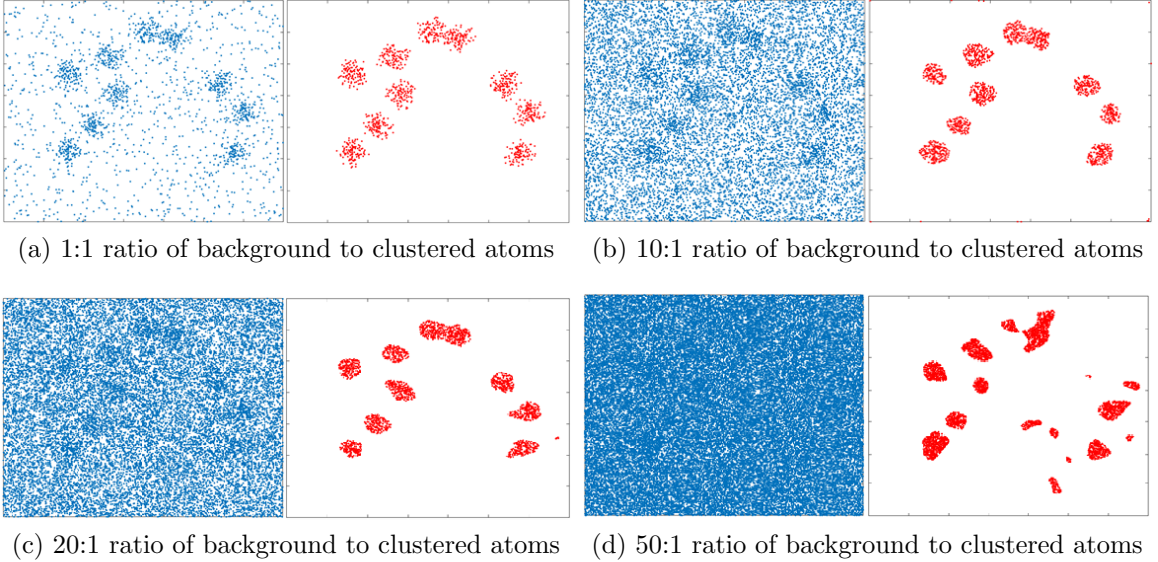


Figure 3.9: Variable background:clustered atom ratios with the corresponding graph cut solutions for a synthetic, 2D dataset

As Figure 3.9 details, the algorithm does an excellent job of identifying the locations of the clusters for relatively noisy datasets, even if the denoted clusters are denser than the actual synthetic cluster. In the 50:1 background:cluster (BG:C) case, displayed in Figure 3.9d, even picking out the clusters by eye is nearly impossible. However, the graph cut adequately captures the locations of clusters, albeit with some additional noise and some smaller faux-clusters. The number of identified clusters remains consistent and accurate up to a 10:1 ratio, with a small, additional noisy cluster generated in the 20:1 case. The scaling parameters of  $\alpha$  for each respective case are given below in Table 3.3, as  $\omega$  for both cluster and background atom pairings was 0.

We also wanted to test the algorithm against increasingly sparse clusters to see how dense the clusters need to be for sufficient results. To achieve this, the 10:1

Table 3.3: Scaling parameters corresponding to the cases displayed in Figure 3.9, where subscript BG represents favoring background atom designation and C is related to clusters

BG:C Atomic Ratio	$\alpha_{BG}$	$\alpha_C$
1:1	$1.6 \times 10^4$	$5.0 \times 10^0$
10:1	$3.9 \times 10^5$	$3.1 \times 10^3$
20:1	$7.8 \times 10^4$	$1.6 \times 10^4$
50:1	$2.0 \times 10^6$	$2.5 \times 10^1$

ratio dataset was chosen and atoms from each cluster were iteratively redistributed into the background. This not only increases the BG:C atomic ratio, but it also decreases the density of each respective cluster, effectively making it more difficult to probabilistically define the likelihood that certain locations contained clusters or not. The results are displayed in Figure 3.10.

As the number of displaced clustered atoms reaches around 50% (Figure 3.10d), diminishing the number of atoms from each cluster down to 50, the algorithm does a decent job of identifying the clustered locations. Furthermore, the number of atoms flagged as a cluster is limited, even as the density of each respective cluster is decreased dramatically. Although the edges show an increasing amount of noise with each additive displacement of clustered atoms, the amount of noise contained within the middle of the dataset remains low, and 10 clusters are recognized by the graph cutting technique for each given case. The amount of atoms within every cluster for each displacement iteration can be seen below in Table 3.4.

Although the algorithm tends to add atoms to each cluster, the results are promising and would suggest further development of the model to obtain more accurate and

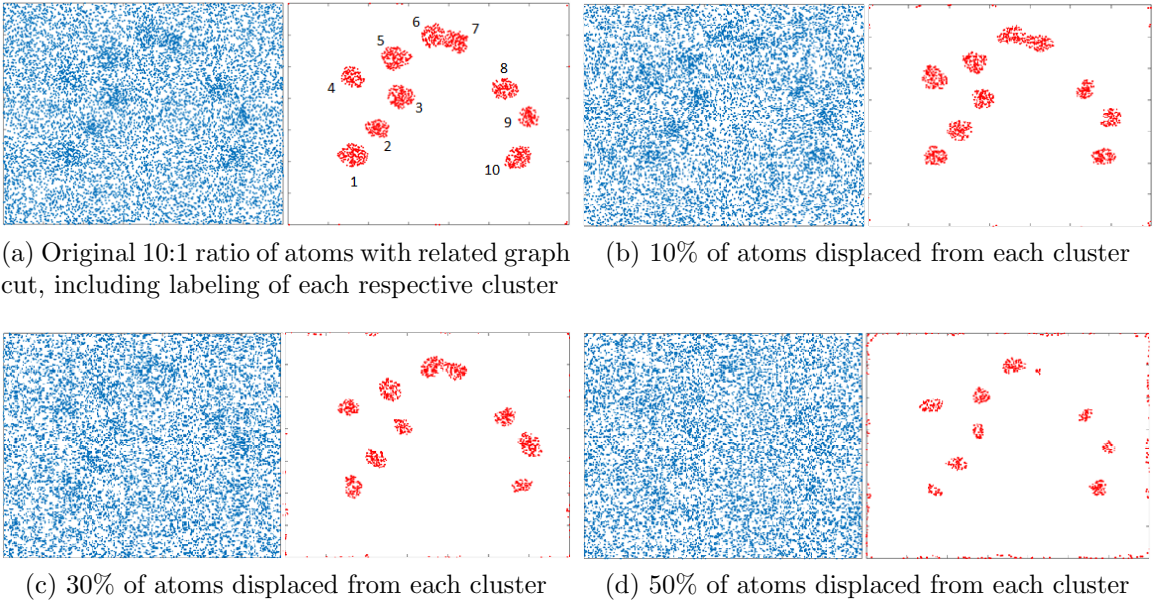


Figure 3.10: Performance of graph cuts when removing clustered atoms and randomly dispersing them throughout the background. The number of clusters is consistent with those denoted in Table 3.4

Table 3.4: The percentage of atoms removed from each synthetic cluster and dispersed within the background compared with the amount of flagged atoms in each cut cluster for the 10:1 BG:C ratio

Cluster Label	1	2	3	4	5	6	7	8	9	10
0%	168	142	168	180	162	147	220	179	142	133
10%	128	108	107	118	100	107	149	105	111	143
30%	125	133	86	94	126	113	132	73	84	91
50% *	58	74	105	91	88	79	104	25	87	114

\* Additional cluster containing 5 atoms

consistent results. Again,  $\omega$  was 0 for each specific case, and Table 3.5 details the scaling parameters for  $\alpha$  for both background and cluster designations.

Table 3.5: Scaling parameters corresponding to Figure 3.10, where atoms were randomly displaced from clusters and added to the background

% of Displaced Atoms	$\alpha_{BG}$	$\alpha_C$
0%	$3.9 \times 10^5$	$3.1 \times 10^3$
10%	$1.6 \times 10^4$	$6.3 \times 10^2$
30%	$2.0 \times 10^6$	$7.8 \times 10^4$
50%	$3.9 \times 10^5$	$3.1 \times 10^3$

Finally, a modified  $k$ -means approach [94] was implemented as a rudimentary comparison to the presented graph cutting approach using the built-in MATLAB function. Since the datasets are synthetic and therefore the number of clusters was known a priori, the number of clusters to identify was automatically set to 10 to optimize results. Additionally, the distance between each atom and the central point for each determined cluster was also computed. However, considering the function only groups the atoms into corresponding clusters without exclusion, there would be no atoms flagged as having come from the background. To rectify this, a tolerance was added that compared the distance of an atom's location with that of its nearest cluster's central point. If the distance exceeded the tolerance, the atom was rejected from the cluster and re-indexed as a background atom. This tolerance was then adjusted until the most reasonable results were established for each case in Figure 3.9 from the graph cutting technique. The latter cases, of a 20:1 and 50:1 background to cluster ratio break down and thus do not need to be shown. The background atomic arrangement fluctuates from those presented in the graph cutting case but

the clustered atomic positions are equivalent. The results are presented below in Figure 3.11 along with the optimized tolerance values:

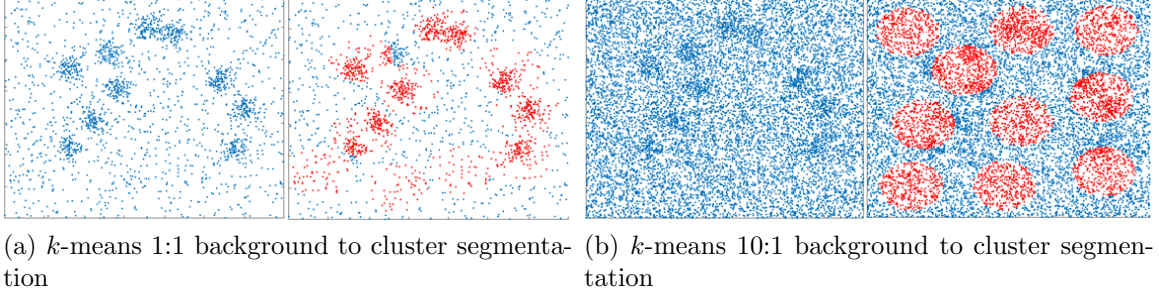


Figure 3.11: The  $k$ -means segmentations for the graph cut cases represented in Figure 3.9 with relative distance tolerances of 0.025 and 0.025 for the 1:1 and 10:1 background to cluster ratio, respectively.

### 3.5 Discussion

The above examples demonstrate that our proposed graph-cutting framework can be used for a wide range of segmentation and clustering problems across a spectrum of input data types that commonly arise in advanced materials characterization. The main advantage of the graph-cut framework is the ease at which complex regularized optimization problems can be posed and subsequently solved. The graph structure itself gives a visual interpretation to the problem which aids in formulation. When developing the case studies presented above, the authors were surprised that often naive or “first-stab” ideas worked nearly as well as specialized algorithms such as EM/MPM [39]. This strongly suggests that if paired with a well thought out graphical user interface, the method could be developed into a robust and user friendly materials data analysis tool and be integrated with commercial and open source image analysis

tools such as BlueQuartz Software LLC, MIPAR [145], Thermo Scientific<sup>TM</sup> Amiro-Avizo Software, MATLAB's Image Processing Toolbox<sup>TM</sup>, etc.

For the specific example of image segmentation of  $\gamma'$  particles, there are clear issues with particle separation for all three tested methods, as some particles with a small separation between each other get lumped together into one large particle. However, the relative location and geometry of most of the particles is captured with a reasonably high signal-to-noise ratio. Compared with the EM/MPM technique, graph cutting results in a significantly less noisy image with improved particle attributes. The Otsu threshold method is slightly better at segmenting images with a large contrast between particles and matrix, as seen with the René 88 DT dataset. However, when more complicated images with less contrast need to be segmented, such as with the René 104 dataset, the graph cut segmentations contained the most geometrically accurate particles with the least amount of noise. This is because the intra-particle intensity gradients within the larger particles can be regularized with the graph cutting technique based on adjacent-pixel intensity values. A wider variety of images would need to be tested to most thoroughly test the efficacy of the three methods, but the examples here demonstrate graph cutting technique is a viable option for image segmentation in materials science applications.

With respect to microstructure constituent segmentation in hyperspectral data, the results show that the graph cutting technique produces reasonable results, albeit without ground-truth validation. The determined location of the ferrite and bainite, clustered together and occupying points of high-IQ values, makes logical sense and is visually consistent with the IQ map. Additionally, the ability to produce repeatable results in the presence of excessive noise is a strong indicator of the robustness of

the approach. Reproducibility suggests that a statistical test might be developed to determine the accuracy of the segmentation when results across a large number of EBSD scans are considered.

As mentioned previously, the motivating application for the graph-cut technique was the analysis of transformation microstructure, particularly the identification of prior-transformation grains. This example study shows the limited case of identifying the points associated with a single prior-austenite grain given a reasonable estimate of the orientation. One can imagine an iterative search over the orientation space to identify the remainder of the grains and complete the reconstruction. However, specification and implementation of a complete and robust algorithm is well beyond the scope of this work. Here, the intention is simply a demonstration of how flexible the graph-cut approach is with respect to the data used to formulate the fidelity and penalization terms and to highlight an example that is outside the general set of problems associated with segmentation. When compared with the MTEX approach that employs a flood fill inspired algorithm, we can see where the limitations exist. Too low of a misorientation tolerance identifies most martensite features as their own PAGs. Too high of a tolerance results in clustering the martensite features into a single, giant PAG. Even with the moderate tolerance that produces quasi-reasonable results, we can see the grains, most notably the large, centralized one we segment using the graph cutting technique, is littered with noise and regions extend across the presumed boundaries.

Atom clustering segmentation showed sufficiently good results when being solved by graph cutting. As the density of the background atoms was increased, the density of the clusters increased as well. There seems to be no way around this, but the

algorithm did work well for identifying possible nucleation sites in spite of high levels of noise. The noisy edges incorrectly flagged as clusters when the atoms were being displaced from the clusters may be the result of those atoms having fewer nearest neighbors, thereby resulting in skewed neighboring distances and increasing the likelihood that they came from clusters. This issue could possibly be prevented through the addition of a periodic boundary condition or mirrored interfaces, where a spatial pseudo-distribution of atoms with similar density to the dataset surrounding the atoms would increase the edge atoms nearest neighbor count and thus classify them as probabilistically more likely to have come from the background. The ability to characterize clusters even when the atoms are not as locally concentrated would be a considerable gain with respect to analysis of APT data. In comparison to the  $k$ -means algorithm, which determines centrally located points around presumed clusters, our results show a much better ability at accurately identifying the location of clusters. Although the presented  $k$ -means technique is not considered state of the art, the vast difference in reconstruction results suggests that the graph cutting approach is a prospective new approach to atomic cluster segmentations from APT data. The next step would be to compare the results with some of the more established clustering algorithms to see how the graph cut technique manages.

### 3.6 Conclusion

The graph cutting algorithm is a powerful technique that can be used to efficaciously solve inverse problems in materials science and other fields of engineering. The results for problems in image segmentation, microstructure constituent segmentation, parent grain segmentation applied to the  $\gamma \rightarrow \alpha'$  transformation and atomic

clustering identification are promising, suggesting that the technique can be used to handle difficult analysis issues within the computational materials science community. Implementation of models is simple, relying upon *Bayesian* statistical methods that can produce desirable results in the face of high levels of noise. Basing assumptions in probabilistic terms allows for a quantitative analysis of the results. Validation using experimental techniques would help bolster the approaches taken to solve each problem, and more profound models would only serve to improve upon results. The versatility of the technique suggests that more problems could be solved so long as effective networks of nodes can be established.

## **Chapter 4: Analysis of Misorientation Relationships between Austenite Parents and Twins**

The following chapter has been published in Metallurgical and Materials Transactions A [26] with the authors Dr. Victoria Yardley, Dr. Stephen Niezgoda and Dr. Eric Payton. The introduction has been truncated and added to Section 2 to reduce redundancy, with the remaining sections reproduced in their entirety.

### **4.1 Introduction**

To develop the in-plane weights related to the prior for applying the graph cutting technique introduced in Chapter 3 to the reconstruction of the austenite microstructure, it is necessary to utilize the misorientation information related to prior austenite grains and their annealing twins. Martensitic variant formation from pre-transformation austenite was introduced in Chapter 2 through a crystallographic lens. The specific variants that form from a prior austenite grain preserve vital information about the state of the transformation, such as the orientation relationship of the sample and the inherent noise associated with the transformation, indicators of variant selection, which could be associated to prior austenite grain size. Another key factor related to the transformation is the misorientation relationship between pairs of

intersecting variants. An improved understanding of the variant-to-variant misorientation relationships may be used to improve electron backscatter diffraction (EBSD)-based reconstruction techniques of the prior austenite phase. The prior austenite microstructure can significantly affect physical properties of the phase-transformed material through microstructure scale [143] and potentially through crystallographic texture.

In the present work, composition tables of the misorientation relationships between variants within a single prior austenite grain and its annealing twins are calculated for three separate orientation relationships: KS, NW, and one which has been experimentally determined [127], building off of the work by Cayron [31]. It is currently not possible to accurately measure the c-axis extension that would distinguish bct from bcc at higher C content using EBSD (resulting in pseudosymmetry in the experimental results). As such, bct martensite in EBSD is typically indexed as bcc. To determine whether this has any impact on the misorientation data, both cubic (point group  $m\bar{3}m$ ) and tetragonal (point group  $4/mmm$ ) symmetry are used to compute the misorientations in standalone composition tables.

## 4.2 Materials and Methodology

Starting from a single prior austenite orientation aligned with the sample reference frame (Bunge Euler angles of  $\phi_1 = \Phi = \phi_2 = 0$ ), the four  $\Sigma 3$  face-centered cubic annealing twin orientations were calculated from the four unique rotations of  $60^\circ$  about  $\langle 111 \rangle$ . A number of experimentally observed orientation relationships have been determined from EBSD analysis of SEM and TEM characterized microstructures [85, 112]. For this paper, the experimentally measured orientation relationship

was established based on the procedure outlined in references [127, 175–177] on a sample of low carbon steel, which may be expected to have a KS-like orientation relationship. The orientation relationship was determined through the use of measured  $\xi$  angles, with untwinned PAGs being identified and selected manually within a given micrograph range. The datasets were then rotated to coincide the PAG orientation with the sample reference frame, with the angular deviation between the primary axis of the rotation matrix and the axes of the closest Bain correspondence matrix representing the orientation relationship in terms of three parameters. The composition, thermal history, and data collection parameters are published in reference [114] and the modal orientation relationship values are published in reference [177] and listed in Table 1. Here,  $\xi_1$  is the smaller deviation from  $<110>$ -type Bain correspondence axis,  $\xi_2$  is the large deviation from the  $<110>$ -type axis and  $\xi_3$  is the deviation from the  $<001>$ -type axis. This resulted in 24 crystallographic variants, the same number attained with the KS orientation relationship. For convenience of comparison, the three NW and KS modal values and corresponding Bunge Euler angles for a single variant ( $V_1$ ) are also listed in Table 1.

Each of the resulting five orientations (the PAG and its four annealing twins) was then rotated by the 12  $\gamma \rightarrow \alpha'$  variant rotations for the NW OR, the 24  $\gamma \rightarrow \alpha'$  rotations of the KS OR, or the 24 rotations of an experimentally measured (irrational) orientation relationship. This produced a total of 7260 post-transformation orientations (inclusive of misorientations between identical variants) for the experimental and KS relationships and 1830 orientations for NW. The minimum-angle misorientations between each of these orientations was then calculated assuming either cubic or tetragonal symmetry elements (representing the as-transformed martensite and the

tempered martensite ferritic microstructures, respectively). Duplicate misorientation operations were identified to produce the set of potentially observable boundary misorientations within a single twinned PAG, and the unique misorientations were then numbered. Henceforth we will refer to these boundary misorientations as “intersections.” We have chosen to represent the variant intersections by a misorientation angle about a specific crystallographic direction. The misorientation that results from a given variant-variant intersection is labeled in a composition table with the cell colored according to the misorientation angle. Additionally, the misorientation axis is plotted in an inverse pole figure. These tables and figures effectively display which misorientation will be observed upon the intersection of two variants.

The numbering of the variants has been conducted in the same manner as in Payton et. al., [127] where consecutive variants are grouped into subsets of six that are formed on the same  $\{111\}_\gamma$  (i.e.,  $\mathbf{V}_1$  through  $\mathbf{V}_6$  would share one  $\{111\}_\gamma||\{011\}_{\alpha'}$  relationship,  $\mathbf{V}_7$  through  $\mathbf{V}_{12}$  would share a different  $\{111\}_\gamma||\{011\}_{\alpha'}$  relationship and so on). Additionally, successive variant pairs have the same Bain correspondence matrices ( $\mathbf{V}_1$  and  $\mathbf{V}_2$ ,  $\mathbf{V}_5$  and  $\mathbf{V}_6$ ,  $\mathbf{V}_9$  and  $\mathbf{V}_{10}$ , etc.). Likewise, the numbering of misorientations corresponds to the aforementioned sub-block (low-angle), block and packet boundaries, all differing types of intragranular variant-variant ( $\mathbf{V}_i - \mathbf{V}_j$ ) interfaces. Misorientations will be denoted as  $\Delta g_i$ , where  $\Delta g_0$  is an identity misorientation operator (identity rotation about an arbitrary or undefined axis to bring the two variants into coincidence with one another). Identity misorientations are the result of two equivalent variants from the same PAG sharing an interface. When applying the KS orientation relationship, some variants originating from annealing twins in the parent austenite are exactly the same orientation. This can result in no observed

misorientation across a  $\Sigma 3$  austenite twin boundary [1, 2, 36, 105], as will be further analyzed in the present work. Additionally, misorientations labelled  $\Delta g_1$  correspond to a sub-block boundary and block boundaries are distinguished by  $\Delta g_{2-4}$ . Misorientations  $\Delta g_{5-16}$  refer to packet boundaries, and the aforementioned misorientations all refer to intra-parent cases, where a variant formed from the PAG intersects with another variant that formed from the PAG. For misorientations  $\Delta g_{17+}$ , which involve twin-variants, the  $\mathbf{V}_i - \mathbf{V}_j$  interfaces are undefined packet boundaries.

## 4.3 Results

### 4.3.1 Kurdjumov-Sachs Orientation Relationship With Cubic Symmetry

Given a single parent austenite grain transformed to martensite, the composition table assuming the KS orientation relationship is displayed in Figure 1. The two axes in the table correspond to a particular variant, numbered according to Tables AI through AIII in the Appendix section, which details the unique misorientation relationships that exist between variants for certain cases (intra-parent, parent-twin and twin-twin). Figure 1 covers the intra-parent case, where variants within a PAG intersect with variants within that same PAG. The plot itself is symmetric, so the top half mirrors the filled in bottom half of the plot. The identity misorientations ( $\mathbf{V}_i - \mathbf{V}_i$ ) that occur between like variants are unobservable interfaces due to the lack of a misorientation and will later be found outside of the intra-parent case for the KS (and NW) orientation relationships.

The boxes in the table corresponding to the variant-variant misorientations are colored by the degree of misorientation, from light to dark, according to the corresponding colorbar. For cubic systems, the maximum misorientation angle is  $62.8^\circ$  [68].

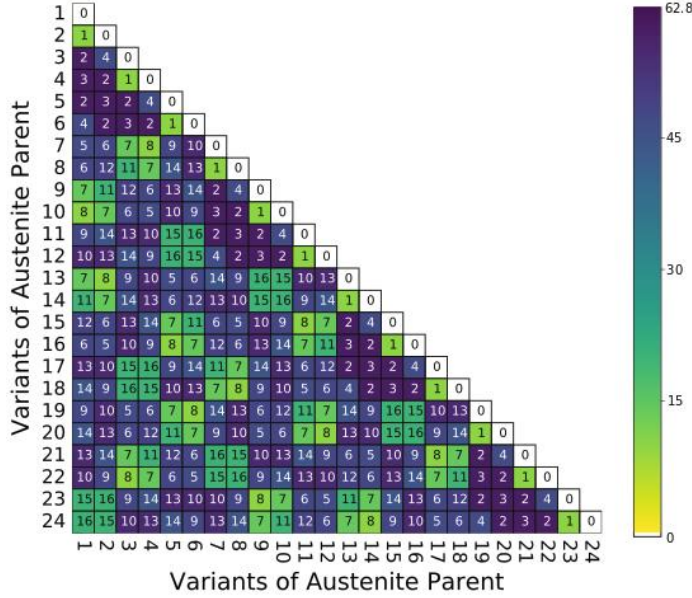


Figure 4.1: Composition table exhibiting the possible variant-variant misorientations for prior intra-parent austenite grains.

The majority of the misorientation squares are dark, meaning the misorientation angle is large for most of the variant intersections. Referring to Table AI, four of the possible 16 misorientations have angles near  $60^\circ$ , within 10% of the maximum possible cubic value, and there exist only 16 misorientations that occur from variant intersections out of 276 possibilities for the KS orientation relationship (excluding the  $\mathbf{V}_i - \mathbf{V}_i$  and symmetric cases). However, it is also known that the austenite grains may contain FCC annealing twins before the phase transformation to martensite occurs [34], which would result in twin-related variants. Thus, it is necessary to determine what unique misorientations—if any—would result with the intersection of a parent austenite variant and a twinned austenite variant.

For sake of space and redundancy, only one parent-twin interaction will be presented since the results for all four produce identical sets of misorientations (although

the misorientations appear in different locations within the composition table). The full composition tables for each specific case are available as supplemental data to the present paper in Figures S1-S9. The parent- $60^\circ[111]$  twin composition table can be found in Figure 2, with corresponding misorientation keys in Table AII.

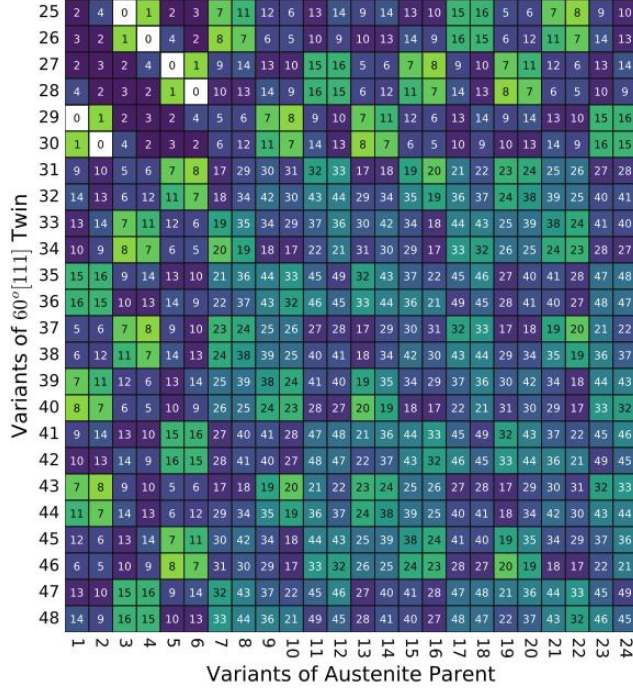


Figure 4.2: The possible variant-variant misorientations for prior parent- $60^\circ[111]$  twin austenite grains.

As can be seen from Figure 2, the parent-twin interactions introduce considerably more misorientations than the intra-parent case alone, with 49 in total being observed. Additionally, the 16 misorientations found within the intra-parent case are repeated in the parent-twin cases, leaving 33 unique misorientations that would indicate the presence of at least one twin within the parent austenite grain. Again, we can see that

the intersection squares all tend to be darker, indicative of higher misorientation angles, especially with regards to the unique parent-twin misorientations. The existence of six identity misorientations, consistent for each respective twinning case, results in the possibility of no observable interface within the transformed microstructure where an annealing twin boundary once existed for the KS orientation relationship.

Although rarer than  $\Sigma 3$  annealing twins, it is possible for twin-twin variant intersections ( $\Sigma 9$  boundaries [134]) to occur in the parent austenite microstructure. This would consist of the intersection of two variants that transformed from austenite twins of differing rotations that nucleated within the same parent austenite grain; i.e. the former boundary between two different twins of the same parent austenite. Composition tables were constructed for these interactions, with the composition table for the intersections between  $60^\circ [\bar{1}\bar{1}1]$  and  $60^\circ [111]$  twins from the same austenite grain shown in Figure 3. The corresponding list of misorientation angle-axis pairs can be found in Table AIII. The same misorientations result from all other twin-twin composition tables; the complete set of tables is available in the supplemental material as Figures S1-S3.

The twin-twin case includes misorientations  $\Delta g_5$  to  $\Delta g_{139}$ , indicating a large number of the misorientations found with the intra-parent and parent-twin cases will also appear in twin-twin variant intersections. Additionally, we see that no identity misorientations exist in the twin-twin cases. The twin-twin intersections bring about 90 unique misorientations that can only be observed in twin-twin intersections, and are thus indicative of a prior  $\Sigma 9$  boundary.

The existence of misorientations numbered above 16 would necessitate that at least one of the variants being observed came from an austenite twin. Twin variants

	Variants of $60^\circ[1\bar{1}1]$ Twin																																	
49	32	43	37	22	45	46	50	68	74	56	84	90	98	110	120	128	134	135	131	124	115	104	137	136										
50	33	44	36	21	49	45	51	69	75	57	85	91	99	111	121	129	135	136	132	125	116	105	139	137										
51	17	18	19	20	21	22	52	70	76	58	86	92	100	101	102	103	98	99	109	108	107	106	105	104										
52	29	34	35	19	36	37	53	71	77	59	87	93	101	112	113	114	110	111	119	118	117	107	116	115										
53	30	42	34	18	44	43	54	72	78	60	88	94	102	113	122	123	120	121	127	126	118	108	125	124										
54	31	30	29	17	33	32	55	73	79	61	89	95	103	114	123	130	128	129	133	127	119	109	132	131										
55	22	37	43	32	46	45	56	74	68	50	90	84	104	115	124	131	136	137	128	120	110	98	135	134										
56	21	36	44	33	45	49	57	75	69	51	91	85	105	116	125	132	137	139	129	121	111	99	138	135										
57	20	19	18	17	22	21	58	76	70	52	92	86	106	107	108	109	104	105	103	102	101	100	99	98										
58	19	35	34	29	37	36	59	77	71	53	93	87	107	117	118	119	115	116	114	113	112	101	111	110										
59	18	34	42	30	43	44	60	78	72	54	94	88	108	118	126	127	124	125	123	122	113	102	121	120										
60	17	29	30	31	32	33	61	79	73	55	95	89	109	119	127	133	131	132	130	123	114	103	129	128										
61	24	38	39	25	40	41	62	80	83	67	82	81	70	71	72	73	68	69	79	78	77	76	75	74										
62	23	24	25	26	27	28	63	62	67	66	65	64	52	53	54	55	50	51	61	60	59	58	57	56										
63	28	41	40	27	48	47	64	81	82	65	96	97	92	93	94	95	90	91	89	88	87	86	85	84										
64	27	40	41	28	47	48	65	82	81	64	97	96	86	87	88	89	84	85	85	94	93	92	91	90										
65	26	25	24	23	28	27	66	67	62	63	64	65	58	59	60	61	56	57	55	54	53	52	51	50										
66	25	39	38	24	41	40	67	83	80	62	81	82	76	77	78	79	74	75	73	72	71	70	69	68										
67	9	14	13	10	15	16	27	40	41	28	47	48	21	36	44	33	45	49	32	43	37	22	45	46										
68	10	13	14	9	16	15	28	41	40	27	48	47	22	37	43	32	46	45	33	44	36	21	49	45										
69	5	6	7	8	9	10	23	24	25	26	27	28	17	29	30	31	32	33	17	18	19	20	21	22										
70	6	12	11	7	14	13	24	38	39	25	40	41	18	34	42	30	43	44	29	34	35	19	36	37										
71	7	11	12	6	13	14	25	39	38	24	41	40	19	35	34	29	37	36	30	42	34	18	44	43										
72	8	7	6	5	10	9	26	25	24	23	28	27	20	19	18	17	22	21	31	30	29	17	33	32										
	25	26	27	28	29	30	31	32	33	34	35	36	37	38	39	40	41	42	43	44	45	46	47	48										

Figure 4.3: Composition table exhibiting the possible variant-variant misorientations for differing twins that nucleated from the same parent austenite grain.

of the same rotation intersecting with each other (for example, the composition table of  $60^\circ$   $[\bar{1}\bar{1}1]$  and  $60^\circ$   $[\bar{1}\bar{1}1]$ ) produce the exact same composition table as Figure 1. Since these cases are highly unlikely, it can be assumed that the observance of  $\Delta g_1$  through  $\Delta g_4$  would indicate that at least one of the variants would have had to have nucleated from a parent austenite grain. These tables can also be found in the supplemental material as Figure S2. Additionally, out of all possible misorientations, only three could be considered as low-angle:  $\Delta g_1(10.53^\circ)$ ,  $\Delta g_7(14.88^\circ)$ , and  $\Delta g_8(10.53^\circ)$ . The minimum misorientation angles are  $\Delta g_1$  and  $\Delta g_8$ , both ( $10.53^\circ$ ), and the maximum misorientation angle is  $\Delta g_{55}(60.83^\circ)$ .

To better visualize the directional aspects of the misorientations with respect to cubic symmetry, the axes for the intra-parent, parent-twin and twin-twin cases were plotted on stereographic triangles and displayed in Figure 4. Tables AI to AIII can be used to identify the misorientation angles corresponding to each respective misorientation axis. Misorientation axes are colored according to misorientation angle using the same color key as used in Figure 1. Several misorientations are found to exhibit the same axes as one another. We can also see from the tables that some of the misorientation angles are very similar. This will be addressed in the Discussion section of this paper.

#### 4.3.2 Nishiyama-Wassermann Orientation Relationship

NW has half of the number of variants as compared to KS due to the alignment of symmetry operators between parent and product phases. As such,  $\mathbf{V}_1$  and  $\mathbf{V}_2$  in the KS orientation relationship refer to  $\mathbf{V}_1$  in the NW orientation relationship,  $\mathbf{V}_3$

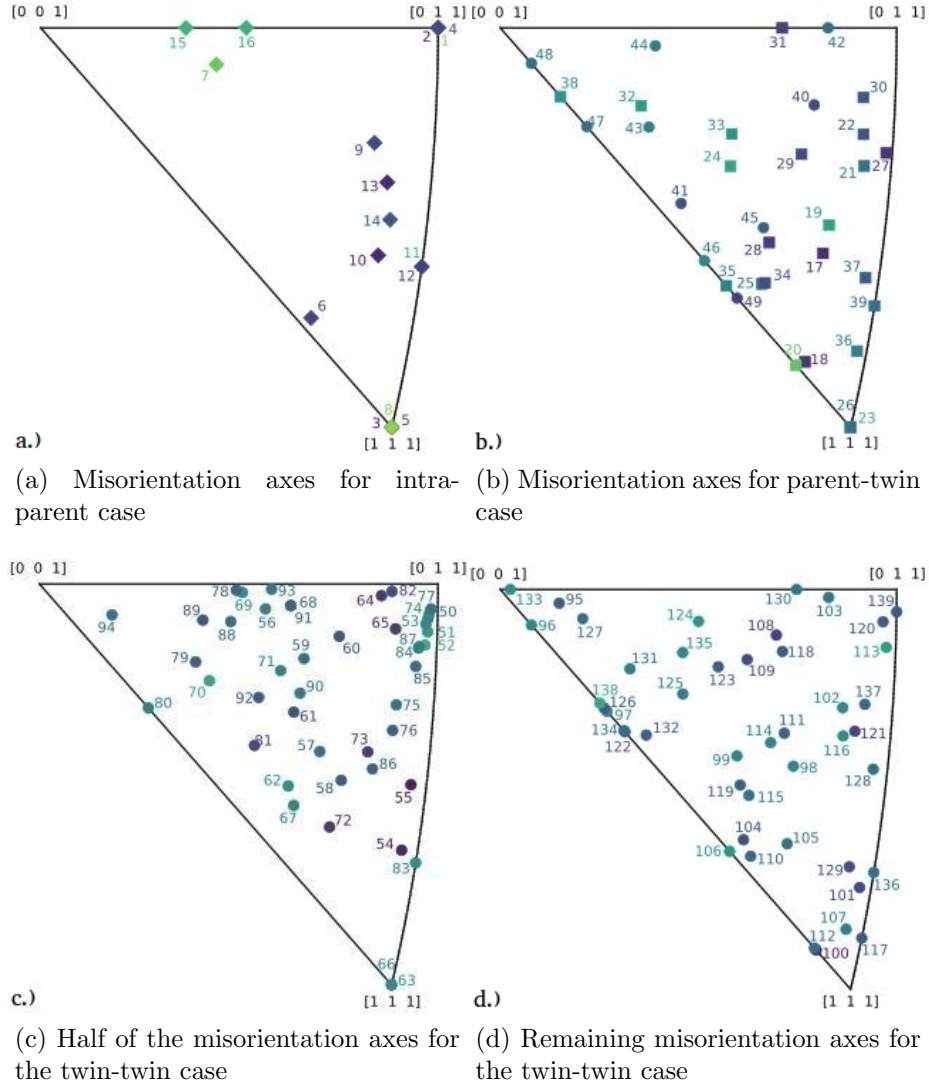


Figure 4.4: Misorientations directional axes overlayed on stereographic triangles for the KS orientation relationship for: (a) the intra-parent case, (b) the parent-twin case, and (c) and (d) the twin-twin case (split into two subfigures to reduce the density of points).

and  $\mathbf{V}_4$  in KS are  $\mathbf{V}_2$  in NW, and so on. Due to the reduced number of orientation relationship variants, far fewer unique misorientations can be observed and a complete composition table exhibiting all of the possible variant combinations can be simultaneously represented in Figure 5.

The figure consists of two parts. The main part is a large grid of numbers representing variant combinations. The numbers are color-coded according to a key located at the top right. The key shows a 4x4 grid of colors: white, purple, green, blue, red, orange, yellow, and black. The subfigure at the top right is a smaller version of the main grid, also with a color key, showing a truncated portion of the full table.

Variant	Color	Variant	Color	Variant	Color	Variant	Color	Variant	Color
0	White	1	Purple	2	Green	3	Blue	4	Red
5	Orange	6	Yellow	7	Cyan	8	Magenta	9	Black
10	Light Green	11	Light Blue	12	Light Red	13	Light Orange	14	Light Yellow
15	Dark Green	16	Dark Blue	17	Dark Red	18	Dark Orange	19	Dark Yellow

Figure 4.5: Full composition table derived from NW orientation relationship. The subfigure at the upper right can be identified within the full table and comprises the truncated portions at the upper left and lower right portions of the table, representing misorientations derived from intra-parent variant intersections. The key relates the variant numbers to the parent or twin type of the grain the martensite transformed from.

The intra-parent case applying the NW orientation relationship involves five unique misorientations, while the parent-twin case has 15 misorientations and includes all of the intra-parent misorientations. Additionally, we can see the existence of three identity operators instead of six as in the KS case. Finally, in terms of the differing twin-twin variant intersections, there exist  $\Delta g_2$  through  $\Delta g_{40}$ , excluding only  $\Delta g_1$ . In comparing the tables for KS and NW, it is apparent that NW  $\Delta g_1$  seems to combine KS  $\Delta g_2$ - $\Delta g_3$ , in the process eliminating the existence of KS  $\Delta g_1$ . As expected, the NW orientation relationship also results in almost all high misorientation angles, with one possible low-angle boundary,  $\Delta g_3(13.76^\circ)$  as opposed to three in the KS case. Table BIV in the Appendix section lists all of the respective NW misorientations with the corresponding angle-axis pairing. There were no misorientations with axes or angles within  $1^\circ$  of those of another misorientation within the NW orientation relationship. The misorientation axes for each case are plotted on the stereographic triangle in Figure 6.

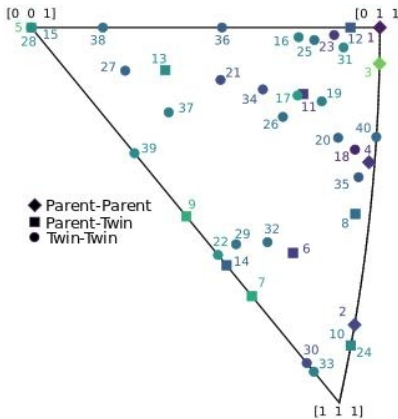


Figure 4.6: Stereographic triangle plotting all misorientation axes with colored points corresponding to degree of misorientation angle for the NW orientation relationship.

### 4.3.3 Experimentally Observed Orientation Relationship

The composition table for the intra-parent case of the experimentally observed (i.e., irrational) orientation relationship is given in Figure 7. Interestingly, calculation resulted in exactly the same misorientation numbering (with only 16 unique misorientations) as Figure 1, but with small deviations in the misorientation angles and/or directional axes from KS. The same color scale is used in Figure 6 as in Figure 1, such that direct comparison of the colors in each box illustrates the misorientation angle differences. The misorientation numbering and the respective angle-axis pairing for each misorientation is given in Tables CV-CVII.

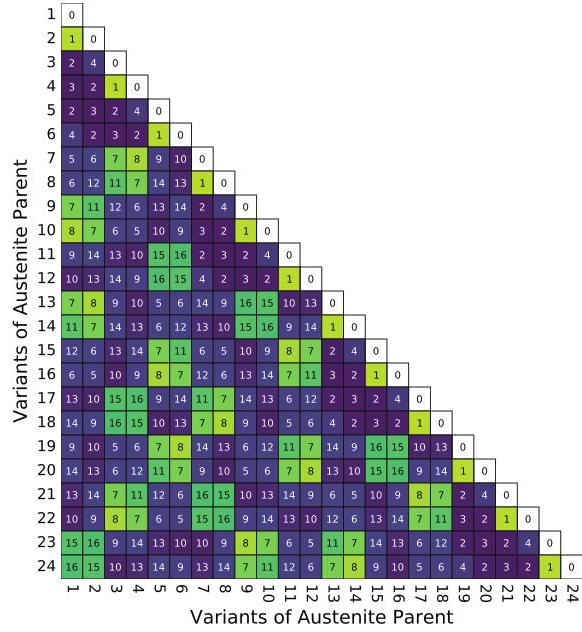


Figure 4.7: Composition table exhibiting intra-parent variant intersections given an experimentally determined orientation relationship.

The parent-twin case was analyzed next, with resultant composition table displayed in Figure 8. Two noticeable differences between the KS and experimental cases are readily observed when comparing Figure 7 to Figure 2. First, the identity operators found in the KS orientation relationship (for example, between  $\mathbf{V}_{30}$  and  $\mathbf{V}_2$  in Figure 2) are replaced by a low angle misorientation,  $\Delta g_{19}$  ( $3.19^\circ[337]$ ). The second main difference is the number of misorientations present, increasing from 49 total in the KS case to 71 misorientations using an experimentally measured orientation relationship, resulting in 22 extra misorientations. This difference can be partially explained by the fact that only  $\Delta g_2$  from the intra-parent case is observed in the parent-twin case, with all other misorientations being unique to the parent-twin case. In comparison, all sixteen misorientation operators in KS shared between the parent and the twin.

The twin-twin composition table for the  $60^\circ[111]-60^\circ[\bar{1}\bar{1}1]$  twins using the experimental orientation relationship is given in Figure 9. The remaining composition tables can be found in the supplemental material as Figures S4-S7. Similar to the parent-twin case, several misorientations exist in addition to the comparative KS case and the only misorientation to exist in both the twin-twin case and the parent-twin or intra-parent cases is  $\Delta g_4$ . All others are unique to the twin-twin case. There exist 156 unique misorientations for the twin-twin case, with a total of 227 misorientations for the experimental orientation relationship as a whole. This is significantly higher than the 139 misorientations found for the KS orientation relationship. Eight low-angle boundaries exist within the experimental orientation relationship. Three are at the same variant-variant intersection numbers as the KS case, meaning that they are produced from the same variant pairings:  $\Delta g_1(6.60^\circ)$ ,

	Variants of $60^\circ[111]$ Twin																															
	1	2	3	4	5	6	7	8	9	10	11	12	13	14	15	16	17	18	19	20	21	22	23	24	25	26	27	28	29	30	31	32
25	4	18	19	20	4	17	33	34	35	36	37	38	21	22	23	24	25	26	27	28	29	30	31	32								
26	17	4	20	19	18	4	30	29	28	27	32	31	24	23	22	21	26	25	36	35	34	33	38	37								
27	4	17	4	18	19	20	21	22	23	24	25	26	27	28	29	30	31	32	33	34	35	36	37	38								
28	18	4	17	4	20	19	24	23	22	21	26	25	36	35	34	33	38	37	30	29	28	27	32	31								
29	19	20	4	17	4	18	27	28	29	30	31	32	33	34	35	36	37	38	21	22	23	24	25	26								
30	20	19	18	4	17	4	36	35	34	33	38	37	30	29	28	27	32	31	24	23	22	21	26	25								
31	21	24	27	36	33	30	39	51	52	53	54	55	39	40	41	42	43	44	45	46	47	48	49	50								
32	22	23	28	35	34	29	40	56	64	52	65	66	51	56	57	41	58	59	46	60	61	47	62	63								
33	23	22	29	34	35	28	41	57	56	51	59	58	52	64	56	40	66	65	47	61	60	46	63	62								
34	24	21	30	33	36	27	42	41	40	39	44	43	53	52	51	39	55	54	48	47	46	45	50	49								
35	25	26	31	38	37	32	43	58	66	55	67	71	54	65	59	44	67	68	49	62	63	50	69	72								
36	26	25	32	37	38	31	44	59	65	54	66	67	55	66	58	43	71	67	50	63	62	49	72	69								
37	27	36	33	30	21	24	45	46	47	48	49	50	39	51	52	53	54	55	39	40	41	42	43	44								
38	28	35	34	29	22	23	46	60	61	47	62	63	40	56	64	52	65	66	51	56	57	41	58	59								
39	29	34	35	28	23	22	47	61	60	46	63	62	41	57	56	51	59	58	52	64	56	40	66	65								
40	30	33	36	27	24	21	48	47	46	45	50	49	42	41	40	39	44	43	53	52	51	39	55	54								
41	31	38	37	32	25	26	49	62	63	50	69	72	43	58	66	55	67	71	54	65	59	44	67	68								
42	32	37	38	31	26	25	50	63	62	49	70	69	44	59	65	54	68	67	55	66	58	43	71	67								
43	33	30	21	24	27	36	39	40	41	42	43	44	45	46	47	48	49	50	39	51	52	53	54	55								
44	34	29	22	23	28	35	51	56	57	41	58	59	46	60	61	47	62	63	40	56	64	52	65	66								
45	35	28	23	22	29	34	52	64	56	40	66	65	47	61	60	46	63	62	41	57	56	51	59	58								
46	36	27	24	21	30	33	53	52	51	39	55	54	48	47	46	45	50	49	42	41	40	39	44	43								
47	37	32	25	26	31	38	54	65	59	44	67	68	49	62	63	50	69	70	43	58	66	55	67	71								
48	38	31	26	25	32	37	55	66	58	43	71	67	50	63	62	49	70	69	44	59	65	54	68	67								
	1	2	3	4	5	6	7	8	9	10	11	12	13	14	15	16	17	18	19	20	21	22	23	24								

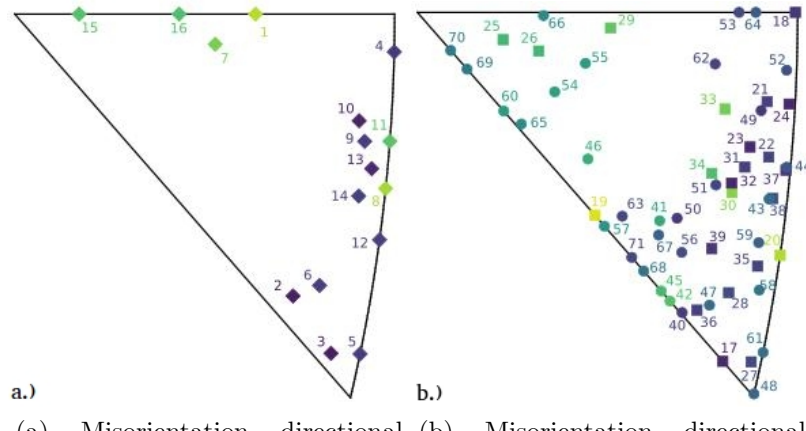
Figure 4.8: Composition table displaying parent-twin variant intersections given an experimentally determined orientation relationship.

$\Delta g_7(12.58^\circ)$ , and  $\Delta g_8(8.12^\circ)$ . There are five additional low angle misorientations:  $\Delta g_{19}(3.19^\circ)$ ,  $\Delta g_{20}(6.93^\circ)$ ,  $\Delta g_{30}(11.15^\circ)$  and  $\Delta g_{33}(13.14^\circ)$  unique to the parent-twin case, and  $\Delta g_{95}(14.07^\circ)$ , unique to the twin-twin case.

	Variants of $60^\circ[\bar{1}11]$ Twin																								
	25	26	27	28	29	30	31	32	33	34	35	36	37	38	39	40	41	42	43	44	45	46	47	48	
49	4	96	102	78	118	124	138	156	162	144	172	178	186	198	208	216	222	223	219	212	203	192	225	224	
50	73	97	103	79	119	125	139	157	163	145	173	179	187	199	209	217	223	226	220	213	204	193	227	225	
51	74	98	104	80	120	126	140	158	164	146	174	180	188	189	190	191	186	187	197	196	195	194	193	192	
52	75	99	105	81	121	127	141	159	165	147	175	181	189	200	201	202	198	199	207	206	205	195	204	203	
53	76	100	106	82	122	128	142	160	166	148	176	182	190	201	210	211	208	209	215	214	206	196	213	212	
54	77	101	107	83	123	129	143	161	167	149	177	183	191	202	211	218	216	217	221	215	207	197	220	219	
55	78	102	96	4	124	118	144	162	156	138	178	172	192	203	212	219	224	225	216	208	198	186	223	222	
56	79	103	97	73	125	119	145	163	157	139	179	173	193	204	213	220	225	227	217	209	199	187	226	223	
57	80	104	98	74	126	120	146	164	158	140	180	174	194	195	196	197	192	193	191	190	189	188	187	186	
58	81	105	99	75	127	121	147	165	159	141	181	175	195	205	206	207	203	204	202	201	200	189	199	198	
59	82	106	100	76	128	122	148	166	160	142	182	176	196	206	214	215	212	213	211	210	201	190	209	208	
60	83	107	101	77	129	123	149	167	161	143	183	177	197	207	215	215	221	219	220	218	211	202	191	217	216
61	84	108	113	89	130	135	150	168	171	155	170	169	158	159	160	161	156	157	167	166	165	164	163	162	
62	85	109	112	88	131	134	151	150	155	154	153	152	140	141	142	143	138	139	149	148	147	146	145	144	
63	86	110	111	87	132	133	152	169	170	153	184	185	180	181	182	183	178	179	177	176	175	174	173	172	
64	87	111	110	86	133	132	153	170	169	152	185	184	174	175	176	177	172	173	183	182	181	180	179	178	
65	88	112	109	85	134	131	154	155	150	151	152	153	146	147	148	149	144	145	143	142	141	140	139	138	
66	89	113	108	84	135	130	155	171	168	150	169	170	164	165	166	167	162	163	161	160	159	158	157	156	
67	90	114	115	91	136	137	131	130	135	134	133	132	120	121	122	123	118	119	129	128	127	126	125	124	
68	91	115	114	90	137	136	134	135	130	131	132	133	126	127	128	129	124	125	123	122	121	120	119	118	
69	92	93	94	95	90	91	85	84	89	88	87	86	76	74	75	76	77	4	73	83	82	81	80	79	78
70	93	116	117	94	114	115	109	108	113	112	111	110	98	99	100	101	96	97	107	106	105	104	103	102	
71	94	117	116	93	115	114	112	113	108	109	110	111	104	105	106	107	102	103	101	100	99	98	97	96	
72	95	94	93	92	91	90	88	89	84	85	86	87	80	81	82	83	78	79	77	76	75	74	73	4	

Figure 4.9: Composition table showing differing twin-twin variant intersections given an experimentally determined orientation relationship.

Stereographic triangles of the misorientation axes corresponding to Figures 6-8 are given in Figure 10. It is clear from the figure that the experimentally observed orientation relationship tends to produce several misorientations with rotation axes that are essentially parallel, where several of the points are very close to one another in the plot. The colors again relate to the degree of the misorientation by the same color scale as given in Figure 1, while the marker shapes indicate whether the  $\Delta g$  originates from the intra-parent, parent-twin, or twin-twin composition tables.

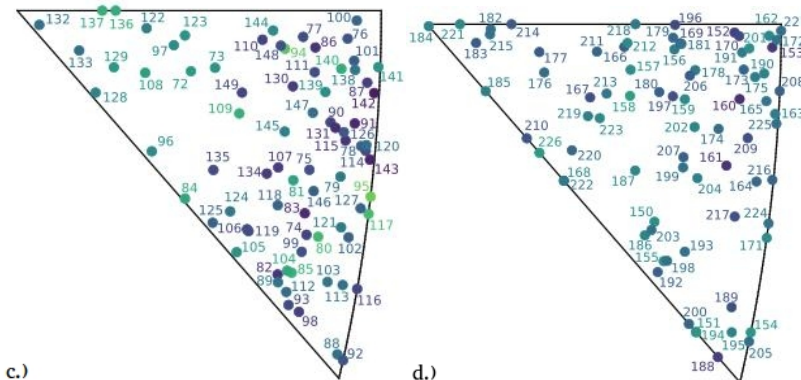


a.)

(a) Misorientation directional axes for experimental intra-parent case

b.)

(b) Misorientation directional axes for experimental parent-twin case



c.)

(c) Half the misorientation axes for experimental twin-twin case

d.)

(d) Remaining misorientation axes for twin-twin case

Figure 4.10: Misorientations directional axes overlayed on stereographic triangles for the experimentally-measured orientation relationship for: (a) the intra-parent case, (b) the parent-twin case, and (c) and (d) the twin-twin case (split into two subfigures to reduce density of points).

A pole figure containing the variant orientations for the three orientation relationships analyzed in Section 3 is displayed in Figure 4.11. In each case, the prior austenite orientation is aligned with the sample reference frame. The martensite variants of the parent austenite are indicated with black dots circumscribed by a colored circle indicating the hemisphere of the pole in stereographic projection. Each twin of the parent austenite orientation is represented by a different marker style according to the legend in the lower left. This figure concisely collects all of the variants so they can be easily compared, either within an orientation relationship to examine the differences between PAG and twin variants, or across orientation relationships to discover disparities. Close examination of the pole figures reveals that the locations of intra-parent variants from KS and NW overlap with those of variants generated from  $\Sigma 3$  twin boundaries, as has been reported elsewhere [1, 2, 36, 105]; however, this overlap is not observed in the experimentally measured orientation relationship. Since all orientations are unambiguous, this increases the number of unique misorientations observed between the variants, as presented in Figures 4.7 through 4.9.

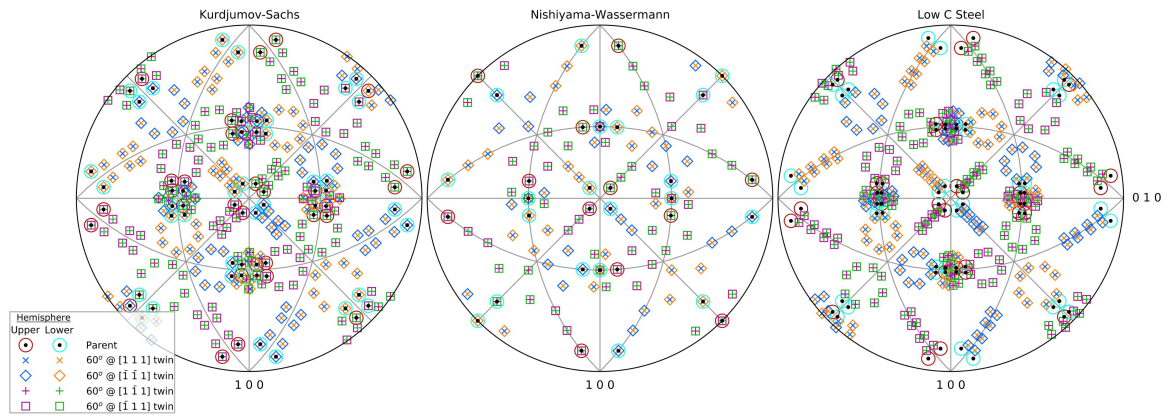


Figure 4.11: Pole Figures containing variant orientations for the three orientation relationships: KS (left), NW, and Experimental (right), all considering cubic symmetry

#### 4.4 KS Orientation Relationship Considering Tetragonal Based Crystal Symmetry

As mentioned above, the previous cases analyzing  $\mathbf{V}_i - \mathbf{V}_j$  intersections from an orientation relationship standpoint were all conducted using cubic symmetry. That is, the *austenite*  $\rightarrow$  *martensite* transformation was really an *fcc*  $\rightarrow$  *bcc* phase transformation. To study whether product crystal structure affects misorientation data, tetragonal symmetry was applied to the variant rotation matrices in the calculation of the composition tables. This corresponds to the *fcc*  $\rightarrow$  *bct* transformation. The KS orientation relationship was used to compare the effects of cubic and tetragonal symmetry on misorientation calculations. Furthermore, intra-parent, parent-twin and twin-twin variant intersections were examined. The intra-parent composition table is given in Figure 11. The colormapping of the composition tables was comparable in style to the cubic case but was normalized to the maximum tetragonal misorientation angle of 98.42° [68] rather than 62.3° for cubic systems, as indicated adjacent to the plot.

In Figure 10, we again see exactly the same misorientation locations within the composition table as both the cubic KS and experimental case, with 16 misorientations in total. Overall, the tetragonal-based misorientation angles seem to fall further away from the maximum misorientation angle. Additionally, as seen in the cubic case, the same three numbered misorientations corresponding to the intra-parent case could be classified as low-angle boundaries:  $\Delta g_1(10.53^\circ)$ ,  $\Delta g_7(14.88^\circ)$ , and  $\Delta g_8(10.53^\circ)$ . It is interesting to note that all three of these misorientation numbers were low-angle boundaries across orientation relationship and cubic symmetry when considering 24 variants. All the rest of the misorientations correspond to high-angle boundaries.

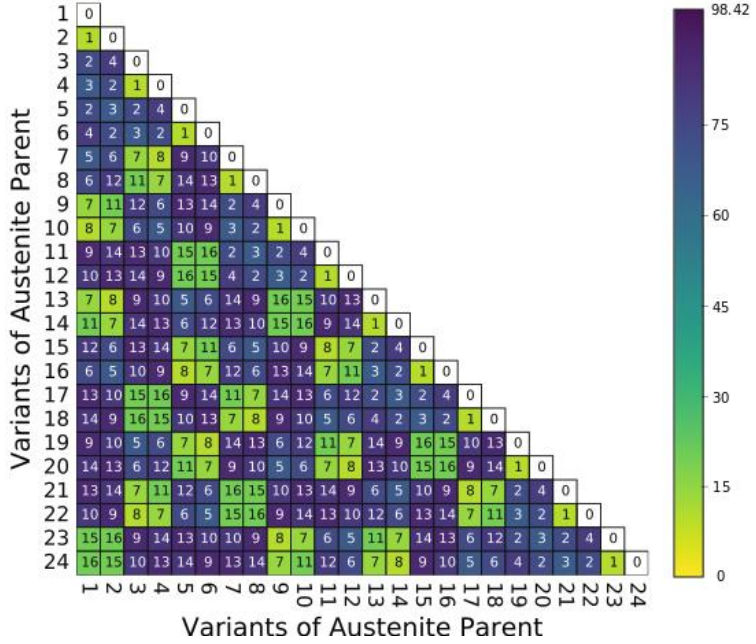


Figure 4.12: intra-parent composition table for tetragonal symmetry using KS orientation relationship.

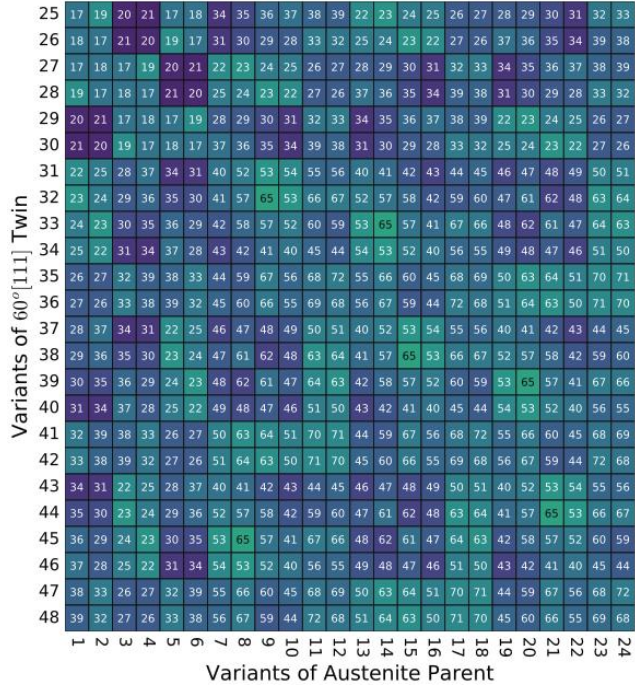


Figure 4.13: Composition table exhibiting the possible variant-variant intersections for prior parent-twin austenite grains using tetragonal symmetry.

When considering the parent-twin case for tetragonal symmetry for all four possible twin rotations, all of the misorientation angles are rather large, with none falling below  $40^\circ$ . Again, we see that there are no shared variants, but in this case, the location where the shared variants exist in the cubic KS case (section 3) is not low angle, coming in at  $90.00^\circ$  (M3). Not only is this misorientation angle very far from an identity rotation, no misorientations from the intra-parent case overlap with the parent-twin case. Each misorientation is unique. A total of 55 unique misorientations exist, adding 16 relative to the cubic-KS case. The corresponding composition table is displayed in Figure 12.

	Variants of $60^\circ[111]$ Twin																								
	49	73	97	103	79	119	125	139	157	163	145	173	179	187	199	209	217	223	224	220	213	204	193	226	225
50	74	98	104	80	120	126	140	158	164	146	174	180	188	200	210	218	224	227	221	214	205	194	228	226	
51	75	99	105	81	121	127	141	159	165	147	175	181	189	190	191	192	187	188	198	197	196	195	194	193	
52	76	100	106	82	122	128	142	160	166	148	176	182	190	201	202	203	199	200	208	207	206	196	205	204	
53	77	101	107	83	123	129	143	161	167	149	177	183	191	202	211	212	209	210	216	215	207	197	214	213	
54	78	102	108	84	124	130	144	162	168	150	178	184	192	203	212	219	217	218	222	216	208	198	221	220	
55	79	103	97	73	125	119	145	163	157	139	179	173	193	204	213	220	225	226	217	209	199	187	224	223	
56	80	104	98	74	126	120	146	164	158	140	180	174	194	205	214	221	226	228	218	210	200	188	227	224	
57	81	105	99	75	127	121	147	165	159	141	181	175	195	196	197	198	193	194	192	191	190	189	188	187	
58	82	106	100	76	128	122	148	166	160	142	182	176	196	206	207	208	204	205	203	202	201	190	200	199	
59	83	107	101	77	129	123	149	167	161	143	183	177	197	207	215	216	213	214	212	211	202	191	210	209	
60	84	108	102	78	130	124	150	168	162	144	184	178	198	208	216	222	220	221	219	212	203	192	218	217	
61	85	109	114	90	131	136	151	169	172	156	171	170	159	160	161	162	157	158	168	167	166	165	164	163	
62	86	110	113	89	132	135	152	151	156	155	154	153	141	142	143	144	139	140	150	149	148	147	146	145	
63	87	111	112	88	133	134	153	170	171	154	185	186	181	182	183	184	179	180	178	177	176	175	174	173	
64	88	112	111	87	134	133	154	171	170	153	186	185	195	176	177	178	173	174	184	183	182	181	180	179	
65	89	113	110	86	135	132	155	156	151	152	153	154	147	148	149	150	145	146	144	143	142	141	140	139	
66	90	114	109	85	136	131	156	172	169	151	170	171	165	166	167	168	163	164	162	161	160	159	158	157	
67	91	115	116	92	137	138	132	131	136	135	134	133	121	122	123	124	119	120	130	129	128	127	126	125	
68	92	116	115	91	138	137	135	136	131	132	133	134	127	128	129	130	125	126	124	123	122	121	120	119	
69	93	94	95	96	91	92	86	85	90	89	88	87	75	76	77	78	73	74	84	83	82	81	80	79	
70	94	117	118	95	115	116	110	109	114	113	112	111	99	100	101	102	97	98	108	107	106	105	104	103	
71	95	118	117	94	116	115	113	111	109	110	111	112	105	106	107	108	103	104	102	101	100	99	98	97	
72	96	95	94	93	92	91	89	90	85	86	87	88	81	82	83	84	79	80	78	77	76	75	74	73	
	25	26	27	28	29	30	31	32	33	34	35	36	37	38	39	30	40	41	42	43	44	45	46	47	
	48																								

Figure 4.14: Composition table exhibiting the possible variant-variant intersections for differing twin-twin PAGs using tetragonal symmetry.

The total number of misorientations for the entire tetragonal system increases to 228, substantially more than the 139 found specific to the KS cubic symmetric case. There also seems to be a much larger range of misorientation angle distributions than the parent-twin case, and again no misorientations overlap from either the intra-parent or parent-twin case. It can be concluded that, theoretically, the introduction of tetragonal symmetry to the KS orientation relationship produces purely unique misorientations with regards to the three observed cases of intra-parent, parent-twin or twin-twin variant intersections. For small c/a ratios, the pole figure corresponding to the present case of tetragonal symmetry would be virtually indistinguishable from the KS pole figure presented in Figure 11.

## 4.5 Discussion

For the results given, an angular tolerance in radians was taken to four decimal places for the entire  $\mathbf{V}_i - \mathbf{V}_i$  intersection list. The unique misorientations were then taken from this list and given in the composition tables and corresponding tables within the Appendix. However, varying the number of angular decimal places does result in some differences in the misorientation angles, usually within a hundredth of a degree, and can also affect the number of unique intersections observed. For example, if too few decimal places were used, more misorientations are deemed to be identical and the total number of unique intersections is reduced. Four places were chosen because this produced consistent, realistic results that agreed with prior work by Payton et al [127].

Experimental error in orientation measurement with EBSD will result in some misorientations being indistinguishable from one another. Bingham *et al.* [17] found

that 99% of intragranular orientation measurements within a well annealed grain structure fell within  $0.91^\circ$  of one another. Taking  $1^\circ$  as a conservative estimate of the angular resolution tolerance for EBSD, it is found in our results that the cubic KS orientation relationship would give three indistinguishable misorientations, as given in Table EXI. Two exist in the twin-twin case ( $\Delta g_{50}-\Delta g_{77}$ ,  $\Delta g_{84}-\Delta g_{87}$ ) and one ( $\Delta g_{39}-\Delta g_{136}$ ) exists in both the parent-twin and the twin-twin tables. The tetragonal KS would give four indistinguishable misorientation operators, where again one misorientation could be misinterpreted within the parent-twin case and the twin-twin case ( $\Delta g_{62}-\Delta g_{225}$ ) and three could be misidentified within twin-twin interaction ( $\Delta g_{139}-\Delta g_{166}$ ,  $\Delta g_{142}-\Delta g_{163}$ ,  $\Delta g_{173}-\Delta g_{176}$ ). Finally, our investigated experimental orientation relationship would give three possible indistinguishable misorientations, where two overlap between the parent-twin and the twin-twin case ( $\Delta g_{59}-\Delta g_{102}$ ,  $\Delta g_{61}-\Delta g_{205}$ ) and one within only the twin-twin case ( $\Delta g_{147}-\Delta g_{174}$ ). Cubic NW would give zero indistinguishable misorientation operators.

This observation could be significant for a number of reasons. When considering Table EXI, some of the possible indistinguishable misorientations stem from variant intersections of  $\Sigma 3$  twins in the parent grain while others stem from variant intersections of former  $\Sigma 9$  twins, with none being specific to the intra-parent case. Experimentally, it may be difficult to distinguish between  $\Sigma 3$  and  $\Sigma 9$  boundaries if some of the misorientation angle-axis pairings are so similar to each other. In terms of austenite reconstruction codes, this could possibly result in misclassifications of certain variant-variant intersections and thus suggest a parent-twin boundary segment where a twin-twin boundary segment should exist (or vice-versa). It is also worth noting that the scatter in crystallographic orientations for any given variant within

the prior austenite grain is typically significantly larger than the experimental error in EBSD [177].

The repetition of misorientation operators between the intra-parent and parent-twin composition tables may have a significant impact on possible austenite reconstructions, because it means the position of the boundary itself is ambiguous in the cubic-KS orientation relationship. Furthermore, for the parent-twin case, the cubic-KS orientation relationship results in an (unobservable) identity misorientation. This would manifest itself in the transformed microstructure as the former twin boundary appearing discontinuous. Abbasi et al. [2] attributed the apparent discontinuities at parent austenite  $\Sigma 3$  boundaries to a prevalence of these identity operator variants at the twin interface, and justified their variant selection through an energy minimization argument. Shared variants between parent and twin minimize interfacial energy, effectively resulting in a higher-probabilistic choice of these variants forming at prior austenite  $\Sigma 3$  grain boundaries. Our “KS-like” experimentally determined orientation relationship delivers a misorientation for variant pairs where one is not observed for KS, but at  $\sim 3.2^\circ$ , it is smaller than a typical threshold for boundary identification in EBSD. The low misorientation angle may result in a minimized interfacial energy between these variants while remaining consistent with the ambiguous  $\Sigma 3$  grain boundaries characterized by EBSD.

Although not shown in the present work, analysis of several other experimental orientation relationships resulted in similar misorientation distributions with varying misorientation angle-axis pairings. This paper compared the KS and experimental KS-like orientation relationships to show that specific orientation relationships must be applied to differing samples of steel if an accurate analysis of the material is to

be constructed. For example, the KS misorientation  $\Delta G_1$  has an angle axis pairing of  $10.53^\circ @ <110>$  whereas the experimental orientation relationship misorientation  $\Delta G_1$  exhibits an angle axis pairing of  $6.59^\circ @ <047>$ . Thus, it is clear that the sub-block boundary is substantially different between KS and the experimentally observed orientation relationship, even though the latter is similar to the rational KS orientation relationship. If a separate orientation relationship is used that differs vastly from the KS orientation relationship, it can be assumed that the observable misorientations will differ even more. This would suggest a substantial impact on the accuracy and efficacy of reconstructed austenite microstructures when disparate steel samples are being analyzed. The present work illustrates the potential importance of measuring the orientation relationship in each alloy for reconstruction, since the actual (irrational) misorientations between variants can be significantly different from those in the KS or NW orientation relationships.

Not only does the orientation relationship itself have a considerable impact on the possible misorientations that can exist between variants generated from an austenite grain, but symmetry plays a major role as well. It is known that we cannot measure the actual orientation when assuming a tetragonal structure due to pseudosymmetry, and as such the common practice is to assume cubic symmetry and neglect any tetragonal c-axis distortion. However, the present work demonstrates that differences exist between the sets of misorientation operators one would expect for the KS orientation relationship when the crystal symmetry is tetragonal as opposed to cubic. First, the latter produces significantly more misorientations than the cubic case (228 compared with 139, respectively). Furthermore, the tetragonal case does not produce any identity misorientations between the parent-twin case, as does the cubic case. In fact, the

parent-twin table for tetragonal symmetry does not produce a misorientation angle  $< 50.0^\circ$  whereas the cubic case contains 8 unique cases where the misorientation angle is  $< 30^\circ$ , including the case where no misorientation angle exists. The variants that generate identity misorientations in the cubic KS case produce misorientation angles of  $90^\circ$  when tetragonality is considered (see Table DIX in Appendix D,  $\Delta g_{20}$ ). This would suggest that variants adjacent to austenite twin boundaries should not overlap with parent boundaries. In fact, they should be easily distinguishable for austenite reconstruction codes if an advancement in EBSD indexing technique enabled unambiguous definition of the martensite crystal orientation through identification of the tetragonal c-axis [33]. Since practical limitations of camera and Hough transform resolution result in better indexing using cubic symmetry, until the time that such a characterization advancement is realized, it may be the case that austenite reconstructions exhibit larger errors with increasing carbon content (tetragonality).

## 4.6 Conclusions

Both orientation relationship and martensite crystal structure significantly affect possible martensite variant intersections, introducing varying numbers of misorientations and degrees of misorientation. Furthermore, inclusion of prior austenite twins increases the total number of possible misorientations between intersecting variants. From the present work, the following conclusions were drawn:

1. If the KS or NW orientation relationships were exactly exhibited in a material, then the prior location of an austenite annealing twin boundary would be ambiguous on observation of the product martensite phase due to the presence of identity operators and intra-parent misorientation operators.

2. Although experimentally observed orientation relationships in Fe alloys are irrational, the number of misorientations exhibited within a single prior austenite orientation are the same as the KS case (16).
3. The presence of certain characteristic misorientations can be indicative of the presence of a  $\Sigma$ 3 or  $\Sigma$ 9 boundary in a prior austenite grain; however, the large number of these possible characteristic misorientations and their similarity to other misorientations that could be exhibited within a single prior austenite grain present a challenge in uniquely identifying the location of the boundaries related to prior austenite annealing twins.

The results presented here may be useful in austenite reconstruction, as they provide constraints on how an austenite grain could have transformed given the observable martensite.

# **Chapter 5: Characterization of Martensite Orientation Relationships in Steels and Ferrous Alloys from EBSD Data using Bayesian Inference**

The following chapter is under review for publication in a peer-reviewed journal [27] and was written with the co-authors Dr. Vikas Sinha, Dr. Victoria Yardley, Dr. Eric Payton, and Dr. Stephen Niezgoda. Similar to the previous chapter, the introduction section has been shortened for redundancy purposes.

## **5.1 Introduction**

As mentioned previously, the plane and direction parallelism in these orientation relationships have long been known not to be followed closely in real alloys. Greninger and Troiano described an irrational orientation relationship that falls somewhere between the KS and NW ORs in 1949 [60] (from here on in the present work referred to as GT). The actual irrational orientation relationship varies with composition for a given alloy [105, 127]; however, challenges in characterizing the orientation relationship usually lead to the assumption of one of the above two relationships. While the variation in the orientation relationship with composition can theoretically be predicted with the phenomenological theory of martensitic transformations [20–22, 95, 96, 118, 167, 169], the theory cannot account for the variability in

the orientation relationship which is experimentally observed within a nominally uniform specimen. Deviations may arise from local fluctuations in composition, cooling rate, and the extent of plasticity [85,99,116]. Therefore, steels of the same grade from different lots or subjected to differing thermomechanical processing routes could each exhibit a slightly different orientation relationship.

As reconstruction of austenitic microstructures from observations of martensite is desired for a number of applications, and reconstruction reliability is improved with a measurement of the orientation relationship, there is a general need for programs that can accurately, efficiently, and automatically measure the orientation relationships in steels. Especially desirable would be programs that are user-friendly, allowing those with limited computational experience to effectively run them whilst performing the measurement in a timely manner.

Most existing methods for characterizing the orientation relationship in steels are tedious and require significant crystallographic expertise [108,127]. Some require the isolation of a PAG before the OR can be computed [105,130,177]. This limits the definition of an “automated” approach since a considerable amount of time must first be spent partitioning the PAG. Furthermore, the segmentation is presumptive, based on assumed PAG boundaries, thereby potentially limiting the accuracy of the results or requiring a tedious examination of the martensite microstructure in order to capture a certain PAG boundary. Other techniques exist that do not require the isolation of a PAG, relying instead on misorientation information of neighboring martensitic points [58,150,185]. However, these techniques are highly dependent upon user-input tolerances and selection of the most “popular” Euler angle variants. This in turn can limit the accuracy, efficiency, and reproducibility of the results.

The following Chapter introduces a rapid, effective, and automatable method for characterization of the orientation relationship in martensitic steels. The OR measurements were performed using MATLAB (R2016a, Mathworks, Inc., Natick, MA USA) from EBSD datasets of transformed martensite with use of the MTEX crystallographic data analysis toolbox [7].

## 5.2 Methodology

It is well known that 24 crystallographic variants are observed for the martensitic transformation in steel, with the notable exception of the NW OR [84,111]. The crystallographic rotations corresponding to the variants may be described through the use of Euler angles. However, the Euler angle description is verbose since a full description of the OR requires a set of 24 Euler angles which are not unique, but vary by reference frame and convention for the order of rotation operation. A more compact notation for describing the orientation relationship, known as  $\xi$  angles, has been proposed by Yardley & Payton [127,175–177] The three  $\xi$  angles, representing deviations of primary  $\alpha'$  axes from the Bain correspondence matrix of the phenomenological theory, can fully describe the entire OR. The procedure used to represent the OR through use of said  $\xi$  angles is almost equivalent to the one described by Kurdjumov and Sachs [89].

A complete description of these angles can be found in [177] and, as such, a brief description will be provided below. To characterize the orientation relationship using  $\xi$  angles, Yardley & Payton manually selected regions from a single prior austenite grain in their martensite EBSD datasets, avoiding twins; then rotated the data so that the PAG orientation was coincident with the sample reference frame. The

angular deviation between the closest Bain correspondence matrix axes [9] and the primary axis of the rotation matrix could then be measured, producing  $\xi_1$ ,  $\xi_2$  and  $\xi_3$ , which correspond to the smaller and larger deviations between the  $\langle 110 \rangle$ -type Bain correspondence axis, and the deviation from the  $\langle 001 \rangle$ -type Bain correspondence axis, respectively.

### 5.2.1 Formulation of the Bayesian Inference Problem

The computation of the experimental OR was achieved by framing the problem as Bayesian inference [11], described in detail in Chapter ???. The Bayesian casting of potential solutions in terms of possible states of truth is useful when analysis must be performed on noisy and uncertain data [13, 122]. The martensitic microstructure in steels can exhibit up to  $m \times 24$  crystallographic variants for  $m$  prior austenite grains. Unique determination of the parent austenite orientation requires observing an appropriate combination of variants. In addition, transformation-induced plasticity, variation in the OR, and uncertainty in the measurement further obfuscate the parent austenite orientation.

One of the main benefits of our approach is that the entire PAG does not need to be segmented in order to capture an accurate OR. Rather, in order to perform the measurement, a small section or window is extracted from the transformed EBSD dataset, containing a set of  $n$  martensite orientations,  $G_{\alpha'} = [g_{\alpha'}^{(1)}, g_{\alpha'}^{(2)}, \dots, g_{\alpha'}^{(n)}]$ . Ideally, this region corresponds to a section of martensite points that have all transformed from the same assumed PAG with respect to the sample-specific OR—albeit, as demonstrated below, this is not absolutely necessary. The size of the selected region does affect the quality of the OR measurement, although the technique is robust enough

to where the region can extend across what amounts to a PAG boundary while producing an accurate measurement. This is due to the Bayesian implementation, which can designate the overflowing orientations as variable noise and consequently identify orientations associated with the respective PAG. Additionally, the region can be small enough to where only a few different martensite variants reside, although too small of a region within the grain will result in a poor measurement (examples of extracted windows are displayed later in Figure 5.3).

Before describing the actual OR estimation procedure, it is instructive to consider a schematic picture model of how the measured martensite orientations,  $G_{\alpha'}$ , were produced from a prior austenite grain. Consider  $g_\gamma$  to be the orientation of the idealized prior austenite grain. What's meant by idealized orientation is an assumption that the grain is a perfect single crystal with no orientation gradients, misindexed points, etc. The transformation to martensite can then be represented by transforming  $g_\gamma$  as  $\Delta g_{\gamma \rightarrow \alpha'}(\Xi^{(i)}) \equiv \Delta g_{\gamma \rightarrow \alpha'}(\xi_1, \xi_2, \xi_3, v_i)$ , which consequently produces an ideal martensite orientation. The OR is then represented by  $(\xi_1, \xi_2, \xi_3)$ , and  $v_i$  indicates the transformation variant associated with an observed martensite point,  $g_{\alpha'}^{(i)}$ . Note that  $\Delta g_{\gamma \rightarrow \alpha'}(\Xi^{(i)})$  is a random variable as there are 24 possible martensite variants for the OR. For simplicity, we can ignore variant selection and assume that for each variant, the probability is 1/24 and the probability of a  $\Delta g_{\gamma \rightarrow \alpha'}(\Xi^{(i)})$  that doesn't correspond to an exact variant of the OR is zero. This idealized picture is overly simplistic, so an additional rotation is incorporated that accounts for noise or uncertainty,  $\Delta g_{\gamma \rightarrow \alpha'}^{(i)}(\kappa)$ . This noise accounts for any source of deviation of the martensite orientation from the ideal transformation orientation and can in principle include: *i*) variability in the OR due to compositional effects or lattice parameter variations, *ii*) plastic deformation

during the martensite transformation, *iii*) variability in the prior-austenite grain orientation, *iv*) misindexed points or other sources of noise in the EBSD measurement, and *v*) points within the window excluding those from either a different prior austenite grain or prior austenite annealing twin. The noise is also a random misorientation assumed to be sampled from a unimodal misorientation distribution function, with halfwidth,  $\kappa$ , centered on the identity misorientation. The austenite to martensite transformation can now be modeled as:

$$g_{\alpha'}^{(i)} = \Delta g_{\gamma \rightarrow \alpha'}^{(i)}(\kappa) \Delta g_{\gamma \rightarrow \alpha'}(\Xi^{(i)}) g_\gamma \quad (5.1)$$

Our objective is to infer the OR given the observed martensite orientations,  $G_{\alpha'}$ . In Bayesian terms, this inference can be cast as:

$$\pi(\Xi, \kappa | G_{\alpha'}) \propto \prod_{i=1}^N f(g_{\alpha'}^{(i)} | g_\gamma, \Xi, \kappa) f(g_\gamma | \Xi, \kappa) \pi(\Xi) \pi(\kappa) \quad (5.2)$$

where  $\pi(\Xi, \kappa | G_{\alpha'})$  is the posterior probability distribution of the orientation relationship and noise level given the observed martensite orientations. Additionally, the likelihood of observing the measured martensite orientations given values of the prior austenite orientation, OR, and noise is  $f(G_{\alpha'} | g_\gamma, \Xi, \kappa) = \prod_{i=1}^N f(g_{\alpha'}^{(i)} | g_\gamma, \Xi, \kappa)$ . Note that the prior austenite orientation is an unknown and can be considered a hidden variable in the model, and  $f(g_\gamma | \Xi, \kappa)$  is a likelihood of the prior austenite orientation given the OR and noise. The product,  $f(G_{\alpha'} | g_\gamma, \Xi, \kappa) f(g_\gamma | \Xi, \kappa)$ , is the overall data likelihood and can then be interpreted as the overall probability of observing the martensite orientations given both the OR and noise. Finally, the prior probability distributions on the OR and noise are  $\pi(\Xi)$  and  $\pi(\kappa)$ , respectively.

The data likelihood function is constructed by considering the schematic model of the martensite transformation described above. With this consideration, the prior austenite grain can be transformed by the OR to generate orientations related to all 24 potential martensite variants. These variants are then convolved with the noise kernel (unimodal ODF with halfwidth  $\kappa$ ) to produce an ODF. When this ODF is evaluated for any martensite orientation, it returns the probability that the martensite orientation was generated by the transformation of the prior austenite orientation given the OR and noise. Therefore, this ODF serves as our desired likelihood function,  $f(g_{\alpha'}|g_{\gamma}, \Xi, \kappa)$ <sup>1</sup>.

The likelihood function for the prior austenite orientation,  $f(g_{\text{prior}}|\Xi, \kappa)$ , is also an ODF but unfortunately does not appear to have a simple form and thus must be approximated. This approximate likelihood can be constructed by the following process: 1) Compute the inverse of the transformation  $\Xi$  to get the set of martensite  $\rightarrow$  austenite OR. 2) Apply the inverse transformation to all martensite orientations in  $G_{\alpha'}$ . This will result in 24 potential austenite orientations for each for each observed orientation. 3) Compile the complete set of potential austenite orientations over all observed martensite orientations and calculate an ODF by kernel density estimation using a narrow smoothing kernel. An ODF constructed in this manner turns out to be an excellent approximation for the probability distribution for a prior austenite orientation. Ultimately, the construction of the ODF can be likened to a voting process. Each observed martensite “votes” for 24 potential austenite orientations

<sup>1</sup>Strictly speaking, this results in an ODF that is proportional to—not equal to—the ODF. The ODF is not formally a probability distribution as it is scaled by multiples of the uniform random distribution, making it easy to interpret relative probability in terms of “times random.” This results in a proportionality factor equal to the volume of the fundamental zone for cubic orientations. However, this can be neglected as it is a constant term which can be divided out and incorporated into the proportionality factor in Equation 5.2

(given the OR). Since all of the martensite orientations ideally come from the same prior-austenite grain, all of the “votes” for the actual austenite orientation will be clustered and the other 23 will be spread nearly uniformly over the orientation space. Kernel density estimation produces an ODF with one very dominant mode that is sharply peaked. In practice, the estimation is not very sensitive to the halfwidth of the kernel used for ODF construction, provided it is not too broad, as it has the same effect on all of the “votes.” The modal orientation of the ODF is remarkably insensitive to the kernel halfwidth. A value of  $0.25\kappa$  or even smaller was found to be sufficient for the ODF estimation. In testing with virtual datasets, where the prior austenite orientation was known *a priori*, it was found that, provided a reasonable window was selected to create  $G_{\alpha'}$ , the modal orientation was virtually always within  $\leq \pm 1^\circ$  (or approximately to within the accuracy of EBSD measurement) to the ground-truth prior austenite orientation. This allows us to simplify the calculation of the posterior by only considering the modal prior austenite orientation,  $g_\gamma^{modal}$ :

$$\pi(\Xi, \kappa | G_{\alpha'}) \propto \prod_{i=1}^N f(g_{\alpha'}^{(i)} | g_\gamma^{modal}, \Xi, \kappa) f(g_\gamma^{modal} | \Xi, \kappa) \pi(\Xi) \pi(\kappa) \quad (5.3)$$

This effectively transforms the unknown hidden variable into a known quantity, thereby reducing the dimensionality of the search space and simplifying the inference problem.

Payton and Yardley [175] previously observed that the measured values for the angles  $(\xi_1, \xi_2, \xi_3)$  fit well to a folded or wrapped normal distribution, which takes the form:

$$p(x) = \frac{1}{\sigma\sqrt{2\pi}} e^{-\frac{(x-\mu)^2}{2\sigma^2}} + \frac{1}{\sigma\sqrt{2\pi}} e^{-\frac{(x+\mu)^2}{2\sigma^2}} \quad (5.4)$$

For this work, we adopt this observation to form the prior probability,  $\pi(\Xi) = \pi(\xi_1)\pi(\xi_2)\pi(\xi_3)$ , where each  $\xi_k$  value is assumed to be a priori independent and  $\pi(\xi_k)$  is represented by a wrapped normal. The means were set to  $\mu_{\xi_1} = 5^\circ$ ,  $\mu_{\xi_2} = 9^\circ$ ,  $\mu_{\xi_3} = 10^\circ$ , which is approximately in-between the GT and KS ORs, and the standard deviations were set to  $\sigma = 1.2^\circ$ . This was found to work well for the full range of ORs from NW to KS. It is expected that, provided the window is reasonably selected, the noise kernel should be relatively small, therefore the prior monotonically decreases and approaches zero at large noise values. For simplicity, we also chose a wrapped normal for  $\pi(\kappa)$  with  $\mu_\kappa = 1^\circ$  and a standard deviation of  $2^\circ$ . This approximates a uniform probability over the range from  $[0, 1]$  rather than a fairly rapid decay.

### 5.2.2 MAP estimate and Posterior distribution

A Maximum A Posteriori (MAP) estimate of the OR and noise halfwidth was achieved by way of maximization of the aforementioned likelihoods in Equation 5.3. The optimization was achieved with a built-in MATLAB function, “fminunc”, which applies an unconstrained gradient search approach. An initial guess for both the OR ( $\Xi^i$ ) and the halfwidth ( $\kappa^i$ ) were provided, where  $\Xi^i$  was chosen to be the KS OR and  $\kappa^i$  was arbitrarily chosen to be  $3^\circ$ . Although the initial choice for the OR is chosen as KS as an “outer-bound” of a physically relevant OR, the technique is robust enough to handle a wide range of values. For instance, the KS, NW, and a randomly chosen OR outside the range of the two cited ORs produced consistent results for the same respective sample.

The MAP estimate provides us with our best guess of the average OR relationship given the observed martensite orientations. However, for this work, we are also interested in quantifying the uncertainty in the OR measurement. We adopt a Markov Chain Monte Carlo (MCMC) method to generate samples from the posterior distribution of the OR. MCMC combines two differing properties: *Monte Carlo* and *Markov Chain*. The former refers to an estimation of the properties of a particular distribution through an examination of random samples from the distribution. *Markov Chain* is then related to the notion that a sequential process generates the random samples. In other words, a sample obtained from a previous iteration is consequently used to generate the next random sample, and so on.

We apply the standard Metropolis Hasting algorithm [64, 103] to generate samples from the posterior distribution. For the interested reader, refer to additional standard texts for a complete description of the method [50, 53]. Conceptually, the algorithm is quite straightforward, beginning with the generation of a sequence of samples from the posterior distribution using the Metropolis Hasting algorithm. At each iteration, the algorithm picks a candidate OR through a slight perturbation of the current value. If this candidate has a higher likelihood than the current OR, it is accepted. If it has a lower likelihood, it is either accepted with a probability based on the ratio detailing the likelihood of the candidate OR with the likelihood for the current OR. In other words, the probability of acceptance is dependent upon how much worse the candidate is vs. the current value. Therefore, if the proposed likelihood is 50% worse than the current likelihood, the probability of acceptance would be 0.5.

In our case, we chose to sample the  $\xi$  angles individually rather than in a block. We found that the OR and corresponding noise parameters were converged after

approximately 2e4 iterations, with  $\lesssim 0.1^\circ$  variation in the mean value of the  $\xi$  angles reached in less than 20 minutes on a 3.4 GHz single core processor. From the generated distributions, the resultant mean of the individual  $\xi_k$  angles is taken as the output OR, which comes with a corresponding likelihood value that can effectively detail the accuracy of the computation. Additionally, a random set of orientations computed from the designated OR corresponding to the transformation  $g_\gamma \rightarrow G_{\alpha'}^a$  can be plotted as a pole figure and compared with the input martensite orientations from the PAG to ensure an appropriate OR was constructed.

### 5.3 Results

A selection of different martensitic steel and binary ferrous alloy data sets expected to exhibit disparate ORs (KS-like, GT-like, and NW-like) due to variability in composition were chosen to illustrate the robustness and range of applicability of the method, as well as highlight the deviation from ideal ORs that has been analyzed previously in the literature [26, 60, 127, 130, 177]. Additionally, the effects of the number of data points from a single PAG and the effects of inclusion of points from different PAGs were analyzed using different window sizes with a window centered over a single PAG in a dataset. Finally, a large data set was chosen where regions from several different grains were selected in order to test the precision of the code for repeat measurements on materials of the same composition and processing history.

#### 5.3.1 Variation of OR with Composition

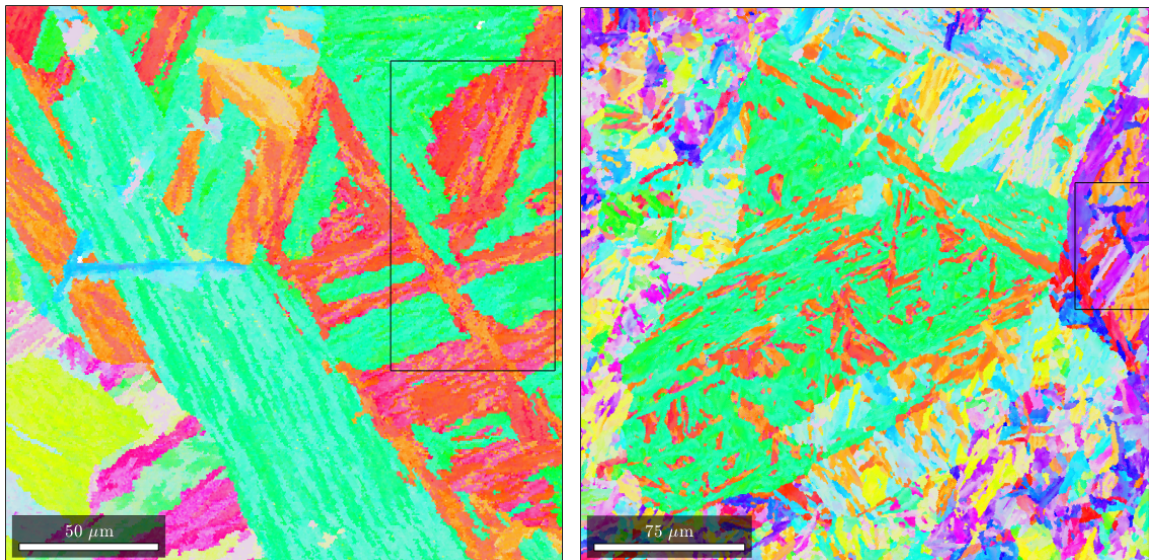
The ORs for three samples with distinctly different compositions were determined and compared with experimental validation pulled from results by Payton and Yardley [177]. The two steel samples were a low-carbon steel, whose composition can

be found in [114] and would suggest a KS-like OR; FV535 steel (German grade X8CrCoNiMo11), a tempered martensitic, heat-resistant steel that should fall in-between KS and NW, and thus exhibits a ‘GT-like’ OR; and the binary ferrous alloy was an Fe-30 at. % Ni alloy that should have a NW-like OR [84,85]. For experimental details, including specimen processing methodology and data acquisition information, the reader is referred to [177].

The Low-C and the FV535  $\gamma \rightarrow \alpha'$  transformations go to full completion, while the Fe-30Ni sample has a substantial amount of retained austenite ( $\sim 15\%$ ), which shows up as the black spaces in Figure 6.6. Austenite data points were excluded from the analysis and the inverse pole figure (IPF) maps for the sample surface normal direction (Z) for the martensite phase are given in Figure 5.1 for each steel. The window boundaries shown in black correspond to the analyzed regions containing only data from a single PAG.

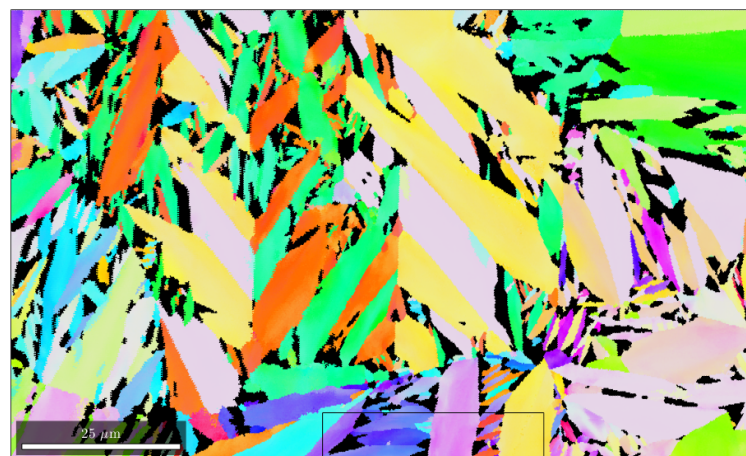
Visual inspection of the IPF maps for each steel reveals substantial variation in the transformed martensite microstructure. The low-C sample (Figure 5.1a) exhibits lath-like crystallite morphology whereas the Fe-30Ni sample (6.6) exhibits a more plate-like morphology, with retained austenite sprinkled throughout the microstructure. The scale of the microstructure is different for each material, with the largest block and packet scale being observed in the low carbon steel.

The previously measured ORs for each specimen are given in Table 5.1 along with the Bayesian OR estimate, the expected approximate theoretical OR (KS, NW, or GT), the noise, and the variance associated with each respective  $\xi$  value,  $\sigma^2$ . It should be noted that for GT, there are a range of ORs which can satisfy multiple ORs. To obtain the GT OR used in the present work, the mean  $\xi$  parameters were obtained



(a) Low-Carbon Steel

(b) FV535 Steel



(c) Fe-30Ni Steel

Figure 5.1: IPF maps for the low-C (top left), FV535 (top right), and Fe-30Ni (bottom) samples, with overlaying IPF key.

from a simulated dataset consisting of 5e5 random orientations that met the criteria described by Greninger and Troiano [60]:

1.  $1^\circ$  deviation of  $\{111\}_\gamma$  from  $\{011\}_\gamma$
2.  $2.5^\circ$  deviation of  $\langle \bar{1}01 \rangle_\gamma$  from  $\langle \bar{1}\bar{1}1 \rangle_{\alpha'}$
3.  $2.0^\circ$  deviation of  $\langle \bar{1}\bar{1}2 \rangle_\gamma$  from  $\langle 0\bar{1}1 \rangle_{\alpha'}$
4.  $6.5^\circ$  deviation of  $\langle 0\bar{1}1 \rangle_\gamma$  from  $\langle 1\bar{1}1 \rangle_{\alpha'}$

Table 5.1: Bayesian measurement of ORs and corresponding halfwidth and OR distribution variance for the three samples compared with prior experimental measurements [177] (indicated by “P-Y”) and the KS, GT, and NW theoretical ORs.

Steel Sample	$\xi_1$	$\xi_2$	$\xi_3$	$\kappa$	$\sigma^2(*1e^{-3})$
NW	$0.0^\circ$	$9.74^\circ$	$9.74^\circ$		
Fe-30Ni P-Y	$1.87^\circ$	$9.16^\circ$	$9.18^\circ$		
Fe-30Ni	$1.63^\circ$	$9.19^\circ$	$9.19^\circ$	1.10	[8.1, 2.2, 1.9]
GT	$2.16^\circ$	$8.06^\circ$	$8.30^\circ$		
FV535 P-Y	$2.73^\circ$	$9.01^\circ$	$9.20^\circ$		
FV535	$2.42^\circ$	$9.09^\circ$	$9.24^\circ$	1.42	[7.4, 3.5, 4.4]
KS	$5.26^\circ$	$10.30^\circ$	$10.53^\circ$		
Low-C P-Y	$3.38^\circ$	$8.31^\circ$	$8.60^\circ$		
Low-C	$3.17^\circ$	$8.27^\circ$	$8.62^\circ$	1.61	[17.4, 4.9, 8.5]

The results of the Bayesian OR estimation show good agreement with the previous experimental measurements from Yardley and Payton [177]. The measured ORs for each of the steels are clearly distinguishable from one another, highlighting the robustness of  $\xi$  parameter approach to characterizing the OR. The discrepancy between the commonly-cited theoretical ORs and their respective experimentally-observed counterparts, especially low-C with KS, underscores that the measured ORs

differ substantially from the theoretical ORs that are typically cited in the literature for these compositions. This topic will be detailed further in the Discussion section.

Since many readers may not be familiar with the  $\xi$  angle OR characterization technique,  $\{001\}_\gamma$  pole figures have also been plotted in Figure 5.2 and the Bunge Euler angles for a representative variant of each Bayesian estimate for the OR were computed. The pole figures in the center column of Figure 5.2 are a sample of 2000 martensite orientations from within the boxed regions in Figure 5.1. The “computed” pole figures show 2000 martensite orientations obtained by sampling our distribution centered by the prospective austenite orientation,  $g_\gamma$ , which in turn is transformed into a set of randomly generated martensite orientations based on the  $\xi$  values and relative noise,  $\kappa$ , associated with the input dataset. The computed austenite orientations are listed here in terms of Euler angles  $(\phi_1, \Phi, \phi_2)$ : for the Fe-30Ni sample,  $g_\gamma = [111.78^\circ, 40.77^\circ, 286.05^\circ]$ ;  $g_\gamma = [4.26^\circ, 42.97^\circ, 4.55^\circ]$  for the FV535 sample; and for the low-C sample,  $g_\gamma = [339.63^\circ, 0.29^\circ, 19.54^\circ]$ . Additionally, the computationally determined half widths ( $b$ ) and variance of the  $\xi$  angles ( $\sigma^2$ ) after 2e4 iterations are also listed in Table 5.1.

Finally, for comparison, the  $\{001\}_\gamma$  pole figures for martensite orientations generated from the computed ORs, the EBSD-indexed martensite orientations, and their respective, commonly cited theoretical counterparts are plotted in Figure 5.2. The commonly cited ORs (KS, GT, and NW) have two different pole figures. The red points represent single variant orientations without the inclusion of any scatter or noise, and the blue points are a set of 2000 martensite orientations generated using the same halfwidth parameter as the computational cases for low-C, FV535, and Fe-30Ni, but use the theoretical OR instead of the Bayesian estimate as the mean variant

locations. This creates an image that allows for a visual analysis of the accuracy of the computed ORs by comparison to the experimental martensitic data.

Note that the experimental and computed martensite orientations are almost exactly aligned for each case, barring variant selection and/or incomplete martensitic orientation data. The similarities between the experimental and computed pole figures for each specific sample coupled with the proximity of the numeric  $\xi$  angles in Table 5.1 suggests high accuracy of the Bayesian technique. The KS case is observed to differ significantly from the low-C steel experimental observation and computed OR, while a significantly smaller discrepancy between the theoretical OR and either the experimental observation or the Bayesian estimate is observed in the case of NW/Fe-30Ni or GT/FV535.

### 5.3.2 Effect of Varying Window Size During OR Estimation

To assess the robustness of our algorithm, the OR was measured for a series of six window sizes, capturing the effects on the number of observed variants, number of included data points, and data points corresponding to orientations from different prior austenite grains. The first four windows (A-D in Figure 5.3) contain only data from a single prior austenite grain, while windows E and F contain data points from multiple adjacent PAGs. For this analysis, a fourth steel specimen was used: an ASTM P122 12 wt%Cr steel, for which processing and data collection conditions have also been described elsewhere, in references [175, 176]. Again, results are compared with a prior experimental determination of its OR [175].

If too few variants are observed, a unique prior austenite orientation cannot be determined. If a sufficient number of variants is observed for a unique PAG orientation

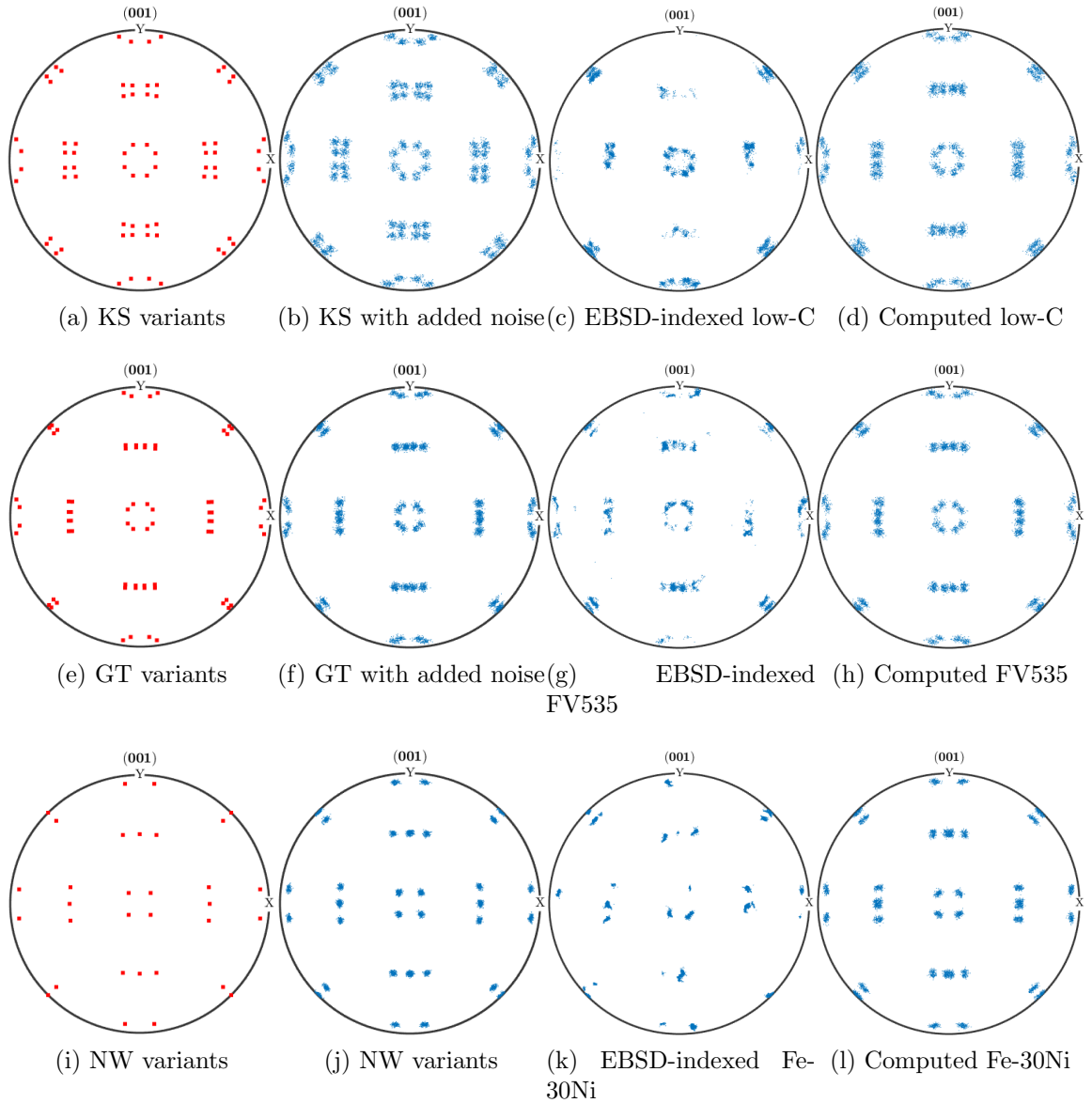


Figure 5.2: The set of variants for the theoretical ORs of KS, GT, and NW (far left column), martensite orientations rotated by the inverse of their respective austenite orientations and displayed on {001} pole figures for KS, GT, and NW (middle left column), the experimental martensite data for the low-C, FV535, and Fe-30Ni samples (middle right column) and the martensite points generated from the  $\Xi$ ,  $\kappa$  parameters from the input experimental data (far right column)

determination but too few data points are included for each of those variants, then the scatter in the orientation relationship will not be well-characterized. If data points from multiple PAGs are included for fitting the OR and PAG orientation, the accuracy of proposed austenite orientations and corresponding likelihoods becomes diminished, resulting in poor choices of  $\Xi$ .

For the EBSD data shown in Figure 5.3, the presumed PAG is centrally located in the IPF-Z map. For validation, the authors performed a single grain austenite reconstruction on this same data set in [25], verifying the identity of the PAG. The computed ORs from the  $G_{\alpha'}$  array extracted from each window are give below in Table 5.2, which also includes the number of data points within each window and the experimentally determined OR for validation.

Table 5.2: Computationally determined  $\xi$  angles for variable window sizes of the P122 steel sample, including number of data points for each window and the Payton-Yardley (P-Y) determined OR

Figure Label	$\xi_1$	$\xi_2$	$\xi_3$	Number of Data Points
Window A	2.31	10.35	10.28	328 pts
Window B	2.56	9.19	9.39	812 pts
Window C	2.59	8.87	9.11	6521 pts
Window D	2.61	8.99	9.21	16927 pts
Window E	2.57	8.88	9.10	31901 pts
Window F	9.87	14.55	14.20	51119 pts
P-Y	2.62	8.98	9.21	

For each respective case, the number of randomly chosen martensite orientations for  $G_{\alpha'}$  was 2000 from within the window size except for Windows A and B, which had only a maximum of 328 and 885 indexed data points. With only the slight increase

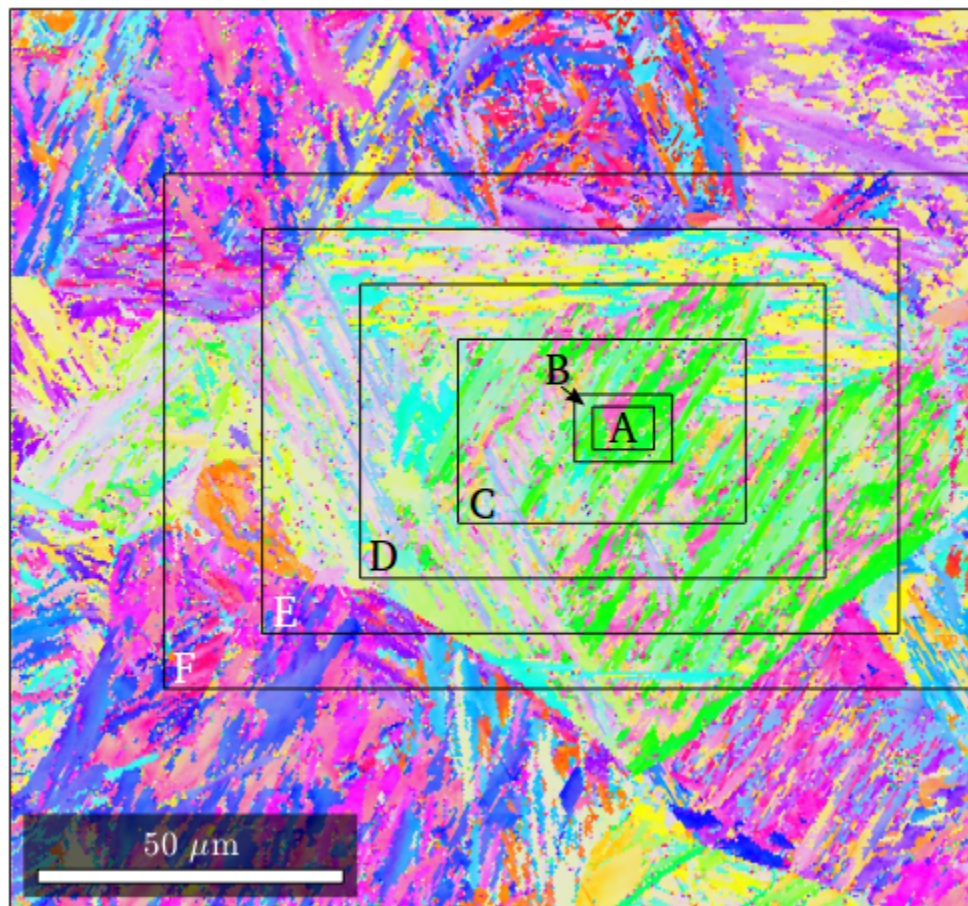


Figure 5.3: IPF map of P122 martensitic steel containing variable window sizes of martensitic variants

in window size from A to B, however, a sufficient number of additional variants is observed for accurate characterization of the OR. Note that most of the possible variants are still not observed within Window B. This again suggests a robustness to the code that allows it to handle not only a wide range of different martensitic steel data sets but also regions within PAGs that may not fully represent the  $\gamma \rightarrow \alpha'$  transformation. As Table 5.2 suggests, Windows B through E produce accurate results, with Window D producing almost exactly the same OR as the one from Payton and Yardley [177].

Window A contains too few variants and Window B, with only the addition of a few more, regains traction and is reasonably accurate. Conversely, we can see that while Window E extends across the PAG boundaries, the fraction of data points from other PAGs is small enough that an accurate OR can still be reasonably characterized. Window F stretches too far outside of the PAG boundary, resulting in too much noise and thus a poor characterization of the OR. The pole figures for these four cases are shown in Figure 5.4 and exhibit the effect of window size on variant accessibility, where the addition of only a few more variants in Window B separates it from Window A. Additionally, it also displays how the algorithm can handle some noise present in Window E but, if the fraction of spurious points becomes too large, such as in Window F, it becomes too hard to sift through the noise to capture variants consistent to the prior austenite orientation.

It is clear that Window E contains a substantial amount of noise from orientations extending outside of the desired PAG and/or poorly-indexed orientations, but the determined OR retains accuracy. The pole figure corresponding to Window B lacks the characteristic symmetry common for martensite pole figures from single PAGs

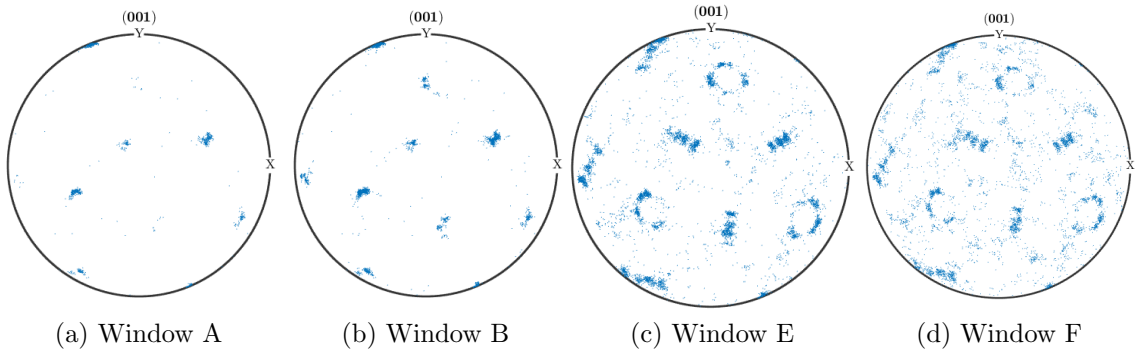
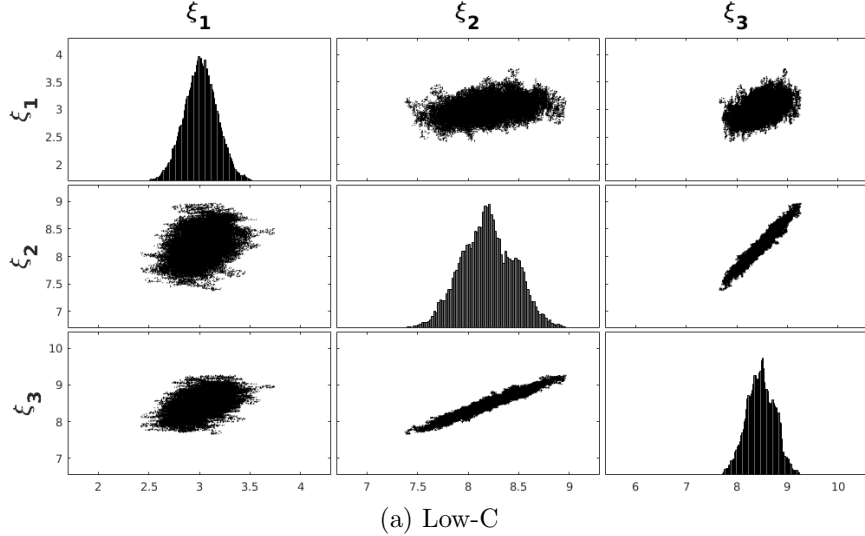


Figure 5.4: {001} martensitic pole figures on ASTM P122 12 wt%Cr steel sample for a selection of four variable windows

(Bain circles, etc.); however, the code is still able to converge upon a reasonable guess for the OR from the few present variants. The polar cases of Window A and Window F contain too few variants or too much noise to produce an accurate guess as to the PAG orientation.

## 5.4 Correlation of $\xi$ Angles

The MAP-estimated  $\xi$  angles exhibit some correlation trends which were examined using matrix-based scatter plots, shown in Figure 5.5 for the low-C sample examined in the present work. The diagonal components display the posterior distributions of the individual  $\xi$  angles as histograms, where 2e4 sets of  $\xi$  angles were computed. It should be noted that these distribution should be interpreted as a measure of the uncertainty in the measurement of the average OR. They are not representative of the spatial variability of the OR within a sample which will have a significantly larger variance than our estimate of the average or effective OR. The offset regions detail scatter plots of  $\xi_i vs. \xi_j$ , where the relative correlation can be visually assessed.



(a) Low-C

Figure 5.5: Correlation plots and histogram distributions of computed  $\xi$  angles for the low-C steel specimen

We can see that  $\xi_1$  shows no correlation to either  $\xi_2$  or  $\xi_3$ , as the distribution is a randomly dispersed cloud. However,  $\xi_2$  and  $\xi_3$  show a strong, linear correlation to each other. This hints at the possibility of characterizing the OR through only a pair of angles with the inclusion of  $\xi_1$  if a full measurement be unavailable, and then extrapolating to find the value of whichever angle of  $\xi_2$  or  $\xi_3$  was not used.

#### 5.4.1 Reproducibility of OR Measurement

To assess the repeatability of OR measurements within a single specimen, we computed the OR for several different PAGs within a large area EBSD scan from a low-alloy, high-performance steel, AF9628 [4]. Processing parameters for this specimen have been published elsewhere, in reference [143]. The regions from single PAGs selected for analysis can be seen below in the IPF-Z map in Figure 5.6. Measurement results are given in Table 5.3.

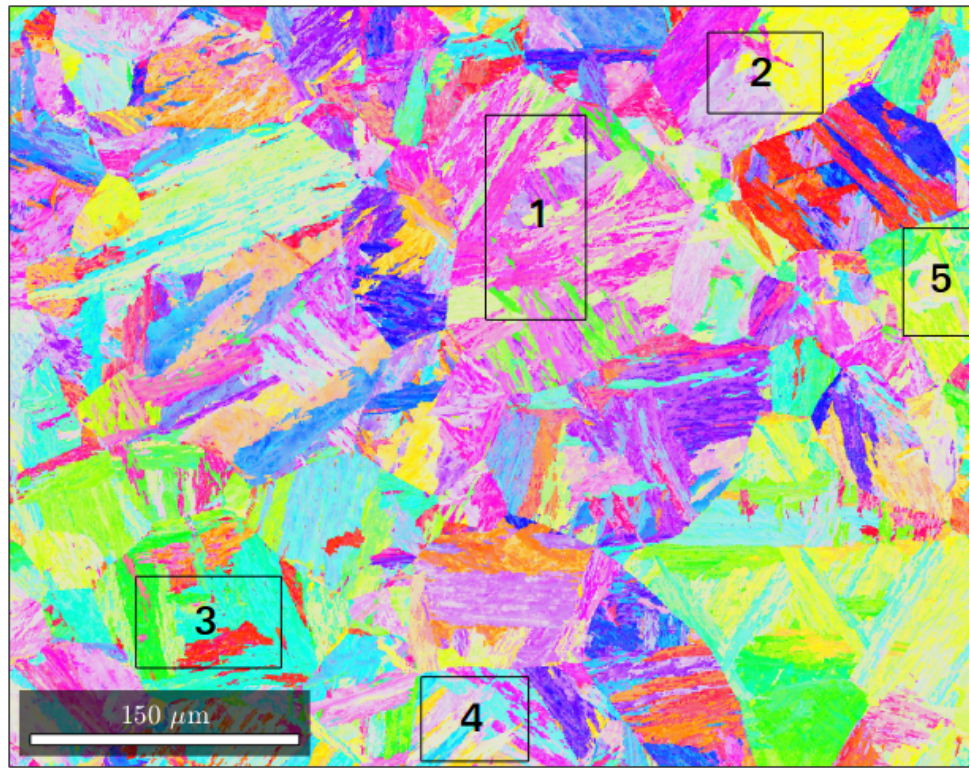


Figure 5.6: Five labeled regions within five independent grains for the same AF9628 steel sample

Table 5.3: Computed ORs from five different grains within the same AF9628 steel specimen, with numbering corresponding to Figure 5.6

Grain	$\xi_1$	$\xi_2$	$\xi_3$	Likelihood	Data Points in Windows
Grain 1	3.09	8.10	8.48	550.4	25877
Grain 2	3.07	8.12	8.57	513.7	11739
Grain 3	3.09	8.15	8.56	530.9	16789
Grain 4	3.02	8.11	8.53	547.3	11495
Grain 5	3.04	8.15	8.57	511.6	9638

As can be seen in Table 5.3, the Bayesian estimate results are very consistent and repeatable across several grains within the same dataset. Although the PAGs themselves vary in both size of and number of transformed martensite variants, the  $\xi$  values obtained for each grain are consistent to two significant figures.

## 5.5 Discussion

Employing a Bayesian approach explicitly acknowledges the probabilistic nature of the OR estimate given the convolution of the observed scatter in the OR with measurement uncertainty. Section 3.1 examined characterization of the OR on three steels with different compositions. The three compositions were selected to illustrate the breadth of applicability of this approach to different compositions and the robustness to transformation product morphology and crystallography. Low-C steels exhibit a lath-like morphology with a crystal structure exhibiting little, to any, tetragonality depending on the carbon content and are typically assumed to exhibit a KS-like OR [66, 84]. The hierarchical arrangement of 24 variants can produce 16 boundary misorientations within a single PAG [26], and these boundaries serve as hindrances to plastic deformation affecting the toughness of the transformed steels [61, 86, 101, 113]. Steels with a Ni content above 28 percent exhibit NW-like ORs [66, 85, 158], for which it is often assumed there are only 12 variants corresponding to five unique boundary misorientations [26]. The variations between the actual, irrational ORs and the idealized versions commonly cited are also evident when the {001} pole figures in Figure 5.2 are analyzed. For instance, the circular arrangement of PAG-transformed martensite orientations in the center of the pole figures is much larger in the KS case

as opposed to the experimental/computational low-C case. Additionally, if we consider the streaks of orientations similar to lines surrounding the circular region, we can see variable numbers of “clusters” of points. With KS, eight distinct clusters are visible, but the corresponding lines with the actual low-C sample show only four distinct clusters. The Fe-30Ni and NW case show a similar arrangement of orientations, although the former case displays clusters with broader ranges and thus encompasses more of the orientation spectrum. Furthermore, the pole figures here include noise, which further broadens the range of martensite locations and provides better agreement with experimental observation than the KS or NW OR descriptions, which do not account for any irrational variation between the parallel planes and directions.

The Bayesian approach exhibited robustness to a relatively small number of observed variants as well as to the incidental inclusion of orientations not belonging to the prior austenite grain of interest (Figures 5.3 and 5.4). We found the results from the approach to have excellent duplicability within different grains in a specimen (Figure 5.6 and Table 5.3). Furthermore, all results agreed well with prior work. Accurate and repeatable measurement of the OR is a necessary prerequisite for reconstruction of the prior austenite microstructure from the observable martensitic data. Miyamoto et. al. [105] have shown that implementing an incorrect OR on austenite reconstructions leads to errors in both predictive PAG boundaries and orientations.

## 5.6 Conclusion

The analysis of the four steel and ferrous binary alloy samples was performed to determine the accuracy and efficacy of the proposed Bayesian austenite to martensite orientation relationship measurement technique in steels. The proposed technique

and methodology can be used to compute accurate OR measurements for the  $\gamma \rightarrow \alpha'$  transformation across a broad range of steel compositions and martensite morphologies, is repeatable, and is reasonably robust so long as a sufficient number of variants is observed and a reasonable fraction of the EBSD data points originate within a single PAG.

# **Chapter 6: Probabilistic Reconstruction of Austenite Microstructure from Electron Backscatter Diffraction Observations of Post-Transformation Martensite Using Graph Cutting**

This chapter has been prepared for submission to a peer-reviewed publication with co-authors Toren Hobbs, Dr. Vikas Sinha, Dr. Eric Payton and Dr. Stephen Niezgoda contributing to this chapter. Additionally, the written experimental procedure in Section 6.4.6 and the characterization of the 22V Columnar fusion zone sample was completed by Dr. Collin Whitt [170]. My specific contributions were the bulk of the text, analysis, methodology and code used to generate the results.

## **6.1 Introduction**

The main goal of the thesis was to utilize the information presented in Chapters 3, 4, and 5 for the effective reconstruction of the prior austenite microstructure from EBSD-indexed data sets of transformation martensite. This is because the prior austenite microstructure has a direct influence on the properties related to martensite. For one, the size and locality of packet boundaries are influenced by both the size and morphology of the prior austenite phase field, which in turn contribute to the strengthening behavior of the transformed material. Additionally, mechanisms

such as impurity segregation at prior austenite grain boundaries leading to temper embrittlement [10, 71], the classification of creep and cavitation sites [83, 175], and the occurrence of ductile to brittle fracture based on increasing prior austenite grain sizes [70, 176] can greatly affect the mechanical properties of the transformed martensite. For these reasons, reconstruction of the prior austenite microstructure can drastically improve both processing and performance conditions of the pre-transformed steel and subsequent analysis of the post-transformation steel.

Although the idea seems simple enough, and visual inspections of the martensite microstructure can oftentimes distinguish between the majority of prior austenite grains, deduction of the prior austenite phase field becomes obfuscated for a variety of reasons. For one, the  $\gamma \rightarrow \alpha'$  transformation typically goes to full completion. This requires any analysis on the prior austenite phase field to be performed from inferences on the transformed martensitic microstructure. This becomes further complicated due to the resultant transformation crystallography, where a single PAG can result in 24 crystallographic variants [84, 112]. Therefore, a pre-transformation microstructure consisting of 100 grains could result in up to 2400 martensite orientations, all of which can exhibit variable orientations. Furthermore, the violent nature of the shear-induced transformation, uncertainty in the EBSD measurement process, annealing twins within PAGs and variations in the orientation relationship (OR) also contribute to hindrances in determining the prior austenite microstructure.

Experimentally, chemical etching has been used to identify PAG grain boundaries for a variety of compositions [45, 78, 104, 161, 184]. However, the etching itself is severely time-intensive, is inconsistent, requires impure samples which segregate

to the PAGs and cannot be used for small PAGs. Furthermore, most etchant techniques are sensitive to specific compositions of the steels, such as the McQuaid-Ehn test on low-carbon ( $\leq 0.25\%$ ) steels or Nital on hardened and tool steels. Therefore, delineation of PAG boundaries for a variety of steel compositions would require a different chemical etchants. This has resulted in an influx of computational austenite reconstruction algorithms which could effectively reproduce pre-transformation microstructures based on EBSD-indexed post-transformation data.

Of the several computational austenite reconstruction algorithms that do exist, most employ a point-to-point methodology where the assumed prior austenite orientations are used in conjunction with transformation and rotational matrices with respect to misorientations between neighboring martensitic variants. The results are then compared to user-defined tolerances, which heavily influence the extent of the prior austenite grain boundaries [14, 31, 36, 65, 105, 150]. Other austenite reconstruction algorithms employ clustering algorithms or a combination of point-to-point and clustering to reconstruction the prior austenite microstructure [52, 58, 135]. Point-to-point reconstructions seem like the obvious choice because misorientations between adjacent martensitic points can be assigned as having come from the same PAG. Therefore, deviations between computed and expected misorientations are assumed as points separated by a PAG boundary. However, the extent of shearing involved with the martensite orientation, the deviation of the OR within the steel sample, uncertainty and noise inherent within EBSD indexing measurements, and variation of the parent austenite orientation hinder the practicality of point-to-point methodologies.

As mentioned in Chapter 5, variations in the composition, cooling rate, and the extent of ausforming have all been shown to cause deviations in the OR [85, 99, 116]. This strongly suggests that reconstruction algorithms utilizing the KS or NW orientation relationship will be significantly hindered, and that the OR must be computed for individual steel samples to optimize reconstruction results. Additionally, most austenite reconstruction algorithms severely struggle with the characterization of twins within the reconstructed microstructures. This can be attributed to similar misorientation groupings between variants originating from PAGs and those originating from prior austenite twins (PATs) and the existence of shared variants between said parent and twin variants [1, 2, 26, 36, 105]. The resultant variant-variant misorientations are unobservable, making it difficult to differentiate between the parent and twin interface.

In the following Chapter, an austenite reconstruction technique is proposed that accounts for the abovementioned limitations. Specifically, the OR is easily and automatically measured using an in-house computational technique that uses Bayesian inference and corresponding probabilistic calculations, the methodology of which is expounded upon in Chapter 5. Additionally, the algorithm utilizes a well known yet highly under-utilized computational technique known as graph cutting [24, 59] that bypasses the point-to-point methodology in order to effectively cluster groups of misorientations into PAGs. This was already applied in Chapter 3 for a single PAG segmentation using the KS OR, and is expounded upon here to iteratively reconstruct the entire prior austenite microstructure with corresponding likelihood plots. Accompanying each reconstruction is a feature that identifies each respective twin with their corresponding parents. Finally, untwinned PAGs can be isolated and clustered

into packets with clearly identifiable boundaries. The code was written in MATLAB (R2016a, Mathworks, Inc., Natick, MA USA) using only input EBSD-indexed martensite data with aid from the crystallographic data analysis toolbox MTEX [7].

## 6.2 Methodology and Implementation

First and foremost, a description of the method used to describe the OR throughout the rest of the paper must be given. It is well known that, for most steel ORs outside of NW, 24 crystallographic variants are observed [84, 111]. Most crystallographic rotations are described through the use of Euler angles, or Bunge Euler angles. Although popular, and thereby convenient, describing an OR through the use of Euler angles is verbose since each specific crystallographic variant would require its own set of Euler angles. As such, to fully describe the OR, and not just individual variants, a set of 24 Euler angles would be necessary. To bypass this requirement, a rotational descriptor known as  $\xi$  angles [127, 175–177] will be utilized since a single set of three  $\xi$  angles can fully describe the entire OR. Interestingly enough, the procedure used to describe said  $\xi$  angles is almost equivalent to the one described by Kurdjumov and Sachs [89], although advancements in imaging techniques can now better identify the precise deviation between ideality associated with experimental steel samples.

In terms of the manual interpretation of  $\xi$  angles, a single martensitic dataset is first analyzed, and assumed PAGs with suspected twins are omitted. The remaining points are then rotated to coincide individual PAG orientations with the sample reference frame. The angular deviation between the closest Bain correspondence matrix axes [9] and the primary axis of the rotation matrix therefore relates the OR in terms of three measurable parameters:  $\xi_1$ ,  $\xi_2$  and  $\xi_3$ . Here,  $\xi_1$  and  $\xi_2$  are the smaller

and larger deviations between the  $\langle 110 \rangle$ -type Bain correspondence axis, respectively, and  $\xi_3$  represents the deviation from the  $\langle 001 \rangle$ -type Bain correspondence axis.

The main Bayesian framework used as the model for the reconstruction algorithm is explained in more detail in Chapter 3, and the implementation remains almost identical in terms of our prior and posterior distributions to the layout presented in Chapter 5. This approach was utilized for the reconstruction algorithm as well because of the violent nature of the martensite transformation, which results in dynamic orientation relationships that vary with composition and cooling rate. Additionally, the noise and uncertainty associated with the  $\gamma \rightarrow \alpha'$  transformation are effectively accounted for when analyzing the transformation through a Bayesian lens.

### 6.2.1 Graph Cutting

The foundation of the reconstruction algorithm is a clustering technique known as graph cutting, the specifics of which were presented in Chapter 3. Therefore, only a brief overview of notation and the nature of the algorithm will be presented here. It begins with the formation of a graph,  $\mathcal{G} = \langle \mathcal{V}, \mathcal{E} \rangle$ , containing a network of  $n$  interlinked nodes,  $\langle \mathcal{V} \rangle = [v^{(1)}, v^{(2)} \dots v^{(n)}]$  with adjoining nodes being connected by a set of  $m$  edges,  $\langle \mathcal{E} \rangle = [e^{(1)}, e^{(2)} \dots e^{(m)}]$ . Two terminal nodes, the source,  $s$ , and the sink,  $t$ , lie outside of what is known as a grid,  $g$ . A grid consists of the selected nodes that hold the information that is looking to be analyzed, such as the series of EBSD-indexed points corresponding to the post-transformation orientation information. The purpose of a graph cut is to separate the graph into two distinct, mutually exclusive subsets,  $\{\mathcal{S}$  and  $\mathcal{T}\}$ , where it unequivocally holds that  $s \in \mathcal{S}$  and

$t \in \mathcal{T}$ . This partitioning of the graph is achieved by performing a cut,  $\mathbf{C} = \{\mathcal{S}, \mathcal{T}\}$ , that severs a series of adjacent edges.

In order to determine the path of a cut, each edge connecting nodes  $v^{(i)}$  and  $v^{(j)}$ , has assigned to it a corresponding weight,  $w(v^{(i)}, v^{(j)})$ . The weights serve to drive the cut forward by finding an energy minimized cut, or maximum flow path across edges. This admittedly enigmatic abstraction can be made tangible by analogizing graph theory to a series of interlocked pipes with variable diameters carrying water from an initial “source,” say a faucet, to an ultimate “sink,” say the sewer. If the goal becomes redefined to maximize the flow of water from the facet to the sewer by way of the interconnected pipes, this would be achieved by shutting off, or “severing,” pipes with smaller diameters since these would effectively retard the overall flow rate. This directly relates to the maximum flow description. Equivalently, if instead of shutting off water to the pipes we decided to physically saw through them, the energy minimized cut would be again be achieved by cutting the pipes with a smaller diameter since it would require less energy than sawing through a large-diametered pipe. This is the basis of the Ford-Fulkerson theorem, which is expounded upon in more detail in [49].

Additionally, each respective edge can be either directed or undirected, which essentially dictates the number of edges associated with a pair of nodes. The former refers to a pair of nodes containing two respective edges, where each edge has associated with it a unidirectional, independent flow (weight). In other words, one of the edges would flow in the forward direction and one would flow in the backward direction, or  $w(v^{(i)}, v^{(j)}) \neq w(v^{(j)}, v^{(i)})$ . In contrast, an undirected edge would essentially have a single edge since the the forward and reverse flows would be equivalent,

namely  $w(v^{(i)}, v^{(j)}) = w(v^{(j)}, v^{(i)})$ . A visual description of the two different graph set ups used to perform the reconstruction can be seen below in Figure 6.1.

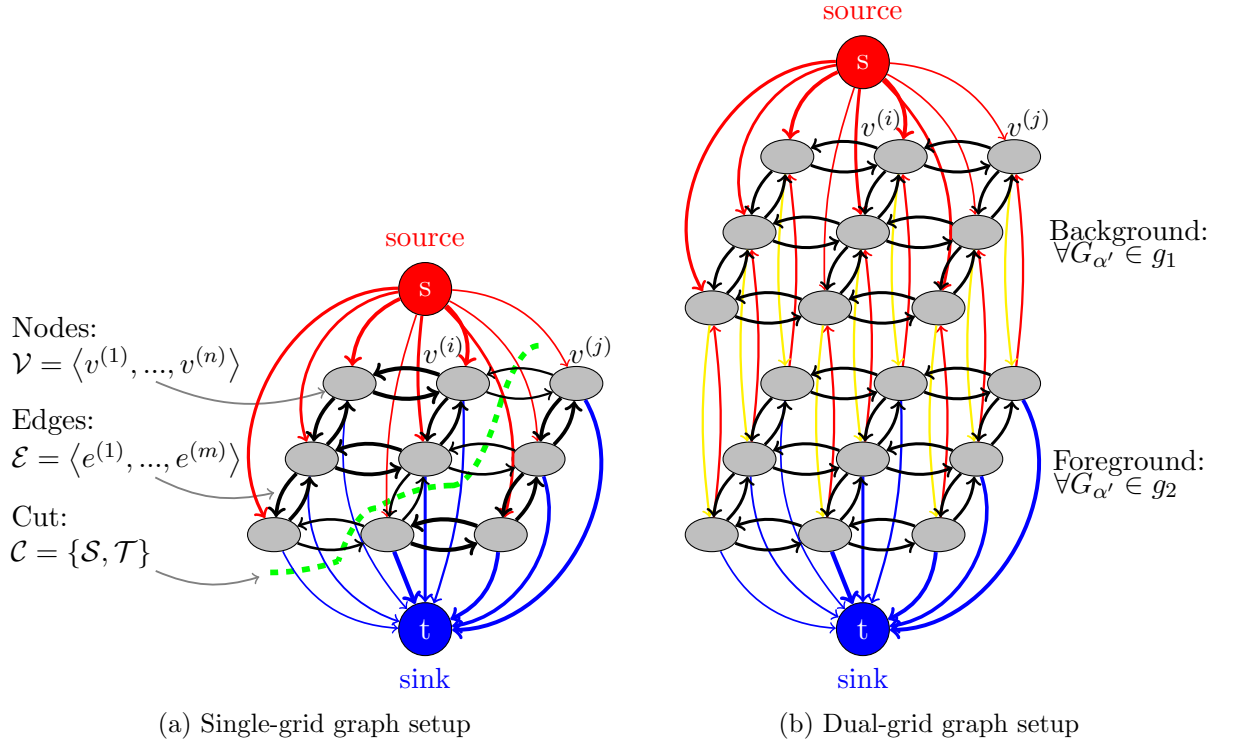


Figure 6.1: Graph construction where  $g$  is separated by the terminal nodes,  $s$  and  $t$ . The  $t$ -link edges are colored in red and blue and the  $n$ -link edges are colored in gray, with corresponding cut colored in green.

In terms of the austenite reconstruction algorithm, the associated edges are directed and carry weights that are probabilistically related to the crystallographic nature of the austenite  $\rightarrow$  martensite transformation. What are referred to as in-plane edge weights relate to clustering martensite variants into those likely transformed from the same PAG. The out-of-plane nodes then serve to assign austenite orientations to a group of similar martensite variants, and corresponding cuts are applied

in an iterative fashion to flesh out the resultant transformation microstructure. For a complete description of graph cutting theory, the interested reader can refer to the following references [24, 59] or Chapter 3, which also provides a more complete description of the notation used throughout the rest of the paper.

### 6.3 Austenite Reconstruction Algorithm

The austenite reconstruction can actually be performed in three separate manners depending on the “reconstruction” space; either “austenite,” “martensite,” or “mixed.” What is meant by reconstruction space is the specific phase that drives the probabilistic calculations which ultimately determine the assignment of the weights. In other words, calculations performed in martensite space are dependent solely on the martensite variants, and calculations performed in austenite space utilize the potential transformed austenite for pertinent calculations. Both of these graph setups require a dual-grid system, seen in Figure 6.1b. This allows the algorithm to compare a current, prospective cut with the PAGs that have already been added to the microstructure so as to ensure new cuts only add to the probabilistic certainty of the microstructure. The “mixed” space then uses advantageous components from both the austenite and martensite spaces to optimize the results, and therefore takes precedence in the ensuing description of the algorithm. This system only uses a single grid graph as seen in Figure 6.1a. However, in order to make more apparent which space is being operated in, the following section is subdivided into two parts for the reader’s convenience.

We start with an initial definition of our mixed-space graph,  $\mathcal{G}(G_{\alpha'}) = \langle \mathcal{V}(G_{\alpha'}), \mathcal{E}(G_{\alpha'}) \rangle$ , where each node within the graph is an observable, indexed martensite orientation,

$G_{\alpha'} = [g_{\alpha'}^{(1)}, g_{\alpha'}^{(2)}, \dots, g_{\alpha'}^{(n)}]$ . As Chapter 5 details, we can choose a subset of orientations extracted from points within a window contained, or slightly extended past, a presumed PAG in order to automatically calculate the steel-specific OR,  $\Xi$ . Along with the OR determination comes a numerical value for the degree of scatter inherent within the OR, denoted as our halfwidth,  $\kappa$ . For the AF9628 steel sample, whose composition and data collection can be found in [4], these parameters were both determined to be  $\Xi = [3.09, 8.10, 8.48]$  and  $\kappa = 1.67^\circ$ , respectively.

From both of these parameters, all theoretical misorientations between martensite points can be calculated and denoted as  $\Delta G_{\alpha'}$ . Through a convolution of the misorientations with a de La Valee Poissin kernel function [7], these can now be represented as a misorientation distribution function,  $f(\Delta G_{\alpha'})$ . Since each martensite orientation is considered an *n-link* node within the internal grid,  $v^{(i)}$ , an adjacency array can be constructed that then relates each node with all neighboring nodes. From this, the EBSD-indexed, adjacent martensite-martensite misorientations can be calculated,  $\Delta G_{\alpha'}(\mathcal{V}^{(i)}(G_{\alpha'}), \mathcal{V}^{(j)}(G_{\alpha'}))$ . A probabilistic comparison between the set of misorientations and the corresponding misorientation distribution function (MODF) is now modeled as our set of in-plane weights, the model of which remains consistent regardless of which algorithm is being used:

$$w^{IP}(v^{(i)}, v^{(j)}) = \lambda f(\Delta G_{\alpha'}(\mathcal{V}^{(i)}(G_{\alpha'}), \mathcal{V}^{(j)}(G_{\alpha'}))) | f(\Delta G_{\alpha'}) + \beta \quad (6.1)$$

This equates to the likelihood that adjacent martensite orientations came from the same PAG and serves as all in-plane weights for subsequent sub-graphs. The term  $\lambda$  serves as a regularization parameter and  $\beta$  limits the facility with which a cut can partition two nodes, representative of the interfacial energy between PAGs. Both of

these terms effectively account for noise and other associated hindrances (misindexed points, variation in austenite orientation, etc.) that result in deviations from the ideal austenite → martensite transformation.

### 6.3.1 Martensite Space

With the in-plane weights in place, we now enter the “martensite” space portion of the code. This means that we do not need to consider any calculations related to austenite, such as orientations, rotations, orientation distribution functions (ODFs), etc. The first set of OP weights, from  $s \rightarrow g$ , are simply a uniformly distributed constant equivalent to the Bayesian fidelity term in Bayes Theorem,  $P(B)$ . For the second set of OP weights (from  $g \rightarrow t$ ), we first select a random, high confidence martensite orientation,  $g_{\alpha'}^{(i)} \in G_{\alpha'}$ . We then construct an array of misorientations between the single point and all other existing martensite orientations:

$$\Delta g_{\alpha'}^{(i)} = g_{\alpha'}^{(i)}^{-1} * G_{\alpha'} \quad (6.2)$$

This allows for a comparison between the point-specific misorientations and the MODF, which in turn relates to the probability that variants within  $G_{\alpha'}$  came from the same PAG as  $g_{\alpha'}^{(i)}$ . This term can be denoted  $f(\Delta g_{\alpha'}^{(i)} | f(\Delta G_{\alpha'}))$  and serves as the corresponding out-of-plane weights that connect the intra-grid nodes to the sink:

$$w_{\alpha'}^{g \rightarrow t}(v^{(i)}, v^{(j)}) = \lambda f(\Delta g_{\alpha'}^{(i)} | f(\Delta G_{\alpha'})) + \beta \quad (6.3)$$

The subscript  $\alpha'$  simply denotes the fact that these weights exist solely within martensite space. Once the weights have been established, an initial cut,  $\mathcal{C}_i$ , is performed that segments an initial guess of the PAG. Although the segmentation is oftentimes

representative of a potential PAG, a few issues arise with the martensite space algorithm. For starters, variants transformed from a PAG with a similar orientation (or to twin-transformed variants from another grain) can show a somewhat strong probability of coming from the same PAG. This can result in disjointed cuts of two, nonadjacent PAGs that will be assigned a single PAG orientation. Secondly, the aforementioned existence of shared variants between parent and twin austenite grains results in a significant number of missed twins. Instead of ambiguously defining the twin-transformed variants as an annealing twin, these regions are simply assigned the parent austenite orientation. A subsequent cut would then need to be performed based on non-shared variant within that same twin, which becomes a probabilistic uncertainty when the choice of  $g_{\alpha'}^{(i)}$  is randomized.

### 6.3.2 Austenite Space

Due to the limitations involved with solely existing in the martensite space, the algorithm now utilizes the “austenite” space in order to clean up the initial cut and assign an austenite orientation to the corresponding martensite points. First, a subgraph,  $\mathcal{G}(\mathcal{C}_i) = \langle \mathcal{V}(\mathcal{C}_i), \mathcal{E}(\mathcal{C}_i) \rangle$ , is created with the dual grid system described in reference [25],  $g_1$  and  $g_2$ . The numerical subscript denotes the grid position (1 connects to  $s$ ; 2 connects to  $t$ ), and  $\mathcal{C}_i$  is a simple reminder that the graph is now only composed of nodes that were contained within the first cut in martensite space. Therefore, we can redefine our set of martensite orientations to those bounded within our initial cut,  $G_{\alpha'}(\mathcal{C}_i) \in G_{\alpha'}$ . The dual-grid assignment helps bisect our graph into two inter-related yet independent systems, one corresponding to the martensite space and the other to the austenite space. Since the goal of our next cut is to define the “true”

PAG boundary, the dual-grid system ensures the probabilities assigned in the austenite space take precedence over those assigned in martensite space. Additionally, the in-plane weights remain the same as those calculated in Equation 6.1 but are limited to adjacent nodes contained within  $\mathcal{C}_i$ .

With the addition of a second grid, we must now define three sets of out-of-plane weights. The first set, from  $s_\gamma \rightarrow g_1$ , is attributed an uncuttable value in order to bound the cut within a single grid. The second set, connecting  $g_1 \rightarrow g_2$ , is the inverse of Equation 6.3 such that high-probabilistic regions found in the martensite space become favorable regions to cluster in austenite space, and those with lower probabilities (such as those variants transformed from a similarly oriented PAG as to that containing  $g_{\alpha'}^{(i)}$ ) are clustered into martensite space. The out-of-plane weights connecting  $g_2 \rightarrow t$  must now relate the available martensite orientations to the most likely austenite orientation candidate. This is determined by first translating each martensite orientation whose confidence index is greater than 0.05 into the 24 crystallographic austenite variants and constructing a local, unimodal austenite ODF,  $f(G_{\alpha'}(\mathcal{C}_i))$ . A relative maximum is then computed as the modal orientation value within  $f(G_{\alpha'}(\mathcal{C}_i))$  and consequently used as our proposal austenite orientation,  $g_\gamma^i$ . The modal orientation is only calculated for indexed points that have a confidence interval value of 0.05 or greater assigned to them, which means only points where the confidence interval is incredibly small will be ignored. The reason for this will become more evident in Section 6.4.4, which tested the algorithms ability to handle excessive noise.

Although we could continue on with only the austenite orientation (as the complete austenite space algorithm does), and consequently omit the twin orientations, we run

the risk of cutting out the twin-transformed martensite variants. Additionally, it is well known that a face-centered cubic parent grain can contain up to four  $\Sigma 3$  annealing twins. Therefore, the chosen prior austenite orientation was rotated by the four unique rotations of  $60^\circ$  about  $\langle 111 \rangle$  to produce a set of four possible twin-specific austenite orientations,  $g_{\Sigma 3}^i$ . The entire set of austenite orientations related to a single parent can now symbolically represented as  $g_{\gamma-\Sigma 3}^i$ , where it holds that  $\{g_\gamma^i \wedge g_{\Sigma 3}^i\} \in g_{\gamma-\Sigma 3}^i$ . We can now denote the transformation of all 5 possible parent and twin austenite orientations to the full set of 120 possible martensite variants as  $\Delta g_{\gamma-\Sigma 3 \rightarrow \alpha'}^i$ . A convolution of this transformation with a model for the noise,  $\kappa$ , and the representative orientation relationship,  $\Xi$ , provides us with an ODF that is directly related this transformation:  $f(\Delta g_{\gamma-\Sigma 3 \rightarrow \alpha'}^i(\Xi, \kappa))$ . Therefore, the likelihood of attaining the observed martensite orientations given our proposal austenite parent-twin system is denoted as  $f(G_{\alpha'}(\mathcal{C}_i)|f(\Delta g_{\gamma-\Sigma 3 \rightarrow \alpha'}^i(\Xi, \kappa)))$  and represents the second set of out-of-plane weights in Equation 6.4:

$$w^{g_2 \rightarrow t}(v^{(i)}, v^{(j)}) = \lambda f(G_{\alpha'}(\mathcal{C}_i)|f(\Delta g_{\gamma-\Sigma 3 \rightarrow \alpha'}^i(\Xi, \kappa))) + \beta \quad (6.4)$$

With all sets of weights in place, a second cut is initiated,  $\mathcal{C}_\gamma$ , to eliminate extraneous martensite orientations and identify the boundaries for our PAG. We can now separate the parent austenite orientation with potential twins by creating a third subgraph,  $\mathcal{G}(\mathcal{C}_\gamma) = \langle \mathcal{V}(\mathcal{C}_\gamma), \mathcal{E}(\mathcal{C}_\gamma) \rangle$ , defined by the boundaries produced in  $\mathcal{C}_\gamma$ . The subscript  $\gamma$  is used to denote the fact that the cut itself encompasses the entire PAG, including both parent-and twin-transformed variants. This set up again utilizes a dual-grid system, where the  $s \rightarrow g_1$  out-of-plane weights are uncuttable; the  $g_1 \rightarrow g_2$  weights give us the likelihood of observing the martensite orientations from our parent

orientation, and then through an iterative scheme, the  $g_2 \rightarrow t$  weights correspond to the likelihood that the martensite variants were transformed from one of the four  $\Sigma 3$  annealing twin orientations. These are all computed in analogous manner to Equation 6.4 except we replace “ $g_{\gamma-\Sigma 3}^i$ ” with either the sole parent austenite orientation or one of the  $\Sigma 3$  twin orientations. If a cut is not made for a specific twin, nothing happens and we continue on to the next twin iteration. However, if a reasonable cut does exist for the first twin iteration,  $g_{\Sigma 3}^1$ , the weights corresponding to this twin are then added to our  $g_1 \rightarrow g_2$  weights to prevent redundant, overlapping twin cuts:

$$w^{g_1 \rightarrow g_2}(v^{(i)}, v^{(j)}) = w^{g_1 \rightarrow g_2}(g_{\gamma}^i) + w^{g_2 \rightarrow t}(g_{\Sigma 3}^1) \quad (6.5)$$

Here, the weights typically denoted as a function of the nodes  $v^{(i)}$  and  $v^{(j)}$  are replaced with either  $g_{\gamma}^i$  or  $g_{\Sigma 3}^1$  to express which austenite orientation the ODFs are being calculated from, in this case the parent orientation and the first annealing twin orientation, respectively. Indexed nodes corresponding to this twin cut are then assigned the respective twin austenite orientation. This continues on until all four twin iterations have had a chance to stake claim to the set of martensite variants contained within our first, initial cut.

After each cut is made, the remaining nodes within  $\mathcal{C}_{\gamma}$  that have not been collected by a twin are assigned the parent austenite orientation,  $g_{\gamma}^i$ , and a truncation is performed where all nodes contained within  $\mathcal{C}_{\gamma}$  are removed from  $\mathcal{G}(G_{\alpha'})$ , or  $\mathcal{V}(G_{\alpha'}(\mathcal{C}_{\gamma})) \not\subset \mathcal{G}(G_{\alpha'})$ . This is done as a time-optimization technique since the amount of time required to perform a cut in the graph cutting algorithm scales poorly with the number of indexed points, albeit in a manner that is still computationally more efficient than a corresponding flood-fill or point-to-point reconstruction technique.

This also allows for an automatic indexing of parent and twin grains, which is not possible in the single-space cases and therefore requires a separate function to sort everything.

Finally, for the algorithm to reach completion, either all martensite points have been transformed,  $G_{\alpha'}(\{\emptyset\})$ , or 10 consecutive cuts must be run in which a single cut is not made within martensite space. This suggests that existing martensite orientations may actually be either retained austenite or transformed bainite, or a sufficient  $g_{\gamma}^i$  cannot be found due to clustered regions contain few martensite variants, the transformation was violent/scattered enough to produce a large deviation from the OR, or an issue in the EBSD-indexing has occurred. The fundamental formulation of the code is presented below in Algorithm 1 as an accessible pseudo-code.

## 6.4 Results

All reconstructions provided throughout the rest of the paper are presented in their most optimized form, meaning regularization parameters were adjusted to conceive the most likely results. Each reconstruction was performed on the same AF9628 steel dataset with the same computer, a 3.40 Gz core processor with 15.6 GB of RAM, where the time of computation was recorded for each run. In terms of the single space reconstruction algorithms, the characterization of twins must be performed separate from the austenite reconstruction function due to the nature of the cuts. In contrast, the mixed space reconstruction algorithm integrates twin characterization into the reconstruction function. Therefore, all recorded times for these results include both reconstruction and twin identification for consistency and due to the nature of ASTM grain size calculations, which effectively ignore twin boundaries, thereby requiring

---

**Algorithm 1** Mixed Space Reconstruction Algorithm

---

```

1: procedure AUSTENITE RECONSTRUCTION
2:   Measure  $\rightarrow (\Xi, \kappa)$ 
3:   Construct  $\rightarrow f(\Delta G_{\alpha'})$ 
4:   UnCutCount  $\leftarrow$  # of consecutive counts with no cut
5:   while  $G_{\alpha'} \neq \{\emptyset\}$  & UnCutCount < 10 do:
6:     Construct  $\rightarrow \mathcal{G}(G_{\alpha'}) = \langle \mathcal{V}(G_{\alpha'}), \mathcal{E}(G_{\alpha'}) \rangle$ 
7:     Martensite Space:
8:       Compute  $\rightarrow w^{IP}(v^{(i)}, v^{(j)})$ 
9:       Find:  $g_{\alpha'}^i \leftarrow$  high confidence
10:      Compute  $\rightarrow \Delta g_{\alpha'}^{(i)}$ 
11:      Compute  $\rightarrow w_{\alpha'}^{g \rightarrow t}(v^{(i)}, v^{(j)})$ 
12:      Initiate "Martensite Variant" Cut:  $\rightarrow \mathcal{C}_i$ 
13:      if  $\exists \mathcal{C}_i \in g$  then:
14:        Construct  $\rightarrow \mathcal{G}(\mathcal{C}_i) = \langle \mathcal{V}(\mathcal{C}_i), \mathcal{E}(\mathcal{C}_i) \rangle$ 
15:      Austenite Space:
16:         $w^{g_1 \rightarrow g_2}(v^{(i)}, v^{(j)}) \approx w^{g \rightarrow t}(v^{(i)}, v^{(j)})^{-1}$ 
17:        Compute  $\rightarrow g_{\gamma-\Sigma 3}^i$ 
18:        Compute  $\rightarrow w^{g_2 \rightarrow t}(v^{(i)}, v^{(j)})$ 
19:        Initiate "Prior Austenite Grain" Cut:  $\rightarrow \mathcal{C}_{\gamma}$ 
20:      Bound by Prior Austenite Grain (Subscript  $\gamma$ ):
21:        Construct  $\rightarrow \mathcal{G}(\mathcal{C}_{\gamma}) = \langle \mathcal{V}(\mathcal{C}_{\gamma}), \mathcal{E}(\mathcal{C}_{\gamma}) \rangle$ 
22:        Assign  $\rightarrow w^{g_1 \rightarrow g_2}(g_{\gamma}^i)$ 
23:        for twin = 1:4 do:
24:          Assign  $\rightarrow w^{g_2 \rightarrow t}(g_{\Sigma 3}^{(twin)})$ 
25:          Initiate "Twin" Cut  $\rightarrow \mathcal{C}_{\Sigma 3}^{twin}$ 
26:          if  $\exists \mathcal{C}_{\Sigma 3}^{twin}$  then:
27:            Assign  $\rightarrow G_{\alpha'}(\mathcal{C}_{\gamma}(\mathcal{C}_{\Sigma 3}^{twin})) = g_{\Sigma 3}^{twin}$ 
28:            Reassign  $\rightarrow w^{g_1 \rightarrow g_2}(v^{(i)}, v^{(j)})$ 
29:          else:
30:            UnCutCount = UnCutCount + 1
31:            goto Line 5
32:          Delete  $\rightarrow \mathcal{V}(G_{\alpha'}(\mathcal{C}_{\gamma}))$ 
33:          UnCutCount = 1

```

---

the combination of parent and twins into a single entity. The mixed space algorithm, utilizing aspects from both the austenite and martensite space algorithms, is then compared with to an experimental optical etchant of the same sample provided by Sinha et al [143] as validation of the reconstruction code.

Along with each reconstruction comes a corresponding likelihood plot, described in Equation 6.4. The specific coloring system utilized helps visually distinguish the computed probability the martensite variants transformed from whatever austenite orientation (either parent or twin) was chosen for them. Lighter colors would suggest a high likelihood of that specific transformation, and darker regions would suggest a poor choice of  $g_\gamma^i$ . Reconstructed austenite grain boundaries are outlined in black, but identified twin boundaries contain no outline for easier discernment between parent and twin grains. Additionally, all pockets of martensite that were unassigned to an austenite grain at the conclusion of the algorithm are colored in black. This prevents any possible confusion that may arise from austenite grains residing adjacent to unassigned martensite variants. Finally, all plotting was performed using builtin functions in MTEX [7] that were tied into the reconstruction algorithms. The representative IPF maps are therefore in direct, pixel-to-pixel correspondence with the likelihood plots in terms of the same grid-based coordinate frame from the EBSD-indexed data.

#### 6.4.1 Pure-Space Reconstructions

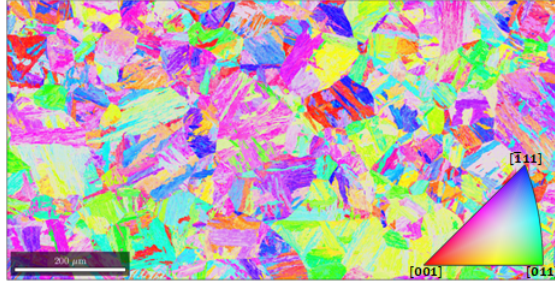
The fundamental methodology for each technique can be extracted from the description provided in Sections 3.1 and 3.2 with minor variations. One major difference between these algorithms and that described in the mixed space description is how the single-space algorithms require a user-defined “gridification” of the martensite

microstructure. This determines either the martensite point used to compute the misorientation profile in the martensite space or a group of orientations that construct the proposal austenite orientations. The latter of which are chosen by computing a local ODF of the martensite to austenite transformation contained within the grid and computing the modal austenite orientation as our local guess for that region. The gridification is necessary in order to accurately and adequately “scan” the entire data set to avoid missing PAGs. Additionally, since the first run through will most likely miss several PAGs, each grid box is bisected and overlaid on the likelihood map to extract the areas of low-likelihood. If desired, extra iterations are run based on the likelihood regions to capture PAGs that may not have been extracted yet. However, the number of requisite iterations that will provide adequate reconstructions varies widely based on the number and/or size of assumed PAGs, one of several factors that ultimately led to the mixed-space algorithm taking precedence over the pure-space ones.

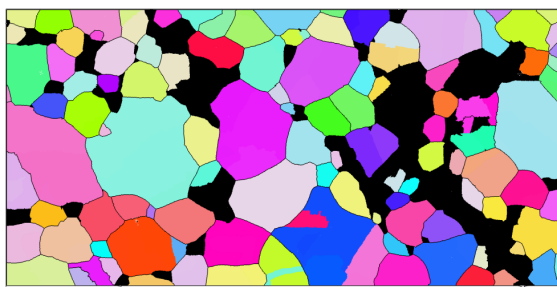
Nevertheless, the pure-space algorithms were used to both highlight the specific qualities and shortcomings of each respective technique as well as analyze the effect of the OR on the relative accuracy of the reconstruction results. The chosen ORs are the KS and experimentally determined OR since the KS is commonly applied in other reconstruction algorithms. Additionally, reconstructions were also performed using the GT and NW for completeness, but the results are not presented for the sake of redundancy. In total, five reconstructions were performed and displayed in Figures 6.2 and 6.4; the first figure contains reconstructions using pure martensite space and austenite space but applying the KS OR to relevant calculations. The latter figure then details the reconstructions performed using the experimentally observed OR and

a variable number of applied iterations. A total of 1042 iterations were applied to both the martensite space reconstruction and KS reconstruction. The in-plane and out-of-plane parameters used for the martensite and KS reconstructions were  $\lambda^{IP} = 7 \& 15$ ;  $\beta^{OP} = 5 \& 8$ ;  $\lambda^{OP} = 0.175 \& 0.2$ ; and  $\beta^{OP} = 2 \& 2$ , respectively. These two reconstructions can be found below in Figure 6.2 along with their corresponding likelihood plots.

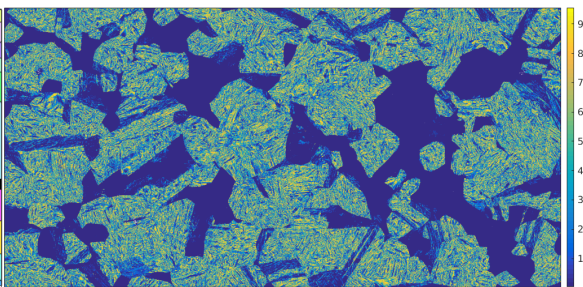
As can be seen from Figure 6.2, the martensite space methodology results in a significant portion of the transformation martensite having unassigned austenite orientations. It was found that the optimization of the grid structure used to compute the martensite space reconstructions was difficult to establish. This was because too much refinement of the grid resulted in excessively long reconstruction times (over 4 times what is presented below), but too large of a grid size could not adequately capture the diversity of the martensite microstructure (too much martensite was not assigned to an austenite orientation). However, the choice of the majority of the PAGs are reasonable, as the likelihood map relating the martensite variants to chosen PAG orientations are typically high. Additionally, the lack of assigned twins is also apparent throughout the microstructure. Even if a twin is assigned, it seems to be smaller than what it should be or abruptly ends in the middle of the PAG instead extending across the entire PAG. This is most likely due to the algorithm's lack of a comparison to proposal austenite orientations. In order to adequately capture twins, it would necessitate a random martensite orientation being chosen from within a twin that varies from the parent variants. As several people have noted before, this becomes difficult since there exist shared (or distinctly similar) variants between parent and twin [1, 2, 26, 36, 105].



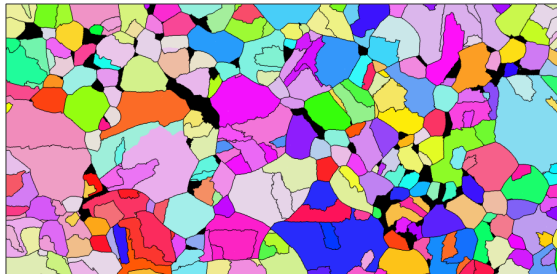
(a) IPF of post-transformation microstructure



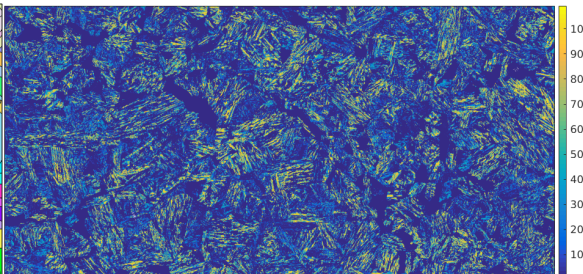
(b) Martensite space reconstruction



(c) Martensite space reconstruction likelihood plot



(d) Austenite space reconstruction; KS OR



(e) Austenite space; KS OR likelihood plot

Figure 6.2: Transformation microstructure for AF9628 sample (top) with reconstructions performed using the martensite space feature with the experimental OR (middle left) and the austenite space using the KS OR (bottom left) with adjacent likelihood maps.

The reconstruction performed using the austenite space algorithm with application of the KS orientation relationship resulted in a poorly-representative pre-transformation microstructure. Families of martensite variants that all correspond to a single PAG are divided into multiple PAGs, oftentimes with jagged, physically dubious grain boundaries. Some of these smaller grains could possibly be attributed to the variation in the transformation, but most are simply ill-posed PAGs. This is represented with the sparsity of the likelihood map, where the few regions of high probability are consistently surrounded by more regions of lower probability. Additionally, a total of 252 grains were identified as single parent grains, whereas only 3 cuts were characterized as a parent-twin system. This lack of consistent twin identification can be attributed to the KS OR and emphasizes the necessity to measure the experimental OR when attempting to optimize the reconstruction results.

In order to accentuate the crystallographic differences in the KS and AF9628 ORs,  $\{001\}_\gamma$  pole figures were plotted which display the corresponding  $\gamma \rightarrow \alpha'$  variant transformation of an arbitrary austenite orientation directly aligned with the sample reference frame (Euler angles of  $\phi_1 = \Phi = \phi_2 = 0^\circ$ ) to the 24 corresponding martensitic variants using either the KS or experimentally determined OR. Two sets of figures are plotted here for each OR case; one is related to the 24 unhindered (purely theoretical) martensite variants, the other to a set of 2000 martensite orientations that were generated with the same applied halfwidth of  $\kappa = 1.67$ . This produces scatter about the theoretical variants, thereby exhibiting a more realistic representation of how PAG-transformed martensite variant orientations would look if characterized from an actual EBSD-indexed data set. The resultant  $\{001\}_\gamma$  pole figures are shown below in Figure 6.3.

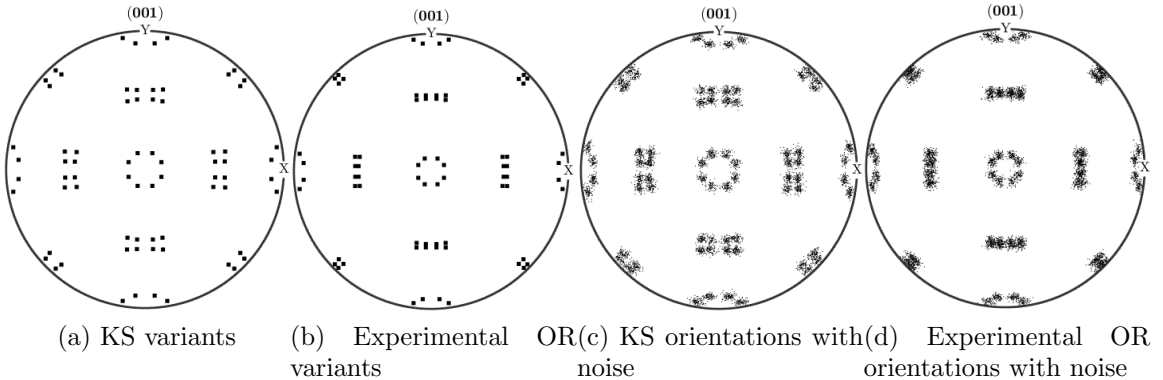


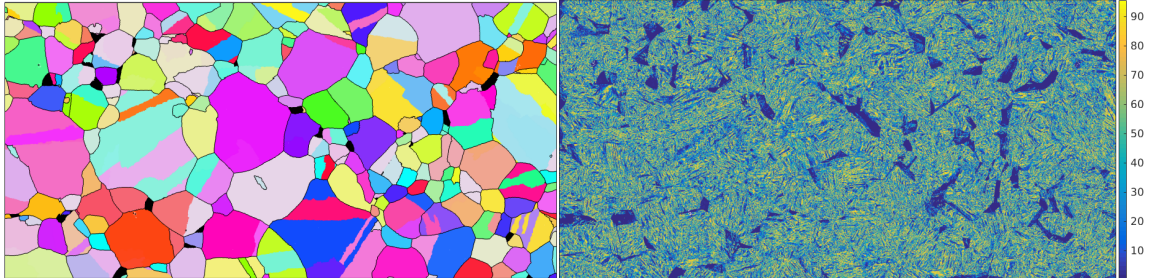
Figure 6.3:  $\{001\}_\gamma$  pole figures displaying the KS variants (left), the experimental OR variants (middle left), KS-generated noisy martensite orientations (middle right), and the experimental-OR generated noisy martensite orientations (right).

Comparison of the  $\{001\}_\gamma$  pole figures clearly displays a distinguishable difference between the KS and experimentally determined OR. Mainly, the KS variants are far more spread out, which increases dramatically as we include noise. This explains why the KS orientation relationship identifies so many more PAGs which do not agree with the expected morphology. Since the larger spread deviates from what is experimentally indexed with respect to a specific PAG, orientations become misconstrued as having transformed from different PAGs when in fact they all evolved from the same one. This demonstrates the necessity to compute the actual OR for a specific sample rather than apply the KS as some other reconstruction algorithms do.

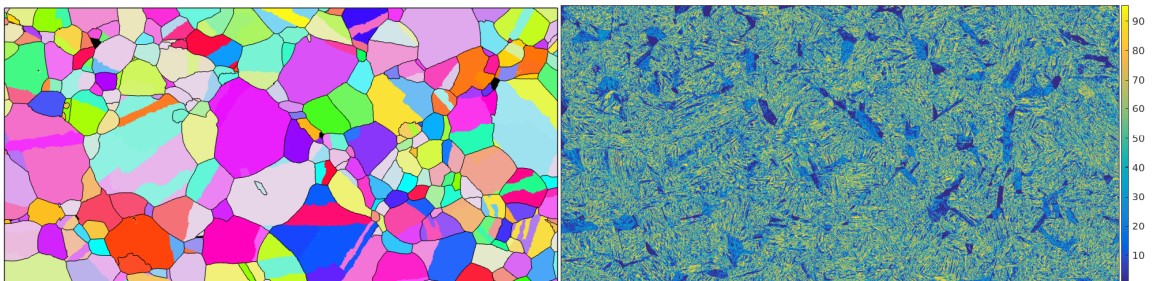
The austenite space reconstructions using the experimental OR produced much better results in a shorter amount of time, and therefore were separated from the martensite space and KS reconstructions. As described previously, a gridification was performed that optimized the number of extracted PAGs within a reasonable time frame. For each austenite space reconstruction (and the abovementioned KS one), this

gridification amounted to a total of 756 iterations. The first reconstruction therefore stops after all of these iterations have completed. The two remaining reconstructions then utilize additional iterations that are “biased” towards regions of low-likelihood. This results in the subsequent austenite orientations that likely stem from areas where a PAG has not been assigned, a twinned region has not been captured, or a poor guess orientation has been applied. Therefore, the first reconstruction added 286 iterations for a total of 1042 iterations (consistent with the number assigned to the martensite space and KS reconstructions); the last example added 716 iterations for a total of 1472 iterations. The parameters used for all three reconstructions remained consistent in order to determine results are affected by the number of iterations affects. The optimized parameters were  $\lambda^{IP} = 7$ ;  $\beta^{OP} = 5$ ;  $\lambda^{OP} = 0.175$ ; and  $\beta^{OP} = 2$ , and these reconstructions are shown below in Figure 6.4 along with their respective likelihood plots.

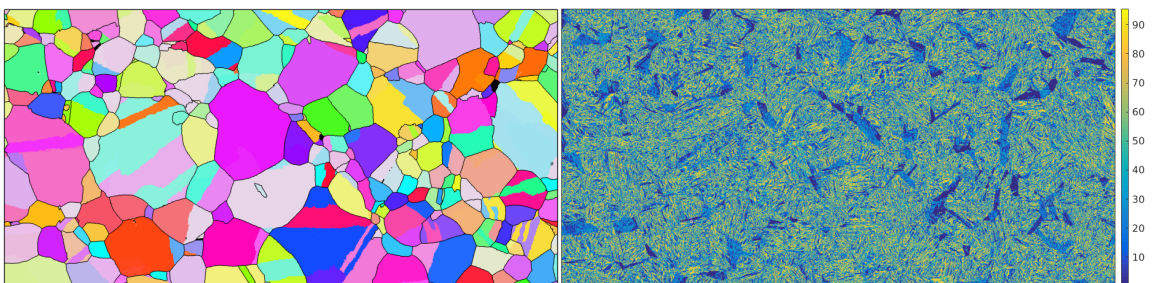
The austenite space methodology results in a better overall austenite reconstruction than the martensite space, most notably in the ability to capture prior austenite twins. This is because the austenite orientations are used to produce the out-of-plane weighting factors, with each being generated by the modal orientation described above in the description of the mixed-space algorithm. Therefore, regions containing PATs will produce a proposal austenite orientation related to the twin orientation, which allows for the algorithm to separate twins from the parents. Additionally, it is clear that some of the chosen PAGs or PATs have an orientation gradient due to variation of martensite variants across the same PAG. These regions highlight the amount of noise that is introduced to the observable data set as a result of the transformation.



(a) Austenite space reconstruction; 756 iterations  
(b) Austenite space; 756 iterations likelihood plot



(c) Austenite space reconstruction; 1042 iterations  
(d) [Austenite space; 1042 iterations likelihood plot



(e) Austenite space reconstruction; 1472 iterations  
(f) Austenite space; 1472 iterations likelihood plot

Figure 6.4: Austenite reconstructions and likelihood maps generated by only using the austenite space reconstruction algorithm for 756 iterations (top), 1042 iterations (middle), and 1472 iterations (bottom).

Overall, both pure-space algorithms leave behind some clusters of low-likelihood regions, most notably the martensite space reconstructions. The austenite space seems to pick up considerably more twins than the martensite space, but struggles to capture smaller grains. Conversely, the martensite space methodology can typically capture some of the smaller grains, but fails to capture a significant number of twins. Additionally, both require pre-processing user-defined input in order to effectively gridify the microstructure to optimize the austenite reconstruction. Therefore, the mixed algorithm, which was previously described in Section 6.3, serves as the default methodology of the algorithm. The mixed-space results are now presented in conjunction with the optically etched micrograph as validation to the complete austenite reconstruction technique.

#### 6.4.2 Algorithm Validation and Comparison to Optical Etch

The mixed space algorithm was described above in Section 6.3 and serves as the main algorithm for the reconstruction code. The reconstruction provided used only the experimental OR, as comparisons with the KS orientation relationship would be redundant. Along with the aforementioned benefits of combining the pure space algorithms, the computational efficiency increases for larger data sets due to the truncated nature of the code. Since a PAG is essentially “scanned” for twins, each iteration that adds a grain to the microstructure truncates those nodes from the graph. This results in a systematic increase in the computational efficiency with each successful iteration, and large datasets can be handled with relative ease.

As mentioned previously, an optical etch and corresponding SEM analysis was performed on the same AF9628 sample by Sinha et al [143]. This optical etch provides

a 1-to-1 correspondence with the reconstruction algorithm and remains the most advanced etching procedure for this specific steel composition as of yet. To the author's knowledge, this remains the only computational austenite reconstruction that can be directly compared with experimental results. The resultant reconstruction and optical micrographs of etched surfaces can be found below in Figure 6.5, along with post-transformation martensitic microstructure and the corresponding likelihood plot. The optimized regularization parameters chosen for this reconstruction were  $\lambda^{IP} = 6$ ;  $\beta^{OP} = 4$ ;  $\lambda^{OP} = 0.175$ ; and  $\beta^{OP} = 2$ .

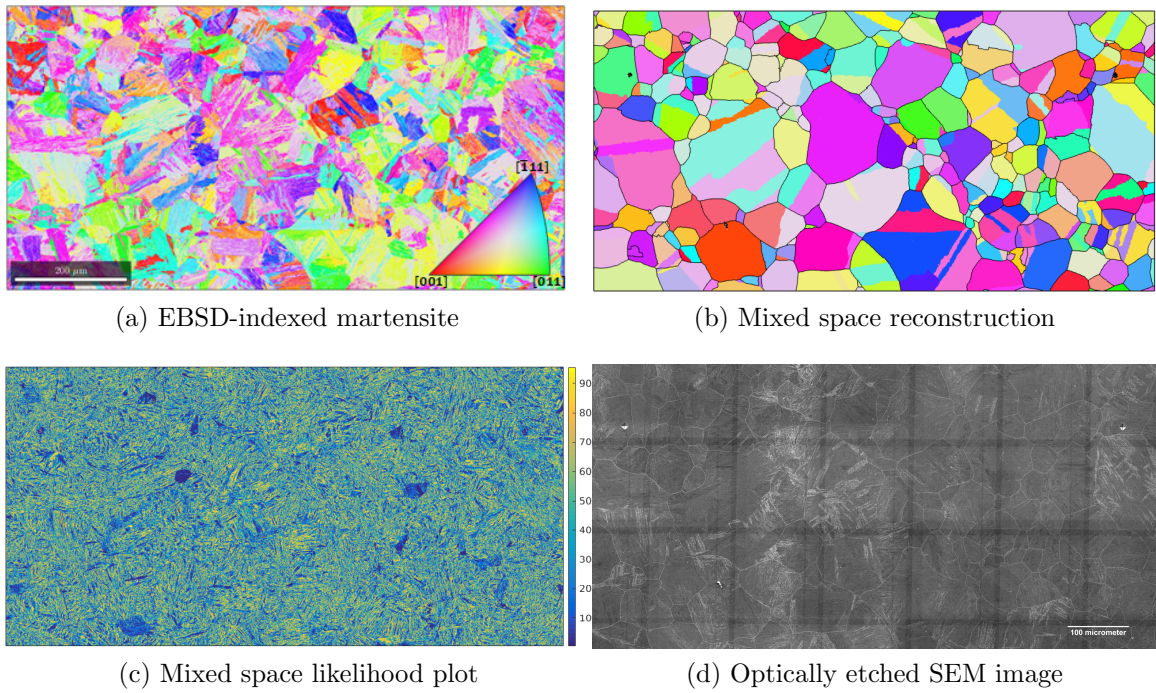


Figure 6.5: The post-transformation martensite microstructure (top left), mixed space austenite reconstruction (top right), corresponding likelihood plot with colorbar (bottom left) and optically etched micrograph image (bottom right).

As can be seen, the reconstructed result shows a strong correlation with the optical micrograph, as both grain size and geometry exhibit a striking resemblance to each other. There still exist a few regions of poor likelihood in Figure 6.5c, where it seems like grains are either extending past the probabilistic boundaries or the chosen guess austenite orientation is incorrect. Considering the stochastic nature of the technique, where the graph cutting technique aims to find the energy-minimized cut based on probabilistic input, the final results are expected to vary based on both the regularization and parameterization values.

Although some packet boundaries can be distinguished from within PAG boundaries, it is clear that the etchant technique fails to capture a large number of twin boundaries within the microstructure. On the other hand, the reconstruction algorithm does a good job at capturing possible twins, identifying a total of 94 twin grains compared with 84 single (twin-less) parent grains. This suggests that the technique can adequately identify twins, although validation can only be assumed based on the corresponding likelihood plot and not with experimental results.

Nevertheless, since prior austenite grain boundaries are so conspicuous with the optical etching, the ASTM grain size number for the corresponding microstructure were able to be computed. This involves merging twins into a single parent grain and computing the relative mean grain size rather than recognizing twins as separate grains. The calculated ASTM grain size numbers typically employ a standard deviation of about 0.5, and only grains of 100 pixels or more count towards the ASTM grain size number [45]. The grain size numbers computed using the computational grain function in MTEX [7] with a misorientation boundary tolerance of  $2^\circ$ . Although small, this allows the reader to effectively determine which prior austenite grains were

computed within a single cut, and which ones may have required an additional cut. For comparison's sake, the ASTM grain numbers were calculated for all three algorithms and displayed in Table 6.1, along with additional pertinent information such as the percent of martensite that was assigned an austenite orientation and the amount of time required for each reconstruction.

Table 6.1: Comparative information for the martensite space, KS, three different austenite techniques and the mixed space reconstructions as well as the optically etched micrograph.

Reconstruction Method	ASTM Grain Size #	% $\gamma$ Assigned $\gamma$	Total Time
Martensite	4.83	84%	1:05:45
Austenite (KS)	6.35	95.8 %	01:06:03
Austenite (756 iters)	5.9	99.03 %	00:12:02
Austenite (1042 iters)	5.9	99.85%	00:17:28
Austenite (1472 iters)	6.1	99.87%	01:04:50
Mixed	6.0	$\sim$ 100%	00:18:22
Experimental	5.2	$\sim$ 100%	

As can be seen from Table 6.1, all three techniques show a close agreement of ASTM grain size numbers with the optical etchant method. Although all of the reconstruction methods produce an ASTM grain size number outside of the optically produced one ( $5.2 \pm 0.5$ ), the experimental calculations are biased in favor of larger average grain sizes and selected grains can be arbitrarily designated by the user. The mixed space method is typically slower than the austenite space for a reasonable range of iterations, but produces a greater amount of assigned austenite points.

### 6.4.3 Algorithm Validation of Proposed Austenite Orientations

Along with the validation to the chemically etched optical micrographs, reconstructions were performed on an Fe-30 at. % Ni binary ferrous alloy with a plate-like morphology and an OR similar to that identified by Nishiyama and Wassermann [117, 166], with processing conditions and acquisition of the data set found in reference [177]. Since the sample contains a large amount of nickel, the transformation produces a plate-like morphology rather than contrasting laths, which results in significantly fewer martensitic variants than the AF9628 steel sample. Additionally, the sample contained a significant amount of retained austenite ( $\sim 15\%$ ), which is scattered evenly throughout the the microstructure. Although the retained austenite is most likely deformed from the martensitic transformation, a comparison can be made between what remains in the sample and the proposal orientations chosen by the algorithm.

The austenite reconstruction of the binary ferrous alloy can be found below in Figure 6.6 along with the martensite microstructure and the corresponding likelihood plots. Regions highlighted in black correspond to the retained austenite in the sample, with the reconstructed austenite grains shown without highlighted boundaries. The sparse nature of the data set made highlighting the MTEX-generated grain boundaries of the reconstructed austenite difficult. For this reason, the retained austenite regions are outlined in black so the reader can easily distinguish between the reconstructed and retained austenite. In this sense, “validation” can only be considered

approximate, but it gives a good idea as to the veracity of the chosen austenite orientations. The chosen regularization parameters were  $\lambda^{IP} = 5$ ;  $\beta^{OP} = 4$ ;  $\lambda^{OP} = 0.15$ ; and  $\beta^{OP} = 2$ .

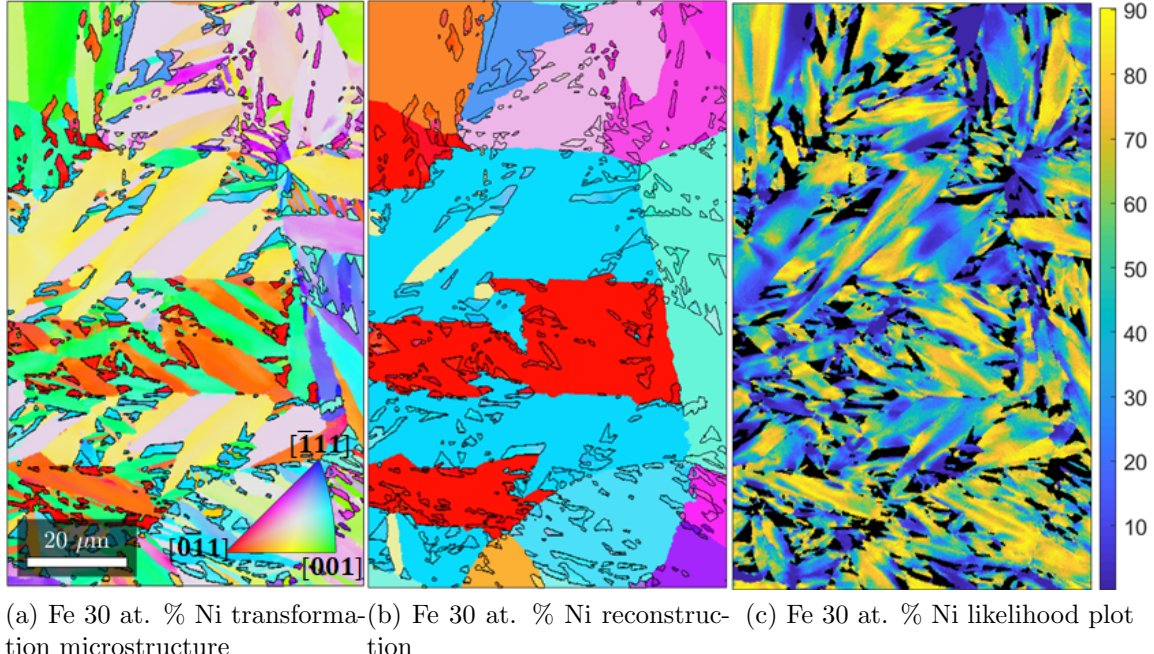


Figure 6.6: The transformation microstructure (left), resultant reconstruction (middle), and corresponding likelihood plot with color bar (right) for the Fe 30 at. % Ni binary ferrous alloy.

It is clear from Figure 6.6 that there exists a significant amount of retained austenite within the transformation microstructure. Although clear orientation gradients can be identified across the retained austenite, the majority of regions match up remarkably well with the reconstructed austenite grains for the majority of the grains. Additionally, some of the reconstructed grains have their own orientation gradients that match up well with the retained austenite regions. It can also be seen that even

sparse data sets with spatially inconsistent martensitic data points can be effectively handled with the graph cutting technique, and these do not adversely affect the proposed choice for austenite orientation. The data set was significantly smaller than the AF9628 data set, containing only 204,524 EBSD-indexed data points. Therefore, the reconstruction took  $\sim 15$  minutes to complete, which was substantially faster than the AF9628 sample.

#### 6.4.4 Misindexed Points

One of the main benefits of the graph cutting technique that distinguishes it from several other existing clustering algorithms is the ability to handle noise. Reconstruction techniques that utilize a point-to-point or flood-fill methodology suffer tremendously as the number of poorly indexed data points increases. Although some noise in an EBSD measurement is unavoidable, experimental errors can result in copious amount of noise that make it difficult or impossible to analyze the final microstructure. Therefore, the ability to sift through noise and produce accurate results is of utmost importance with regards to any computational analysis tool. In order to test the efficacy of the reconstruction technique in the face of excessive noise, a truncated portion of the transformation microstructure was isolated and 25%, 50% and 75% of the data points were randomly “misindexed” by changing their orientation to coincide with the reference frame, i.e.  $\phi_1 = \Phi = \phi_2 = 0^\circ$ . This coincides with how EBSD typically defines poorly indexed points with too low of a confidence interval, and these orientations are shown in red for the truncated martensite data sets. Additionally, as before, the corresponding reconstructions color the martensite points that have not been assigned an austenite orientation in black in Figure 6.7.

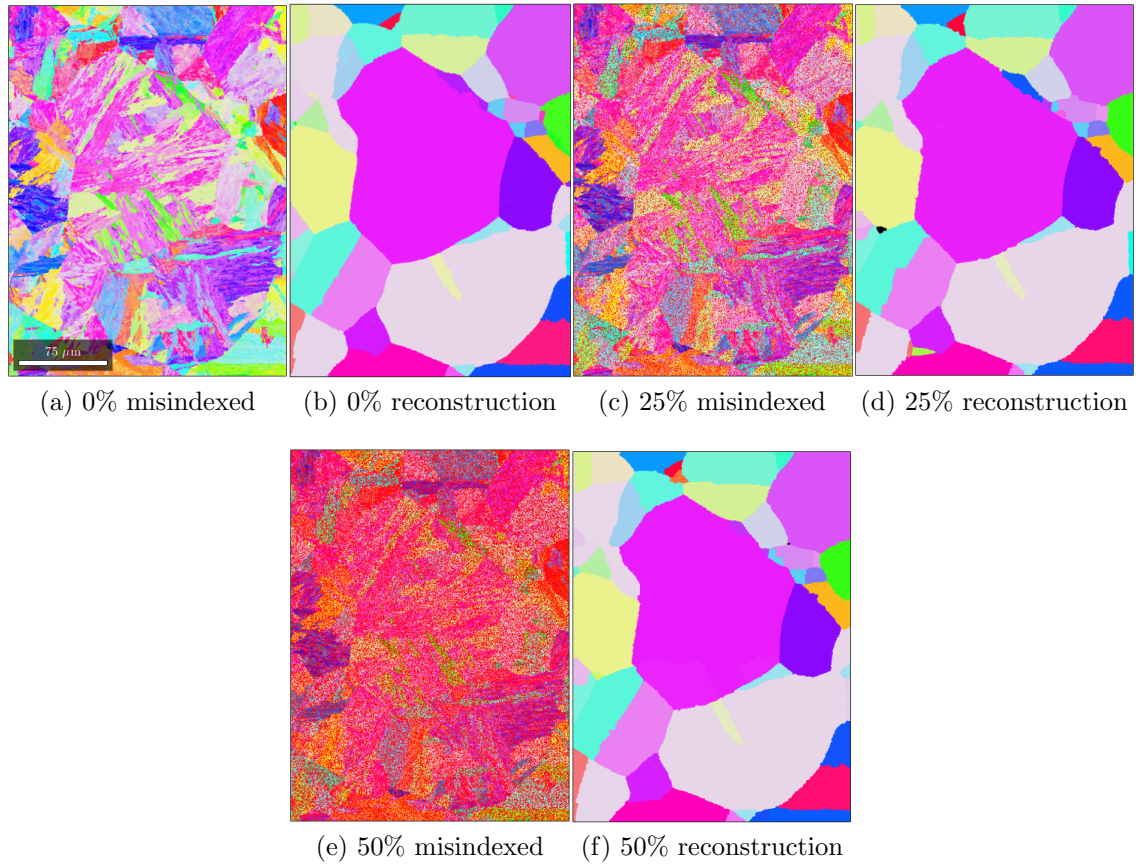


Figure 6.7: Truncated portion of the original martensite data set (top left), same region with 25% (top middle right) and 50% (bottom left) of orientations misindexed with respective reconstructions to the immediate right of each figure.

As can be seen from Figure 6.7, the addition of noise to the martensite data sets does not hinder the reconstruction results. In fact, with up to 50% of points misindexed, the reconstruction is remarkably similar to the case where no noise was added. The grain boundaries show similar geometry, with little to no grain-boundary overlap when compared with the reconstruction from the original data. What is also evident is how the chosen austenite orientations are similar for most of the cut grains. This suggests the methodology for choosing the austenite orientations is consistent and less dependent on the number of data points than the authors initially assumed. Additionally, the algorithm does a fantastic job at picking up twins in the face of noise, even when the parent-twin system has been truncated and only a small region of either remains. If one closely examines Figure 6.7a, it is clear that a limited number of martensite variants are observable in the parent-twin system located at the bottom of the reconstructed figures (blue and pink IPF coloring). This suggests that the correct, or at least consistent, austenite orientation is not highly dependent on the number of observable martensite variants. Therefore, smaller transformed prior austenite grains or Ni-based steel alloys of plate-like morphology and thus limited numbers of variants may still result in adequate reconstructions and chosen austenite orientations.

At excessive noise levels, where over 75% of the orientations have been misindexed and the original martensite orientations are barely visible, it becomes almost impossible to distinguish the properly indexed martensite orientations. Thus, one would expect the results to be severely depleted in terms of the reconstructed microstructure. However, as Figure 6.8 shows, this is not the case. Included with the noisy data set and the reconstruction is the likelihood plot for the chosen austenite orientations.

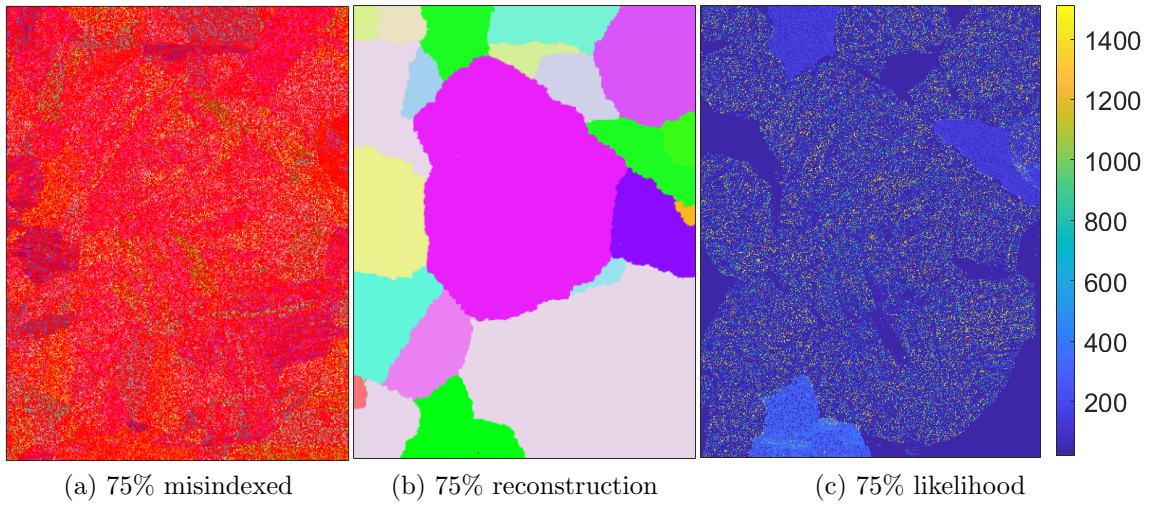


Figure 6.8: Truncated portion of same data set in Figure 6.7 with 75% misindexed orientations (left), the reconstruction (middle) and the corresponding likelihood plot

This excessively noisy reconstruction portrayed in Figure 6.8 remains surprisingly sufficient in the face of all that copious noise. For the most part, the chosen austenite orientations remain consistent with the untampered data set reconstruction, and even a few twins are captured. Additionally, the corresponding likelihood plots can be used to determine the efficacy of the reconstruction. Note how the “sparkled” regions correspond to cut PAGs with a similar orientation to that chosen in the other reconstructions, and clustered dark regions convey poor austenite orientation choices, usually the result of PAGs whose boundaries over-consumed neighboring regions and/or embedded twins.

In order to perform these reconstructions, the regularization parameters had to be increased in order to favor the clustering of neighbored, poorly-misindexed points rather than splitting everything up into a series of choppy, ill-defined PAGs. As such,

the corresponding in-plane ( $\lambda^{IP}, \beta^{IP}$ ) and out-of-plane ( $\lambda^{OP}, \beta^{OP}$ ) parameterization values for each of the cases presented above can be found in Table 6.2.

Table 6.2: Regularization parameters for respective cases of misindexed points using the mixed reconstruction method.

% Misindexed	$\lambda^{IP}$	$\beta^{IP}$	$\lambda^{OP}$	$\beta^{OP}$
0%	7	5	2	0.2
25%	23	20	5	1
50%	23	20	5	1
75%	23	21	7	2.75

#### 6.4.5 Twin Identification

One of the more difficult aspects of austenite reconstruction is the identification of  $\Sigma 3$  annealing twins in prior austenite microstructures. In fact, it is estimated that over 25% of twins are missed by current reconstruction techniques. The authors previously published a paper analyzing martensite misorientations for three specific cases: intra-parent misorientations (variant-variant interactions from within the same PAG), parent-twin misorientations (interactions between a variant originating from the PAG and a variant originating from an FCC annealing twin inside of said parent), and twin-twin interactions, which did not hold any significance [26]. The results generated give some insight onto the nature of this difficulty, which can be attributed to two specific crystallographic features of martensite variants. The first lies in the fact that misorientations generated from two variants that transformed from either the same PAG or the same PAT display an identical misorientation profile. The lack of unique misorientations therefore requires both a classification of martensite

variants based on the prior austenite grain orientation since the PAG and PAT orientations will differ by a misorientation of  $60^\circ$  about  $\langle 111 \rangle$  and a proper identification of misorientations defined by a parent-transformed variant and a twin-transformed variant. This latter perspective leads us to the second major hindrance in twin grain identification, namely, how some parent and twin variants are shared (KS orientation relationship) or, for experimentally observed ORs, almost identical, a fact that has been previously noted by several authors [1, 2, 26, 36, 105]. This can be seen in Figure ?? below through plotting both the parent and  $60^\circ \langle 111 \rangle$  twin variant orientations in a  $\{001\}_\gamma$  pole figure for both the KS (open red circles) and experimental ORs (closed black circles).

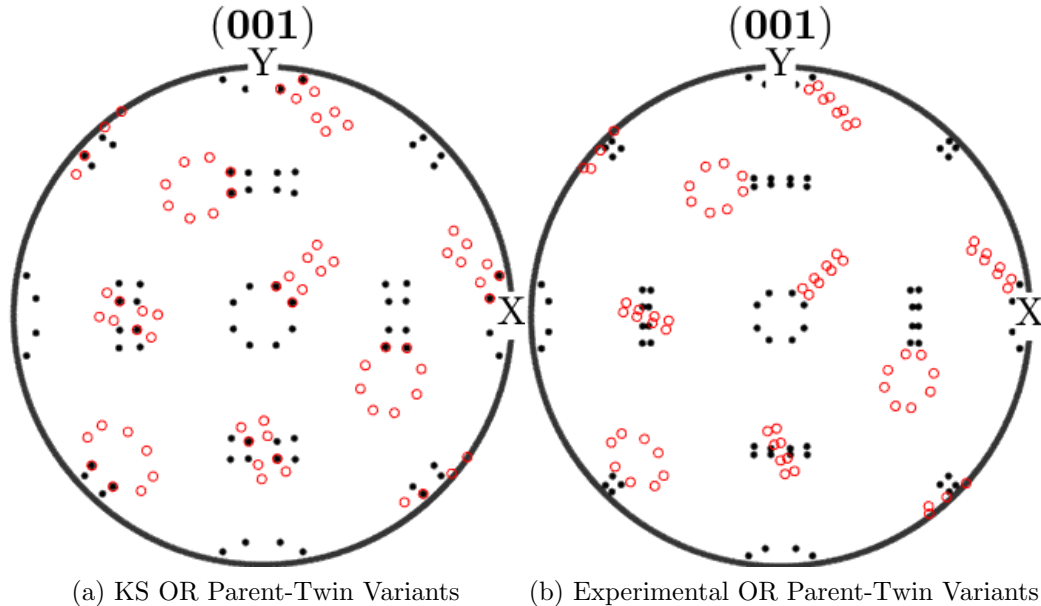


Figure 6.9: Parent (black) and  $60^\circ \langle 111 \rangle$  twin (red) variants plotted on a  $\{001\}_\gamma$  pole figure for the KS OR (left) and experimental OR (right).

This existence of shared variants for the KS orientation relationship and slightly offset variants in the experimental OR would therefore produce no discernible misorientation (or one that is remarkably small) between these variants. This results in computational assumptions that these two variants were actually generated from the same prior austenite grain and not from a twin. This explains why the point-to-point misorientation-based reconstruction techniques have such difficulty identifying twin boundaries, and why those that are identified are typically jagged. The methodology employed by our reconstruction algorithm therefore accounts for both of these factors and, as a result, produces a number of twins.

Although these produced twins cannot be validated due to the lack of a proper etchant technique that can adequately identify austenite twin boundaries, the associated likelihood maps give some insight into how veritable the results could be. A parent-twin system was chosen which contained the existence of three distinct  $\Sigma 3$  twins;  $60^\circ$  rotations of  $g_\gamma^i$  about the  $\langle 111 \rangle$ ,  $\langle \bar{1}\bar{1}1 \rangle$ , and  $\langle \bar{1}11 \rangle$  directional axes. The corresponding orientations of both the parent grain and the aforementioned twins in terms of Euler angles were  $g_\gamma^i = [296.6^\circ, 51.8^\circ, 49.6^\circ]$ ;  $g_{\Sigma 3}^{60^\circ \langle 111 \rangle} = [313.7^\circ, 97.3^\circ, 81.5^\circ]$ ;  $g_{\Sigma 3}^{60^\circ \langle \bar{1}\bar{1}1 \rangle} = [359.9^\circ, 50.1^\circ, 44.0^\circ]$ ; and  $g_{\Sigma 3}^{60^\circ \langle \bar{1}11 \rangle} = [252.3^\circ, 79.5^\circ, 106.1^\circ]$ , respectively. Finally, not only does this system consist of an eccentrically shaped combined boundary, which can also be seen in the optical micrograph in Figure 6.5d, but the  $\langle \bar{1}\bar{1}1 \rangle$ , and  $\langle \bar{1}11 \rangle$   $\Sigma 3$  twins intersect at a common interface, effectively comprising a  $\Sigma 9$  boundary. The parent-twin system is presented below in Figure 6.10 in terms of the transformed martensite variants, the reconstructed parent and twin austenite regions, and the corresponding likelihood maps partial to a specific parent or twin orientation.

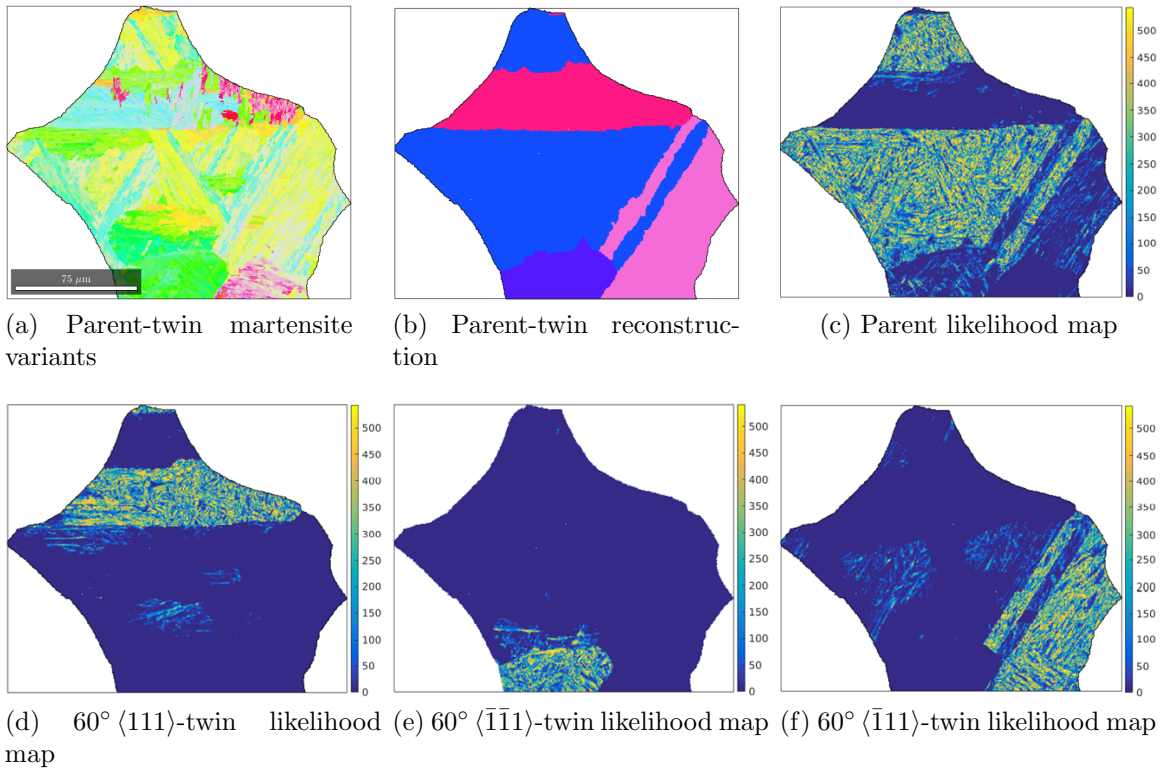


Figure 6.10: An isolated parent-twin system presented as both the transformation variants (top left) and reconstructed austenite (top middle) with respective likelihood maps related to the parent orientation (top right) and the three rotational twins  $\langle 111 \rangle$  (bottom left),  $\langle \bar{1}\bar{1}1 \rangle$  (bottom middle), and  $\langle \bar{1}11 \rangle$  (bottom right).

Referring to the likelihood maps corresponding to the parent austenite orientation and twin orientations displayed in Figures 6.10c, 6.10d, 6.10e, and 6.10f, there exists a clear probabilistic difference between martensite orientations that are assigned to the parent orientation and those assigned to the twin orientations. These likelihood plots highlight the algorithm's ability to sort through possible twin cuts and assign the PAG or PAT transformed martensite variants accordingly. They also reveal areas where a likely twin was not fully segmented, such as the dark-pink colored  $60^\circ \langle 111 \rangle$  twin that shows a high likelihood at the top of the parent grain but only a minuscule region is cut within those bounds. Although the veracity of the twin cannot be validated, the results make physical sense—in the majority of cases, the twin bisects the parent grain in a directed manner from one edge of the boundary to another.

It can also be seen that the cut twins do not display a characteristic straight-line boundary but rather seems to zigzag in certain areas. Additionally, scattered regions of high likelihood based on the parent orientation coincide with portions assigned to the twin orientations, and vice versa. Both the non-linear nature of the cut twins and the shared probability of martensite variants assigned to both the parent and the twin could be indicative of possible locations for shared variants between the specific parent and twin. These occurrences highlight some of the main difficulties in identifying twins when performing austenite reconstructions and detail how point-to-point methodologies would likely fail when attempting to sort through these issues.

#### 6.4.6 Variable Steel Compositions

In addition to the AF9628 steel and Fe-30 at.% Ni binary ferrous alloy samples, the algorithm was tested on three other steel samples, all of whose ORs were measured

by the authors for that specific sample. As was seen previously with the Fe-30 at. % Ni binary ferrous alloy, the reconstruction algorithm does a good job when the morphology shows a plate-like microstructure with an NW-like OR. The other samples presented below therefore serve to showcase the range of the technique across samples with variable compositions and morphologies. The first is a lath-martensite, low-carbon steel whose composition can be found in [114], and which is expected to contain a KS-like OR. The collection of this data set and related processing condition descriptions can be found in reference [177]. The optimized regularization parameters for this reconstruction were determined to be  $\lambda^{IP} = 6$ ;  $\beta^{OP} = 4$ ;  $\lambda^{OP} = 0.15$ ; and  $\beta^{OP} = 2$ . The reconstruction is presented below in Figure 6.11 along with the input transformation microstructure and corresponding likelihood plot.

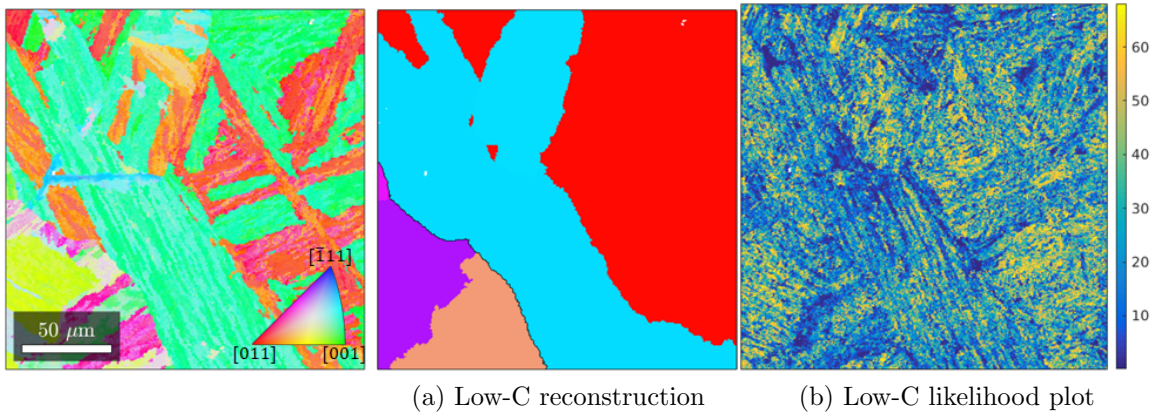


Figure 6.11: The post-transformation microstructure (left), austenite reconstruction (middle) and likelihood map for the KS-like low-C steel sample

The reconstruction in Figure 6.11a reveals extremely large PAGs that are also heavily twinned. In fact, when combining the parent and twin grains together, only

two grains are present in the microstructure, as can be seen by the black outline. The likelihood plot seems to suggest an accurate result, although the morphology of the largest twin (light blue) is odd. Additionally, the likelihood regions corresponding to twins are sparser than those of the parent reconstructions, indicating some uncertainty may exist between whether these regions should be assigned to the parent or the twin. Unfortunately, validation could not be performed on an experimentally complimentary sample, therefore the likelihood map serves as the only measurement to the accuracy of the result. The transformation data set consisted of 94,196 data points and the algorithm took a little under seven minutes to complete.

Reconstructions were also performed on a second sample, an ASTM P122 12 wt%Cr tempered martensitic steel with an OR that should fall between NW and KS and whose processing and data collection conditions can be found in [175, 176]. This steel was chosen because the PAG boundaries (excluding twins) are relatively conspicuous, meaning the human brain has a good idea of what the reconstruction should look like before the computational approach is applied. Because of this, a manual reconstruction was previously performed by on the P122 sample by Dr. Victoria Yardley. First, an assumed PAG boundary was located by eye and isolated with use of TSL OIM EBSD analysis software. Crystallographic analysis was then performed on the martensite variants to determine whether the orientation map was related to the same PAG. If it was observed that a twin existed within the PAG structure, this was consequently isolated and analyzed to locate the most likely boundaries. Once a PAG/PAT was completed, a second boundary was located by eye and the same meticulous analysis was performed until the austenite microstructure was fully developed.

Although it cannot be considered a ground truth reconstruction, it does offer a comparison between what the human eye interprets as the underlying PAG boundaries with how the algorithm utilizes the experimentally observed crystallographic information to perform the automated reconstruction. Each PAG was identified with a number and the letter “a”, and related twins were then identified using the same number and a sequential lettering system (“b”, “c”, etc.). However, note that the original manual reconstruction image was performed on a rotated data set disparate from the coordinate frame the automated reconstructions were performed on. Therefore, this image was digitally rotated to coincide with the automated data set, which inverts the number/lettering system and uses a slightly different orientation coloring map scheme (clearly evident with the heart-shaped, centralized grain and the triangular portion at the bottom of the data set). This results in a fair comparative assessment of the chosen PAG/PAT boundaries between the automated and manual reconstructions, but an assumed one in orientational space. Nevertheless, the transformation microstructure, automated reconstruction, and likelihood map are given below in Figure 6.12 along with the manual reconstruction. Regularization parameters for this reconstruction were  $\lambda^{IP} = 3$ ;  $\beta^{OP} = 0$ ;  $\lambda^{OP} = 0.5$ ; and  $\beta^{OP} = 0$ .

The automated and manual reconstructions seem to match up nicely in Figure 6.12, with pretty much a one-to-one correspondence in terms of the parent grains. Although the parent austenite grain boundaries are relatively conspicuous within the transformation microstructure, the twin-transformed regions are far more ambiguous as to whether they are continuations of parent-transformed variants or standalone twin variants. Therefore, the algorithm’s ability to capture twins is on full display

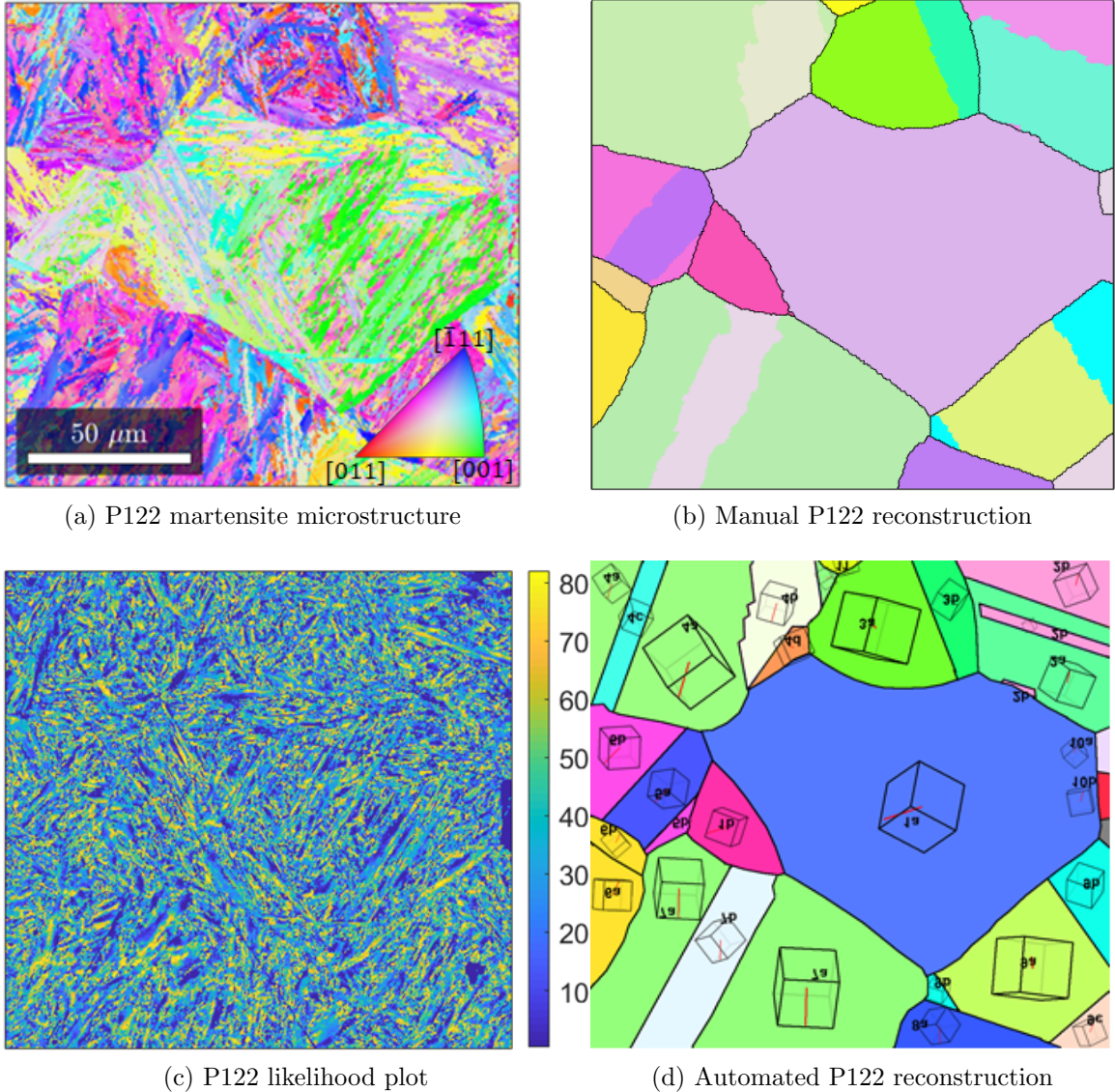


Figure 6.12: The post-transformation martensite microstructure for the P122 12 wt%Cr steel sample (top left) along with the automated reconstruction (top right), automated likelihood map (bottom left) and manual reconstruction (bottom right) for automated reconstruction.

as five prominently sized combinations of parent and twinned grains are easily distinguished and compare directly with the manual results. The main discrepancies between the two reconstructions are essentially only isolated to the upper left grain, where two additional twins are located in the manual reconstruction but not in the automated one, and the upper right grain, where the twin protrudes through the PAG structure a second and third time. Note, however, that the latter portion was almost picked up by the automated technique.

The likelihood plot related to the automated reconstruction shows a strong correlation between the martensite and generated austenite microstructures. A couple small regions of low-likelihood do exist, but the ones hugging the edges could be related to the truncation of the data set. These regions are considered separate grains in the manual reconstruction, but are so small and inconspicuous that they can be ignored. If comparing the “missed twins” in the automated reconstruction in terms of the likelihood map, this fact becomes ambiguous. Therefore, it remains unclear whether these are missed twins by the automated technique. Additionally, the small region at the lower right, which looks almost like a small missed grain, was determined to be a location of poor indexing after closer analysis. Overall, the algorithm took  $\sim 20$  minutes to perform the entire reconstruction for a data set consisting of 106590 indexed data points.

The last reconstruction was performed on a 22V columnar fusion zone weldment sample. The 22V (2.25Cr-1Mo-0.25V) low-alloy steel submerged arc welds were produced using AC 50 % balanced polarity. Weldments were prepared using a V-groove joint geometry, on 24.5mm thick A36 steel base plate. 17 passes were required to fill the joint, using a  $204^{\circ}C$  preheat temperature and  $250^{\circ}C$  interpass temperature.

The fusion zone in multipass welds contains two distinct regions; a columnar region of unrefined weld metal which solidifies upon deposition and is not reheated, and a refined region which is reheated above A<sub>1</sub> during subsequent weld passes resulting in a refined grain size. The specimen shown in Figure 6.13 was extracted from the unrefined weld metal region of a 22V multipass weld. After welding, weldments were post-weld heat treated (PWHT) at 710°C for 8 hours.

A reconstruction was performed on this sample due to the enhanced variability introduced in the  $\gamma \rightarrow \alpha'$  transformation. Welding is one of the most dynamic processing conditions a metal undergoes during processing. Rapid heating, cooling, and solidification create large residual stress gradients in steel weldments. The complicated thermal and residual stress gradients in the fusion zone produced by multipass arc welding create an excellent case study to test the efficacy of the algorithm, when faced with martensite microstructures that underwent transient processing conditions. The optimized regularization parameters for this reconstruction were  $\lambda^{IP} = 8$ ;  $\beta^{OP} = 7$ ;  $\lambda^{OP} = 0.2$ ; and  $\beta^{OP} = 2$ . The results are presented below in Figure 6.13 along with the corresponding likelihood map.

The martensite microstructure shows a considerable amount of variance throughout, which makes it difficult to determine where some of the PAG boundaries lie. However, the algorithm seems to do a sufficient job at capturing a majority of the PAGs. The morphologies reveal the columnar structure expected for this sample, and the related likelihood map shows a relatively strong correspondence between the chosen austenite orientations and the transformation martensite. There are regions that are ambiguous as to the efficacy of the reconstruction. Consider the long and thin, pink twin in the reconstruction. The related likelihood region is very low, but

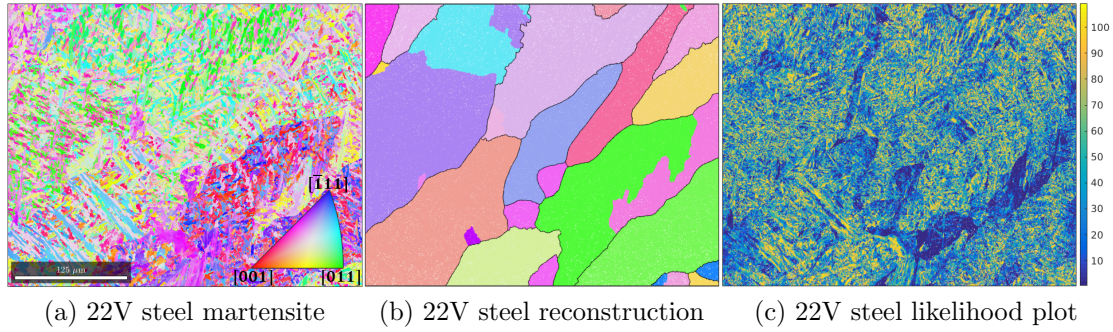


Figure 6.13: Transformation microstructure (left), austenite reconstruction (middle), and likelihood map (right) for a 22V-low alloy weldment steel

inspection of the martensite microstructure reveals a considerable disparity between the martensite orientations in this region and surrounding ones. This suggests that a twin/grain does exist here, but the chosen orientation is off. Conversely, it also seems like the twin should maybe split a single grain in half instead of lying at the interface of two similarly orientated grains. The data set consisted of 867,048 data points and took about 55 minutes to complete.

## 6.5 Discussion

The results suggest that the graph cutting algorithm is an effective approach to austenite reconstructions due to its inherent clustering nature. The computational reconstructions show a strong correlation to the optically etched sample of the same material and locality. The overarching PAG boundary geometries (ignoring twins) for both experimental and computational results are almost identical to the naked eye. Although all graph cutting ASTM grain size numbers are higher than that calculated for the optically etched sample, this could be for a variety of reasons. For one, there

exist several remnants of grains at the border of the image that are unambiguously captured by the reconstruction algorithm but seem blended into surrounded grains in the optical etch. This would indubitably increase the computational grain size number by including these as independent “grains” when in reality they are just truncated portions of grains extended outside of the data set. Furthermore, the grain calculation methodology implemented through MTEX [7], although robust, can sometimes draw boundaries faux grains-within-grains or around twins even when they have been merged together with the parent grain. Finally, the experimental method is not 100% accurate and can combine adjacent grains into a single entity if the etchant remained thin in that area. Therefore, a visual comparison between the the results and the corresponding likelihood maps should be most prominently regarded in the assessment of the reconstruction results.

Although the algorithm can be run for three separate reconstruction spaces; martensite, austenite, and mixed, the former does a poor job at identifying twins and would require far too much time to reconstruct the full austenite microstructure. As can be seen from Figure 6.2b, it appears that a large number of twins were not successfully identified within the cut PAG boundaries. When comparing back to the mixed space reconstruction, a significant number of twins are missed when using the pure martensite space method. The algorithm was also unable to assign an austenite orientation to a significant portion of the microstructure (16%). This was considerably worse than all of the other methods, including the KS-reconstruction. It is unclear why this was the case, as the mixed space algorithm uses the same methodology to initially define the PAG, and the microstructure was almost 100% austenite. It is assumed that towards the end of the mixed-space reconstruction, the grains become

more difficult to define based on noise or size. However, truncating the graph forces several attempts at identifying a sufficient misorientation distribution on the same general location. Considerable time spent on a single region therefore allows for more poor choices to be made before a sufficiently defined martensite orientation can be chosen to produce a reasonable misorientation profile. Overall, the pure martensite space method is far worse than the austenite and mixed space reconstructions, and therefore is not recommended when performing reconstructions.

The austenite space algorithm is typically faster depending on how large the data set is and how small of a gridification is needed to adequately capture the pre-transformation microstructure. It can also discover a significant number of twins and produces reasonable austenite microstructures. However, the mechanism requires more user-input and typically results in a poorer reconstruction when compared with the mixed-space methodology, even as the number of iterations increase. For fewer iterations, the technique misses several of the smaller PAGs and over-extends larger PAG boundaries to swallow up adjacent twins and refined PAGs. This may be the result of smaller PAGs that were constrained by larger ones in the austenite phase and severely limited in size. Upon cooling and subsequent transformation to the martensite phase field, these PAGs may have contained only one or two martensite variants, making a strong, representative  $g_\gamma^i$  highly difficult to attain. As the number of iterations increase, the results become enhanced and several more of these low likelihood regions found in Figure 6.4 improve, but at the cost of computational speed. This can be seen in the results provided in Table 6.1 for all reconstructions presented for the AF9628 data set using the experimental OR. Judging by the corresponding likelihood maps, the technique then reaches a plateau at the 1042 iteration mark,

where the overall reconstruction time is almost equivalent to mixed space results but the reconstruction is worse. Increasing the number of iterations by  $\sim 40\%$  offers virtually no improvement to the reconstruction, suggesting that the technique hits its peak with several missing twins and smaller PAGs.

The application of the pure-space algorithms also requires+ an analysis of the EBSD data set and subsequent determination of the grid size. If the gridification is too small, the results will take a longer amount of time than the mixed space, but if it is too large, the user runs the risk of missing smaller grains and generating an incomplete reconstruction. A final comparison to the mixed space results show that, although it is typically a bit slower than the austenite space technique, it does a more thorough job at searching through the transformation microstructure for the most likely fits. Additionally, since the pure-space algorithms cannot truncate the data set without missing a significant number of twins and smaller grains, as the data sets grow larger and larger, the overall reconstruction time will swing in favor of the mixed space algorithm. Therefore, for the most accurate and physically consistent austenite reconstructions, both the martensite misorientation profile and a probabilistic assignment of austenite orientations must be taken into consideration. This effectively lumps the martensite orientations into two probabilistically dictated categories; one based on martensite misorientations and the other on the orientational transformation into austenite. If a region produces a set of data points that are favorable in both categories, there is a high chance those orientations will be clustered together; if the region is unfavorable in both, it is likely it will remain uncut. The difficulty exists when the region is inconsistent, stemming from a variety of reasons that have already been mentioned, from the nature and uncertainty ingrained in the transformation to

the possibility of a vast number of formed martensite variants based on the number of PAGs within a sample. Reflection on the likelihood maps associated with each reconstruction and presented throughout the manuscript expound upon this notion.

Consider Figure 6.5, which displays the results of the mixed space reconstruction for the AF9628 sample. Even in well-defined austenite grains, where observations of the EBSD-indexed martensite show clear, distinguishable PAG boundaries, comparison to the likelihood map in Figure 6.5c show small regions of low likelihood confined within these boundaries. This brings forth the inherent noise associated with the transformation, which produces deviations in the presumed martensite variants that render it difficult to accurately assess the crystallography of these regions. A point-to-point technique would fall apart at these regions by likely assuming these indicate the existence of a new PAG boundary. Subsequent “marching” would then retreat back to the initial guess austenite grain, either producing a physically unrealistic grain that floats within a larger grain or classifying all three regions as three separate grains. Since these low likelihood regions are typically surrounded by high likelihood regions, the graph cutting technique finds them too energetically costly to cut through the high likelihood portion to get to the low likelihood portion, and subsequently clusters them together and classifies this region as noise rather than a separate grain.

Comparison of the reconstructed grains with retained austenite against the likelihood map, such as presented in the Fe-30 at. % Ni case, can also be used to determine regions where the algorithm fails to adequately capture the grain. This is evident in the parent-twin system at the upper right portion of Figure 6.6b, where the lighter-colored parent grain extends too far into the darker twin. Analysis of the transformation microstructure in Figure 6.6a shows a large, single variant within

this region. This suggests that the variant is shared between both parent and twin, and the ambiguity results in equal likelihood of assignment between parent and twin. When observing the transformation microstructure, it is clear that only a few variants exist within each reconstructed austenite grain due both to the plate-like morphology and their significant size. What is also clear is that the algorithm does a sufficient job at locating the PAGs and PATs when comparing the orientation color mapping of the retained austenite with the reconstructed grains. This suggests that the algorithm can effectively handle a limited number of variants within PAGs. Since diminishing the PAG sizes in the austenitic phase field can improve certain mechanical properties, the ability for the algorithm to capture minuscule PAG sizes containing limited number of variants could significantly assist optimization of processing conditions. However, more validation is required before it could be definitively pronounced that the algorithm can handle small PAGs with limited numbers of variants.

The versatility of the graph cutting technique with respect to spatial correspondence in the mixed algorithm case is highlighted with the methodology of the approach. The ability to use the martensite space to produce a rough estimate of a PAG based on the misorientation profile and then subsequently truncate into only nodes contained within said PAG proves both beneficial. Truncating the graph into fewer nodes will increase computational time exponentially and allow for subsequent cuts to be performed almost instantaneously. The martensite space helps prevent two PAGs that are similarly oriented but not adjacent to each other from being assigned to the same PAG while the austenite space helps trim the edges of superfluous boundaries that have leaked into surrounding grains. This is also evident by the algorithms ability to handle the random locality of martensite variants in the binary

ferrous alloy with relative ease. It could be assumed that reconstructions on microstructures with more retained austenite, or mixtures of austenite and other phases such as ferrite, could also be performed with confidence.

When excessive noise was systematically added to the EBSD-indexed transformation microstructure, the graph cutting algorithm showed remarkable resilience. Even at a mis-indexing fraction of 0.75, a majority of the reconstructed grains were similar in appearance to the same unaltered data set in grain geometry, orientation, and even the existence of twins. The likelihood maps were then still able to adequately resolve a likely microstructure, detailing where notable features were either missed or incorrectly assigned to other grains. This again highlights the need for a clustering-type approaches in terms of austenite reconstruction algorithms. Since the graph cutting algorithm is inherently good at handling noise, it does a good job of ignoring the misindexed orientations and identifying similar transformation variants. Simply increasing the regularization parameters deters the algorithm from cutting through an edge connected to a misindexed point, instead requiring a clear crystallographic disparity (i.e. grain boundary) to effectively render an edge cuttable.

With regards to twin identification, which has long been a notable difficulty in austenite reconstruction algorithms, it was found that the algorithm does a good job at capturing likely twins hidden within PAGs. This can be attributed to the algorithms assessment of both martensite and austenite space. Since shared variants between parent and twin would most likely be indistinguishable through EBSD limitations, consideration of only martensite misorientations would be unable to unambiguously define twins. Therefore, rotating the most likely parent austenite orientation to account for the four  $\langle 111 \rangle$   $60^\circ$  fcc- annealing twin orientations and consequently

performing cuts does a much better job at handling twins. As can be seen from the likelihood plots specific to the parent and twin system in Figure 6.10, the given likelihood maps can adequately characterize a set of martensitic variants as having been transformed from either the PAG or the PAT in a probabilistic fashion. What remains ambiguous is the identification of shared variants that stretch across the parent-twin interface, as clear jagged boundaries can be found to separate a number of parent-twin systems. However, a more rigorous crystallographic analysis would be required to determine where these variants may reside and therefore exceeds the scope of this paper.

Additional reconstructions were then performed on three other EBSD data sets. The first one corresponded to a low-C steel with an OR similar to KS, which produced respectable results, although the likelihood maps indicate there could be an issue with the classification of the twin boundaries. Portions of these regions exhibit a reduced likelihood when compared to the rest of the plot, most notably regions that were denominated as parent grains (grains colored in red and purple). This could represent ambiguous regions of shared variants where the classification could be probabilistically equivalent when considering these variants as having transformed from the parent or twin. Conversely, this issue could be due to one of the minor pitfalls with mixed algorithm methodology. For a parent-twin system, the algorithm defines the parent grain orientation as the modal orientation computed from the local ODF of clustered, transformed martensite regions. Therefore, if the twinned region is larger than the parent region, the twinned grain will be erroneously considered as the parent grain and vice versa. If additional twins were generated within the actual parent, they

will not be uniquely identified and will instead be classified as either a portion of the identified parent or twin.

Another reconstruction was performed on an ASTM P122 12 wt%Cr tempered martensitic steel with an OR that should fall between KS and NW. The resultant austenitic microstructure seemed authentic, and the corresponding likelihood plot supported this supposition. The algorithm was again able to capture several existing annealing twins embedded within larger PAGs. Additionally, the arrangement of the transformation martensite variants made it relatively easy to identify the pre-transformation PAG boundaries within the sample. This allowed for the automated results to be compared to a manual reconstruction performed by Dr. Yardley . Although not a ground truth, it offers insight into the human eye's interpretation of a PAG. More specifically, a direct comparison can be made between the combined efforts of human intuition and consequent crystallographic analysis with the automated methodology applied by the reconstruction algorithm. The striking similarity between the microstructures therefore suggests that the algorithm can do at least as well as what an expert in steel metallurgy can ocularly and crystallographically define as the prior austenite microstructure.

The last reconstruction was performed on a 22V (2.25Cr-1Mo-0.25V) low-alloy arc weld steel. The dynamic processing conditions produced a martensitic microstructure that was inundated with noise and variability, resultant from the transient processing conditions and the residual stress gradients. The majority of the reconstruction shows a strong agreement with the observed martensite orientations, but low-likelihood regions still exist throughout. It is possible that the chosen half-width was too low to fully capture the noise and uncertainty within the transformation due to the dynamic

processing conditions. It is worth noting that the determination of the OR was extremely difficult for this reconstruction, and an accurate representation may not have been fully captured. It could also be possible that the OR varies significantly across the same microstructure, which is why only a specific region of the likelihood map seems inconsistent. Therefore, more analysis would be required to determine whether what is causing the ambiguity in the microstructure, and whether the poor likelihood regions are missed PAGs/PATs or simply incorrect choices for austenite orientations.

The summation of the results indicate a robustness to the code, which can effectively handle martensitic samples that range across the entire spectrum of ORs. Additionally, since the Fe-30 at.% Ni, low-C, and P122 data sets are considerably smaller than the AF9628 sample, it is clear that the graph cutting algorithm scales considerably with both the size of the data set and the number of latent PAGs within the transformed martensite. Consider the low-C sample and the P122 sample, whose data sets are similar in size. The former only contained two (large) grains with three twins and took only seven minutes to complete, whereas the latter took about 20 minutes but contained eight total grains and six additional twins. The existence of more PAGs that are smaller in scope results in less of a grid truncation per cut, which extends the total reconstruction time. Since the AF9628 steel sample contained almost 2 million points and numerous additional grains and twins, it makes sense that the computational efficiency suffers as a result. This could potentially be rectified through parallelization processing of the algorithm up to a certain point to perform multiple cuts at the same time, although it would further complicate the implementation of the code.

## 6.6 Conclusion

The graph cutting technique was effectively applied to the reconstruction of the pre-transformation austenite microstructure from EBSD-indexed post-transformation martensite for an AF9628 steel sample. An automated measurement of the orientation relationship was applied for a more accurate representation of the transformation. It is evident that using the KS orientation relationship for the reconstruction basis resulted in far too many PAGs and physically inconsistent PAG boundaries that developed within other PAGs without coherency to the adjoining boundaries. Therefore, determination of the actual OR is crucial in optimizing the reconstruction results. A combination of martensite misorientation analysis and probabilistic comparisons between martensite variants and possible austenite orientations were utilized in a Bayesian implementation in order to perform the reconstruction. Comparison to an optically etched micrograph of the same surface area showed strong correlations to the reconstruction in both prior austenite grain size and geometry. Even with excessive noise added to the EBSD data, the algorithm produced adequate results that resemble the reconstructions on unaltered data sets. Reconstruction of a binary ferrous alloy also provided reasonable validation to the accuracy of the technique in the form of orientational comparisons. Since a substantial fraction of retained austenite was scattered throughout the martensitic microstructure, an IPF map could be used to plot both retained austenitic pockets encompassed by reconstructed grains. What resulted was a strong correlation between the retained austenite and the reconstructed grains, suggesting that the technique is not only reasonably accurate with regards to the PAG morphology, but also in terms of the proposed PAG orientations.

Additionally, the technique did a good job of capturing twins within the transformation microstructure. Overall, the technique seems to do an effective job at austenite reconstruction from martensitic steels.

# **Chapter 7: Application of Graph Cutting to Probabilistic Segmentation of Martensitic Packet Boundaries and Analysis of Shared Variants Across Parent-Twin Interfaces**

This chapter was written for the thesis using a similar methodology from the austenite reconstruction chapter. Therefore, the notation and references to figures are directly related to Chapter 6.

## **7.1 Introduction**

Since  $\gamma \rightarrow \alpha'$  transformation has been covered extensively in previous chapters, it will be passed over here in favor of a brief description of the underlying morphology of lath martensite, which is influenced by the size and morphology of the underlying prior austenite phase field. A single prior austenite grain transforms to up to 24 variants through a composition and cooling rate specific orientation relationship. Although seemingly random, a relationship exists between transformed laths that contribute to the mechanical properties of the transformation microstructure. Structurally, a sub-block consists of a single lath, which pairs with another similarly orientated lath creating a low-angle boundary at the interface. These pairs of sub-blocks compose a single block, which are connected to two other blocks through a shared habit plane. Blocks cluster together in triads to compose a single packet, and the boundaries

related to both blocks and packets serve as barriers to dislocation motion in steels [61, 84, 85, 101, 112, 113].

In general, the size of packet boundaries increases with PAG diameters, whereas block boundary widths tend to increase linearly with PAG size up to about  $200\mu m$ , at which point the relationship becomes stagnant and block widths cease growing [113]. This leads to a Hall-Petch relationship [62, 128], where increasing packet size results in decreasing yield strength and toughness [113, 120, 121, 181]. Additionally, since dislocations cannot propagate through block and packet boundaries, these boundaries also serve as hindrances to crack propagation in martensitic steels [63, 79, 165]. The effect of sub-block boundaries is typically considered either insignificant or inconclusive, with some suggesting that sub-block boundaries have no effect on strengthening [139] while others claiming increasing numbers of block sub-block boundaries result in increased strength and fracture toughness [43]. Since martensite is ubiquitously found in industrial applications of high-strength steels, effective identification and segmentation of packet boundaries within transformed PAGs can result in preemptive measures to optimize the performance of processed steel.

## 7.2 Methodology

The graph cutting technique was also applied to the segmentation of martensite packet boundaries within individual prior austenite grains. A complete description of the graph cutting technique was provided in Chapter 3, and the implementation with regards to packet segmentation was similar to that presented in the Chapter 6 on prior austenite reconstruction. Since up to 24 martensite variants exist within a single PAG, the variant ordering sequence described in Chapter 2 is used. This effectively

groups the variants into corresponding blocks and packets, so consecutive pairs of variants,  $\mathbf{V}_1$  and  $\mathbf{V}_2$ , compose blocks,  $\mathbf{B}_i$ , which are clustered together into triads to form packets, all of which are dictated by the experimental OR. The establishment of the abovementioned variant ordering consequently allows for a similar correspondence with regards to misorientations between PAG-transformed variants.

As seen in Chapter 4, out of the possible 276 unique interactions between the 24 variants, there exist only 16 distinct misorientations from untwinned PAG variants. The abovementioned labeling can then be used to classify misorientations as either sub-block, block, or packet boundaries (either from intra-parent, parent-twin, or twin-twin interfaces). Following the same presentation, a misorientation labeled as  $\Delta g_0$  represents an identity misorientation;  $\Delta g_1$  corresponds to a sub-block boundary;  $\Delta g_{2 \rightarrow 4}$  represent block boundaries; and  $\Delta g_{5 \rightarrow 16}$  are packet boundaries. Any misorientations denoted  $\Delta g_{17+}$  represent packet boundaries which require at least one of the variants having transformed from a PAT.

In order to perform the segmentation of the packet boundaries, the graph had to first be defined in terms of the reconstructed microstructure. Recall how, in Chapter 6, the cut corresponding to a parent-twin system is denoted  $\mathcal{C}_\gamma$ . This notation will be continued within this chapter, such that a desired PAG selected with a well-defined austenite orientation,  $g_\gamma^i$ , consequently serves as the graph,  $\mathcal{G}(\mathcal{C}_\gamma) = \langle \mathcal{V}(\mathcal{C}_\gamma), \mathcal{E}(\mathcal{C}_\gamma) \rangle$ . Equivalent to the pure-space reconstruction methodology, the graph composed of the PAG consists of two separate grids,  $g_1$  and  $g_2$ , each composed of nodes representing the original martensitic data points. This allows for the effective distinction of

a desired packet from the three other possible ones. All martensite orientations confined within the cut grain boundary,  $G_{\alpha'}(\mathcal{C}_\gamma)$ , are then isolated as the corresponding vertices, or nodes.

In-plane weights are calculated in a manner similar to that used for the austenite reconstruction case in Chapter 6, where the misorientations between adjacent points  $v^{(i)}$  and  $v^{(j)}$  are computed and the entire distributions of misorientations can be denoted  $\Delta G_{\alpha'}(\mathcal{C}_\gamma)$ . However, instead of convolving the martensite orientations with all 228 theoretical intra-parent misorientations that result from the intersections of the 120 unique parent and twin-transformed variants, only the intra-packet misorientations,  $\Delta g_0 \rightarrow \Delta g_4$ , are considered. The same halfwidth value used to reconstruct the austenite microstructure,  $\kappa = 1.67^\circ$ , was also used to construct the block-based misorientation distribution function,  $f(\Delta G_{\alpha'}(\mathcal{C}_\gamma)^{\Delta g_0 \rightarrow \Delta g_4})$ . A probabilistic relationship between the block-based MODF and the corresponding misorientations represent the in-plane weights, shown below in Equation 7.1:

$$w^{IP}(v^{(i)}, v^{(j)}) = \lambda^{IP} f(\Delta G_{\alpha'}(\mathcal{C}_\gamma) | f(\Delta G_{\alpha'}(\mathcal{C}_\gamma)^{\Delta g_0 \rightarrow \Delta g_4})) \quad (7.1)$$

This effectively represents the likelihood that neighboring points are being separated by a sub-block or block boundary, which would indicate variant interfaces confined within the same packet. The regularization parameter,  $\lambda$ , is similar to that described in Chapter 6 with the superscript of “IP” denoting their association to the in-plane weights. However, the parameter  $\beta$  has been omitted from both in-plane and out-of-plane packet segmentations because it tended to either over-regularize the weights or produce no effect. The weighting system allows for the assignment of the in-plane weights with respect to adjacent misorientations related to sub-block and

block boundaries facilitates the clustering of nodes into groups of the same packet rather than the entire PAG, which ultimately favors cuts to bisect adjacent data points that are representative of packet boundaries.

In order to calculate the out-of-plane weights, four separate iterations are performed that isolate a specific set of packet variants from the remaining three sets. Consider how a set of six variants are associated with a given packet. For the case of the first iteration, this leaves us with a subset of six variants composing packet #1 and a subset of 18 variants composing packets #24. However, these theoretical variants have an assigned prior austenite orientation coincident with the reference frame (Euler angles of  $0^\circ$ ). They must then be rotated by the assigned austenite orientation, which crystallographically aligns the theoretical variant orientations with the actual transformed martensitic orientations. These rotated, packet-specific variants can be denoted as  $\mathbf{P}_i$  and  $\mathbf{P}_j$ , respectively.

By convolving the rotated variants with a kernel halfwidth of  $\kappa = 1.67^\circ$  and the OR, two separate orientation distribution functions (ODFs) are constructed that correspond to either the single, distinguished packet,  $f(\mathbf{P}_i(\Xi, \kappa))$ , or the remaining packets,  $f(\mathbf{P}_j(\Xi, \kappa))$ . The implementation of the dual-grid system is crucial here in establishing the two sets of out-of-plane weights, which are used to weight the nodes based on the likelihood they came from a certain packet. Therefore, the second set of out-of-plane weights connecting  $g_2 \rightarrow t$  represent the likelihood that the PAG-transformed martensite orientations are related to the specific set of packet variants, denoted  $f(G_{\alpha'}(\mathcal{C}_\gamma)|f(\mathbf{P}_i(\Xi, \kappa)))$ , shown below in Equation 7.2:

$$w^{g_2 \rightarrow t}(v^{(i)}, v^{(j)}) = \lambda^{OP} f(G_{\alpha'}(\mathcal{C}_\gamma)|f(\mathbf{P}_i(\Xi, \kappa))) \quad (7.2)$$

Here, the superscript of “OP” designates these as remaining constant across both sets of out-of-plane weights ( $s \rightarrow g_1$  and  $g_2 \rightarrow t$ ). Additionally, the first set of out-of-plane weights are set up in a similar fashion and represent the likelihood that the PAG-transformed martensite variants are related to the remaining three packets. The cut then serves to segment martensite orientations as being contained as a part of the first packet. After the first iteration is performed, the subsets of packet-based variants are altered such that  $\mathbf{P}_i$  now relates to packet #2 and  $\mathbf{P}_j$  is related to packets #1, 3, and 4. Two more subsequent iterations are performed to cycle through each packet, leaving each martensite node with four individual likelihood values related to each respective packet designation. Each data point is then assigned to a specific packet by taking the maximum of the four respective likelihood values.

However, poorly indexed data points and those exhibiting substantial scatter will have no likelihood favoring any of the packets and therefore will not be assigned to any packet. If a large cluster of non-packet assignments exist, these are likely indicative of sections of martensite orientations having been transformed from a twin, data points that should have been assigned to a neighboring PAG, or other outlying factors such as retained austenite, bainitic packets, surface scratches, etc. Otherwise, a spattering of non-packet assignments consisting of single or few neighboring points are indicative of sparse noise from a misindexed point. Therefore, a secondary denoising cut is performed on only the unassigned points. The procedure remains the same as above except a faux-likelihood is given to a single point based on the average of the likelihoods of surrounding points for each respective packet. This way, larger regions of nodes with a poor likelihood remain unassigned to a packet but the sparser,

inconsistent data points take in the most likely packet based on the nearest neighbor assignments.

## 7.3 Results

The packet segmentations were performed on the large, heart-shaped grain from the ASTM P122 12 wt.% Cr tempered martensitic steel data set reconstructed in Chapter 6 and an adjacent, smaller prior austenite grain using a desktop computer with a 3.40 Gz core processor and 15.6 GB of RAM. Additionally, a parent-twin system was also chosen for segmentation in order to determine the efficacy of the technique in identifying the packets which contain shared variants.

### 7.3.1 Packet Segmentation

The larger PAG was deemed to be twin-less, had a calculated equivalent diameter of  $95.9\mu m$ , and was characterized as having an austenite orientation of  $[\phi_1, \Phi, \phi_2] = [305.0^\circ, 43.7^\circ, 35.1^\circ]$  in Euler angles. Additionally, the regularization parameters for this segmentation were chosen to be  $\lambda^{IP} = 5$ ,  $\lambda^{OP} = 2e^{-1}$ , and  $\beta^{OP} = 0$ . This specific grain was selected because its large size garnered assumptions that all four packets would be identifiable. Additionally, a visual inspection of the PAG-transformed martensite laths shows a pretty clear distinction between the orientation coloring for the majority of the laths. This allows readers to make their own assumptions when determining how reasonable the results are. The graph cut segmentations can be found below in Figure 7.1, where the coloring is chosen to easily distinguish between different packets. Here,  $\mathbf{P}_1$  is colored in red;  $\mathbf{P}_2$  is in light blue;  $\mathbf{P}_3$  takes on the color green; and  $\mathbf{P}_4$  is yellow. All regions colored in black contain indexed nodes that were

unassigned to a given packet in both the initial segmentation and the corresponding denoising cut.

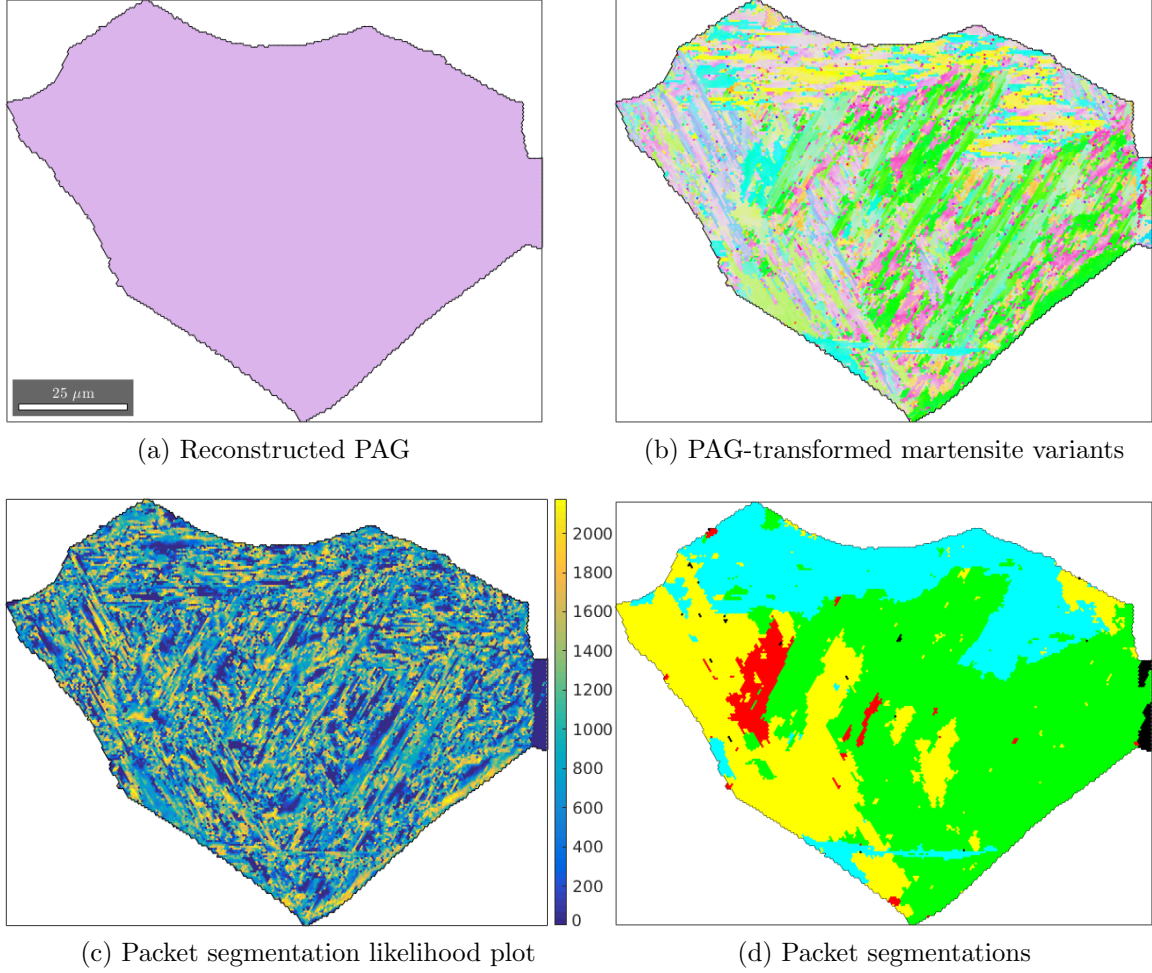


Figure 7.1: The reconstructed large PAG under analysis (top left), corresponding transformed martensite orientations (top right), likelihood plot of packet segmentations including color bar scale (bottom left) and the resultant segmentations for the four distinct packets (bottom right).

As can be seen from Figure 7.1, the chosen packet segmentations appear to make logical sense. If we track the mixture of light blue and yellow variants in Figure

7.1b, they coincide with the cut for  $\mathbf{P}_2$ . Similarly, the set of green and darker pink variants seem to align with the cut for  $\mathbf{P}_3$ . Although the set of light blue variants corresponding to the cut for  $\mathbf{P}_1$  seem like they should be assigned to  $\mathbf{P}_2$  instead, a closer analysis revealed a large misorientation angle between the two sets of similarly colored martensite variants,  $\sim 52^\circ$ . The packet sizes vary widely between the four packets, with  $\mathbf{P}_1$  showing significantly smaller dimensions than the other segmented packets. Conversely,  $\mathbf{P}_3$  exhibited the largest packet size and the most continuous set of connected martensite variants. It is unclear whether the smaller families of martensite variants encompassed by disparate packets represent mis-cuts in the technique or reveal more about the nucleation of packet-specific variants.

The authenticity of the packet segmentation technique was not compared with experimental results as of yet, but a crystallographic analysis can provide approximate verification of the technique. This was achieved by first rotating the 24 theoretical (noiseless) variants by the parent austenite orientation and separating them into their respective sets of six orientations per packet, then extracting the martensite data points assigned to each packet and plotting the corresponding orientations on individual  $\{001\}_\gamma$  pole figures. This helps determine whether the experimentally observed orientations assigned to a specific packet align with their theoretical counterparts.

Additionally, a pole figure of a set of 2000 randomly assigned martensite orientations transformed from the PAG are plotted along with the set of 24 rotated crystallographic variants, the latter of which contain a circular region surrounding them colored with respect to the segmentation colors used in Figure 7.1. For each experimental set of martensite orientations assigned to a given packet, the number of randomly designated orientations were also limited to a maximum of 2000 data

points for clarity, which is the case for every packet segmentation except  $\mathbf{P}_1$ , which only contains 1037 total data points. These plots can be found below in Figure 7.4.

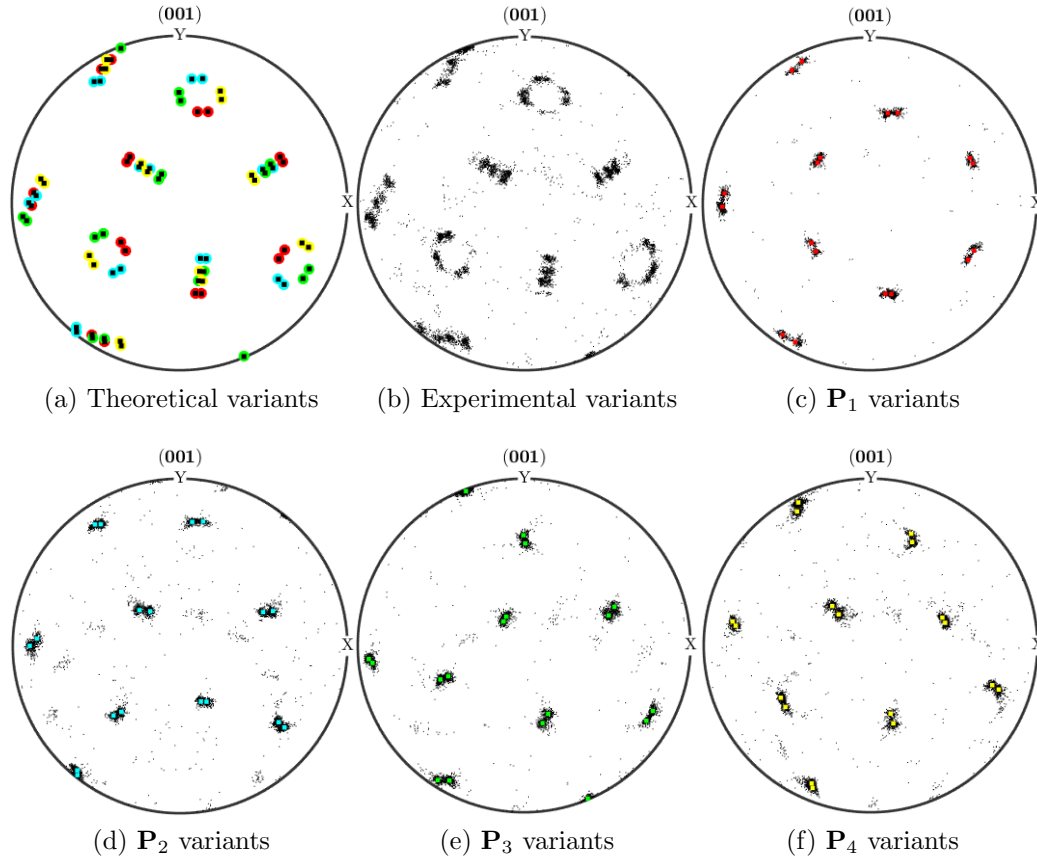


Figure 7.2: Sets of  $\{001\}_{\gamma}$  pole figures displaying the theoretical variants with surrounding colors corresponding to those used for the packet segmentations in Figure 7.1 (top left) with 2000 experimentally observed martensite orientations from same PAG (top middle) and a combination of colored theoretical and experimentally observed, packet-segmented orientations for every packet.

As can be seen from Figure 7.4, the experimentally assigned orientations show a substantial alignment with their theoretical counterparts. It is clear that some noise exists within each packet designation, but these seem to suggest typical noise rather

than mis-assigned data points. The clustered region colored in black in Figure 7.1 represents martensite orientations that were not identified as having come from a packet related to this PAG. This small region could be indicative of shared variants between the parent and a respective twin that was not identified in the reconstruction algorithm. Alternatively, this could simply be a region that was incorrectly clustered into a single PAG when it should have signified a second PAG.

A second segmentation was run on the smaller, adjacent PAG to analyze how the size of the PAG affects the formation of the martensite packets. As such, the chosen grain had an equivalent diameter of  $26.6\mu m$ , significantly smaller than the previously analyzed grain, and an austenite orientation of  $[\phi_1, \Phi, \phi_2] = [107.2^\circ, 19.8^\circ, 233.1^\circ]$ . Additionally, the parameterization was optimized with the following regularization parameters;  $\lambda^{IP} = 11$  and  $\lambda^{OP} = 7e^{-2}$ . The resultant segmentations used the same packet coloring map as that used in Figure 7.1 and can be seen below in Figure 7.3.

The results are similar to those shown for the larger PAG, where two larger packets ( $\mathbf{P}_1$  and  $\mathbf{P}_4$ ) seemingly dominate the transformation space. However, the number of data points within each segmented packet are markedly different than those for the larger PAG. For  $\mathbf{P}_1 \rightarrow \mathbf{P}_4$ , the number of data points within each packet transformed from the larger PAG are: 1037, 7470, 16289 and 8362. This is in stark opposition to the assigned packets transformed from the smaller PAG: 1206, 148, 278 and 923. To visually display this discrepancy,  $\{001\}_\gamma$  pole figures of the largest and smallest packets,  $\mathbf{P}_1$  and  $\mathbf{P}_2$ , were plotted below in Figure 7.4 to highlight this orientational sparsity from the smaller PAG. It was obvious variant selection was evident within  $\mathbf{P}_2$ , therefore these theoretical variants were plotted with disparate markers to designate uniqueness of these six variants.

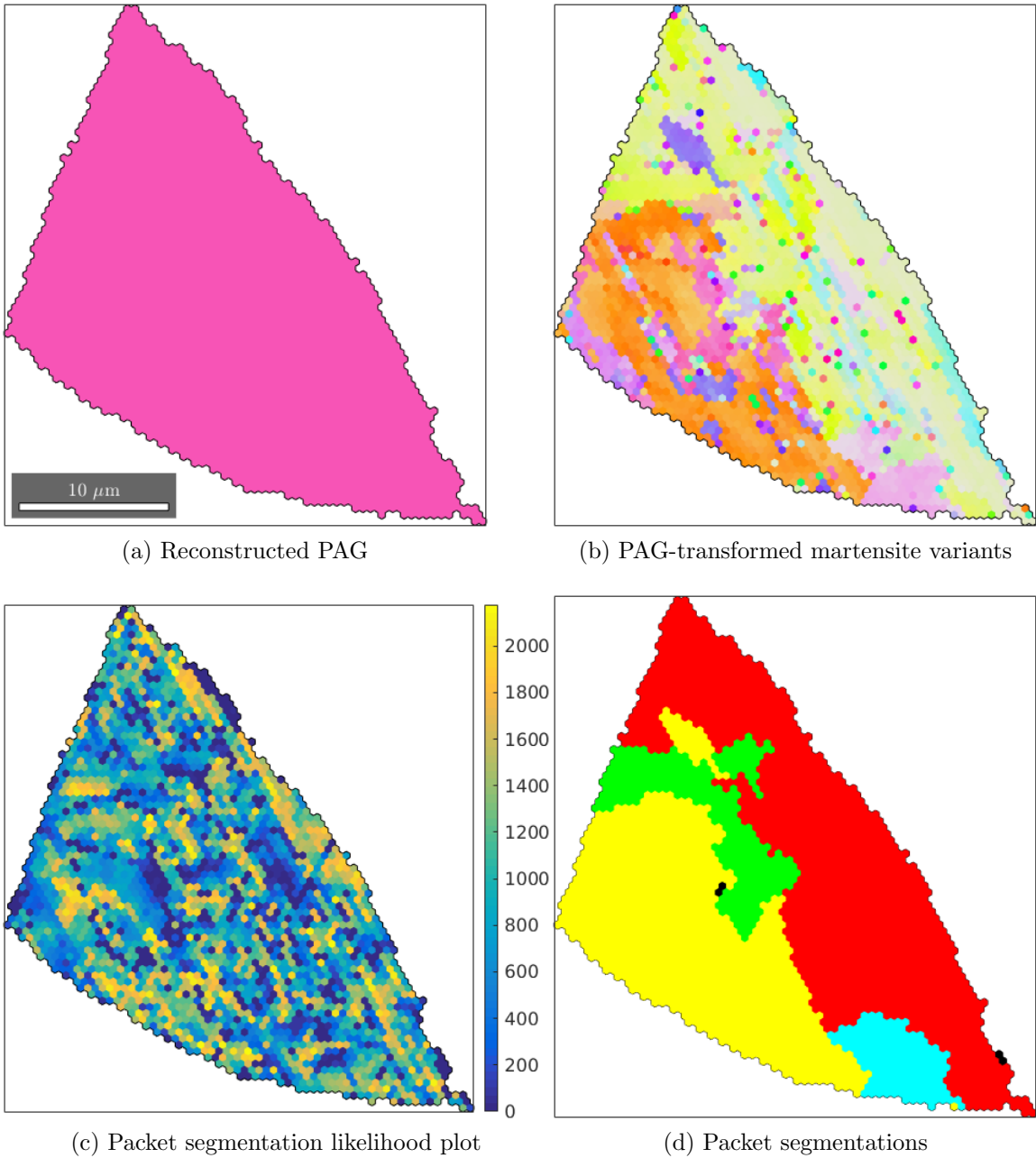


Figure 7.3: Smaller reconstructed PAG (top left), transformation martensite (top right), corresponding likelihood map (bottom left) and four distinct packet segmentations (bottom right).

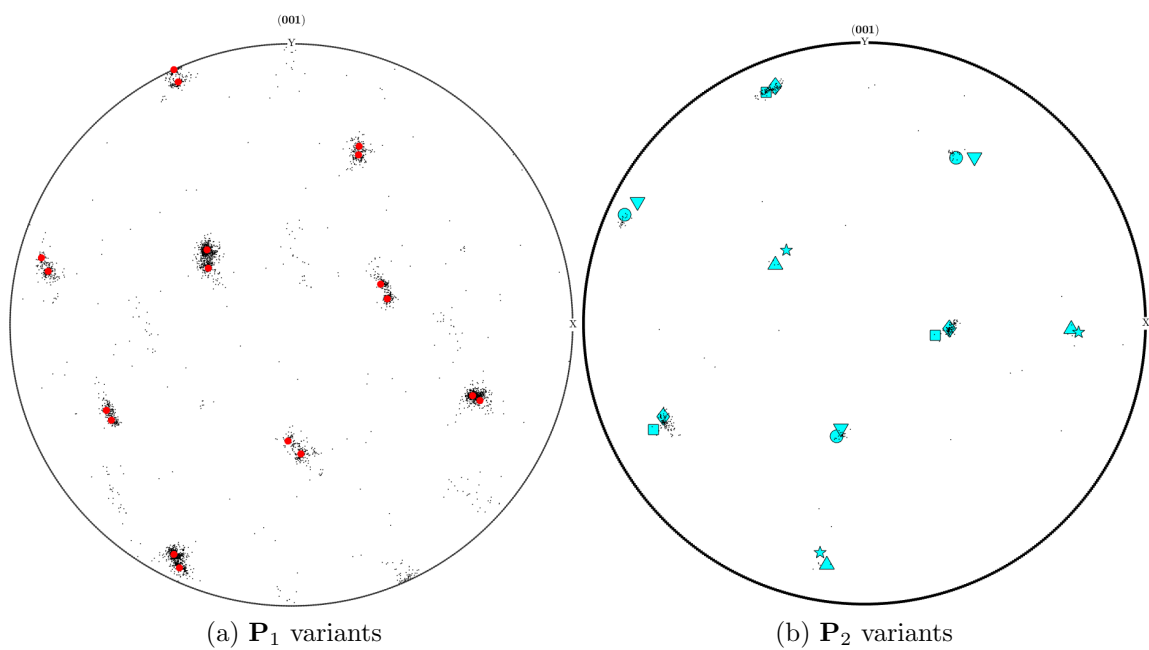


Figure 7.4: The  $\{001\}_\gamma$  pole figures displaying the experimentally observed variants (black) assigned to  $\mathbf{P}_1$  (left) and  $\mathbf{P}_2$  (right), along with their corresponding theoretical counterparts (colored) transformed from the smaller PAG.

From Figure 7.4b, it is clear that only two variants exist within  $\mathbf{P}_2$ :  $\mathbf{V}_7$  (circle) and  $\mathbf{V}_{10}$  (diamond). There is also the slight possibility that  $\mathbf{V}_{11}$  (triangle) transformed as a single sub-block, although it is unclear whether this is coincidental noise or not. Nevertheless, the results indicate that the graph cutting technique can consistently identify packets regardless of how many observed martensite variants relate to a given PAG.

### 7.3.2 Packet Segmentation for Twin Analysis of Shared Variants

As previously mentioned, the martensite variants that were transformed from the parent austenite grain vary from those that are formed from annealing twins. However, there exist variants transformed from both the parent and twin whose interfaces result in an identity misorientation with the KS orientation relationship or exceptionally low angle misorientation boundaries for the experimentally observed ORs [1,2,26,36,105]. In fact, for the same ASTM P122 12 wt.% Cr tempered martensitic steel data set was used for the packet segmentations performed in the preceding section, and in keeping with the same misorientation classification of angle-axis pairings discussed in Chapter 4 and Appendix A, the theoretical misorientation between these similar parent and twin variants was determined to be  $2.08^\circ \langle 112 \rangle$ . With such a minuscule misorientation separating these respective boundaries, it is likely that EBSD-indexing would classify these variants as one and the same. Therefore, based on the packet segmentation technique presented in the previous section, it was determined that it could potentially be used for the analysis of parent-twin systems to potentially identify these shared variants across parent-twin interfaces.

This was achieved by performing the same packet segmentation technique as in the previous section, except rotations of the theoretical martensite variants were performed not only by the parent orientation but also by the twin orientation. This would deliver packet segmentations specific to both the parent and twin grains, and any data points that were grouped into both categories would indicate the presence of shared variants. To perform the analysis, a large parent-twin system was chosen where it was easy to distinguish between the parent and the twin. For this specific parent-twin system, the twin orientation,  $g_{\Sigma 3}^i$ , was achieved through the rotation of  $g_\gamma^i$  about  $60^\circ \{1\bar{1}1\}$ . The reconstructed parent-twin system and corresponding transformation martensite variants are shown below in Figure 7.5.

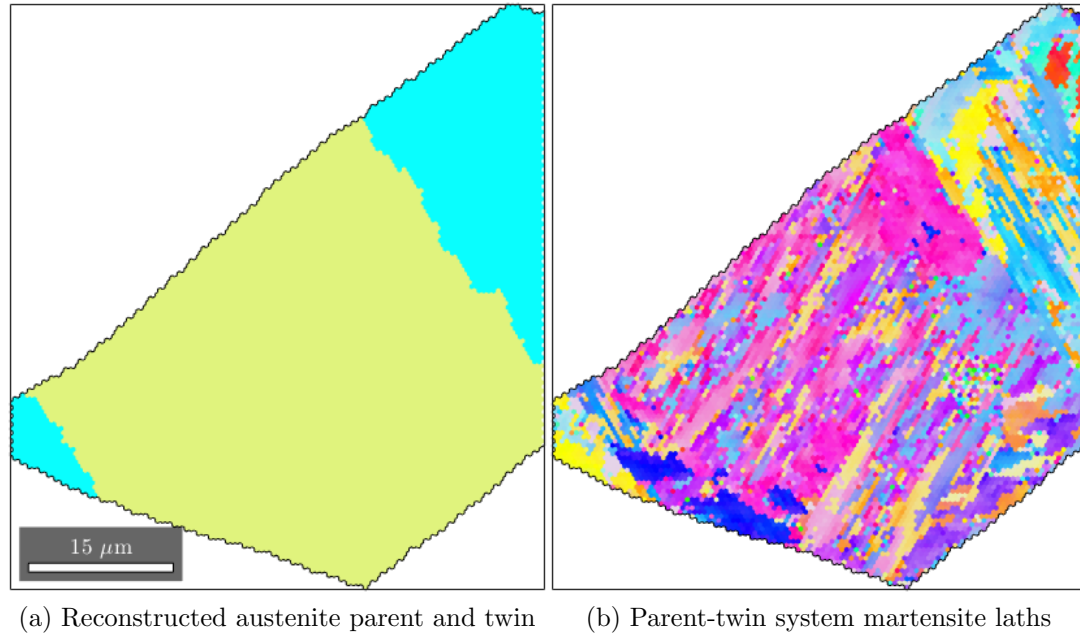


Figure 7.5: The reconstructed parent-twin system (top left) and PAG/PAT transformed martensite laths (top right) used to identify shared variants.

In Euler angles, the parent grain was assigned an austenite orientation of  $[\phi_1, \Phi, \phi_2] = [277.4, 30.2, 80.2]$  and is sandwiched between the twinned grain regions of orientation  $[\phi_1, \Phi, \phi_2] = [250.0, 74.1, 135.4]$ . The classification of which grain is the parent and which is the twin could be incorrect, as the sandwiched portion is typically indicative of a twin that bisected the parent grain. However, in accordance with the reconstruction algorithm, the parent orientation is automatically assigned to the modal austenite orientation extracted from the parent-twin system. Therefore, if the twinned region is larger than the parent region, as is the case in Figure 7.5, the twinned grain will be designated as the parent grain and vice versa. With this specific system, this creates no issue because only a single twin would be formed regardless of which orientation is chosen as the parent, so the designation becomes arbitrary.

For sake of clarity, martensite variants transformed from the parent grain are denoted  $\mathbf{V}(g_\gamma^i)$ , and those transformed from the twin are denoted  $\mathbf{V}(g_{\Sigma 3}^i)$ . Both sets of packet segmentations utilized the same coloring scheme as the previous section, where  $\mathbf{P}_1$  cuts are colored in red;  $\mathbf{P}_2$  is takes on the color of light blue;  $\mathbf{P}_3$  is represented in green; and  $\mathbf{P}_4$  is colored yellow. The resultant segmentations and corresponding likelihood maps are displayed below in Figure 7.6 specific to rotational variants of both the parent and twin austenite orientation.

From Figure 7.6, it is clear that the segmentations on  $\mathbf{V}(g_\gamma^i)$  overlap into the denoted twin region, and segmentations on  $\mathbf{V}(g_{\Sigma 3}^i)$  overlap into the parent region. These cuts, colored in yellow in Figures 7.6a and 7.6c, also share a similar geography and geometry with each other. This would indicate the existence of shared variants within the  $\mathbf{P}_4$  packets for both parent and twin variants, which is consistent with

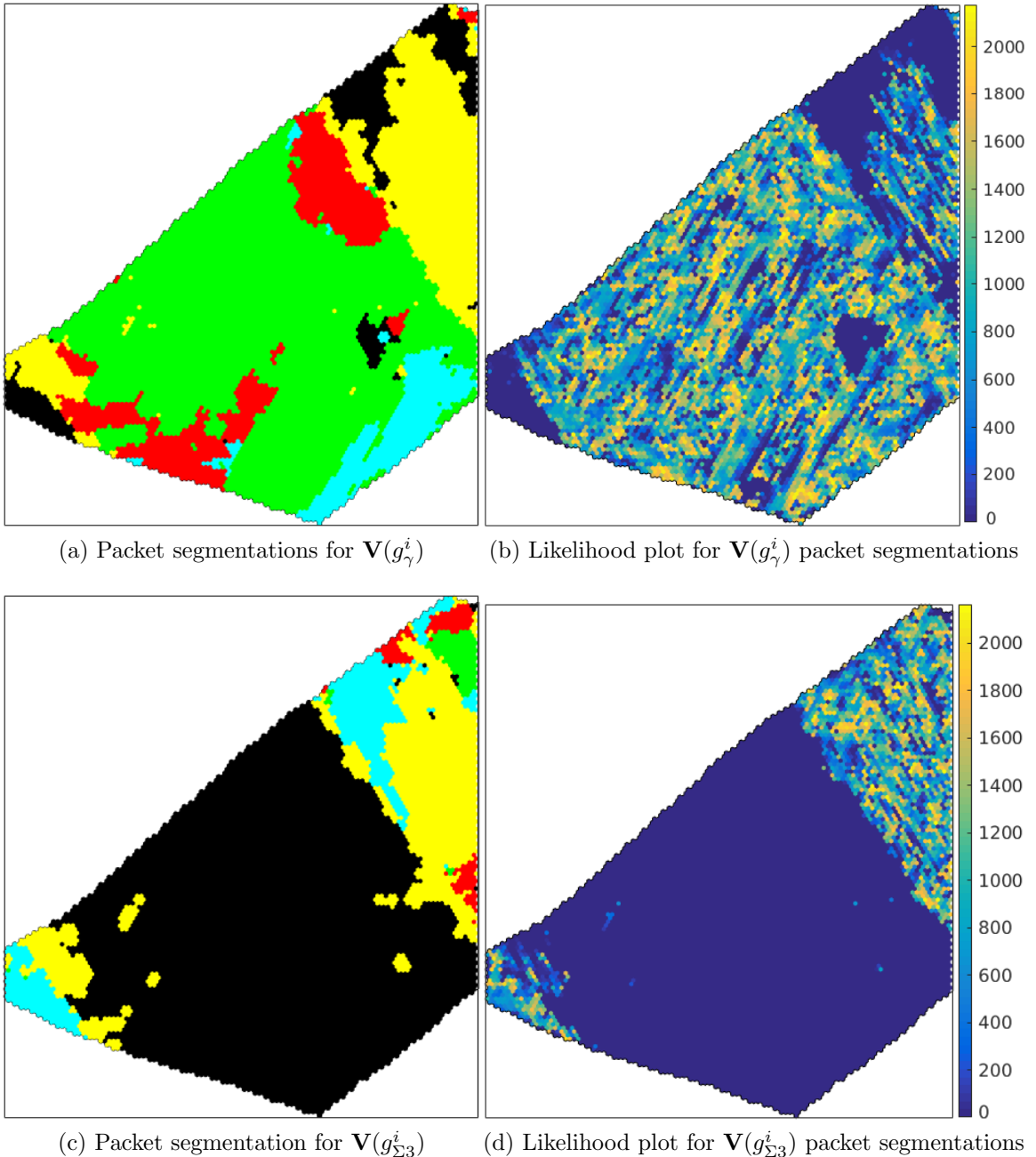


Figure 7.6: The packet segmentations from the parent-twin system defined in Figure 7.5 performed on either  $\mathbf{V}(g_\gamma^i)$  (top left) or  $\mathbf{V}(g_{\Sigma 3}^i)$  (bottom left) with likelihood maps directly adjacent to the segmentations.

the parent- $60^\circ\{\bar{1}\bar{1}1\}$  sets of theoretical variants. Examination of the coincident composition table presented in the Supplemental Section confirms this, where both sets of shared variants exist within the respective  $\mathbf{P}_4$  designations ( $\mathbf{V}_{19 \rightarrow 24}$  for the parent and  $\mathbf{V}_{67 \rightarrow 72}$  for the twin, respectively).

The corresponding likelihood maps also support this notion, most notably in the case of  $\mathbf{V}(g_\gamma^i)$ , where a large portion of the twin is probabilistically favored as having come from the parent-transformed  $\mathbf{P}_4$ . These regions are then surrounded by un-cut regions, where indexed data points are not assigned to any packet, most notably in the case of  $\mathbf{V}(g_{\Sigma 3}^i)$  with respect to the parent orientation. A small clustered region within the parent also contains a clustered non-cut region, but closer inspection of the transformation data set suggested that this was most likely an indexing error during extraction of the data set.

## 7.4 Discussion

The application of the graph cutting technique to the segmentation of packets within transformed PAGs exhibited promising results. Adjusting the in-plane weights to consider variants based on sub-block and block boundary misorientation pairings does an effective job of confining martensite variants within packet boundaries. Subsequent comparisons of the experimentally observed data points to the theoretical variant orientations can extract the similar nodes and classify them accordingly. Although experimental validation was not performed, crystallographic analysis revealed strong correlations between the martensite data points that were assigned to a packet and their theoretical counterparts. The alignment of experimentally segmented orientations with their corresponding variants also serves as validation to the chosen

austenite orientations determined by the reconstruction algorithm from Chapter 6 for the specific grains analyzed. If the chosen PAG orientations were off, the noiseless transformation to the corresponding martensite variant orientations would show no alignment with experimental data.

It was also shown that the packet segmentations remained theoretically verifiable regardless of the size of the reconstructed PAG. Transformed martensite variants were distributed into their respective packets, even if some experimentally observed variants were missing, as was the case with the smaller PAG transformed variants within  $\mathbf{P}_2$ . This further attests to the versatility of the graph cutting technique, where even small groups of data points can be probabilistically clustered into related groups. Refinement of austenitic microstructures will directly correlate with smaller packet sizes, which would be expected to consist of fewer variants. The ability to characterize these packets could further both the optimization of the processing parameters and subsequent analysis on the transformation microstructures. This could effectively lead to a better understanding of how these materials would react under certain loading conditions.

When applying the segmentation technique to a parent-twin austenitic system, it was shown that the  $\mathbf{P}_4$  packets extended across the parent-twin interface, as is expected when parent variants intersect with  $60^\circ \langle \bar{1}\bar{1}1 \rangle$  twin variants. Additionally, these packets shared a similar geometry, which strongly suggests that shared variants exist across the grain boundary separating both the parent and twin. An extension of the packet segmentation technique would be required to actually locate the shared variants from within the segmented packet. However, the ability to adequately perform these segmentations could further the understanding of the formation of these

variants across parent-twin interfaces. Subsequent analysis on a variety of different compositional and morphological steels could help determine whether these attributes affect the formation of these shared variants.

## 7.5 Conclusion

Graph cutting was effectively applied to the segmentation of martensitic packets on the tempered ASTM P122 12 wt.% Cr martensitic steel data set that was reconstructed in Chapter 6. Both a large and small parent austenite grain were extracted and packet segmentations were performed in order to demonstrate the flexibility in the technique with respect to variable packet sizes. Additionally, a parent-twin system was analyzed in order to determine whether the technique could effectively identify the packets and possible locations of shared variants. For the parent segmentations, theoretical validation was performed by crystallographic comparisons of the expected variant orientations for given packets to those clustered into the corresponding segmentations. The alignment of assigned experimental and expected theoretical variants suggests that the technique does an effective job at grouping martensitic variants into their respective packets. As the packet sizes diminished in size, and variant selection took place resulting in the observation of only 2-3 variants, the corresponding packet contained orientations that remained consistent with their theoretical counterparts. Analysis on the parent-twin systems revealed the expected packets as containing the shared variants, and portions of these packets overlapped across the austenitic parent-twin interface. Exact locations of these shared variants were not determined, but a slight modification to the graph cutting technique to account for the the respective orientations and the corresponding misorientation could potentially resolve this.

## Chapter 8: Conclusions and Future Work

### 8.1 Summary of Results

The graph cutting algorithm was effectively applied to a number of inverse problems in materials science with a focus on the characterization of microstructures of ferrous alloys. Problems in image segmentation, microstructural phase/constituent segmentation, and atomic clustering were tackled in a probabilistic fashion. The most pertinent application of the graph cutting algorithm with regards to the thesis was its application to austenite reconstruction from transformation martensite microstructures. An extensive analysis on misorientation profiles of martensite variants transformed from both parent and twin austenitic grains was performed and used to facilitate the reconstruction process. Additionally, the differences in misorientation profiles for ORs specific to compositional steel samples were highlighted. An automated measurement of the orientation relationship in a variety of steel and binary ferrous alloys was then performed and used within the austenite reconstruction algorithm. The application to austenite reconstruction proved fruitful and was validated against an optical etching of the PAG boundaries for the same sample region. The reconstruction was then performed on a variety of samples, and graph cutting was used to segment packet boundaries within single PAGs. Finally, a quick analysis on

the effect of variant sample size on the precision of guessing austenite orientations was performed in relation to the optimization of processing parameters to minimize PAG sizes.

### **8.1.1 Summary of Graph Cutting Implementation to Inverse Problems in Materials Science**

Graph cutting was applied with a basic, Bayesian framework to perform energy-minimized cuts on inverse problems such as image segmentation, microstructure/parent phase segmentation, and atomic clustering of synthetic atomic probe tomography data. The technique proved to be easy to execute yet surprisingly effective in comparison to other, typical methodologies for basic implementations and it is assumed that more comprehensive frameworks would only serve to enhance the effectiveness of the results. The application to image segmentation provided low-noise segmentations for two variable sets of nickel superalloy back scattered electron images. In comparison to other existing techniques, such as the Otsu threshold method [123] or EM/MPM algorithm [39], it was shown that the graph cutting technique does as good or better at segmenting the  $\gamma'$  particles. Segmentation of ferrite, bainite, and martensite from kernal average misorientation and image quality values showed great promise, although a comparison to other techniques could not be completed due to the lack of any existing technique to both quantify and locate the phases/constituents. Validation to experimental results was also not performed, and should be considered in future experiments to analyze the overall performance of the graph cutting technique. Reconstruction of the prior austenite phase from transformation martensite proved effective and was further validated in a subsequent chapter. Locating clusters of atoms dispersed in a background of variable “noise” proved surprisingly effective

with a simple, probabilistic implementation. The ability to consider each atom as a single entity and connect them with surrounding atoms with respect to random spatial indexing prove the graph cutting technique to be especially effective. Comparison to an admittedly basic  $k$ -means [94] approach proved the technique to be vastly superior, although it would enhance the results to compare against more advanced techniques. Overall, the versatility of the approach was shown for a variety of problems, and it is assumed that similar inverse problems could be approached with the graph cutting technique in an effective manner.

### 8.1.2 Summary of the Martensite Analysis of Misorientations Between Martensite Parent and Twin Variants

The effect of orientation relationship and martensite crystal structure were analyzed with respect to the misorientation profile of martensite variant interactions. It was shown the number of misorientations from parent-transformed variants remains unchanged at 16 in total, regardless of OR or crystal structure. However, the misorientations themselves vary to some degree. The introduction of twin-transformed variants adds complexity to the misorientation profile, as experimentally observed (and therefore irrational ORs) produce significantly more unique misorientations in the cubic case. Additionally, it was shown that the KS/NW ORs result in shared variants, whereas the experimental ORs contain small misorientations (which may still be indistinguishable with respect to EBSD data). Tetragonality in the martensite crystal structure would provide unambiguous parent/twin variants, even in the KS and NW cases, but the inability to index it with EBSD makes this a moot fact for now. The presence of  $\Sigma 9$  boundaries produce distinguishable misorientation characteristics; however, the vast number of these misorientations would most likely make

it impossible to uniquely identify the location of these boundaries. Nevertheless, the results proved a useful addition to the austenite reconstruction methodology.

### **8.1.3 Summary of the Measurement of the Orientation Relationship Via Bayesian Inference**

A computational measurement of the OR for four different steel samples and a ferrous binary alloy were performed through use of Bayesian statistics. Analysis was conducted and four of the resultant measurements were compared with experimentally measured results to determine the accuracy of the results. The comparisons suggested that the given technique did an excellent job at determining an accurate OR measurement regardless of composition and morphology of the martensite. Additionally, it was confirmed that KS-like and NW-like sample ORs deviate significantly from the ideal ORs. Additionally, the technique is robust enough to handle small windows of variant orientations, even when few can be experimentally observed or when excessive noise from grain boundaries, misindexed points, or even portions of twins are included in the measurement data set. It was confirmed that the OR varies across the same steel sample given different PAGs, but that the resultant measurement remains consistent. The resultant methodology was then implemented in the austenite reconstruction algorithm.

### **8.1.4 Summary of the Probabilistic Reconstruction of the Prior Austenite Microstructure from EBSD-Indexed Martensite Data Using the Graph Cutting Algorithm**

The graph cutting technique was successfully applied to the reconstruction of austenite from the transformation martensitic microstructure in steels for a variety of differing steel samples. The utilization of the martensite misorientation analysis

information along with the measurement of the experimental OR was deemed crucial in the overall success of the algorithm. Specifically, the KS OR produced far too many grains with physically unreasonable PAG boundaries, such as ones within grains that are not connected to neighboring grain boundaries. Therefore, determination of the actual OR is crucial in optimizing the reconstruction results. Reconstructions were performed on three different steel samples and a binary ferrous alloy ranging from a KS-like to NW-like sample. All respective results looked reasonable by eye, but validation could be assumed on two of the samples. The Fe-30Ni ferrous alloy had a significant amount of retained austenite in its transformation microstructure,  $\sim 15\%$ , which was evenly spread out across the microstructure. Therefore, the reconstructed grains were compared with the retained austenite regions, and the results showed a very good alignment between the reconstructed PAGs and the retained austenite portions embedded within them. Additionally, since the AF9628 steel sample had an optical micrograph of the chemically etched microstructure which revealed the PAG boundaries, a comparison between the optical micrograph and the reconstruction was possible. The results showed a majority of the PAGs had an almost exact one-to-one, and the calculated ASTM grain size number was similar. A second reconstruction was performed on a binary ferrous alloy with a plate-like morphology. This transformation microstructure contained a significant amount of retained austenite which, although highly deformed, could be used as validation to the reconstructed PAGs. The results showed a strong correlation between the two, which suggests that the proposed austenite reconstruction algorithm can accurately reconstruct both the morphology and the likely prior austenite granular orientations in steels and ferrous alloys. Additionally, an excessive amount of noise was added to a portion of the AF9624 sample

by randomly assigning 25%, 50%, and 75% of pixels to Euler angles of  $0^\circ$ , and results remained relatively consistent for all three cases in both the chosen grains and the proposed austenite orientation. The technique does a good job at identifying a number of likely twins within the PAGs without compromising the parent structure, but the accuracy of twin locations and orientations cannot be verified as of now. Overall, the algorithm can adequately and effectively capture the prior austenite microstructure from EBSD-indexed martensite regardless of the morphology and composition of the steel or ferrous alloy.

### **8.1.5 Summary of Application of Graph Cutting to Probabilistic Segmentation of Martensitic Packet Boundaries and Analysis of Shared Variants Across Parent-Twin Interfaces**

The application of graph cutting to the segmentation of martensite packets showed promising results. Three different types of reconstructed austenite grains were chosen to be analyzed from the ASTM P122 12 wt%Cr tempered martensitic steel data set; one large, corresponding to larger packet boundaries; one small, with some packets exhibiting few transformed variants; and a parent-twin system where the theoretical variants were rotated by either the parent or the twin austenite orientation. Crystallographic analysis was performed by comparing the martensite orientations assigned to respective packets with the theoretically expected variants for both the larger and the smaller PAG-transformed variants. The results revealed a strong correlation between the segmented orientations and the expected variants, suggesting that the technique can effectively identify respective packets and packet sizes. Even as the PAG size decreased and the smallest segmented packet exhibited variant selection,

where only 2-3 variants were observed, the results remained consistent and accurate. The technique also proved useful in identifying the packets containing shared variants across the austenitic parent-twin interface. These packets contained similar geometrical features and exhibited overlap across the interface. The exact locations of the shared variants were not determined, but an extension of the graph cutting technique to identify selected variants could potentially rectify this.

## 8.2 Outlook and Future Work

Throughout this thesis, the graph cutting technique has been successfully shown to handle a variety of inverse problems in materials science. The majority of these have been shown difficult to solve accurately and consistently, and a variety of different techniques have been applied to no avail, or to mixed results. A large contributor to these issues is the inherent noise associated with these problems as well as the similar contributions to a shared data set between competing features. This is seemingly handled by the graph cutting technique's Bayesian foundation, where utilizing prior knowledge is utilized to effectively define a series of features that, if defined well enough, can be effectively clustered into similar families. Additionally, its versatility in handling both random and ordered spatial arrangements of data points make it potentially applicable to a variety of problems in materials science. Therefore, extensions of the technique to both additional contributions to the existing work as well as new problems in materials science will now be presented.

### 8.2.1 Application of Graph Cutting to Additional Problems in Materials Science

The successful application of the graph cutting technique to image segmentation, microstructure constituent segmentation, parent grain/microstructure feature segmentation and atomic cluster identification present it as an appealing approach to inverse problems in materials science. Additionally, the inherent Bayesian framework, which allows it to easily handle noise, ease of implementation, and versatility suggest that it could be used for a variety of different problems in materials science. The two main requirements are that the data points are connected to each other through an arbitrary network and that they are related to each other through quantifiable means. If satisfied, the execution of the technique would only require a strong foundation that could successfully cluster together a series of inter-related, yet possibly noisy, nodes based on their ideal configuration. Therefore, some possible problems unrelated to austenite reconstruction were identified as possible candidates for the application of graph cutting.

The first and most simple problem would be the application of the graph cutting software to the reconstruction of other prior phases, such as the  $\beta$ -Ti phase that results from the  $\alpha \rightarrow \beta$  phase transformation. This transformation differs from the  $\gamma \rightarrow \alpha'$  transformation in that the two phases have a different crystal symmetry. (the martensite phase is assumed to have a bcc crystal structure even though it may actually resemble the bct structure instead). In titanium, the low temperature  $\alpha$  phase has an hcp crystal structure, which conforms to a bcc crystal structure upon the transformation to the high temperature  $\beta$  phase. However, inherently built into the code is a symmetric indifference, meaning crystal symmetry is accounted for by

phase and is not assumed to be cubic. Therefore, the code should be able to handle different symmetry-dictated transformations with relative ease. As mentioned, the  $\gamma \rightarrow \alpha'$  transformation in steels is muddled by the plasticity due to the martensite formation, the variation in the orientation relationship, variation in the austenite orientation across a single grain, and the existence of 24 crystallographic variants. In titanium, the OR is assumed to follow closely, if not exactly to, the Burger's OR [28]. Additionally, the transformation produces considerably less noise and results in only 12 crystallographic  $\beta$  variants. For this reason, several reconstruction techniques have already been successfully applied to the reconstruction of  $\beta$ -Ti [51,55]. It would be reasonable to assume that the graph cutting technique could also successfully be applied to titanium as well. Bypassing the point-to-point methodologies applied by existing algorithms would produce better or equal reconstructions in far less time. There is also a symmetric indifference inherently built into the code, meaning the crystal symmetry is accounted for regardless of whether the transformation results in a symmetry difference. Therefore, implementation to the  $hcp \rightarrow bcc$  transformation should be relatively simple and straightforward, and would provide more versatility to the reconstruction algorithm.

The second problem would be to utilize the graph cutting technique in order to clean up noisy EBSD-indexed data sets. Consider an experimentalist attempting to analyze a specific material through EBSD. However, after substantial time was spent preparing the sample and setting up the camera parameters, the Kikuchi patterns revealed an inconclusive surface assessment which resulted in an excessively noisy data set that did little to reveal the material's texture. This could be the result of poor sample preparation, improper parameterization of the Scanning Electron Microscope

(SEM), plastic deformation or non identifying a secondary phase, which would require analysis on another sample. However, it was previously shown in Chapter 6 that reconstructions could be adequately performed on data sets inundated with excessive noise. Therefore, it is reasonable to believe that the graph cutting technique could effectively sift through the excessive noise to “reconstruct” the probabilistic texture based on the indexed points of high confidence.

A suggestion for the implementation of the technique could be similar in nature to that imposed for the austenite reconstruction algorithm. All misindexed and/or low-confidence points would be extracted so as to not contribute to any of the probabilistic calculations. The in-plane weights could possibly be related to the misorientation profile between adjacent nodes. Adjacent nodes exhibiting an identity misorientation would reflect nodes from the same grain; high-angle misorientations would identify a grain boundary. To establish the out-of-plane weights, a high-confidence orientation could be randomly chosen and convolved with noise to produce an ODF. Comparisons between the EBSD-indexed orientations and the ODF would establish a probabilistic foundation to cluster specific nodes into single grains. Additionally, a method could be established to weight mis-indexed points on their spatial correspondence to the high-confidence points. If encompassed by orientations of a similar orientation, it would suggest the nodes came from the same grain. Conversely, if these nodes were adjacent to numerous disparate misorientations, these points could reflect grain boundaries. If still noisy, subsequent denoising cuts could work through the grid points to iteratively reproduce the most probabilistic microstructure.

A third and final application would be to understanding variant selection during the martensitic phase transformation. Several studies have been performed on the occurrence of variant selection based on several different factors. These include favorable alignment of habit planes with corresponding austenite slip systems [106, 151, 160], interactions between dislocations in the prior austenite phase [172], and the size of the prior austenite grain. The technique would be similar in a sense to the OR methodology described in Chapter 5 and used as an extension of the austenite reconstruction algorithm. Essentially, this would be done by utilizing an accurate measurement of the experimental OR to predict the locations of the variants, then using the graph cutting technique coupled with pole figure analysis. These pole figures would then be compared with the variant analysis outlined in Chapter 4 to effectively identify the locations of specific variants. The graph cutting technique would be able to sift through related noise due to the transformation, most notably if the PAGs were thermo-mechanically treated prior to the martensitic transformation. The main contributing factor to the success of this would be an accurate representation of the PAG orientation, since pole figure analysis would be fully dependent on identifying the respective transformation.

### **8.3 Extension of Graph Cutting to Identification of Shared Parent-Twin Austenite Variants**

The graph cutting technique has already been shown to sufficiently segment martensitic packets within PAGs based theoretical misorientation and corresponding variant transformation information. Since the variant ordering within packets and corresponding misorientation information can relate directly to sub-block boundaries

as well, the next logical addition to the reconstruction algorithm would be the segmentation of shared variants across parent-twin interfaces. Reliant again upon the graph cutting technique's versatility, individual packets containing shared variants would serve as the featured graph. A dual-grid system would be required, and the misorientation information that serves as the basis for the in-plane weighting would remain consistent. However, instead of accounting for all intra-packet boundary misorientations ( $\Delta g_{0 \rightarrow 4}$ ), only the shared-variant, low-angle misorientation information would be considered ( $\Delta g_{20}$ , or conversely anything considered a low-angle boundary) for computation of the corresponding MODF. Additionally, the pairs of shared variants are also theoretically known between the parent- and twin-variants (Figure 4.8 in Chapter 4 for the {111} twin). Adjusting the out-of-plane weights to account for these orientation pairings would effectively cluster them together. The segmentations would then exhibit the actual locations of the shared variants, which could be coupled with experimental procedures to study the mobility of dislocations across parent-twin interfaces.

### **8.3.1 Application of Reconstruction Algorithm to Ausforming Examples and Potential Limitations**

The reconstruction examples presented throughout the paper were mostly applied to a variety of tempered martensitic steels, with the exception of the weldment sample. These steels were chosen because of their ubiquitous use within a wide range of industrial applications. The ability to effectively characterize the pre-transformation austenite microstructure would therefore facilitate the manufacturability of these steels and subsequent analysis of the steel and its latent mechanical behavior. However, another technique commonly applied to steel is the deformation of the steel

within the austenite phase field before subsequent transformation to martensite, a thermo-mechanical treatment known as ausforming. Ausforming has been consistently shown to improve both the strength and toughness of the transformed steel as well as significantly influence the morphology of the microstructure [77, 105, 151].

Generally, the resultant microstructure is highly anisotropic and exhibits strong variant selection, where the decrease in block widths brings about fewer developed variants. Although the process has been studied extensively, little to no reconstructions have been performed on the prior ausformed austenite microstructure except for a study performed by Miyamoto et al [105]. Therefore, application of the graph cut-based reconstruction algorithm on a variety of ausformed samples would contribute to the breadth of the reconstruction algorithm. Reconstructions of the ausformed austenite microstructure should be able to be performed with little to no alterations to the existing reconstruction technique. The main hindrance to the efficacy of the reconstructions will be the orientation gradient across the austenite grain that results from the deformation. This will introduce a significant amount of noise into the  $\gamma \rightarrow \alpha'$  transformation, where variants will exhibit small rotations as the orientation changes across a single prior austenite grain. Regularization parameters would subsequently require a substantial enhancement within the in-plane nodes to account for this resultant noise.

A potential secondary limiting factor could be the aforementioned variant selection that results from the deformation of the austenite microstructure. It has been well documented that ausforming produces preferred textures favoring the formation of packet-specific martensite laths [93, 106, 107, 151]. This will result in selective PAG transformed martensite variants. It has been shown that the graph cutting

reconstruction technique can handle PAGs with limited variants, and it is believed that this could extend to PAGs with refined microstructures containing only 2 or 3 variants. However, since the OR will change across a single grain, it is unclear if the orientation gradient coupled with the limited variants will confuse the technique, partitioning cut grains into seconds or even thirds depending on the amount of induced straining. Therefore, a directional and/or geometric aspect may be required as a secondary denoising technique to optimize the resultant microstructure. In other words, if the granular geometry is inconsistent with expectation at certain regions, post-processing cuts could be performed to modify these ill-posed grains and cluster certain truncated PAGs into a single, cohesive entity.

Additionally, since the reverse transformation from  $\alpha' \rightarrow \gamma$  was successfully applied to a variety of different samples in Chapter 6, it could potentially be possible to consider a similar application of the technique towards the forward transformation from  $\gamma \rightarrow \alpha'$ . Although useless for typical applications considering the martensite is readily observable, a two-part reconstruction could be applied to reproduce potential transformation martensite microstructures of the same composition applied to a variety of ausforming techniques. This could potentially be used to effectively assess a variety of thermo-mechanical processing conditions on newly developed or untested ausformed steels for optimization purposes. The process would require four separate steps in order to effectively reproduce the potential ausformed martensite microstructures, with only one of the steps requiring substantially new work in order to complete. The first and most obvious step would simply be reconstructing the prior austenite microstructure from a desired set of martensitic data. The second step would then require the subsequent utilization of crystal plasticity analysis and/or

texture evolution software. A specific set of thermo-mechanical processing conditions would be defined and applied to the reconstructed austenite, and the resultant texture would assume the post-ausforming austenitic microstructure.

The third and most difficult step would involve modifying the graph cutting algorithm to account for the forward transformation from austenite to martensite. However, this step would require the effective implementation of orientation-based variant selection since a probability would have to be assigned that would favor the formation of specific packets, and therefore blocks and sub-blocks within those packets. As previously mentioned, graph cutting could be used as an effective technique to identify selective variants from refined austenitic microstructures. It was already shown in Chapter 7 that packets could be identified with only the existence of 2 or 3 variants, and it seems highly possible that this would also translate to single-variant transformed PAGs. If statistical analysis was applied that identified certain austenite orientational constraints, graph cutting could be used to subsequently relate them to the likelihood of ausformed PAGs forming specific orientational variants as a function of the deformation-based OR. The placement of the martensite variants would then likely have to be randomized, creating an accurate representation of the texture. The final step would then involve crystal plasticity simulations on the resultant martensite microstructure. Repeating the technique across a variety of different ausforming conditions could then be used to optimize said parameters for a specific composition.

## Appendix A: Martensite Misorientation Information

### A.1 Appendix

For Tables AI-DX below, which list the complete misorientation list for the analyzed cases, a few of the notations may be new to the reader and as such will be described here briefly. Consistent with the text,  $\Delta g_i$  refers to a specific misorientation resulting from the variant-variant interactions. The term  $\theta(\Delta g_i)$  refers to the misorientation angle, always measured in degrees, while the term  $\vec{r} \equiv [r_1, r_2, r_3]$  is the approximate low-index axis of rotation for the misorientation. Finally, the term  $\delta(\Delta g_i)$  is the deviation of the true axis from the true axis from the approximate low-index axis of rotation. Finally, the concluding table—Table EXI—is the comparison of similar misorientations that fall within  $1^\circ$  of each other. In regards to notation, the differing misorientations are denoted by the subscripts (i,j) such that  $\Delta\theta(\Delta g_{i,j})$  would represent the angular difference between misorientation angles  $\theta(\Delta g_i)$  and  $\theta(\Delta g_j)$ . Additionally,  $\Delta\vec{r}(\Delta g_{i,j})$  would represent the angular difference between misorientation axes  $r_i$  and  $r_j$ .

### A.2 KS-Cubic Orientation Relationship Misorientation Data

Table A.1: Intra-parent misorientation list for KS orientation relationship considering cubic symmetry.

$\Delta g_i$	$\theta(\Delta g_i)$ ( $^\circ$ )	$\vec{r}$	$\delta(\Delta g_i)$ ( $^\circ$ )
0	0.00	[0 0 1]	0.00
1	10.53	[0 1 1]	0.25
2	60.00	[0 1 1]	0.25
3	60.00	[1 1 1]	0.00
4	49.27	[0 1 1]	0.25
5	49.27	[1 1 1]	0.00
6	50.42	[2 2 3]	1.39
7	14.90	[1 3 8]	2.93
8	10.53	[1 1 1]	0.00
9	50.51	[1 4 5]	1.89
10	57.21	[3 5 6]	0.28
11	20.60	[3 5 5]	1.79
12	51.73	[3 5 5]	1.79
13	57.21	[2 5 6]	0.73
14	47.11	[2 4 5]	2.28
15	20.60	[0 1 3]	1.27
16	21.06	[0 3 7]	0.96

Table A.2: Parent-twin misorientation list for KS orientation relationship considering cubic symmetry.

$\Delta g_i$	$\theta(\Delta g_i)$ ( $^\circ$ )	$\vec{r}$	$\delta(\Delta g_i)$ ( $^\circ$ )
17	55.61	[3 5 6]	1.05
18	54.84	[3 3 4]	1.33
19	25.00	[2 4 5]	0.99
20	15.45	[3 3 4]	0.63
21	37.24	[2 6 7]	1.60
22	47.56	[2 6 7]	2.78
23	21.06	[1 1 1]	0.00
24	23.51	[1 2 4]	1.45
25	40.28	[3 4 6]	2.35
26	38.94	[1 1 1]	0.00

continued ...

... continued

$\Delta g_i$	$\theta(\Delta g_i)$ ( $^\circ$ )	$\vec{r}$	$\delta(\Delta g_i)$ ( $^\circ$ )
27	55.23	[1 4 4]	1.34
28	53.51	[2 3 5]	2.26
29	49.19	[2 5 7]	1.27
30	45.80	[1 6 7]	1.20
31	51.32	[0 5 8]	0.74
32	26.11	[1 2 7]	0.70
33	29.12	[1 3 6]	2.27
34	47.56	[3 4 6]	2.10
35	33.57	[1 1 2]	1.71
36	34.85	[4 5 5]	1.15
37	44.35	[3 5 5]	1.45
38	28.41	[1 1 8]	0.00
39	38.94	[2 3 3]	0.76
40	49.19	[1 5 7]	1.22
41	47.83	[3 3 8]	2.17
42	40.28	[0 4 5]	0.92
43	34.85	[1 2 6]	1.33
44	35.45	[0 1 3]	1.81
45	43.00	[2 3 5]	0.48
46	33.57	[1 1 2]	1.71
47	40.28	[1 1 5]	1.35
48	38.94	[1 1 9]	3.65
49	51.80	[4 4 7]	0.00

Table A.3: Twin-twin misorientation list for KS orientation relationship considering cubic symmetry.

$\Delta g_i$	$\theta(\Delta g_i)$ ( $^\circ$ )	$\vec{r}$	$\delta(\Delta g_i)$ ( $^\circ$ )	$\Delta g_i$	$\theta(\Delta g_i)$ ( $^\circ$ )	$\vec{r}$	$\delta(\Delta g_i)$ ( $^\circ$ )
50	38.33	[0 1 1]	3.21	95	45.10	[0 1 8]	1.44
51	27.82	[1 6 6]	2.59	96	31.59	[1 1 9]	3.65
52	21.84	[1 6 6]	1.75	97	33.25	[2 2 9]	0.52
53	32.33	[1 6 6]	3.28	98	33.57	[1 2 3]	1.65
54	59.55	[3 5 5]	1.84	99	33.25	[2 3 6]	1.79
55	60.83	[1 2 2]	2.04	100	57.94	[5 5 6]	0.39
56	33.75	[0 1 2]	2.40	101	49.43	[3 4 4]	1.73
57	38.63	[1 2 3]	0.67	102	32.33	[2 6 7]	1.46

continued ...

... continued

$\Delta g_i$	$\theta(\Delta g_i)$ ( $^\circ$ )	$\vec{r}$	$\delta(\Delta g_i)$ ( $^\circ$ )	$\Delta g_i$	$\theta(\Delta g_i)$ ( $^\circ$ )	$\vec{r}$	$\delta(\Delta g_i)$ ( $^\circ$ )
58	45.54	[3 5 7]	0.73	103	36.93	[0 4 5]	1.02
59	39.87	[1 4 7]	1.25	104	47.91	[4 4 7]	2.19
60	46.75	[1 5 7]	1.73	105	38.94	[4 5 7]	1.00
61	48.70	[2 4 7]	1.49	106	28.05	[4 4 7]	1.45
62	30.26	[2 3 5]	0.69	107	35.43	[4 5 5]	1.85
63	28.41	[1 1 1]	0.00	108	51.73	[1 5 8]	1.73
64	55.06	[0 4 5]	1.17	109	48.08	[1 4 7]	0.77
65	54.92	[1 6 7]	1.98	110	42.11	[4 4 7]	1.30
66	31.59	[1 1 1]	0.00	111	43.13	[1 2 3]	1.65
67	33.25	[3 4 7]	1.27	112	40.28	[5 5 6]	0.00
68	39.87	[0 4 7]	2.11	113	26.45	[1 6 6]	1.75
69	29.87	[0 3 7]	0.92	114	33.57	[1 2 3]	1.81
70	24.01	[1 2 5]	1.71	115	38.94	[3 4 7]	0.41
71	33.75	[1 3 6]	1.71	116	30.93	[2 5 6]	0.79
72	55.06	[3 4 6]	1.21	117	44.08	[4 5 5]	1.40
73	53.85	[2 4 5]	1.66	118	45.54	[1 5 8]	1.06
74	31.96	[0 1 1]	2.82	119	43.40	[3 4 7]	1.54
75	37.94	[2 6 7]	1.23	120	44.26	[0 1 1]	3.21
76	45.10	[2 6 7]	1.37	121	50.75	[2 6 7]	0.83
77	38.63	[0 1 1]	2.37	122	44.73	[2 2 7]	1.12
78	42.85	[0 2 5]	0.64	123	43.87	[1 3 6]	1.22
79	44.35	[1 2 6]	1.17	124	28.05	[0 3 7]	3.23
80	34.36	[2 2 9]	0.52	125	35.43	[1 2 5]	0.00
81	50.75	[2 3 6]	1.19	126	45.80	[2 2 9]	0.00
82	49.43	[0 6 7]	0.90	127	38.94	[0 1 6]	3.04
83	31.59	[2 3 3]	0.76	128	40.28	[2 5 5]	1.54
84	35.78	[1 6 7]	2.57	129	47.91	[2 3 3]	2.51
85	41.21	[1 5 5]	2.15	130	36.92	[0 2 3]	0.91
86	42.11	[2 4 5]	0.00	131	35.43	[1 2 6]	0.65
87	35.11	[1 6 7]	2.61	132	44.08	[2 2 7]	1.75
88	39.99	[1 3 8]	3.46	133	30.93	[0 0 1]	1.15
89	46.95	[1 3 8]	3.26	134	40.28	[1 1 4]	1.39
90	36.93	[1 3 5]	1.04	135	31.96	[1 3 8]	1.01
91	42.85	[0 4 7]	2.26	136	38.33	[2 3 3]	0.15
92	44.35	[1 2 4]	1.55	137	41.21	[2 6 7]	2.31
93	36.93	[0 1 2]	0.89	138	22.75	[2 2 9]	0.83
94	37.94	[0 1 7]	3.18	139	45.80	[0 1 1]	1.94

### A.3 NW-Cubic Orientation Relationship Misorientation Data

Table A.4: Misorientation list for NW orientation relationship with cubic symmetry.

$\Delta g_i$	$\theta(\Delta g_i)$ (°)	$\vec{r}$	$\delta(\Delta g_i)$ (°)	$\Delta g_i$	$\theta(\Delta g_i)$ (°)	$\vec{r}$	$\delta(\Delta g_i)$ (°)
0	0.00	[0 0 1]	0.00	21	48.11	[1 4 8]	1.45
1	60.00	[0 1 1]	0.25	22	30.01	[1 1 2]	0.49
2	50.05	[3 4 4]	0.36	23	52.24	[0 5 6]	0.85
3	13.76	[1 6 6]	3.32	24	31.59	[5 6 6]	0.18
4	53.69	[1 3 3]	0.78	25	38.61	[0 3 4]	1.36
5	19.47	[0 0 1]	0.00	26	39.12	[1 4 6]	1.31
6	51.41	[2 3 4]	1.19	27	42.40	[1 2 9]	1.44
7	24.47	[3 3 5]	0.00	28	31.59	[0 0 1]	0.00
8	40.66	[1 2 2]	2.34	29	37.58	[1 1 2]	2.37
9	23.12	[2 2 5]	0.27	30	49.12	[5 5 6]	0.00
10	38.94	[5 6 6]	0.18	31	31.70	[0 6 7]	1.97
11	52.63	[1 5 7]	0.65	32	38.94	[3 4 6]	1.18
12	45.38	[0 6 7]	0.86	33	35.43	[5 5 6]	1.07
13	30.75	[1 3 9]	1.44	34	46.72	[1 5 8]	1.24
14	42.69	[1 1 2]	1.15	35	45.38	[1 3 3]	2.05
15	38.94	[0 0 1]	0.00	36	43.37	[0 1 2]	1.04
16	33.56	[0 5 7]	0.88	37	35.43	[1 2 6]	0.58
17	27.47	[1 5 7]	0.00	38	38.94	[0 1 6]	0.26
18	58.94	[1 3 3]	2.74	39	31.48	[1 1 4]	0.61
19	34.92	[1 5 6]	1.53	40	41.08	[1 4 4]	0.43
20	41.76	[2 6 7]	1.34				

#### A.4 Experimental-Cubic Orientation Relationship Misorientation Data

Table A.5: intra-parent misorientation list for experimental orientation relationship considering cubic symmetry.

$\Delta g_i$	$\theta(\Delta g_i)$ (°)	$\vec{r}$	$\delta(\Delta g_i)$ (°)
0	0.00	[0 0 1]	0.00
1	6.60	[0 4 7]	0.36
2	59.48	[2 2 3]	2.56
3	60.14	[5 5 6]	1.73
4	53.70	[1 6 6]	3.16
5	52.51	[4 5 5]	1.94

continued ...

... continued

$\Delta g_i$	$\theta(\Delta g_i)$ ( $^\circ$ )	$\vec{r}$	$\delta(\Delta g_i)$ ( $^\circ$ )
6	51.85	[3 4 5]	0.95
7	12.58	[0 3 7]	3.47
8	8.12	[2 5 5]	0.77
9	52.31	[2 6 7]	1.64
10	58.63	[2 6 7]	2.30
11	16.32	[1 3 3]	1.29
12	51.54	[1 2 2]	1.32
13	57.59	[2 5 5]	2.11
14	51.55	[2 4 5]	3.33
15	17.00	[0 1 7]	0.00
16	17.80	[0 3 8]	0.00

Table A.6: Parent-twin misorientation list for experimental orientation relationship applying cubic symmetry.

$\Delta g_i$	$\theta(\Delta g_i)$ ( $^\circ$ )	$\vec{r}$	$\delta(\Delta g_i)$ ( $^\circ$ )	$\Delta g_i$	$\theta(\Delta g_i)$ ( $^\circ$ )	$\vec{r}$	$\delta(\Delta g_i)$ ( $^\circ$ )
17	57.28	[5 5 6]	0.85	45	18.68	[3 3 5]	0.66
18	53.62	[0 1 1]	0.25	46	22.31	[2 3 7]	1.85
19	3.19	[3 3 7]	0.87	47	40.86	[4 5 6]	2.17
20	6.93	[3 5 5]	0.80	48	41.83	[1 1 1]	0.44
21	51.90	[1 5 6]	2.47	49	53.72	[1 5 6]	2.57
22	50.74	[1 3 3]	2.39	50	53.47	[3 4 6]	2.29
23	57.03	[2 6 7]	0.83	51	50.56	[2 4 5]	1.71
24	58.13	[1 5 5]	0.82	52	47.49	[1 6 6]	1.71
25	19.93	[0 1 5]	3.01	53	49.65	[0 4 5]	0.58
26	20.11	[1 2 8]	2.94	54	26.00	[1 2 7]	1.36
27	49.57	[1 1 1]	2.99	55	26.91	[1 3 8]	1.42
28	48.79	[4 5 6]	0.22	56	48.56	[3 4 6]	1.10
29	15.54	[0 3 7]	1.73	57	29.33	[3 3 7]	1.08
30	11.15	[2 4 5]	0.32	58	37.83	[2 3 3]	1.68
31	51.66	[2 5 6]	0.67	59	43.70	[3 5 5]	2.72
32	57.66	[2 4 5]	0.63	60	26.83	[1 1 5]	0.67
33	13.14	[1 4 5]	1.54	61	38.86	[4 5 5]	1.89
34	17.90	[1 2 3]	2.50	62	50.90	[1 5 7]	1.50
35	50.99	[3 5 5]	2.33	63	49.68	[3 4 8]	2.43
36	51.70	[3 3 4]	2.06	64	44.99	[0 6 7]	0.18
37	54.61	[2 5 5]	1.26	65	32.05	[2 2 9]	0.44

continued ...

... continued

$\Delta g_i$	$\theta(\Delta g_i)$ (°)	$\vec{r}$	$\delta(\Delta g_i)$ (°)	$\Delta g_i$	$\theta(\Delta g_i)$ (°)	$\vec{r}$	$\delta(\Delta g_i)$ (°)
38	48.54	[2 5 5]	2.29	66	32.23	[0 2 7]	0.44
39	54.35	[2 3 4]	1.24	67	43.91	[3 4 7]	2.23
40	52.78	[2 2 3]	0.90	68	37.88	[4 4 7]	0.27
41	23.38	[3 4 7]	0.88	69	36.70	[1 1 9]	0.00
42	17.38	[2 2 3]	0.80	70	36.30	[1 1 9]	3.10
43	40.42	[2 5 5]	2.58	71	49.81	[1 1 2]	1.15
44	46.50	[1 3 3]	1.40				

Table A.7: Twin-twin misorientation list for experimental orientation relationship using cubic symmetry.

$\Delta g_i$	$\theta(\Delta g_i)$ (°)	$\vec{r}$	$\delta(\Delta g_i)$ (°)	$\Delta g_i$	$\theta(\Delta g_i)$ (°)	$\vec{r}$	$\delta(\Delta g_i)$ (°)
72	27.85	[1 3 7]	1.03	150	31.29	[3 4 7]	1.39
73	29.15	[1 4 8]	0.97	151	31.47	[4 4 5]	0.00
74	51.26	[2 3 4]	1.42	152	52.44	[0 5 6]	0.89
75	47.47	[2 4 5]	1.50	153	53.97	[0 1 1]	2.56
76	46.40	[0 6 7]	2.86	154	28.76	[4 5 5]	0.82
77	48.93	[0 5 7]	2.77	155	30.95	[3 3 5]	2.44
78	43.57	[1 3 3]	1.60	156	36.40	[0 5 8]	2.74
79	37.51	[2 5 6]	2.51	157	30.75	[1 4 8]	1.21
80	19.19	[3 5 6]	1.68	158	26.18	[1 3 6]	0.84
81	25.33	[3 5 7]	1.83	159	31.83	[1 4 6]	0.53
82	54.79	[4 5 7]	2.03	160	55.66	[1 5 6]	0.71
83	56.60	[2 3 4]	1.38	161	54.33	[2 5 6]	0.36
84	24.58	[2 2 5]	0.64	162	33.20	[0 1 1]	1.82
85	21.43	[3 4 5]	2.23	163	35.86	[1 5 5]	0.82
86	54.57	[1 5 7]	3.46	164	42.00	[2 5 5]	1.93
87	52.32	[1 6 6]	1.30	165	38.51	[1 5 5]	1.64
88	38.94	[1 1 1]	2.18	166	44.43	[0 1 2]	2.58
89	38.07	[2 2 3]	1.92	167	47.93	[1 3 7]	1.72
90	51.18	[2 6 7]	1.37	168	31.80	[1 1 3]	0.50
91	57.28	[2 6 7]	2.09	169	49.11	[0 2 3]	2.07
92	46.63	[1 1 1]	1.57	170	49.94	[0 5 6]	1.21
93	48.62	[3 3 4]	1.23	171	31.95	[3 5 5]	1.67
94	15.89	[1 5 7]	3.10	172	37.96	[0 1 1]	1.54
95	14.07	[1 2 2]	1.24	173	42.28	[1 6 7]	1.51
96	31.95	[2 2 7]	1.70	174	40.90	[1 3 4]	1.03

continued ...

... continued

$\Delta g_i$	$\theta(\Delta g_i)$ ( $^\circ$ )	$\vec{r}$	$\delta(\Delta g_i)$ ( $^\circ$ )	$\Delta g_i$	$\theta(\Delta g_i)$ ( $^\circ$ )	$\vec{r}$	$\delta(\Delta g_i)$ ( $^\circ$ )
97	32.02	[1 3 8]	2.86	175	36.08	[1 6 7]	1.73
98	52.02	[3 3 4]	1.52	176	41.13	[1 2 8]	2.09
99	47.61	[3 4 5]	1.00	177	45.83	[0 1 4]	3.34
100	42.19	[0 6 7]	1.90	178	36.78	[1 5 7]	1.77
101	44.68	[1 6 7]	1.85	179	41.48	[0 5 8]	1.34
102	43.07	[3 5 5]	1.86	180	43.80	[1 4 7]	0.96
103	37.37	[4 5 6]	1.33	181	38.66	[0 2 3]	2.20
104	24.19	[3 4 5]	2.56	182	40.20	[0 1 7]	0.58
105	29.99	[4 4 7]	1.05	183	44.60	[0 1 9]	2.23
106	50.59	[3 4 6]	2.88	184	34.28	[0 0 1]	0.00
107	52.39	[1 2 3]	0.90	185	34.90	[1 1 7]	0.46
108	26.20	[1 2 7]	1.11	186	33.91	[3 4 7]	2.48
109	22.16	[1 2 4]	2.62	187	33.16	[2 3 6]	1.50
110	51.14	[0 3 5]	3.09	188	52.87	[5 5 6]	1.81
111	48.22	[1 5 7]	1.94	189	47.82	[4 5 6]	2.46
112	40.84	[3 3 4]	2.48	190	34.51	[1 6 7]	2.77
113	38.94	[3 4 4]	2.01	191	36.76	[0 6 7]	2.93
114	47.76	[1 3 3]	1.16	192	43.93	[3 3 5]	1.20
115	54.01	[2 6 7]	1.08	193	38.94	[4 5 7]	1.03
116	50.41	[3 4 4]	1.17	194	28.83	[4 4 5]	0.45
117	19.13	[1 2 2]	0.00	195	33.86	[4 5 5]	2.47
118	42.58	[3 5 7]	1.68	196	49.33	[0 5 8]	0.24
119	48.29	[3 4 6]	2.71	197	47.99	[1 4 6]	1.53
120	39.65	[1 3 3]	0.95	198	39.00	[3 4 6]	2.62
121	36.78	[3 5 6]	2.04	199	38.69	[1 2 3]	0.32
122	35.21	[0 2 7]	2.10	200	42.48	[3 3 4]	0.41
123	29.79	[0 2 5]	2.65	201	30.43	[0 6 7]	2.58
124	37.20	[3 4 7]	1.69	202	33.64	[1 3 4]	1.77
125	43.19	[1 1 2]	1.45	203	38.94	[3 4 7]	2.02
126	45.92	[2 6 7]	0.74	204	34.48	[1 2 3]	2.20
127	42.72	[1 2 2]	1.05	205	39.09	[4 5 5]	1.71
128	34.25	[1 1 6]	0.74	206	44.68	[1 5 7]	1.73
129	28.20	[1 2 9]	0.00	207	43.87	[1 2 3]	1.23
130	52.88	[1 4 6]	1.31	208	43.71	[1 6 6]	0.05
131	55.81	[2 6 7]	0.52	209	48.36	[2 6 7]	1.08
132	38.94	[0 0 1]	3.34	210	46.74	[1 1 4]	0.61
133	39.48	[1 1 9]	2.48	211	42.36	[0 2 5]	3.19
134	52.91	[1 2 3]	1.90	212	31.86	[0 1 2]	2.08
135	49.28	[2 3 6]	0.92	213	37.33	[1 3 7]	0.46

continued ...

... continued

$\Delta g_i$	$\theta(\Delta g_i)$ ( $^\circ$ )	$\vec{r}$	$\delta(\Delta g_i)$ ( $^\circ$ )	$\Delta g_i$	$\theta(\Delta g_i)$ ( $^\circ$ )	$\vec{r}$	$\delta(\Delta g_i)$ ( $^\circ$ )
136	22.82	[0 2 9]	0.32	214	45.16	[0 1 5]	0.39
137	22.48	[0 1 5]	0.53	215	38.94	[0 1 7]	1.24
138	37.30	[1 6 7]	1.56	216	42.56	[2 5 5]	0.57
139	31.14	[1 4 5]	0.49	217	47.56	[3 5 6]	1.70
140	23.20	[1 6 7]	0.00	218	37.05	[0 1 2]	0.70
141	29.46	[1 6 6]	1.27	219	35.44	[1 2 5]	0.00
142	59.98	[1 5 5]	0.70	220	41.39	[2 3 8]	1.54
143	58.86	[1 3 3]	1.29	221	32.86	[0 1 9]	2.03
144	32.21	[0 5 8]	2.12	222	36.83	[1 1 3]	0.22
145	34.72	[2 5 7]	1.35	223	32.48	[1 2 5]	1.11
146	43.95	[2 4 5]	0.99	224	38.46	[1 2 2]	0.47
147	40.59	[1 3 4]	1.09	225	39.20	[1 4 4]	0.55
148	47.46	[1 5 7]	3.61	226	27.63	[2 2 7]	0.95
149	50.84	[1 4 7]	1.92	227	40.96	[0 1 1]	0.25

## A.5 KS-Tetragonal Orientation Relationship Misorientation Data

Table A.8: intra-parent misorientation list for KS orientation relationship with respect to tetragonal symmetry.

$\Delta g_i$	$\theta(\Delta g_i)$ ( $^\circ$ )	$\vec{r}$	$\delta(\Delta g_i)$ ( $^\circ$ )
0	0.00	[1 0 0]	0.00
1	10.53	[1 0 1]	0.08
2	76.27	[5 5 1]	0.82
3	70.53	[1 1 0]	0.08
4	82.82	[3 3 1]	0.39
5	71.21	[7 5 0]	0.57
6	77.65	[7 5 1]	0.98
7	14.88	[8 3 1]	2.93
8	10.53	[1 1 1]	0.76
9	90.00	[6 5 1]	2.69
10	84.26	[7 6 1]	3.18
11	20.60	[5 5 3]	1.79
12	83.14	[5 4 0]	0.92
13	90.00	[7 6 1]	2.28
14	85.62	[3 2 0]	2.28

continued ...

... continued

$\Delta g_i$	$\theta(\Delta g_i)$ (°)	$\vec{r}$	$\delta(\Delta g_i)$ (°)
15	20.60	[3 0 1]	1.27
16	21.06	[7 3 0]	0.96

Table A.9: Parent-twin misorientation list for KS orientation relationship with tetragonal symmetry.

$\Delta g_i$	$\theta(\Delta g_i)$ (°)	$\vec{r}$	$\delta(\Delta g_i)$ (°)	$\Delta g_i$	$\theta(\Delta g_i)$ (°)	$\vec{r}$	$\delta(\Delta g_i)$ (°)
17	60.00	[1 0 1]	0.08	45	66.84	[5 2 3]	2.59
18	60.00	[1 1 1]	0.00	46	79.33	[4 0 1]	0.57
19	49.47	[1 0 1]	0.08	47	70.53	[6 0 1]	3.04
20	90.00	[1 0 0]	0.00	48	77.17	[6 1 3]	1.37
21	90.48	[8 0 1]	0.46	49	73.21	[6 0 3]	0.45
22	50.51	[4 1 5]	1.89	50	55.23	[4 1 4]	1.34
23	47.11	[5 2 4]	2.28	51	56.04	[7 1 5]	0.80
24	57.21	[6 2 5]	0.73	52	57.28	[7 2 4]	1.33
25	57.21	[5 3 6]	0.28	53	45.80	[6 1 7]	1.20
26	70.53	[9 1 1]	3.65	54	51.32	[5 0 8]	0.74
27	71.21	[9 1 1]	1.50	55	65.68	[8 1 0]	2.55
28	70.53	[1 1 1]	0.00	56	65.82	[9 1 2]	1.22
29	71.21	[4 3 3]	1.28	57	60.00	[5 0 3]	2.46
30	76.27	[9 1 0]	3.74	58	65.68	[3 1 0]	0.40
31	84.26	[9 0 1]	0.53	59	72.16	[7 0 3]	2.54
32	58.90	[7 2 4]	1.44	60	68.84	[7 1 4]	0.72
33	57.21	[6 3 5]	0.28	61	62.19	[9 0 1]	1.52
34	85.62	[8 1 1]	0.77	62	80.13	[6 0 3]	1.50
35	77.65	[9 2 1]	2.84	63	49.19	[7 1 5]	1.22
36	65.82	[4 1 3]	1.80	64	51.73	[6 0 3]	2.15
37	60.83	[3 0 2]	1.32	65	40.28	[5 0 4]	0.92
38	67.12	[5 2 4]	0.83	66	58.37	[9 2 0]	3.13
39	68.83	[8 2 5]	0.00	67	57.28	[7 1 1]	1.26
40	60.00	[5 1 4]	0.38	68	60.00	[8 1 4]	1.69
41	64.21	[6 0 5]	0.68	69	64.21	[3 0 1]	1.00
42	73.10	[9 2 1]	2.25	70	51.80	[5 0 1]	0.16
43	80.13	[6 1 0]	0.63	71	51.32	[9 1 0]	2.30
44	70.22	[5 1 2]	0.87	72	57.28	[3 0 2]	0.91

Table A.10: Twin-twin misorientation list applying KS orientation relationship with tetragonal symmetry.

$\Delta g_i$	$\theta(\Delta g_i)$ (°)	$\vec{r}$	$\delta(\Delta g_i)$ (°)	$\Delta g_i$	$\theta(\Delta g_i)$ (°)	$\vec{r}$	$\delta(\Delta g_i)$ (°)
73	89.37	[7 1 2]	0.83	151	30.26	[4 3 7]	0.69
74	88.41	[8 3 1]	1.01	152	28.41	[1 1 1]	0.00
75	55.61	[6 3 5]	1.05	153	67.12	[5 3 3]	0.97
76	49.19	[7 2 5]	1.27	154	58.16	[6 4 3]	1.85
77	67.12	[8 3 4]	0.44	155	75.34	[5 2 0]	0.75
78	73.10	[7 4 4]	1.21	156	78.62	[7 3 1]	1.15
79	47.56	[6 2 7]	2.78	157	39.87	[4 0 7]	2.11
80	37.24	[6 2 7]	1.60	158	29.87	[3 0 7]	0.92
81	82.82	[6 0 1]	1.38	159	88.45	[7 1 2]	0.93
82	84.80	[3 0 1]	2.03	160	90.00	[7 1 3]	0.62
83	54.84	[5 4 4]	1.33	161	67.84	[7 5 4]	1.03
84	55.61	[6 5 3]	1.05	162	69.41	[5 4 2]	2.38
85	81.62	[8 2 1]	0.98	163	92.92	[5 0 2]	0.28
86	79.33	[4 1 0]	0.57	164	89.07	[6 3 0]	1.77
87	53.51	[5 2 3]	2.22	165	45.10	[6 2 7]	1.20
88	63.26	[7 3 5]	0.90	166	38.63	[1 0 1]	0.79
89	38.94	[1 1 1]	0.00	167	81.13	[7 3 3]	0.60
90	40.28	[4 3 6]	2.35	168	86.95	[7 4 3]	1.11
91	68.84	[5 3 2]	1.64	169	34.36	[2 2 9]	0.52
92	65.82	[6 5 3]	1.84	170	76.43	[6 3 4]	2.29
93	49.47	[1 1 1]	0.00	171	67.12	[2 1 1]	0.49
94	50.51	[3 2 2]	1.39	172	80.91	[5 2 0]	0.45
95	90.00	[9 1 2]	3.42	173	67.69	[8 2 3]	2.23
96	84.26	[9 1 0]	0.53	174	67.84	[7 3 2]	0.77
97	84.80	[8 2 3]	1.05	175	63.93	[6 1 3]	0.95
98	94.25	[5 1 2]	0.52	176	68.01	[8 2 3]	2.76
99	54.84	[5 4 4]	1.33	177	54.92	[8 2 1]	2.61
100	47.56	[6 3 4]	2.10	178	46.95	[8 3 1]	3.26
101	62.19	[3 1 1]	1.20	179	77.00	[7 2 3]	1.29
102	67.12	[8 4 3]	0.44	180	76.62	[7 3 3]	1.28
103	44.35	[5 3 5]	1.45	181	54.21	[7 1 3]	1.48
104	34.85	[5 4 5]	1.15	182	59.08	[9 2 2]	0.24
105	77.17	[8 1 2]	1.49	183	52.83	[9 0 1]	2.76
106	80.41	[7 1 3]	0.80	184	45.10	[8 1 0]	1.44
107	47.56	[6 4 3]	2.10	185	58.60	[1 0 0]	2.92
108	49.19	[7 5 2]	1.27	186	59.08	[6 1 0]	0.96

continued ...

... continued

$\Delta g_i$	$\theta(\Delta g_i)$ ( $^\circ$ )	$\vec{r}$	$\delta(\Delta g_i)$ ( $^\circ$ )	$\Delta g_i$	$\theta(\Delta g_i)$ ( $^\circ$ )	$\vec{r}$	$\delta(\Delta g_i)$ ( $^\circ$ )
109	90.00	[4 1 1]	2.56	187	75.87	[5 1 2]	1.31
110	86.85	[8 2 1]	2.77	188	85.47	[7 1 3]	0.80
111	47.83	[8 3 3]	2.17	189	57.94	[5 5 6]	0.39
112	57.28	[6 2 3]	0.87	190	49.43	[4 3 4]	1.73
113	40.28	[6 4 3]	2.35	191	68.27	[7 1 2]	1.49
114	38.94	[3 2 3]	0.76	192	72.16	[3 1 1]	0.22
115	63.26	[5 3 1]	0.45	193	47.91	[4 4 7]	2.13
116	58.90	[6 5 2]	1.41	194	38.94	[5 4 7]	1.00
117	51.73	[5 5 3]	1.79	195	69.41	[7 0 2]	1.13
118	84.26	[4 0 1]	0.70	196	71.99	[7 0 3]	1.68
119	76.27	[7 4 2]	2.50	197	52.60	[8 3 4]	0.00
120	78.90	[5 4 1]	1.64	198	52.79	[7 3 2]	1.19
121	67.12	[5 2 1]	0.52	199	77.89	[7 1 4]	0.96
122	73.10	[7 3 0]	3.05	200	81.76	[5 4 3]	1.63
123	35.45	[3 1 0]	1.81	201	40.28	[5 5 6]	0.00
124	29.12	[6 3 1]	2.27	202	73.69	[5 1 1]	2.00
125	81.62	[7 3 1]	0.62	203	77.14	[5 2 1]	0.93
126	83.97	[7 4 1]	0.72	204	38.94	[4 3 7]	0.41
127	62.19	[6 3 2]	1.89	205	30.93	[5 2 6]	0.79
128	67.12	[7 4 1]	0.33	206	75.34	[8 0 5]	0.24
129	34.85	[6 1 2]	1.33	207	56.60	[7 3 2]	0.08
130	26.11	[7 2 1]	0.77	208	58.37	[8 4 1]	2.88
131	79.33	[5 4 2]	0.83	209	66.00	[5 2 2]	2.05
132	71.88	[5 5 2]	0.93	210	67.12	[3 2 1]	0.99
133	38.94	[9 1 1]	3.65	211	50.27	[3 1 0]	0.61
134	40.28	[5 1 1]	1.35	212	43.87	[6 3 1]	1.22
135	75.36	[4 3 1]	2.00	213	82.11	[4 1 1]	1.21
136	83.08	[3 2 1]	1.85	214	82.45	[8 3 2]	1.18
137	20.60	[3 1 0]	1.27	215	47.91	[7 0 2]	0.68
138	21.06	[7 0 3]	0.96	216	38.94	[6 0 1]	3.04
139	38.33	[1 0 1]	3.21	217	67.12	[6 3 1]	2.07
140	27.82	[6 1 6]	2.59	218	69.63	[6 4 1]	0.74
141	90.00	[7 0 2]	0.53	219	36.92	[3 2 0]	0.91
142	92.48	[7 0 3]	0.92	220	86.14	[8 3 2]	1.59
143	59.55	[5 5 3]	1.84	221	87.31	[7 4 2]	0.94
144	61.99	[3 3 1]	1.40	222	30.93	[1 0 0]	1.15
145	93.46	[7 3 1]	0.90	223	40.28	[1 1 4]	1.39
146	85.91	[8 4 1]	1.05	224	31.96	[3 1 8]	1.27
147	45.54	[7 3 5]	0.73	225	79.91	[2 0 1]	1.04

continued ...

... continued

$\Delta g_i$	$\theta(\Delta g_i)$ (°)	$\vec{r}$	$\delta(\Delta g_i)$ (°)	$\Delta g_i$	$\theta(\Delta g_i)$ (°)	$\vec{r}$	$\delta(\Delta g_i)$ (°)
148	39.87	[7 1 4]	1.25	226	83.79	[5 5 3]	1.53
149	72.16	[7 4 3]	2.14	227	22.75	[2 2 9]	0.83
150	78.40	[7 5 3]	1.77	228	86.44	[5 5 2]	0.65

## A.6 Similar Misorientation Comparisons

Table A.11: The possible misorientation pairs that may be indistinguishable upon experimental observation. KS-Cubic refers to KS orientation relationship assuming cubic symmetry, Low-C Expt. is the referenced experimental orientation relationship and KS-Tetrag as the KS orientation relationship assuming tetragonal symmetry.

OR	$\Delta g_i$	$\Delta g_j$	$\Delta\theta(\Delta g_{i,j})$ (°)	$\Delta \vec{r}(\Delta g_{i,j})$ (°)
KS-Cubic	39	136	0.619	0.409
KS-Cubic	50	77	0.309	0.909
KS-Cubic	84	87	0.670	0.115
Low-C Expt.	59	102	0.630	0.772
Low-C Expt.	61	205	0.229	0.010
Low-C Expt.	147	174	0.315	0.725
KS-Tetrag.	62	225	0.223	0.492
KS-Tetrag.	139	166	0.309	0.909
KS-Tetrag.	142	163	0.441	0.354
KS-Tetrag.	173	176	0.315	0.532

## Appendix B: Supplemental Material Related to Chapter 4

The following set of composition tables are related to the information presented within the main manuscript, *Analysis of Misorientation Relationships between Austenite Parents and Twins*. Mainly, in addition to the parent austenite variant interactions with the  $60^\circ \langle 1\bar{1}1 \rangle$  twins that was presented in the main manuscript, the following supplemental data includes the three additional fcc rotational twins:  $60^\circ \langle \bar{1}\bar{1}1 \rangle$ ,  $60^\circ \langle \bar{1}11 \rangle$ , and  $60^\circ \langle 1\bar{1}1 \rangle$  twin rotations and their misorientation interactions with both the parent austenite variants and each other, and themselves. The latter interaction will give composition tables equivalent to the intra-parent case presented within the main manuscript.

The sections are divided in accordance with the main manuscript, from utilizing the cubic-symmetry dictated Kurdjumov-Sachs (KS) orientation relationship, the experimentally observed orientation relationship and the tetragonal-symmetry dictated KS orientation relationship. The full composition table for the Nishiyama-Wassermann (NW) case was included in the main manuscript due to the limited number of variants and corresponding misorientations. Since the misorientation angle-axis pairings are equivalent to those found in the appendix section of the main manuscript (Table A1-A10), these misorientation angle-axis pairings are omitted here for sake of redundancy.

## B.1 Kurdjumov-Sachs Orientation Relationship With Cubic Symmetry

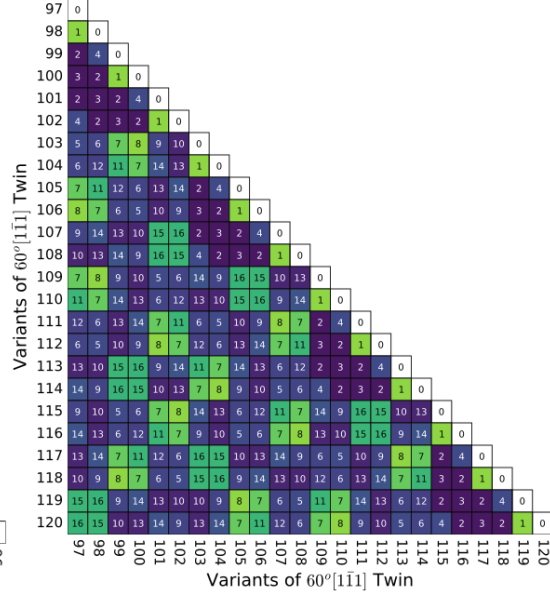
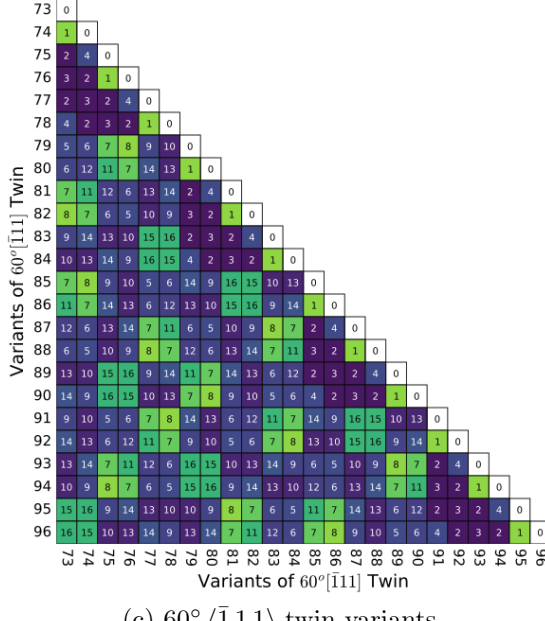
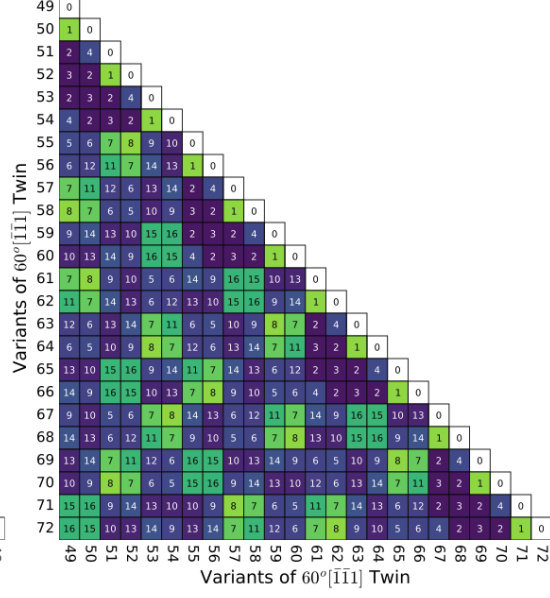
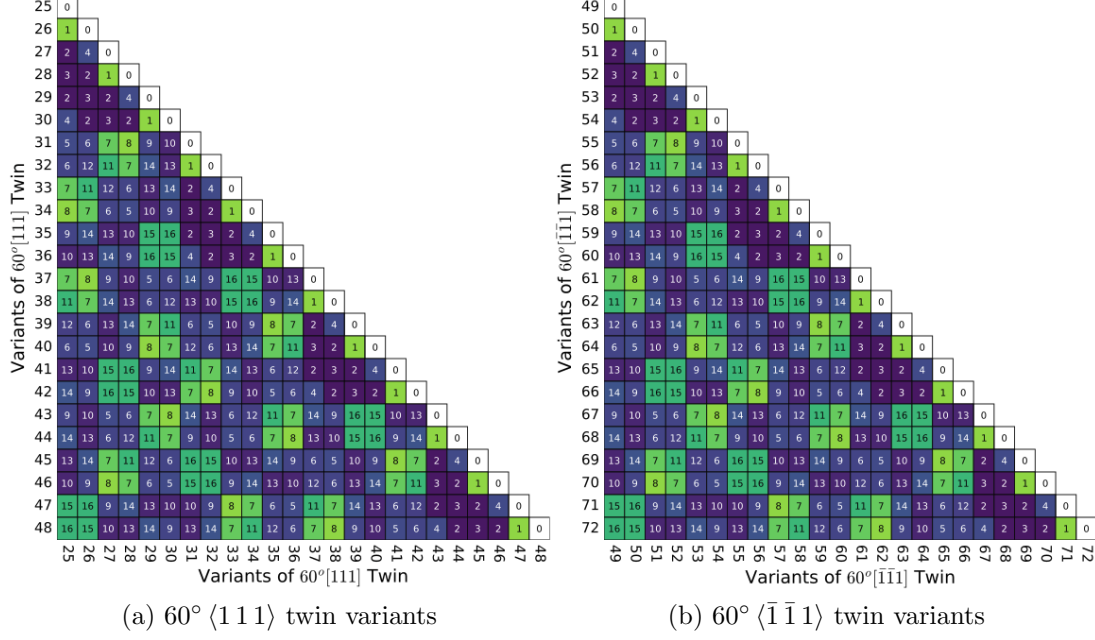


Figure B1: Composition tables displaying misorientation information for twin-generated variants intersecting with themselves.

Variants of  $60^\circ[\bar{1}\bar{1}1]$  Twin

49	45	46	32	43	37	22	48	47	28	41	40	27	36	21	49	45	33	44	13	10	15	16	9	14
50	49	45	33	44	36	21	47	48	27	40	41	28	37	22	45	46	32	43	14	9	16	15	10	13
51	21	22	17	18	19	20	28	27	25	24	23	29	17	33	32	31	30	7	8	9	10	5	6	
52	36	37	29	34	35	19	41	40	25	39	38	24	34	18	44	43	30	42	11	7	14	13	6	12
53	44	43	30	42	34	18	40	41	24	38	39	25	35	19	36	37	29	34	12	6	13	14	7	11
54	33	32	31	30	29	17	27	28	23	24	25	26	19	20	21	22	17	18	6	5	10	9	8	7
55	46	45	22	37	43	32	45	49	21	36	44	33	41	28	47	48	27	40	16	15	10	13	14	9
56	45	49	21	36	44	33	46	45	22	37	43	32	40	27	48	47	28	41	15	16	9	14	13	10
57	22	21	20	19	18	17	32	33	17	29	30	31	25	26	27	28	23	24	10	9	8	7	6	5
58	37	36	19	35	34	29	43	44	18	34	42	30	39	25	40	41	24	38	13	4	7	11	12	6
59	43	44	18	34	42	30	37	36	19	35	34	29	38	24	41	40	25	39	14	13	6	12	11	7
60	32	33	17	29	30	31	22	21	20	19	18	17	24	23	28	25	9	10	5	6	7	8		
61	40	41	24	38	39	25	44	43	30	42	34	18	34	29	37	36	19	35	6	12	11	7	14	13
62	27	28	23	24	25	26	33	32	31	30	29	17	18	17	22	21	20	19	5	6	7	8	9	10
63	48	47	28	41	40	27	45	46	32	43	37	22	44	35	49	21	36	10	13	14	9	16	15	
64	47	48	27	40	41	28	49	45	33	44	36	21	43	32	46	45	22	37	9	14	13	10	15	16
65	28	27	26	25	24	23	21	22	17	18	19	20	30	31	32	33	17	29	8	7	6	5	10	9
66	41	40	25	39	38	24	36	37	29	34	35	19	42	30	43	44	18	34	7	11	12	6	13	14
67	16	16	9	14	13	10	10	9	8	7	6	5	11	7	14	13	6	12	2	3	2	4	0	1
68	16	15	10	13	14	9	13	14	7	11	12	6	7	8	9	10	5	6	4	2	3	1	0	
69	9	10	5	6	7	8	14	13	6	12	11	7	14	9	16	15	10	13	0	1	2	3	2	4
70	14	13	6	12	11	7	9	10	5	6	7	8	13	10	15	16	9	14	1	0	4	2	3	2
71	13	14	7	11	12	6	16	15	10	13	14	9	6	10	9	6	7	2	4	0	1	2	3	
72	10	9	8	7	6	5	15	16	9	14	13	10	12	6	13	14	7	11	3	2	1	0	4	2
1	2	3	4	5	6	7	8	9	10	11	12	13	14	15	16	17	18	19	20	21	22	23	24	

Variants of Austenite Parent

(a)  $60^\circ \langle \bar{1}\bar{1}1 \rangle$  twin variants

Variants of  $60^\circ[\bar{1}\bar{1}1]$  Twin

73	34	29	37	36	19	35	39	25	40	41	24	38	13	14	7	11	12	6	43	44	18	34	42	30		
74	18	17	22	21	20	19	25	26	27	28	23	24	10	9	8	7	6	5	32	33	17	29	30	31		
75	44	33	45	49	21	36	40	27	48	47	28	41	15	16	9	14	13	10	46	45	22	37	43	32		
76	43	32	46	45	22	37	41	28	47	48	27	40	16	15	10	13	14	9	45	49	21	36	44	33		
77	30	31	32	33	17	29	24	23	28	27	26	25	9	10	5	6	7	8	22	21	20	19	18	17		
78	42	30	43	44	18	34	38	24	41	40	25	39	14	13	6	12	11	7	37	36	19	35	34	29		
79	35	19	36	37	29	34	34	18	44	43	30	42	11	7	14	13	6	12	41	40	25	39	38	24		
80	19	20	21	22	17	18	29	17	33	32	31	30	7	8	9	10	5	6	28	27	26	25	24	23		
81	36	21	49	45	33	44	37	22	45	46	32	43	14	9	16	15	10	13	47	48	27	40	41	28		
82	37	22	45	46	32	43	36	21	49	33	44	13	10	15	9	14	48	47	28	41	40	27				
83	29	17	33	32	31	30	19	20	21	22	17	18	6	5	10	9	8	7	27	28	23	24	25	26		
84	34	18	44	43	30	42	35	19	42	30	42	39	12	6	13	14	7	11	40	41	24	38	39	25		
85	12	6	13	14	7	11	6	5	10	9	8	7	2	4	0	1	2	3	16	15	10	13	14	9		
86	6	5	10	9	8	7	12	6	13	14	7	11	3	2	1	0	4	2	15	16	9	14	13	10		
87	13	10	15	16	9	14	11	7	14	13	6	12	2	3	2	4	0	1	10	9	8	7	6	5		
88	14	9	16	15	10	13	12	7	8	9	10	5	6	4	2	3	2	1	0	13	14	7	11	12	6	
89	7	8	9	10	5	6	4	3	9	16	15	10	13	14	1	0	1	2	3	4	14	13	6	12	11	7
90	11	7	14	13	6	12	13	10	15	16	9	14	1	0	4	2	3	2	9	10	5	6	7	8		
91	40	27	48	47	28	41	44	33	45	46	21	36	10	13	14	9	16	15	45	46	32	43	37	22		
92	41	28	47	48	27	40	43	32	46	45	22	37	9	14	13	10	15	16	49	45	33	44	36	21		
93	24	23	28	27	26	25	30	31	32	33	17	29	8	7	6	5	10	9	21	22	17	18	19	20		
94	38	24	41	40	25	39	42	30	43	44	18	34	7	11	12	6	13	14	36	37	29	34	35	19		
95	39	25	40	41	24	38	34	29	37	36	19	35	6	12	11	7	14	13	44	43	30	42	34	18		
96	25	26	27	28	23	24	18	17	22	21	20	19	5	6	7	8	9	10	33	32	31	30	29	17		
1	2	3	4	5	6	7	8	9	10	11	12	13	14	15	16	17	18	19	20	21	22	23	24			

Variants of Austenite Parent

(b)  $60^\circ \langle \bar{1}\bar{1}1 \rangle$  twin variants

Variants of  $60^\circ[\bar{1}\bar{1}1]$  Twin

97	17	29	30	31	32	33	9	10	5	6	7	8	22	21	20	19	18	17	24	23	28	27	26	25
98	18	34	42	30	43	44	14	13	6	12	11	7	37	36	19	35	34	29	38	24	41	40	25	39
99	19	35	34	29	37	36	13	14	7	11	12	6	43	44	18	34	42	30	39	25	40	41	24	38
100	20	29	18	17	22	21	10	9	8	7	6	5	32	33	17	29	30	31	25	26	27	28	24	
101	21	36	44	33	45	15	16	9	14	13	10	46	45	22	37	24	44	33	49	21	36	43	33	41
102	22	37	43	32	46	45	16	19	10	13	14	9	45	49	21	36	44	33	41	28	47	48	27	40
103	7	11	12	6	13	14	2	4	0	1	2	3	2	16	15	10	13	14	9	6	5	11	7	14
104	8	7	6	5	10	9	3	2	1	0	4	2	15	16	9	14	13	10	12	6	13	14	7	

## B.2 Experimentally Observed Orientation Relationship

Variants of $60^\circ[\bar{1}\bar{1}1]$ Twin			Variants of $60^\circ[\bar{1}\bar{1}1]$ Twin		
73	37	36	19	35	34
74	22	21	20	19	18
75	45	49	21	36	44
76	46	45	22	37	43
77	32	33	17	29	31
78	43	44	18	34	42
79	36	37	29	34	35
80	23	22	17	18	19
81	49	45	33	44	36
82	45	46	32	43	37
83	33	32	31	30	29
84	44	43	30	42	34
85	13	14	7	11	12
86	10	9	8	7	6
87	15	16	9	14	13
88	16	15	10	13	14
89	9	10	5	6	7
90	14	13	6	12	11
91	48	47	28	41	40
92	47	48	27	40	41
93	28	27	26	25	24
94	41	40	25	39	38
95	40	41	24	39	35
96	27	28	23	24	25
97	25	26	21	22	23
98	30	31	26	27	28
99	34	29	37	36	19
100	18	17	22	21	20
101	44	33	45	49	21
102	43	32	46	45	22
103	12	6	13	14	15
104	7	11	30	42	34
105	13	10	15	16	9
106	14	9	16	15	10
107	7	8	9	10	5
108	11	7	14	14	13
109	20	27	47	48	27
110	21	28	47	48	27
111	24	23	28	27	26
112	38	24	41	40	25
113	35	40	41	42	38
114	25	26	27	28	23
115	35	19	36	37	29
116	19	20	21	22	17
117	36	21	49	33	44
118	37	22	45	46	32
119	29	17	33	32	31
120	38	18	24	27	28
121	33	32	33	34	35
122	33	32	33	34	35
123	34	35	36	37	38
124	34	35	36	37	38
125	34	35	36	37	38
126	34	35	36	37	38
127	34	35	36	37	38
128	34	35	36	37	38
129	34	35	36	37	38
130	34	35	36	37	38
131	34	35	36	37	38
132	34	35	36	37	38
133	34	35	36	37	38
134	34	35	36	37	38
135	34	35	36	37	38
136	34	35	36	37	38
137	34	35	36	37	38
138	34	35	36	37	38
139	34	35	36	37	38
140	34	35	36	37	38
141	34	35	36	37	38
142	34	35	36	37	38
143	34	35	36	37	38
144	34	35	36	37	38
145	34	35	36	37	38
146	34	35	36	37	38
147	34	35	36	37	38
148	34	35	36	37	38
149	34	35	36	37	38
150	34	35	36	37	38
151	34	35	36	37	38
152	34	35	36	37	38
153	34	35	36	37	38
154	34	35	36	37	38
155	34	35	36	37	38
156	34	35	36	37	38
157	34	35	36	37	38
158	34	35	36	37	38
159	34	35	36	37	38
160	34	35	36	37	38
161	34	35	36	37	38
162	34	35	36	37	38
163	34	35	36	37	38
164	34	35	36	37	38
165	34	35	36	37	38
166	34	35	36	37	38
167	34	35	36	37	38
168	34	35	36	37	38
169	34	35	36	37	38
170	34	35	36	37	38
171	34	35	36	37	38
172	34	35	36	37	38
173	34	35	36	37	38
174	34	35	36	37	38
175	34	35	36	37	38
176	34	35	36	37	38
177	34	35	36	37	38
178	34	35	36	37	38
179	34	35	36	37	38
180	34	35	36	37	38
181	34	35	36	37	38
182	34	35	36	37	38
183	34	35	36	37	38
184	34	35	36	37	38
185	34	35	36	37	38
186	34	35	36	37	38
187	34	35	36	37	38
188	34	35	36	37	38
189	34	35	36	37	38
190	34	35	36	37	38
191	34	35	36	37	38
192	34	35	36	37	38
193	34	35	36	37	38
194	34	35	36	37	38
195	34	35	36	37	38
196	34	35	36	37	38
197	34	35	36	37	38
198	34	35	36	37	38
199	34	35	36	37	38
200	34	35	36	37	38
201	34	35	36	37	38
202	34	35	36	37	38
203	34	35	36	37	38
204	34	35	36	37	38
205	34	35	36	37	38
206	34	35	36	37	38
207	34	35	36	37	38
208	34	35	36	37	38
209	34	35	36	37	38
210	34	35	36	37	38
211	34	35	36	37	38
212	34	35	36	37	38
213	34	35	36	37	38
214	34	35	36	37	38
215	34	35	36	37	38
216	34	35	36	37	38
217	34	35	36	37	38
218	34	35	36	37	38
219	34	35	36	37	38
220	34	35	36	37	38
221	34	35	36	37	38
222	34	35	36	37	38
223	34	35	36	37	38
224	34	35	36	37	38
225	34	35	36	37	38
226	34	35	36	37	38
227	34	35	36	37	38
228	34	35	36	37	38
229	34	35	36	37	38
230	34	35	36	37	38
231	34	35	36	37	38
232	34	35	36	37	38
233	34	35	36	37	38
234	34	35	36	37	38
235	34	35	36	37	38
236	34	35	36	37	38
237	34	35	36	37	38
238	34	35	36	37	38
239	34	35	36	37	38
240	34	35	36	37	38
241	34	35	36	37	38
242	34	35	36	37	38
243	34	35	36	37	38
244	34	35	36	37	38
245	34	35	36	37	38
246	34	35	36	37	38
247	34	35	36	37	38
248	34	35	36	37	38
249	34	35	36	37	38
250	34	35	36	37	38
251	34	35	36	37	38
252	34	35	36	37	38
253	34	35	36	37	38
254	34	35	36	37	38
255	34	35	36	37	38
256	34	35	36	37	38
257	34	35	36	37	38
258	34	35	36	37	38
259	34	35	36	37	38
260	34	35	36	37	38
261	34	35	36	37	38
262	34	35	36	37	38
263	34	35	36	37	38
264	34	35	36	37	38
265	34	35	36	37	38
266	34	35	36	37	38
267	34	35	36	37	38
268	34	35	36	37	38
269	34	35	36	37	38
270	34	35	36	37	38
271	34	35	36	37	38
272	34	35	36	37	38
273	34	35	36	37	38
274	34	35	36	37	38
275	34	35	36	37	38
276	34	35	36	37	38
277	34	35	36	37	38
278	34	35	36	37	38
279	34	35	36	37	38
280	34	35	36	37	38
281	34	35	36	37	38
282	34	35	36	37	38
283	34	35	36	37	38
284	34	35	36	37	38
285	34	35	36	37	38
286	34	35	36	37	38
287	34	35	36	37	38
288	34	35	36	37	38
289	34	35	36	37	38
290	34	35	36	37	38
291	34	35	36	37	38
292	34	35	36	37	38
293	34	35	36	37	38
294	34	35	36	37	38
295	34	35	36	37	38
296	34	35	36	37	38
297	34	35	36	37	38
298	34	35	36	37	38
299	34	35	36	37	38
300	34	35	36	37	38
301	34	35	36	37	38
302	34	35	36	37	38
303	34	35	36	37	38
304	34	35	36	37	38
305	34	35	36	37	38
306	34	35	36	37	38
307	34	35	36	37	3

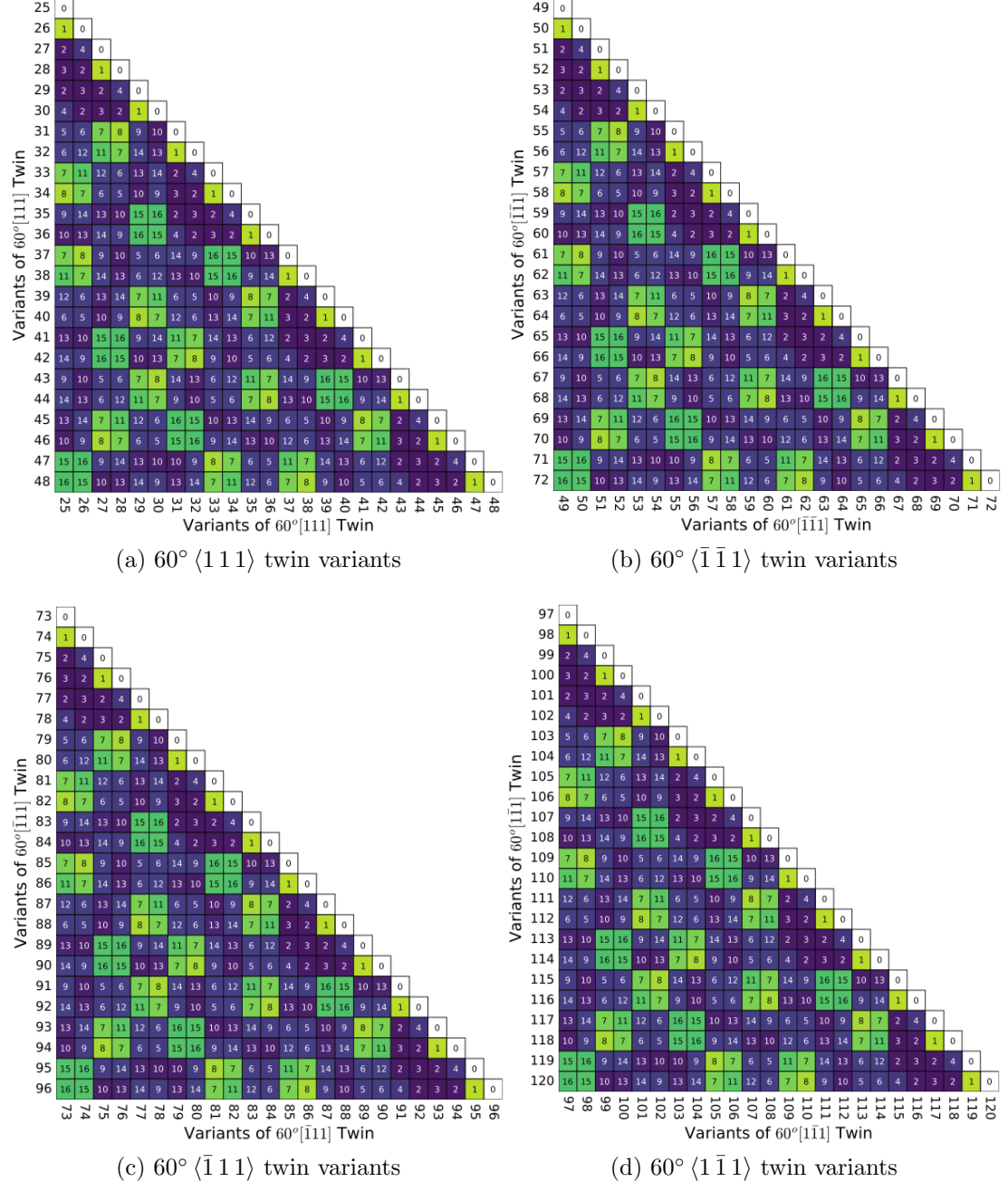


Figure B4: Composition tables displaying misorientation information for twin-generated variants intersecting with themselves.

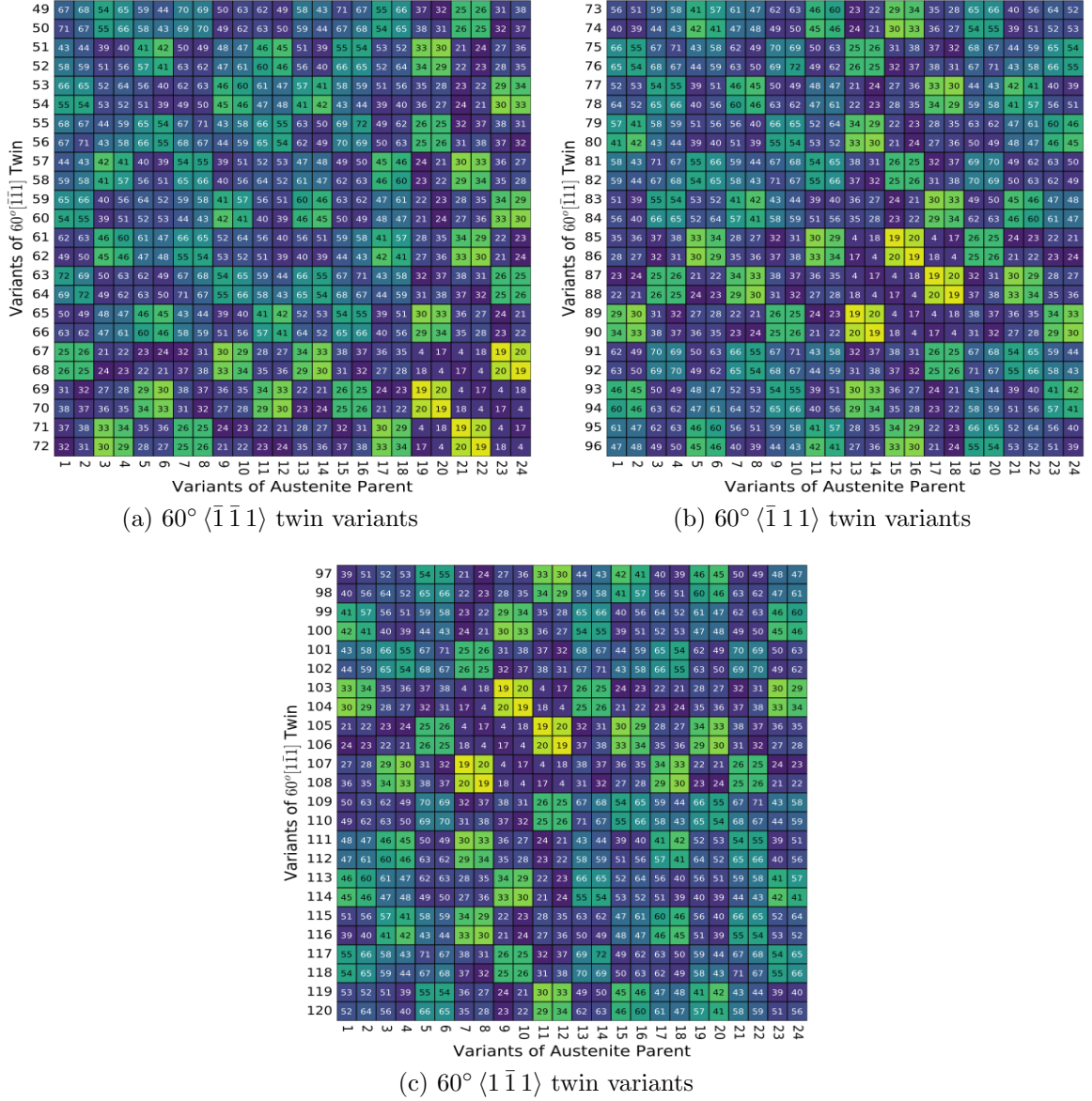
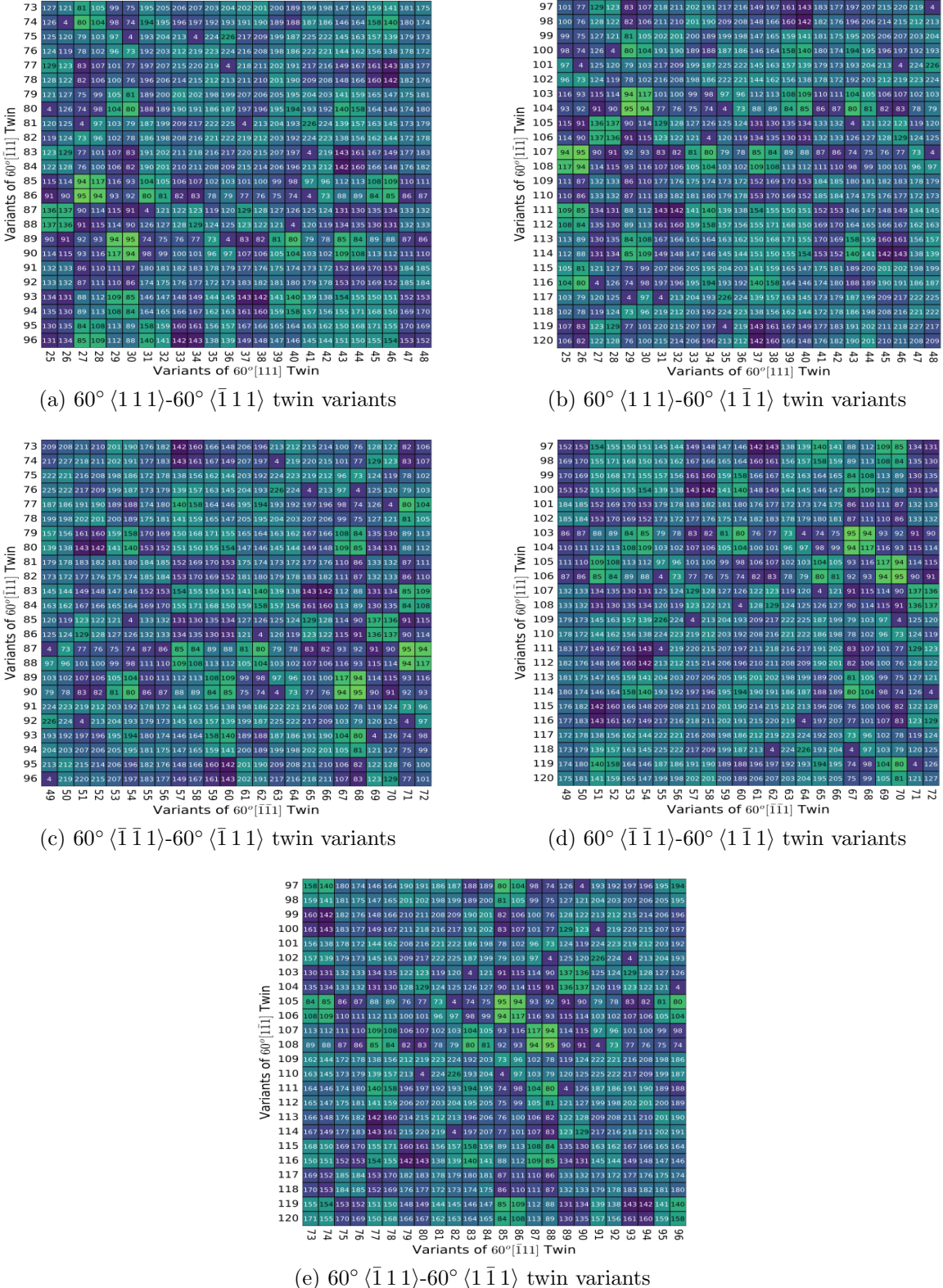


Figure B5: Composition tables displaying misorientation information for parent variants intersecting with the remaining twin-generated variants for the experimental orientation relationship.

### B.3 Kurdjumov-Sachs Orientation Relationship Applying Tetragonal Symmetry



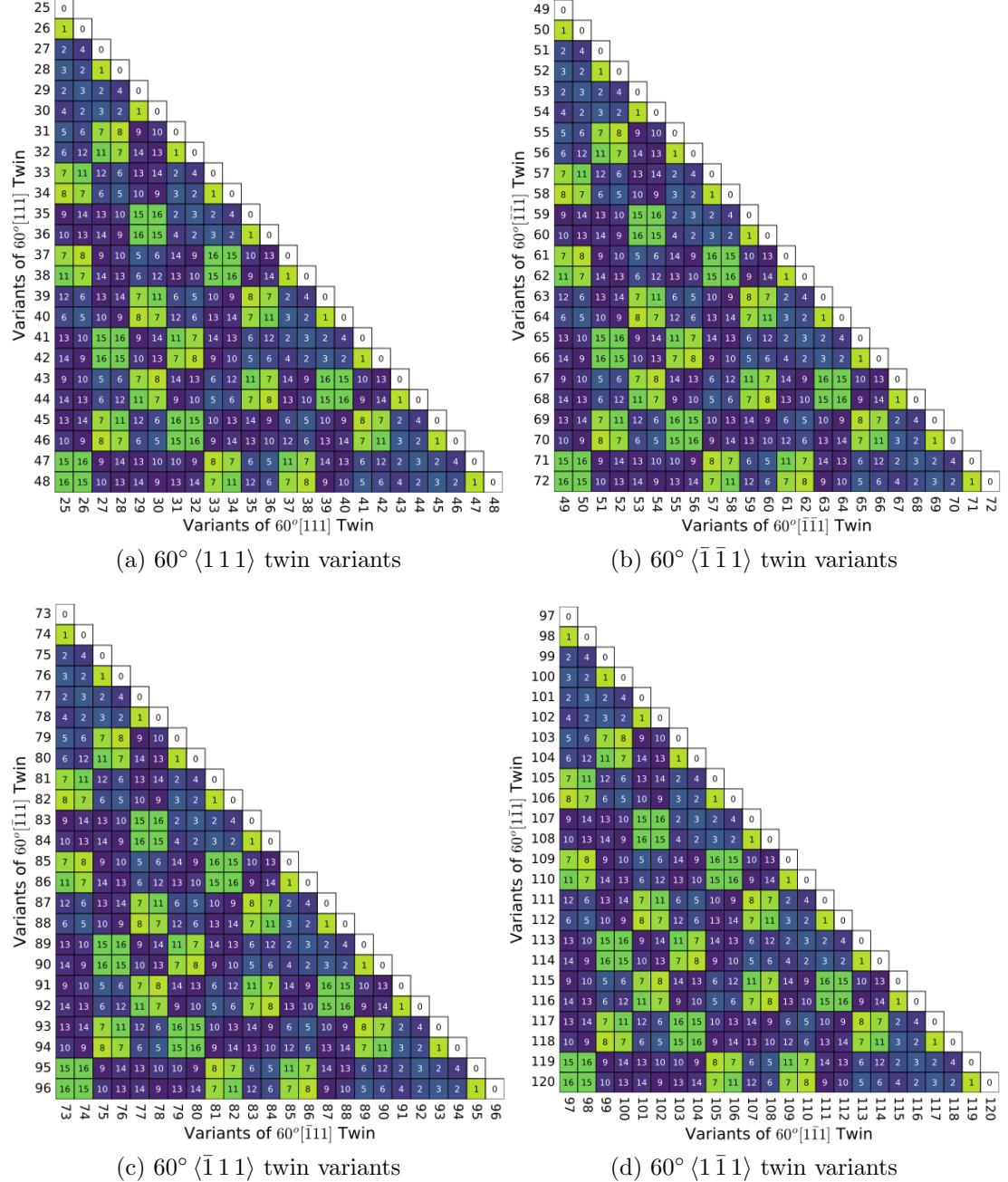


Figure B7: Composition tables showing misorientation information for twin-generated variants intersecting with themselves.

Variants of  $60^\circ \langle \bar{1} \bar{1} 1 \rangle$  Twin

49	68	69	55	66	60	45	71	70	51	64	63	50	59	44	72	68	56	67	38	33	26	27	32	39	
50	72	68	56	67	59	44	70	71	50	63	64	51	60	45	68	69	55	66	39	32	27	26	33	38	
51	44	45	40	41	42	43	51	50	49	48	47	46	52	40	56	55	54	53	34	31	22	25	28	37	
52	59	60	52	57	58	42	64	63	48	62	61	47	57	41	67	66	53	65	35	30	23	24	29	36	
53	67	66	53	65	57	41	63	64	47	61	62	48	58	42	59	60	52	57	36	29	24	23	30	35	
54	56	55	54	53	52	40	50	51	46	47	48	49	42	43	44	45	40	41	37	28	25	22	31	34	
55	69	68	45	60	66	55	68	72	44	59	67	56	64	51	70	71	50	63	27	26	33	38	39	32	
56	68	72	44	59	67	56	69	68	45	60	66	55	63	50	71	70	51	64	26	27	32	39	38	33	
57	45	44	43	42	41	40	55	56	40	52	53	54	48	49	50	51	46	47	25	22	31	34	37	28	
58	60	59	42	58	57	52	66	71	41	57	65	53	62	48	63	64	47	61	24	30	35	36	29	30	
59	66	67	41	57	65	53	60	59	42	58	57	52	61	47	64	63	48	62	23	24	29	36	35	30	
60	55	56	40	52	53	54	45	44	43	42	41	40	47	46	51	50	49	48	22	25	28	37	34	31	
61	63	64	47	61	62	48	67	66	53	65	57	41	57	52	60	59	42	58	29	36	35	30	23	24	
62	50	51	46	47	48	49	50	55	54	53	52	40	41	40	45	44	43	42	28	37	34	31	22	25	
63	71	70	51	64	63	50	66	69	55	66	60	45	67	56	68	72	44	59	33	38	39	32	27	26	
64	70	71	50	63	64	51	72	68	56	67	59	44	66	55	69	68	45	60	32	39	33	26	27	26	
65	51	50	49	48	47	46	44	45	40	41	42	43	53	54	55	56	40	52	31	34	37	28	25	22	
66	64	63	48	62	61	47	59	60	52	57	58	42	65	53	66	67	41	57	30	35	36	29	24	23	
67	26	27	22	23	24	25	33	32	31	30	29	28	35	34	39	38	37	36	17	18	17	18	19	20	21
68	27	26	25	24	23	22	38	39	34	35	36	37	30	31	32	33	28	29	19	17	18	17	21	20	20
69	32	33	28	29	30	31	39	38	37	36	35	34	23	22	27	26	25	24	20	21	17	18	17	19	19
70	39	38	37	36	35	34	32	33	28	29	30	31	24	25	26	27	22	23	21	20	19	17	18	17	18
71	38	39	34	35	36	37	37	27	26	25	24	23	22	29	28	33	32	31	30	17	19	20	21	17	18
72	33	32	31	30	29	28	26	27	22	23	24	25	36	37	38	39	34	35	18	17	21	20	19	17	18
1	2	3	4	5	6	7	8	9	10	11	12	13	14	15	16	17	18	19	20	21	22	23	24	25	
24	23	22	21	20	19	18	17	16	15	14	13	12	11	10	9	8	7	6	5	4	3	2	1		

Variants of Austenite Parent

(a)  $60^\circ \langle \bar{1} \bar{1} 1 \rangle$  twin variants

Variants of  $60^\circ \langle \bar{1} 1 1 \rangle$  Twin

73	57	52	60	59	42	58	62	48	63	64	47	61	24	23	30	35	36	29	66	67	41	57	65	53
74	41	40	45	44	43	42	48	49	50	51	46	47	25	23	31	34	37	28	55	56	40	52	53	54
75	67	66	68	72	44	59	63	50	71	70	51	64	26	27	32	39	38	33	69	68	45	60	66	55
76	66	55	69	68	45	60	64	51	70	71	50	63	27	26	33	38	39	32	68	72	44	59	67	56
77	53	54	55	56	40	52	47	46	51	50	49	48	22	25	28	37	34	31	45	44	43	42	41	40
78	65	53	66	67	41	57	61	47	64	63	48	62	23	24	29	36	35	30	24	29	36	64	63	48
79	58	42	59	60	52	57	57	41	67	66	53	65	35	30	23	24	29	36	64	63	48	62	61	47
80	42	43	44	45	40	41	52	40	56	55	54	53	34	31	22	25	28	37	51	50	49	48	47	46
81	59	44	72	68	56	67	60	45	68	69	55	66	39	32	27	26	33	38	70	71	50	63	64	51
82	60	45	68	69	55	66	59	44	72	68	56	67	38	33	26	27	32	39	71	70	51	64	63	50
83	52	40	56	55	54	53	42	43	44	45	40	41	37	28	25	22	31	34	50	51	46	47	48	49
84	57	41	67	66	53	65	58	42	59	60	52	57	36	29	24	23	30	35	63	64	47	61	62	48
85	36	37	38	39	34	35	29	28	33	32	31	30	17	19	20	21	18	17	27	26	25	24	23	22
86	29	28	33	32	31	30	36	37	38	39	34	35	18	17	21	20	19	17	26	27	22	23	24	25
87	24	25	26	27	22	23	35	34	39	38	37	36	17	18	17	19	20	21	33	32	31	30	29	28
88	23	22	27	26	25	24	30	31	32	33	28	19	17	18	17	21	20	17	38	39	34	36	37	37
89	30	31	32	28	29	23	27	26	25	24	22	27	26	24	25	20	21	17	18	17	19	39	38	37
90	35	34	39	38	37	36	24	25	26	27	22	23	21	20	19	17	18	17	32	33	28	29	30	31
91	63	50	70	71	51	64	67	56	68	72	44	59	33	38	39	32	27	26	68	69	55	66	60	45
92	64	51	70	71	50	63	66	55	69	68	45	60	32	39	38	33	26	27	72	68	56	67	59	44
93	47	46	51	50	49	48	53	54	55	56	40	52	31	34	37	28	25	22	44	45	40	41	42	43
94	61	47	64	63	48	62	65	53	66	67	41	57	30	35	36	29	24	23	59	60	52	57	58	42
95	62	48	63	47	41	57	62	50	59	42	58	29	36	35	30	23	24	67	66	53	65	57	41	
96	48	49	50	51	46	47	41	40	45	44	43	42	28	37	34	31	22	25	26	55	54	53	52	40
1	2	3	4	5	6	7	8	9	10	11	12	13	14	15	16	17	18	19	20	21	22	23	24	25
24	23	22	21	20	19	18	17	16	15	14	13	12	11	10	9	8	7	6	5	4	3	2	1	

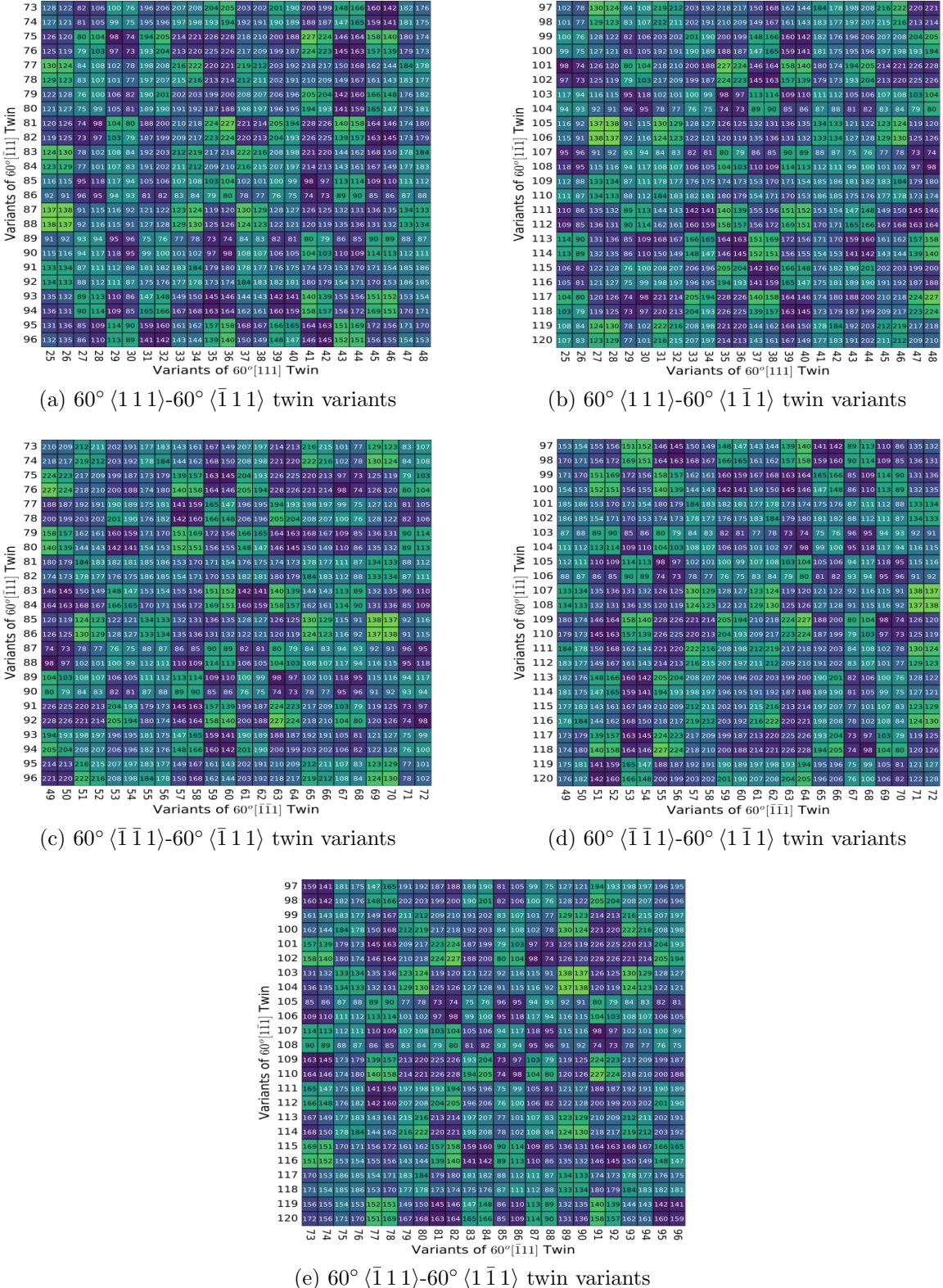
Variants of Austenite Parent

(b)  $60^\circ \langle \bar{1} 1 1 \rangle$  twin variants

Variants of  $60^\circ \langle 1 \bar{1} 1 \rangle$  Twin

107	37	36	35	34	39	38	21	20	19	17	18	17	32	33	28	29	30	31	24	25	26	27	22	23
109	51	64	63	50	71	70	33	38	39	32	27	26	68	69	55	66	60	45	67	56	68	72	44	59
110	50	63	64	51	70	71	32	39	38	33	26	27	72	68	56	67	59	44	66	55	69	68	45	60
111	49	48	47	46	51	50	31	34	37	28	25	27	37	51	50	49	48	47	46	52	40	55</td		



## Bibliography

- [1] M. Abbasi, D.I. Kim, T.W. Nelson, and M. Abbasi. EBSD and Reconstruction of Pre-transformation Microstructures, Examples and Complexities in Steels. *Materials Characterization*, 95:219–231, 2014.
- [2] M. Abbasi, T.W. Nelson, and C.D. Sorensen. Analysis of Variant Selection in Friction-stir-processed High-strength Low-alloy Steels. *Journal of Applied Crystallography*, 46:716–725, 2013.
- [3] M. Abbasi, T.W. Nelson, C.D. Sorensen, and L. Wei. An Approach to Prior Austenite Reconstruction. *Materials Characterization*, 66:1–8, 2012.
- [4] R.A. Abrahams. Low Alloy High Performance Steel. *United States Patent Application Publication*, US 2016/0369362 A1.
- [5] H. Akanuma. The Significance of Early Bronze Age Iron Objects from Kaman-Kalehöyük, Turkey. *Anatolian Archaeology Studies*, 17:313–320, 2008.
- [6] Y. Artan. Interactive Image Segmentation Using Machine Learning Techniques. In *2011 Canadian Conference on Computer and Robot Vision*, pages 264–269, May 2011.
- [7] F. Bachmann, R. Hielscher, and H. Schaeben. Inferential Statistics of Electron Backscatter Diffraction Data from within Individual Crystalline Grains. *J. Appli. Crys.*, 43:1338–1355, 2010.
- [8] E. Bae, J. Shi, and X.C. Tai. Graph cuts for curvature based image denoising. *IEEE Transactions on Image processing*, 20(5):1199–1210, 2011.
- [9] E.C. Bain. The Nature of Martensite,. *Transactions of the American Institute of Mining and Metallurgical Engineering*, 70:25, 1924.
- [10] S.K. Banerji, Jr. C.J. McMahon, and H.C. Feng. Intergranular Fracture in 4340-Type Steels: Effects of Impurities and Hydrogen. *Metallurgical Transactions A*, 9A:237–247, 1978.

- [11] T. Bayes. “An Essay Toward Solving a Problem in the Doctrine of Chance”. In *Philosophical Transactions of the Royal Society of London*, 53:370–428, 1764.
- [12] M. Beheshti, J. Faichney, and A. Gharipour. Bio-Cell Image Segmentation using Bayes Graph-Cut Model. In , 2015.
- [13] José M Bernardo and Adrian FM Smith. *Bayesian theory*, volume 405. John Wiley & Sons, 2009.
- [14] N. Bernier, L. Bracke, L. Malet, and S. Godet. An Alternative to the Crystallographic Reconstruction of Austenite in Steels. *Materials Characterization*, 89:23–32, 2014.
- [15] H. Bhadeshia and R. Honeycombe. *Steels: Microstructure and Properties*. Butterworth-Heinemann, 2017.
- [16] B.A. Bilby and J.W. Christian. The Crystallography of Martensite Transformations. *Journal of Iron and Steel Institute*, 24:122–131, 1961.
- [17] M.A. Bingham, B.K. Lograsso, and F.C. Laabs. A Statistical Analysis of the Variation in Measured Crystal Orientations Obtained through Electron Backscatter Diffraction. *Ultramicroscopy*, 110:1312–1319, 2010.
- [18] A. Borgenstam and M. Hillert. The Driving Force for Lath and Plate Martensite and the Activation Energy for Isothermal Martensite in Ferrous Alloys. *Journal de Physique III*, 7, 1997.
- [19] A. Bovik. *Handbook of Image and Video Processing*. New York: Academic, 2000.
- [20] J.S. Bowles and J.K. Mackenzie. The Crystallography of Martensite Transformations I. *Acta Metallurgica*, 2:129–137, 1954.
- [21] J.S. Bowles and J.K. Mackenzie. The Crystallography of Martensite Transformations III. Face-Centered Cubic to Body-Centered Tetragonal Transformations. *Acta Metallurgica*, 2:224–234, 1954.
- [22] J.S. Bowles and J.K. Mackenzie. The Crystallography of the  $\{225\}_F$  Transformations in Steels. *Acta Metallurgica*, 10:625–636, 1962.
- [23] Y. Boykov and V. Kolmogorov. An Experimental Comparison of Min-Cut/Max-Flow Algorithms for Energy Minimization in Vision. *IEEE Transactions on Pattern Analysis and Machine Intelligence (PAMI)*, 26(9):1124–1137, 2004.
- [24] Y. Boykov and O. Veksler. *Graph Cuts in Vision and Graphics: Theories and Applications*. Springer Science+Business Media, Inc., 2006.

- [25] A.F. Brust, T.J. Hobbs, E.J. Payton, and S.R. Niezgoda. Application of the Maximum Flow–Minimum Cut Algorithm to Segmentation and Clustering of Materials. *Microscopy and Microanalysis*, Under Review, Submitted September 13, 2018.
- [26] A.F. Brust, S.R. Niezgoda, V.A. Yardley, and E.J. Payton. Analysis of Misorientation Relationships between Austenite Parents and Twins. *Metallurgical and Materials Transactions A*, 50(2):837–855, 2019.
- [27] A.F. Brust, E.J. Payton, V. Sinha, V.A. Yardley, and S.R. Niezgoda. Characterization of Martensite Orientation Relationships in Steel from EBSD Data Using Bayesian Inference. *Metallurgical and Materials Transactions A, Under Review, Submitted 3/20/2019*, 2019.
- [28] W.G. Burgers. On the Process of Transition of the BCC Modification in the HCP Modification of Zirconium. *Physica*, 1:561–586, 1934.
- [29] J.W. Cahn and G. Kalonji. Symmetry in Solid State Transformation Morphologies. In , 1982.
- [30] A. Campbell, P. Murray, E. Yakushina, S. Marshall, and W. Ion. New Methods for Automatic Quantification of Microstructural Features Using Digital Image Processing. *Materials & Design*, 141:395–406, 2018.
- [31] C. Cayron. ARPGE: A Computer Program to Automatically Reconstruct the Parent Grains from Electron Backscatter Diffraction Data. *Journal of Applied Crystallography*, 40:1183–1188, 2007.
- [32] R.H. Chan, C.W. Ho, and M. Nikolova. Salt-and-pepper noise removal by median-type noise detectors and detail-preserving regularization. *IEEE Transactions on Image Processing*, 14(10):1479–1485, Oct 2005.
- [33] Y.H. Chen, S.U. Park, D. Wei, G. Newstadt, M. Jackson, J.P. Simmons, M. De Graef, and A.O. Hero. Statistical Estimation and Clustering of Group-invariant Orientation Parameters. *18 International Conference on Information Fusion*, pages 719–726, 2015.
- [34] J.W. Christian. Twinning and Martensite Transformation. *Journal de Physique Colloques*, 35(C7):65–76, 1971.
- [35] H. Chuang and M. Comer. A New Method for Segmentation of Noisy, Low-Contrast Image Sequences. In *Proceedings on IEEE International Conference on Circuits and Systems.*, May/June 2010.

- [36] S. Cluff, T. Nelso, R. Song, and D. Fullwood. Crystallographic Reconstruction of Parent Austenite Twin Boundaries in a Lath Martensitic Steel. *International Conference Series: Materials Science and Engineering*, 375:1–11, 2018.
- [37] M. Cohen. The Strengthening of Steel. *Transactions TSM-AIME*, 224:638–656, 1962.
- [38] M.L. Comer and E.J. Delp. Parameter Estimation and Segmentation of Noisy or Textured Images Using the EM Algorithm and MPM Estimation. In *IEEE International Conference on Image Processing*, pages 650–654, Nov 1994.
- [39] M.L. Comer and E.J. Delp. The EM/MPM Algorithm for Segmentation of Textured Images: Analysis and Further Experimental Results. *IEEE Transactions on Image Processing*, 9(10):1731–1744, 2000.
- [40] W.J. Cook, W.H. Cunningham, W.R. Pulleyblank, and A. Schriver. *Combinatorial Optimization*. John Wiley & Sons, 1998.
- [41] R.G. Davies. Influence of Martensite Composition and Content on the Properties of Dual Phase Steels. *Metallurgical Transactions A*, 9:671–679, 1978.
- [42] I. Despotović, V. Jelač, E. Vansteenkiste, and W. Philips. Noise-Robust Method for Image Segmentation. In J. Blanc-Talo, D. Bone, W. Philips, D. Popescu, and P. Scheunders, editors, *Advanced Concepts for Intelligent Vision Systems*, Berlin, Heidelberg, 2010. Springer Berlin Heidelberg.
- [43] C. Du, J.P.M. Hoefnagels, R. Vaes, and M.G.D. Geers. Block and Sub-block Boundary Strengthening in Lath Martensite. *Scripta Materialia*, 116:117–121, 2016.
- [44] L. Duval, M. Moreaud, C. Couplie, D. Jeulin, H. Talbot, and J. Angulo. Image processing for materials characterization: Issues, challenges and opportunities. In *2014 IEEE International Conference on Image Processing (ICIP)*, pages 4862–4866, Oct 2014.
- [45] ASTM E112-12. Standard Test Methods for Determining Average Grain Size, Developed by Subcommittee E04.08 on Grain Size, 2013.
- [46] N. El-Bagoury and Q. Mohsen. Gamma Prime and TCP Phases and Mechanical Properties of Thermally Exposed Nickel-Base Superalloy. *Phase Transitions*, 84(11-12):1108–1122, 2011.
- [47] M. Faessel and D. Jeulin. Segmentation of 3D Microtomographic Images of Granular Materials with the Stochastic Watershed. *Journal of Microscopy*, 239:17–31, 2010.

- [48] P. Felfer, A.V. Ceguerra, S.P. Ringer, and J.M. Cairney. Detecting and Extracting Clusters in Atom Probe Data: A Simple, Automated Method Using Voronoi Cells. *Ultramicroscopy*, 150:30–36, 2015.
- [49] L. Ford and D. Fulkerson. *Flows in Networks*. Princeton University Press, 1962.
- [50] D. Gamerman and H. Lopes. *Markov Chain Monte Carlo: Stochastic Simulation for Bayesian Inference*. Chapman and Hall/CRC, 2006.
- [51] L. Germain, N. Gey, and M. Humbert. Reliability of Reconstructed  $\beta$ -orientation Maps in Titanium Alloys. *Ultramicroscopy*, 107:1129–1135, 2007.
- [52] L. Germain, N. Gey, R. Mercier, P. Blaineau, and M. Humbert. An Advances Approach to Reconstructing Parent Orientation Maps in the Case of Approximate Orientation Relationships: Application to Steels. *Acta Materialia*, 60:4551–4562, 2012.
- [53] C.J. Geyer. Practical Markov Chain Monte Carlo. *Statistical Science*, 7(4):473–511, 1992.
- [54] E. Girault, P. Jacquest, Ph. Harlet, K. Mols, J. Van Humbeeck, E. Aernoudt, and F. Delannay. Metallographic Methods for Revealing the Multiphase Microstructure of TRIP-Assisted Steels. *Materials Characterization*, 40:111–118, 1998.
- [55] M.G. Glavicic, P.A. Kobryn, T.R. Bieler, and S.L. Semiatin. A Method to Determine the Orientation of the High-temperature Beta Phase from Measured EBSD Data for the Low-temperature Alpha Phase in Ti-6Al-4V. *Materials Science and Engineering A*, 346:50–59, 2003.
- [56] T. Gnäupel-Herold and A. Creuziger. Diffraction study of the retained austenite content in TRIP steels. *Materials Science and Engineering: A*, 528(10):3594–3600, 2011.
- [57] A.V. Goldberg and R.E. Tarjan. A New Approach to the Maximum-Flow Problem. *J. Assoc. Comp. Mach*, 35(4):921–940, 1988.
- [58] E. Gomes and L.A.I. Kerstens. Fully Automated Orientation Relationship Calculation and Prior Austenite Reconstruction by Random Walk Clustering. *IOP Conference Series: Materials Science and Engineering*, 82:1–4, 2015.
- [59] D. Greig, B. Porteous, and A. Seheult. Exact Maximum A Posteriori Estimation for Binary Images. *J. Roy. Stats. Soc.*, 51(2):271–279, 1989.
- [60] A. B. Greninger and A. R. Troiano. The mechanism of martensite formation. *Metals Transactions*, 185:590–598, 1949.

- [61] Z. Guo, C.S. Lee, and J.W. Morris. On Coherent Transformations in Steel. *Acta Materialia*, 52(19):5511–5518, 2004.
- [62] E.O. Hall. The Deformation and Ageing of Mild Steel: III Discussion of Results. *Proceedings of the Physical Society of London*, 64(9):747–753, 1951.
- [63] P. Haslberger, S. Holly, W. Ernst, and R. Schnitzer. Microstructure and Mechanical Properties of High-strength Steel Welding Consumables with a Minimum Yield Strength of 1100 MPa. *Journal of Materials Science*, 53:6968–6979, 2018.
- [64] W.K. Hastings. Monte Carlo Sampling Methods Using Markov Chains and their Applications. *Biometrika*, 57(1):97–109, 1970.
- [65] K. Hata, M. Wakita, K. Fujiwara, and K. Kawano. Development of a Reconstruction Method of Prior Austenite Microstructure Using EBSD Data of Martensite. *Nippon Steel and Sumitomo Metal Technical Report*, 114:26–31, Mar 2017.
- [66] Y. He, Q. Rao, and Y. Tan. Investigation on the Morphology of Martensite in Carbon Steels. *Journal of Central South University of Technology*, 3(2):122–134, 1996.
- [67] T. Heimann and H.P. Meinzer. Statistical shape models for 3D medical image segmentation: A review. *Medical Image Analysis*, 13(4):543–563, 2009.
- [68] A. Heinz and P. Neumann. Representation of Orientation and Disorientation Data for Cubic, Hexagonal, Tetragonal and Orthorhombic Crystals. *Acta Crystallography*, A47:780–789, 1991.
- [69] S.R. Honeycombe H.K.D.H. Bhadeshia. *Steels: 3rd Edition*. Butterworth-Heinemann, 2006.
- [70] S.H. Hong and J. Yu. Effect of Prior Austenite Grain Size on Creep Properties and On Creep Crack Growth in 3.5-Ni-Cr-Mo-V Steel. *Scripta Materialia*, 23:1057–1062, 1989.
- [71] R.M. Horn and R.O. Ritchie. Mechanisms of Tempered Martensite Embrittlement of Low Alloy Steels. *Metallurgical Transactions A*, 9A:1039–1053, 1978.
- [72] B. Hutchinson, L. Ryde, E. Lindh, and K. Tagashira. Texture in Hot Rolled Austenite and Resulting Transformation Products. *Materials Science and Engineering A*, 257:9–17, 1998.

- [73] J.M. Hyde and C.A. English. An Analysis of the Structure of Irradiation Induced Cu-Enriched Clusters in Low and High Nickel Welds. In *Symposium of Microstructural Processes in Irradiated Materials*, pages 27–30, Sept 2000.
- [74] E. Imre, J.-Y. Guillemaut, and A. Hilton. Moving Camera Registration for Multiple Camera Setups in Dynamic Scenes. In *Proceedings of the British Machine Vision Conference*, pages 38.1–38.12. BMVA Press, 2010.
- [75] G. Iyer, J. Chanussot, and A.L. Bertozzi. A graph-based approach for feature extraction and segmentation of multimodal images. In *2017 IEEE International Conference on Image Processing (ICIP)*, pages 3320–3324, Sept 2017.
- [76] T.A. Johansen. On Tikhonov regularization, bias and variance in nonlinear system identification. *Automatica*, 33(3):441 – 446, 1997.
- [77] O. Johari. *Structures and Strength of Ausformed Steels*. PhD thesis, University of California Berkeley, 1965.
- [78] C.A. Johnson. *Metallography Principles and Procedures*. LECO Corporation, 1996.
- [79] J.W. Morris Jr., C. Kinney, K. Pytlewski, and Y. Adachi. Microstructure and Cleavage in Lath Martensitic Steels. *Science and Technology of Advanced Materials*, 14:1–9, 2013.
- [80] J.Y. Kang, D.H. Kim, S.I. Baik, T.H. Ahn, Y.W. Kim, H.N. Han, K.H. Oh, H.C. Lee, and S.H. Han. Phase Analysis of Steels by Grain-Averaged EBSD Functions. *The Iron and Steel Institute of Japan International*, 51(1):130–136, 2011.
- [81] R.R. Keller, A. Roshko, R.H Geiss, K.A. Bertness, and T.P. Quinn. EBSD Measurement of Srstrains in GaAs Due to Oxidation of Buried AlGaAs Layers. *Microelectronic Engineering*, 75(1):96–102, 2004.
- [82] P.M. Kelly, A. Jostons, and R.G. Blake. The Orientation Relationship Between Lath Martensite and Austenite in Low Carbon, Low Alloy Steels. *Acta Metallurgica et Materialia*, 38(6):1075–1081, 1990.
- [83] K. Kimura, N. Ohi, K. Shimazu, and T. Matsuo. Prior Austenite Grain Size on High Temperature Creep Properties of Cr-Mo-V Rotor Steel. *Scripta Materialia*, 21:19–22, 1987.
- [84] H. Kitahara, R. Ueji, N. Tsuji, and Y. Minamino. Crystallographic Features of Lath Martensite in Low-Carbon Steel. *Acta Materialia*, 54:1279–1288, 2006.

- [85] H. Kitahara, R. Ueji, M. Ueda, N. Tsuji, and Y. Minamino. Crystallographic Analysis of Plate Martensite in Fe-28/5 at % Ni by FE-SEM/EBSD. *Materials Characterization*, 54:378–386, 2005.
- [86] G. Krauss. Steels Heat Treatment and Processing Principles. *ASM International*, 1990.
- [87] G. Krauss. *Steels: Processing, Structure, and Performance*. ASM International, 2015.
- [88] G. Krauss and A.R. Marder. The Morphology of Martensite in Iron Alloys. *Metallurgical Transactions*, 2:2343–2357, 1971.
- [89] G. Kurdjumow and G. Sachs. Über der Mechanismus der Stahlhärtung (On the Mechanism of Hardening of Steel). *Z. Physik*, 64:325–343, 1930.
- [90] F.S. LaPera. Improved Etching Technique for the Determination of Percent Martensite in High-Strength, Dual-Phase Steels. *Metallography*, 12:263–268, 1978.
- [91] C. Lee and J. Han. Learning Markov Random Field Image Prior for Pixelation Removal of Fiber Microscopy Using Sparse Coding Based on Bayesian Framework. *International Winter Workshop on Brain-Computed Interface (BCI)*, 2013.
- [92] M. Leskó, Z. Kato, and A. Nagy. Live Cell Segmentation in Fluorescence Microscopy via Graph Cut. In , pages 1485–1488, 2010.
- [93] Z. Li, X. Sun, W. Cao, Q. Yong, Z. Yang, H. Dong, and Y. Weng. Ausforming Effects on Anisotropy of Mechanical Properties in HSLA Martensitic Steel. *Science China Technological Sessions*, 55(7):1806–1813, 2012.
- [94] S.P. Lloyd. Least Squares Quantization in PCM. *IEEE Transactions on Information Theory*, 28(2):129–137, 1982.
- [95] J.K. Mackenzie and J.S. Bowles. The Crystallography of Martensite Transformations II. *Acta Metallurgica*, 2:224–234, 1954.
- [96] J.K. Mackenzie and J.S. Bowles. The Crystallography of Martensite Transformations IV. Body-Centered Cubic to Orthorhombic Transformations. *Acta Metallurgica*, 5:137–149, 1957.
- [97] J. MacQueen. Some Methods for Classification and Analysis of Multivariate Observations. In *Proceedings on the Fifth Berkeley Symposium of Mathematical Statistics and Probability*, volume 1, pages 281–297, 1967.

- [98] J. MacSleynne, M.D. Uchic, J.P. Simmons, and M. De Graef. Three-dimensional analysis of secondary precipitates in Ren-88 DT and UMF-20 superalloys. *Acta Materialia*, 57(20):6251–6267, 2009.
- [99] L. Malet, M.R. Barnett, P.J. Jacques, and S. Godeta. Variant Selection During the  $c\text{-}\alpha_b$  Phase Transformation in Hot-Rolled Bainitic TRIP-aided Steel. *Scripta Materialia*, 61:520–523, 2009.
- [100] J. Marroquin, S. Mitter, and T. Poggio. Probabilistic Solution of Ill-Posed Problems in Computational Vision. *J. Am. Stats. Assoc.*, 82(397):76–89, 1987.
- [101] S. Matsuda, T. Inoue, H. Mimura, and Y. Okamura. Toward Improved Ductility and Toughness. *Climax Molybdenum Development Company Ltd*, pages 45–66, 1971.
- [102] T. McInerney and D. Terzopoulos. Topology Adaptive Deformable Surfaces for Medical Image Volume Segmentation. *IEEE Transactions on Medical Imaging*, 18(10):840–850, Oct 1999.
- [103] N. Metropolis, A.W. Rosenbluth, M.N. Rosenbluth, A.H. Teller, and E. Teller. Equation of State Calculations by Fast Computing Machines. *Journal of Chemical Physics*, 21(6):1087–1092, June 1953.
- [104] O.O. Miller and M.J. Day. Ferric chloride etchant for austenite grain size of low-carbon steel. *Progress in Materials Science*, 56:692–695, 1949.
- [105] G. Miyamoto, N. Iwata, N. Takayama, and T. Furuhara. Mapping the Parent Austenite Orientation Reconstructed from the Orientation of Martensite by EBSD and its Application to Ausformed Martensite. *Acta Materialia*, 58:6393–6403, 2010.
- [106] G. Miyamoto, N. Iwata, N. Takayama, and T. Furuhara. Quantitative Analysis of Variant Selection in Ausformed Lath Martensite. *Acta Materialia*, 60:1139–1148, 2012.
- [107] G. Miyamoto, N. Iwata, N. Takayama, and T. Furuhara. Variant Selection of Lath Martensite and Bainite Transformation in Low Carbon Steel by Ausforming. *Journal of Alloys and Compounds*, 577:S528–S532, 2013.
- [108] G. Miyamoto, N. Takayama, and T. Furuhara. Accurate Measurement of the Orientation Relationship of Lath Martensite and Bainite by Electron Backscatter Diffraction Analysis. *Scripta Materialia*, 60:1113–1116, 2009.
- [109] P.P. Mondal, G. Vicidomini, and A. Diaspro. Markov random field aided bayesian approach for image reconstruction in confocal microscopy. *Journal of applied Physics*, 102(4):044701, 2007.

- [110] S. Morito, Y. Adachi, and T. Ohba. Morphology and Crystallography of Sub-Blocks in Ultra-Low Carbon Lath Martensite Steel. *Materials Transactions*, 50(8):1919–1923, 2009.
- [111] S. Morito, H. Tanaka, R. Konishi, and T. Maki. The morphology and crystallography of lath martensite in Fe-C alloys. *Acta Materialia*, 51:1789–1799, 2003.
- [112] S. Morito, H. Tanaka, R. Konishi, and T. Maki. The morphology and crystallography of lath martensite in Fe-C alloys. *Acta Materialia*, 51:1789–1799, 2003.
- [113] S. Morito, H. Yoshida, T. Maki, and J.W. Morris. Effect of Block Size on the Strength of Lath Martensite in Low Carbon Steels. *Materials Science and Engineering A*, 438–440:237–240, 2006.
- [114] M. Natori, Y. Futamura, T. Tsuchiyama, and S. Takaki. Difference in Recrystallization Behavior Between Lath Martensite and Deformed Ferrite in Ultralow Carbon Steel. *Scripta Materialia*, 53:603–608, 2005.
- [115] A Neubauer. Tikhonov Regularisation for Non-Linear Ill-Posed Problems: Optimal Convergence Rates and Finite-Dimensional Approximation. *Inverse Problems*, 5(4):541–557, 1989.
- [116] M. Nikravesh, M. Naderi, and G.H. Akbari. Influence of Hot Plastic Deformation and Cooling Rate on Martensite and Bainite Start Temperatures in 22MnB5 Steel. *Materials Science and Engineering*, 540:24–29, 2012.
- [117] Z. Nishiyama. X-ray Investigation of the Mechanism of the Transformation from Face-Centered Cubic to Body-Centered Cubic. *Scientific Republic*, 23:637–664, 1934.
- [118] Z. Nishiyama, M.E. Fine, and C.M. Wayman. *Martensitic Transformation*. Academic Press, Materials Science and Technology, 1978.
- [119] S.J. Norton, J.A. Simmons, A.H. Kahn, and H.N.G. Wadley. Research on Inverse Problems in Materials Science and Engineering. *Signal Processing and Pattern Recognition in Nondestructive Evaluation of Materials*, pages 1–21, 1988.
- [120] T. Ohmura, K. Tsuzaki, and S. Matsuoka. Nanohardness Measurement of High-purity Fe-C Martensite. *Scripta Materialia*, 45:889–894, 2001.
- [121] T. Ohmura, K. Tsuzaki, and S. Matsuoka. Evaluation of the Matrix Strength of Fe-0.4 wt % Tempered Martensite Using Nanoindentation Techniques. *Philosophical Magazine A*, 82(10):1903–1910, 2002.

- [122] B.A. Olshausen. Bayesian Probability Theory. Retrieved from: <http://www.rctn.org/bruno/npb163/bayes.pdf>, 2004.
- [123] N. Otsu. A Threshold Selection Method from Gray-Level Histograms. *IEEE Transactions on Systems*, 9(1):62–66, 1979.
- [124] E. J. Payton and G. Nolze. The backscatter electron signal as an additional tool for phase segmentation in EBSD. *Microscopy and Microanalysis*, 19:929–941, 2013.
- [125] E. J. Payton, P. J. Phillips, and M. J. Mills. Semi-automated characterization of the gamma prime phase in Ni-based superalloys via high-resolution backscatter imaging. *Materials Science and Engineering A*, 527:2684–2694, 2010.
- [126] E. J. Payton, P. J. Phillips, and M. J. Mills. Stereology of Backscatter Electron Images of Etched Surfaces for Characterization of Particle Size Distributions and Volume Fractions: Estimation of Imaging Bias Via Monte Carlo Simulations. *Materials Characterization*, 62(6):563–574, 2011.
- [127] E.J. Payton, A. Aghajani, F. Otto, G. Eggler, and V.A. Yardley. On the Nature of Internal Interfaces in a Tempered Martensite Ferritic Steel and their Evolution During Long-Term Creep. *Scripta Materialia*, 66:1045–1048, 2012.
- [128] N.J. Petch. The Cleavage Strength of Polycrystals. *Journal of the Iron and Steel Institute of London*, 173:25–28, 1953.
- [129] R. Petrov, L. Kestens, A. Wasilkowska, and Y. Houbaert. Microstructure and Texture of a Lightly Deformed TRIP-Assisted Steel Characterized by Means of the EBSD Technique. *Materials Science and Engineering A*, 447:285–297, 2007.
- [130] A.H. Pham, T. Ohba, S. Morito, and T. Hayashi. Application of Netwon’s Method for Precise Calculation of Parent Orientation and Orientation Relationship from Orientations of Daughter Phase. *Materials Characterization*, 132:108–118, 2017.
- [131] T Poggio, H Voorhees, and A Yuille. A Regularized Solution to Edge Detection. *Journal of Complexity*, 4(2):106–123, 1988.
- [132] S. Preethi and D. Narmadha. A Survey on Image Denoising Techniques. *International Journal of Computer Applications*, 58(6):27–30, Nov 2012.
- [133] A.L. Ramírez, J. Porcayo-Calderon, Z. Mazur, V.M. Salinas-Bravo, and L. Martinez-Gomez. Microstructural Changes During High Temperature Service of a Cobalt-Based Superalloy First Stage Nozzle. *Advances in Materials Science and Engineering*, 2016:1–7, May 2016.

- [134] V. Randle, G.S. Rohrer, H.M. Miller, M. Coleman, and G.T. Owen. Five-parameter Grain Boundary Distribution of Commercially Grain Boundary Engineering Nickel and Copper. *Acta Materialia*, 10:2363–2373, 2008.
- [135] C. Ranger, V. Tari, S. Farjami, M.J. Merwin, L. Germain, and A. Rollet. Austenite Reconstruction Elucidate Prior Grain Size Dependence on Toughness in Low Alloy Steel. *Metallurgical and Materials Transactions A*, 49:4521–4535, 2018.
- [136] P. Rodríguez. Total Variation Regularization Algorithms for Images Corrupted with Different Noise Models: A Review. *Journal of Electrical and Computer Engineering*, 2013:1–18, 2013.
- [137] B.P.J. Sandvik and C.M. Wayman. Characteristics of Lath Martensite: Part 1. Crystallographic and Substructural Features. *Metallurgical Transactions: A*, 14A:809–822, 1983.
- [138] O. Sherby, J. Wadsworth, D. Lesuer, and C. Syn. The c/a Ratio in Quenched Fe-C and Fe-N Steels - A Heuristic Story. In , July 2006.
- [139] A. Shibata, S. Morito, T. Furuhara, and T. Maki. Substructures of Lenticular Martensites with Different Martensite Start Temperatures in Ferrous Alloys. *Acta Materialia*, 57(2):483–492, 2009.
- [140] H. Shigeta, T. Mashita, T. Kaneko, J. Kikuta, S. Senoo, H. Takemura, H. Matsuda, and M. Ishii. A Graph Cuts Image Segmentation Method for Quantifying Barrier Permeation in Bone Tissue. In , pages 16–19, 2014.
- [141] T. Shinozaki, T. Nakanishi, K. Suzuki, and H. Miura. Measurement of the strength of a grain boundary in electroplated copper thin-film interconnections by using micro tensile-test. In *2016 IEEE 37th International Electronics Manufacturing Technology (IEMT) 18th Electronics Materials and Packaging (EMAP) Conference*, pages 1–5, Sept 2016.
- [142] J.P. Simmons, P. Chuang, M. Comer, J.E. Spowart, M.D. Uchic, and M.D. Graef. Application and Further Development of Advanced Image Processing Algorithms for Automated Analysis of Serial Section Image Data. *Mod. Sim. Mat. Sci. Eng.*, 17:1–22, 2009.
- [143] V. Sinha, E.J. Payton, M. Gonzales, R.A. Abrahams, and B.S. Song. Delination of Prior Austenite Grain Boundaries in a Low-Alloy High-Performance Steel. *Metallography, Microstructure, and Analysis*, 6:610–618, 2017.
- [144] M. Soni, A. Khare, and S. Jain. Problem of Denoising in Digital Image Processing and its Solving Techniques. *International Journal of Emerging Technology and Advanced Engineering*, 4(4):244–250, Apr 2014.

- [145] John M. Sosa, Daniel E Huber, Brian Welk, and Hamish L. Fraser. Development and Application of MIPAR<sup>TM</sup>: A Novel Software Package for Two- and Three-Dimensional Microstructural Characterization. *Integrating Materials and Manufacturing Innovation*, 3:10, 2014.
- [146] E. Soubies, P. Weiss, and X. Descombes. Graph Cut Based Segmentation of Predefined Shapes: Applications to Biological Imaging. In A. Fred and M. De Marsico, editors, *Pattern Recognition Applications and Methods*, pages 153–170. Springer International Publishing, 2015.
- [147] G.R. Speich and W.C. Leslie. Tempering of Steel. *Metallurgical and Materials Transactions B*, 3(5):1043–1054, 1972.
- [148] L.T. Stephenson, M.P. Moody, P.V. Liddicoat, and S.P. Ringer. New Techniques for the Analysis of Fine-Scaled Clustering Phenomena within Atom Probe Tomography (APT). *Microstructure Microanalysis*, 13:448–463, 2007.
- [149] A. Stormvinter, P. Hedström, and A. Borgestam. A Transmission Electron Microscopy Study of Plate Martensite Formation in High-carbon Low Alloy Steels. *Journal of Materials Science and Technology*, 29(4):373–379, 2013.
- [150] T. Nyysönen and M. Isakov and P. Peura and V.T. Kuokkala. Iterative Determination of the Orientation Relationship Between Austenite and Martensite from a Large Amount of Grain Pair Misorientations. *Metallurgical and Materials Transactions A*, 47:2587–2590, 2016.
- [151] I. Tamura, K. Tsuzaki, and T. Maki. Morphology of Lath Martensite Formed From Deformed Austenite In 18 % Ni Maraging Steel. *Journal de Physique Colloques*, 43(C4):551–556, 1982.
- [152] W. Tan. *Investigations of phase transformations in AISI 5160 steel and partially stabilized zirconia via electron backscatter diffraction based techniques*. PhD thesis, Alfred University, 2017.
- [153] W. Tan, D.W. Lipke, S. Dziaszyk, and E.J. Payton. On Quantitatively Identifying Different Constituents in Multicomponent Steel Microstructures in EBSD. *Manuscript submitted for publication*, 2018.
- [154] R. Tibshirani. Regression Shrinkage and Selection via the LASSO. *Journal of the Royal Statistical Society. Series B (Methodological)*, 58(1):267–288, 1996.
- [155] A.S. Tolba and H.M. Raafat. Multiscale Image Quality Measures for Defect Detection in Thin Films. *The International Journal of Advanced Manufacturing Technology*, 79(1):113–122, Jul 2015.

- [156] V. Torre and T. A. Poggio. On Edge Detection. *IEEE Transactions on Pattern Analysis and Machine Intelligence*, PAMI-8(2):147–163, Mar 1986.
- [157] M. Uchic and J. MacSleyn. Ground Truth Segmentation Image. <http://www.bluequartz.net/binaries/Data/Rene88DT-GT.zip>, 2006. [Online; accessed 08-August-2018].
- [158] M. Ueda, H. Yasuda, and Y. Umakoshi. Effect of Grain Boundary on Martensite Transformation Behaviour in Fe-32 at.%Ni Bicrystals. *Science and Technology of Advanced Materials*, 3:171–179, 2001.
- [159] O. Veksler. Extracting dense features for visual correspondence with graph cuts. In *2003 IEEE Computer Society Conference on Computer Vision and Pattern Recognition, 2003. Proceedings*, volume 1, pages I689–I694, June 2003.
- [160] C.S. Da Costa Viana, M.P. Butron-Guillen, and J.J. Jonas. A Variant Selection Model for the Prediction of FCC-to-BCC Transformation Textures. *Textures and Microstructures*, 26–27:599–610, 1996.
- [161] J.R. Vilella. *Metallographic Technique for Steel*. American Society for Metals, 1938.
- [162] J. Waggoner, Y. Zhou, J. Simmons, M. De Graef, and S. Wang. 3D Materials Image Segmentation by 2D Propagation: A Graph-Cut Approach Considering Homomorphism. *IEEE Transactions on Image Processing*, 22(12):5282–5293, 2013.
- [163] J. Waggoner, Y. Zhou, J. Simmons, M. De Graef, and S. Wang. 3D Materials Image Segmentation by 2D Propagation: A Graph-Cut Approach Considering Homomorphism. *IEEE Transactions on Image Processing*, 22(12):5282–5293, Dec 2013.
- [164] J. Waggoner, Y. Zhou, J. Simmons, M. De Graef, and S. Wang. Graph-Cut Based Interactive Segmentation of 3D Materials-Science Images. *Machine vision and applications*, 25(6):1615–1629, 2014.
- [165] C. Wang, M. Wang, J. Shi, W. Hui, and H. Dong. Effect of Microstructure Refinement on the Strength and Toughness of Low Alloy Martensitic Steel. *Journal of Materials Science and Technology*, 23(5), 2007.
- [166] G. Wassermann. Über den Mechanismus der  $\alpha -> \gamma$  Umwandlung des Eisens (On the Mechanism of the  $\alpha -> \gamma$  Transformation of Iron). *Mitteilungen aus dem Kaiser Wilhelm Institut für Eisenforschung*, 17:149–155, 1935.
- [167] C.M. Wayman. *Introduction to the Crystallography of Martensitic Transformations*. Macmillan, Macmillan series in Materials Science, 1964.

- [168] C.M. Wayman. Shear Transformations and Microstructure. *Metallography*, 8:105–130, 1975.
- [169] M.S. Wechsler, D.S. Lieberman, and T.A. Read. On the Theory of the Formation of Martensite. *Transactions AIME*, 197:1503–1515, 1953.
- [170] H. Whitt. *Creep and Creep-fatigue Deformation Studies on 22V and P91 Creep-strength Enhanced Ferritic Steels*. PhD thesis, The Ohio State University, 2019.
- [171] J. Wills, S. Agarwal, and S. Belongie. What went where [motion segmentation]. In *Computer Vision and Pattern Recognition, 2003. Proceedings. 2003 IEEE Computer Society Conference on*, volume 1, pages I–I. IEEE, 2003.
- [172] N.J. Wittridge, J.J. Jonas, and J.H. Root. A Dislocation-based Model for Variant Selection During the  $\gamma$ -to- $\alpha$  Transformation. *Metallurgical and Materials Transactions A*, 32A:889–901, 2001.
- [173] S. Wright, M.M. Nowell, and D.P. Fields. A Review of Strain Analysis Using Electron Backscatter Diffraction. *Microscopy and Microanalysis*, 17(3):316–329, June 2011.
- [174] J. Wu, P.J. Wray, C.I. Garcia, M. Hua, and A.J. DeArdo. Image quality analysis: A new method of characterizing microstructures. *ISIJ international*, 45(2):254–262, 2005.
- [175] V.A. Yardley, E.J., T. Matsuzaki, R. Sugiura, A.T. Yokobori Jr., S. Tsurekawa, and Y. Hasegawa. EBSD analysis of creep cracking in a 12 wt.% Cr tempered martensite ferritic steel. In *Proceedings of the 12th international conference on creep and fracture of engineering materials and structures, Kyoto, Japan*, 2012.
- [176] V.A. Yardley, S. Fahimi, and E.J. Payton. Classification of Creep Crack and Cavitation Sites. *Materials Science and Technology*, 31:547–553, 2015.
- [177] V.A. Yardley and E.J. Payton. The Austenite-Martensite/Bainite Orientation Relationship: Characterisation Parameters and their Application. *Materials Science and Technology*, 30:1125–1130, 2014.
- [178] V.A. Yardley, E.J. Payton, T. Matsuzaki, R. Sugiura, A.T. Yokobori Jr., S. Tsurekawa, and Y. Hasegawa. EBSD analysis of creep cracking in a 12 wt.% Cr tempered martensite ferritic steel. In *Proceedings of the 12th international conference on creep and fracture of engineering materials and structures, Kyoto, Japan*, 2012.
- [179] S. Zaafferer, P. Romano, and F. Friedel. EBSD As a Tool to Identify and Quantify Bainite and Ferrite in Low-Alloyed Al-TRIP Steels. *Journal of Microscopy*, 230:499–508, 2008.

- [180] J. Zelenty, A. Dahl, J. Hyde, G.D.W. Smith, and M. Moody. Detecting Clusters in Atom Probe Data with Gaussian Mixture Models. *Microstructure Microanalysis*, 23:269–278, 2017.
- [181] C. Zhang, Q. Wang, J. Ren, R. Li, M. Wang, F. Zhang, and K. Sun. Effect of Martensite Morphology on Mechanical Properties of an As-quenched and Tempered 25CrMo48V Steel. *Materials Science and Engineering A*, 534:339–346, 2012.
- [182] J. Zhang, W. Modestino, and D.A. Langan. Maximum-Likelihood Parameter Estimation for Unsupervised Stochastic Model-Based Image Segmentation. *IEEE Transactions on Image Processing*, 3(4):404–420, 1994.
- [183] Y. Zhu, A. Wang, and J. Ma. Two-Phase Image Segmentation with the Competitive Learning Based Chan-Vese (CLCV) Model. In D.S. Huang, V. Bevilacqua, J.C. Figueroa, and P. Premaratne, editors, *Intelligent Computing Theories*, pages 183–191, Berlin, Heidelberg, 2013. Springer Berlin Heidelberg.
- [184] D.C. Zipperman. *Metallographic Handbook*. PACE Technologies, 2011.
- [185] N.Y. Zolotorevsky, S.N. Panpurin, A.A. Zisman, and S.N. Petrov. Effect of Aus-forming and Cooling Condition on the Orientation Relationship in Martensite and Bainite of Low Carbon Steels. *Materials Characterization*, 107:278–282, 2015.